Forschungszentrum Karlsruhe
in der Helmholtz-Gemeinschaft

Wissenschaftliche Berichte
FZKA 6854

Limit Strains for Severe Accident Conditions Final Report of the EU-project LISSAC

Contract No. FIKS-CT1999-00012

Compiled by

R. Krieg
Programm Nukleare Sicherheitsforschung

M. Seidenfuß
Staatliche Materialprüfungsanstalt,
Universität Stuttgart

Oktober 2003

Forschungszentrum Karlsruhe

in der Helmholtz-Gemeinschaft

Wissenschaftliche Berichte

FZKA 6854

Limit Strains for Severe Accident Conditions

Final Report of the EU-project LISSAC

Contract No. FIKS-CT1999-00012

Compiled by

R. Krieg
Co-ordinator of the Project
Programm Nukleare Sicherheitsforschung

and

M. Seidenfuß
Staatliche Materialprüfungsanstalt, Universität Stuttgart

Forschungszentrum Karlsruhe GmbH, Karlsruhe

2003

Impressum der Print-Ausgabe:

Als Manuskript gedruckt
Für diesen Bericht behalten wir uns alle Rechte vor

Forschungszentrum Karlsruhe GmbH
Postfach 3640, 76021 Karlsruhe

Mitglied der Hermann von Helmholtz-Gemeinschaft
Deutscher Forschungszentren (HGF)

ISSN 0947-8620

Contributions by

B. Dolensky, T. Jordan, M. Lux, T. Malmberg, G. Messemer, H. Rieger,
Forschungszentrum Karlsruhe (FZK/IRS);

J. Aktaa, E. Diegele, D. Hofer, Mrs. E. Materna-Morris, R. Schmitt,
Forschungszentrum Karlsruhe (FZK/IMF);

P. Julisch, H.-J. Hädrich, H.-P. Seebich,
Staatliche Materialprüfungsanstalt Stuttgart (MPA);

D. Kalkhof,
Paul Scherrer Institut (PSI);

Mrs. H. Talja, H. Keinänen, P. H. Pankakoski,
Technical Research Centre of Finland (VTT);

G. Solomos, E. Pizzinato,
European Commission, Joint Research Centre Ispra (JRC);

E. Aifantis, I. Tsagrakis,
Aristotle University of Thessaloniki (AUT);

L. Cizelj, M. Kovac,
Institut Jozef Stefan (IJS);

C. Caroli,
Ente per le Nuove tecnologie, l'Energia e l'Ambiente (ENEA);

J. H. Fokkens, J. M. Church, S. de Groot,
Nuclear Research and consultancy Group (NRG);

S. Bhandari, C. Benhamou, K. Schramm,
Framatome ANP (Framatome);

P. Verón,
Equipos Nucleares S.A. (ENSA);

R. Kieselbach, G. Hartmann,
Swiss Federal Laboratories for Material Research (EMPA);

Support for preparation of this report:

G. Hailfinger, FZK/IRS

Administrative matters:

H. Plitz, FZK/NUKLEAR

Summary

The local failure strains of essential reactor vessel components are investigated. The size influence of the components is of special interest. Typical severe accident conditions including elevated temperatures and dynamic loads are considered.

The main part of work consists of test families with specimens under uniaxial and biaxial static and dynamic loads. Within one test family the specimen geometries and the load conditions are similar, the temperature is the same; but the size is varied up to reactor dimensions. Special attention is given to geometries with a hole or a notch causing non-uniform stress and strain distributions typical for reactor components. There are indications that for such non-uniform distributions size effects may be stronger than for uniform distributions. Thus size effects on the failure strains and failure processes are determined under realistic conditions.

Several tests with nominal identical parameters are performed for small size specimens. In this way some information is obtained about the scatter. A reduced number of tests is carried out for medium size specimens and only a few tests are carried out for large size specimens to reduce the costs to an acceptable level. To manufacture all specimens sufficient material was available from the unused reactor pressure vessel Biblis C consisting of the material 22NiMoCr37. Thus variations of the mechanical material properties, which could impair the interpretation of the test results, are quite small. This has been confirmed by an adequate number of additional quality assurance tests.

A key problem was the definition of failure and the determination of the local strains at failure for very different specimens under varying load conditions. Here appropriate methods had to be developed including the so-called “vanishing gap method” and the “forging die method”. They are based on post test geometrical measurements of the fracture surfaces and reconstructions of the related strain fields using finite element calculations, for instance.

To deepen the understanding of structural degradation and fracture and to allow extrapolations, advanced computational methods including damage models have been developed and validated. The problems to be treated here are quite difficult. Micro-structural effects, for instance, play an important role. Therefore several approaches were tried in parallel. In some cases so-called non-local concepts, in other cases the description of stochastic properties at the grain size level are considered.

The experimental results indicate that stresses versus dimensionless deformations are approximately size independent up to failure for specimens of similar geometry under similar load conditions. Also the maximum stress is approximately size independent, if failure occurs after the maximum stress is reached.

Cracks are initiated, if the local equivalent strain – here expressed as a true or logarithmic strain, respectively – reaches a critical value, called the local failure strain. It turned out to be more than 50 % for large specimens approaching the dimensions of the reactor pressure vessel.

The local failure strains are size dependent. They reach values around 150 % for small specimens with thicknesses or diameters of a few millimetres.

The parameter describing the size effect is the radius of holes or notches located in critical specimen regions. It is very remarkable and it simplifies the applications that the shape of the specimen and the type of load plays a minor role, only.

Some of the above findings about size effects can be understood by theoretical investigations considering the stochastic, micro structural character of the material. However quantitative predictions based on micro structural models are still beyond the current knowledge.

As expected, the scatter of the results on structural failure is considerable. However statistical evaluations indicate that the failure strains will hardly fall below a lower threshold.

Thus limit strains, i.e. limit values for true equivalents strains depending on the hole or notch radius in the critical specimen region could be proposed. These limit strains are valid for temperatures up to 400 °C. Dynamic loads are included. Limit strains for higher temperatures up to 850 °C are also discussed but their reliability is restricted. If in severe accidents the proposed limit strains will not be exceeded, it can be assumed that the structure will not fail.

Using the limit strains – or acceptable strains – a more realistic strain based evaluation concept can be employed for structural mechanics analyses of severe accident consequences. Furthermore the results on size effects will help to examine, whether findings from small scale model experiments can be converted to reactor conditions.

The applicability of the results can be extended to other geometries and load conditions by using the recommended theoretical models. However, in any case, care must be taken when the stress triaxiality is higher than in the LISSAC specimens. In this case the failure strain may decrease significantly.

A remarkable worth mentioning result is, that under excessive load large fragments of structures can be completely torn off to become missiles. This happened in a biaxial test under quasi static load provided by (almost incompressible) pressurized oil.

Application of the proposed limit strains to selected severe accident problems shows that the admissible load increases by a factor between 1.25 and about 2.0 in comparison to using state-of-the-art rules.

There will be two types of benefits. It will now be possible to show that additional very severe accidents can be carried by the structures; without the LISSAC results the consequences of these accidents could hardly be assessed. On the other hand, certain structural improvements planned to harden the facility against severe accidents might now turn out to be not necessary.

Dehnungsgrenzen für Materialbeanspruchungen bei schweren Unfällen – ausführlicher Abschlussbericht

Zusammenfassung

Die lokalen Versagensdehnungen wesentlicher Komponenten des Reaktordruckbehälters werden untersucht. Der Größeneinfluss der Komponenten ist von besonderem Interesse. Typische Unfallbedingungen wie erhöhte Temperaturen und dynamische Beanspruchungen werden berücksichtigt.

Hauptteil der Arbeiten sind Testfamilien mit Materialproben unter ein- und mehrachsiger statischer und dynamischer Belastung. Innerhalb einer Testfamilie ist die Probengeometrie ähnlich und die Temperatur ist gleich; nur die Probengröße wird variiert bis hin zu Reaktorabmessungen. Die meisten Proben enthalten ein Loch oder eine gerundete Kerbe. Die dadurch hervorgerufenen ungleichmäßigen Spannungs- und Dehnungsverteilungen sind typisch für Reaktorkomponenten. Es gibt Hinweise, dass für solche ungleichmäßigen Verteilungen der Größeneinfluss besonders ausgeprägt ist.

Bei Proben mit kleinen Abmessungen werden mehrere Tests mit nominell identischen Parametern durchgeführt. Dadurch ist es möglich auch Informationen über die Streuung der Ergebnisse zu gewinnen. Bei Proben mit mittleren Abmessungen werden nicht ganz so viele Tests und bei Proben mit großen Abmessungen wird jeweils nur ein Test durchgeführt. Zur Herstellung der Proben stand Material 22NiMoCr37 vom nicht benutzten Reaktordruckbehälter Biblis C zur Verfügung. Dadurch war es möglich, die störenden Variationen der mechanischen Materialeigenschaften klein zu halten. Dies wird durch begleitende Materialstichproben bestätigt.

Ein Schlüsselproblem war die Definition und Bestimmung der lokalen Versagensdehnungen für die sehr unterschiedlichen Geometrien und Testbedingungen. Hierzu mussten spezielle Methoden wie zum Beispiel die „vanishing gap method“ oder die „forging die method“ entwickelt werden. Sie beinhalten geometrische Vermessungen der Bruchoberflächen nach den Tests und erlauben die Rekonstruktion der Dehnungsfelder in den Proben beim Rissbeginn – beispielsweise mit Hilfe von Finite-Elemente-Rechnungen.

Um das Verständnis der beobachteten Materialschädigungen und der Bruchvorgänge zu vertiefen, wurden fortgeschrittene theoretische Modelle entwickelt und – wenn möglich – validiert. Dazu gehören unter anderem so genannte „non-local concepts“, aber auch Modelle, die die stochastischen Materialeigenschaften der einzelnen Körner berücksichtigen. Derartige Modelle sind bei der Extrapolation zu anderen Beanspruchungsbedingungen hilfreich.

Die experimentellen Ergebnisse zeigen, dass für ähnliche Probengeometrien und Belastungsbedingungen die Spannungen über den dimensionslosen Verformungen nahezu größenunabhängig sind – bis zu den jeweiligen größenabhängigen Versagenspunkten. Damit ist auch die Maximalspannung näherungsweise größenunabhängig, vorausgesetzt Versagen erfolgt nachdem die Maximalspannung erreicht wurde.

Risse werden initiiert, wenn die lokale Vergleichsdehnung – hier formuliert als „wahre“ bzw. „logarithmische Dehnung“ – einen kritischen Wert erreicht. Dieser kritische Wert wird als lokale Versagensdehnung definiert. Für große Proben im Bereich der Reaktorabmessungen beträgt sie mehr als 50%.

Die lokale Versagensdehnung ist größenabhängig. Für kleine Proben mit Dicken oder Durchmessern im Millimeterbereich erreicht sie etwa 150%.

Der die Probengröße beschreibende Parameter ist der Radius der Löcher und Kerben in den Proben. Die sonstige Form der Proben und die Art der Belastung hat dagegen nur geringen Einfluss. Dies ist bemerkenswert und erleichtert die praktische Nutzung der Ergebnisse.

Die experimentellen Erkenntnisse können mit Hilfe theoretischer Modelle verstanden werden, die die Existenz von Material-Mikrostrukturen berücksichtigen. Versagensprognosen mit Modellen die die Material-Mikrostrukturen im Detail abbilden sind derzeit jedoch noch nicht möglich.

Wie erwartet sind die Streuungen der ermittelten lokalen Versagensdehnungen erheblich. Statistische Bewertungen zeigen jedoch, dass die lokalen Versagensdehnungen einen unteren größenabhängigen Grenzwert nicht unterschreiten.

Damit war es möglich größenabhängige, d.h. vom Loch- oder Kerbradius abhängige Dehnungsgrenzen vorzuschlagen. Diese gelten für Temperaturvariationen zwischen Raumtemperatur und 400 °C sowie auch für dynamische Belastungen. Dehnungsgrenzen für höhere Temperaturen bis 850 °C werden diskutiert. Wenn bei schweren Unfällen die vorgeschlagenen Dehnungsgrenzen nicht überschritten werden, darf angenommen werden, dass die Bauteile nicht brechen.

Mit Hilfe von Dehnungsgrenzen ist es möglich für schwere Unfälle ein wesentlich realistischeres, auf Dehnungen basierendes Bewertungskonzept anzuwenden. Ferner ist es jetzt möglich zu entscheiden, inwieweit experimentelle Ergebnisse von kleineren Reaktormodellen auf reale Rektorabmessungen übertragbar sind.

Unter Beachtung der theoretischen Untersuchungen sind auch Anwendungen auf andere Geometrien und Beanspruchungsbedingungen möglich. Vorsicht ist jedoch geboten, wenn die Dreiachsigkeit des Spannungszustandes größer ist als bei den hier untersuchten Proben. In diesem Falle können die Versagensdehnungen erheblich abnehmen.

Es soll auch erwähnt werden, dass bei Überbelastung von Bauteilen Bruchstücke abgetrennt und weggeschleudert werden können. Dies wurde demonstriert beim Test einer zweiachsigen Probe unter quasi-statischer Belastung (Druckbelastung durch nahezu inkompressibles Öl).

Die Anwendung der vorgeschlagnen Dehnungsgrenzen auf ausgewählte strukturmechanische Probleme bei schweren Unfällen zeigt, dass im Vergleich zu den bisherigen Bewertungsmethoden, die noch hinnehmbare Belastung um einen Faktor zwischen 1.25 und etwa 2.0 zunimmt.

Die Ergebnisse können auf zweierlei Weise einen Gewinn bedeuten. Es wird jetzt möglich sein zu zeigen, dass von den gegenwärtigen Anlagen weitere schwere Unfälle beherrscht werden können. Ferner ist es denkbar, dass diskutierte sicherheitstechnische Nachbesserung sich jetzt als überflüssig erweisen.

1 OBJECTIVES AND SCOPE

1.1 Overview

In last years postulated severe reactor accidents with only a very small probability to occur have been investigated quite extensively. They are expected to cause excessive loads on the reactor pressure vessel. Advanced structural mechanics codes considering nonlinear geometry and material effects allow rather detailed predictions of the resulting plastic strain fields in the walls of the reactor pressure vessel. However little information is available about plastic strains causing failure. Consequently, reasonable limit strains which should be acceptable under severe accident conditions are lacking, too.

Current rules like the ASME code are mainly stress based concepts and allow only small plastic strains, which is appropriate for design basis accidents. Application of these rules for very unlikely severe accidents, however, would yield overconservative results. The predicted consequences would include unrealistic severe scenarios.

Therefore in the current project the local failure strains of essential reactor vessel components are investigated. The size influence of the components is of special interest. Typical severe accident conditions including elevated temperatures are considered.

The main part of work consists of test families with specimens under uniaxial and biaxial static and dynamic loads. Within one test family the specimen geometries and the load conditions are similar, the temperature is the same; but the size is varied up to reactor dimensions. Special attention is given to geometries with a hole or a notch causing non-uniform stress and strain distributions typical for reactor components. There are indications that for such non-uniform distributions size effects may be stronger than for uniform distributions. Thus size effects on the failure strains and failure processes can be determined under realistic conditions.

Several tests with nominal identical parameters are planned for small size specimens. In this way some information will be obtained about the scatter. A reduced number of tests is carried out for medium size specimens and only a few tests are carried out for large size specimens to reduce the costs to an acceptable level. For all specimens sufficient material is available from the unused reactor pressure vessel Biblis C. Thus variations of the mechanical material properties, which could impair the interpretation of the test results, can be expected to be quite small. Nevertheless, an adequate number of additional quality assurance tests are planned to check the material homogeneity.

To deepen the understanding of structural degradation and fracture and to allow extrapolations, advanced computational methods including damage models will be developed and validated. The problems to be treated here are quite difficult. Microstructural effects, for instance, play an important role. Therefore several approaches will be tried in parallel. In some cases so-called non-local concepts, in other cases the description of stochastic properties at the grain size level are considered.

Based on the results from the present research program and considering the findings in the literature and the experience collected in industry, limit strains will be proposed for severe accident conditions. Using these limit strains – or acceptable strains – a more realistic strain based evaluation concept can be employed for struc-

tural mechanics analysis of severe accident consequences. Furthermore the results will help to examine, whether findings from small scale tests can be converted to reactor conditions.

For demonstration some selected structural mechanics investigations will be performed for severe accident conditions.

1.2 State-of-the-art report

It is well established experimentally that for some steels the stress for initiation of yielding decreases with increasing size of the specimens. Even more importantly also the local strains causing failure decrease with increasing specimens, accompanied by scatter. Investigations of such size effects date back to early times of material testing.

A limited review of scaled experiments at room temperature of geometrically similar specimens made of different steels has recently been prepared within the EU-project REVISA [1]. It refers to the size dependence of the initiation of yielding under non-uniform states of deformation and of the plastic deformation and fracture of smooth tensile specimens. Here only two outcomes are mentioned. The experimental studies related to the first issue frequently showed an increase of the yield stress when the size is decreased. Further, the second issue revealed another size effect which indicates an increase of the area reduction after fracture with decreasing specimen size; this has also been found in corresponding experiments of the REVISA project [2] and this latter trend has also been observed recently in tensile tests of sub-size specimens where surface layer effects have been eliminated by electro-polishing [3].

In the domain of micro-plasticity the micro-hardness indentation size effect (increase of hardness with decreasing indenter size) has recently attracted considerable attention [4 – 9]; also the increase of flow stress in plastic deformation with the decrease in size was demonstrated for the micro-bending of thin foil specimens [10].

In brittle or quasi-brittle materials, like concrete, the size effect in fracture is more evident and has been studied intensively [11].

But also for ductile materials sharp notches or cracks (resulting from fatigue or stress corrosion) clearly represent a great danger for fracture and the size dependence of the fracture stress, failure strain, and also the energy dissipation capability of geometrically similar specimens has been studied (e.g. [12 – 23]). These studies generally demonstrated an increased load carrying capacity and ductility with decreasing size.

However, an increasing number of engineering problems require the determination of failure loads and deformations of structures containing design typical strain concentrators like bore holes, perforations or blunted notches and no sharp notches or cracks. Some testing of geometrically similar specimens of this type but with a relatively small range of sizes has been done, e.g. [24 – 26]. One of the recent contributions was part of the EU project REVISA. An overview is given in [27]. The results obtained so far show increased ductility and scatter for the smaller specimens. However, it appears that systematic testing for a variety of specimen shapes and especially over a large range of sizes (geometric scale factor larger than 10 and up to full size conditions) has not been done yet.

It is rather obvious that the various size effects phenomena are related to different micro-mechanical processes and thus different theoretical models should apply. Accordingly, various theoretical attempts have been made or are in a stage of devel-

opment to account for the observed size effect in material response. It should be mentioned that some of these theoretical concepts originally have been introduced to cope with the "non well posedness" of the more classical material models, which arises when material softening is taken into account. Generally the advanced theories implicate terms which are associated with internal length scales characteristic for the material microstructure. They account in different ways for interactions or heterogeneity over a small but finite material domain on a phenomenological level, still treating the material as a continuum. The interaction between the geometric length of the specimen and the internal length (associated with the underlying microstructure) causes a size-dependent response.

For example, for pre-existing sharp cracks or for sharp notches Linear Elastic Fracture Mechanics or Elastic-Plastic Fracture Mechanics provide a means to capture some size effects; these theories introduce the size dependence via the choice of the fracture criterion without explicitly using an internal material length (instead, a pre-assumed crack length enters into the formulation). To account for size effects in purely plastic deformations, the proposed theories involve internal length scales via integral or gradient terms in the stress-strain relations and/or yield condition (e.g. [1, 28 - 34]). For the treatment of ductile failure and its size dependence a modelling of the damage (a usually scalar variable associated to the void fraction) coupled to the stress-strain relations is necessary. Accordingly, the evolution equation for the "damage" internal variable may be enriched by gradient terms accounting for diffusion [35] or may involve integral measures of state variables, for example a (weighted) integral of the local damage variable over a small but finite size material volume (e.g. [26]). Further, some concepts account for the heterogeneity by introducing an "internal length" via the finite element mesh size which is defined by the average distance of inclusions (e.g. [24]). Also size dependence and scatter may be modelled by the introduction of statistical distributions of some material parameter of the constitutive model (e.g. [24]).

Although some of the models involving internal length scales have been matched successfully to a restricted range of experimental results (e.g. [23, 24, 26, 28, 30 - 34]), most of them require essential further developments. This may refer to different aspects: The motivation from micro-mechanics concepts and the embedding in a continuum-thermodynamics framework, the qualitative understanding and trend assessment of the effects of the non-classical terms by utilising the solutions of simple boundary values problems, the numerical solutions with mesh-independent and convergent numerical schemes, the identification of the material parameters - associated with the internal length scales - using suitable experimental results, and testing of their predictive capability by comparison with experimentally observed size effects in deformation and failure on a family of geometrically similar specimens of the same material.

It should be mentioned that this state-of-the-art report provides only a short overview. A more detailed overview has been documented by Malmberg in SAM-LISSAC D037. It is planned to publish this overview in a further FZKA report.

2 RESEARCH PROGRAM

2.1 Planned experimental work

2.1.1 Preparation of the specimens

2.1.1.1 Definition of test families

As already mentioned, the test families include typical design elements and load cases of a reactor pressure vessel under severe accident condition. An overview of the test families is given in Fig. 2.1.1-1. It starts with the most important family, the flat specimens with a hole at room temperature (RT) under (quasi) static load (Fig. 2.1.1-1, upper part, left hand side). The ratio between the hole diameter and the wall thickness is about the same as the ratio between the holes for the control rod drive mechanisms at the upper vessel head and the wall thickness of this head.

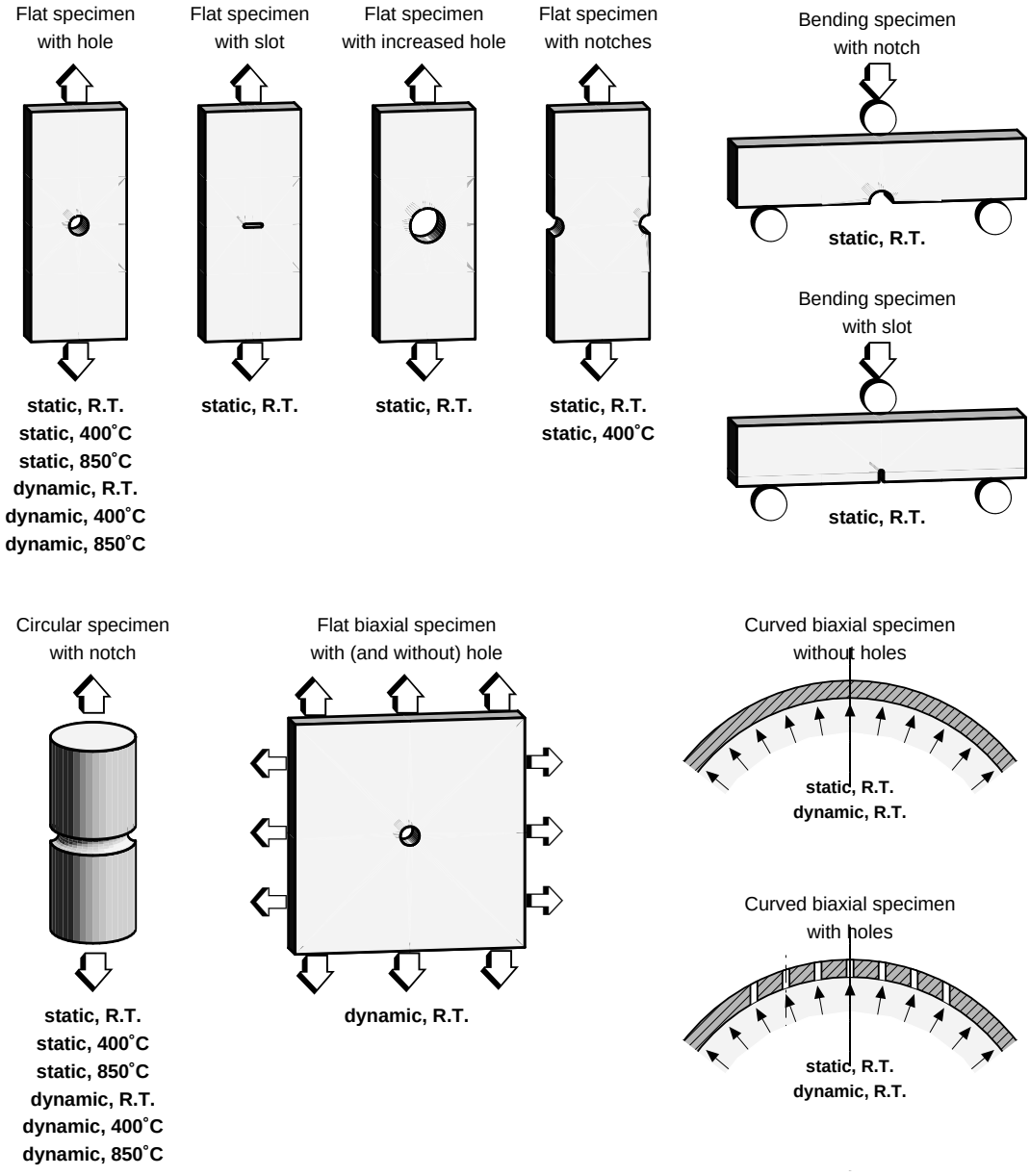

Fig. 2.1.1-1: Overview of the test families

One group of neighbouring families are based on the same specimen shape, but the temperatures are elevated to 400 °C and 850 °C, and dynamic loading is considered, too (the same symbolic drawing). The temperature of 400 °C may be reached in the upper part of the vessel during a severe accident. Much higher temperatures may be reached in the lower part of the vessel; the value of 850 °C was chosen since it is above the phase change of the material, but on the other hand this temperature is still in the region where the experimental effort is acceptable.

Other neighbouring families adress variations of the hole in the flat specimens (Fig. 2.1.1-1, upper part, center). The variations include an increased hole, a slot, and notches. To limit the number of test families, the variation of temperature is restricted and only static load is considered.

Neighbouring families are also the bending specimens with a wide notch (half a hole) and a narrow notch (half a slot), (Fig. 2.1.1-1, upper part, right hand side). For these specimens the peak stresses and strains at the notches are intensified in comparison to the tension tests discussed before. Tests are only performed at room temperature under (quasi) static load.

A bigger step concerning the geometry are the families of circular specimens with notch (Fig. 2.1.1-1, lower part, left hand side). These families are not very typical for a reactor pressure vessel, but they provide some kind of bridge to the standard tension specimens which have also circular shapes. Elevated temperatures and dynamic loading are considered.

It should be pointed out, that the geometrical variations introduced above follow a certain pattern as indicated in Fig. 2.1.1-2. This is expected to be helpful for the interpretation of the results. For instance, if the findings for circular specimens would significantly deviate from the findings for other specimens, one could conclude that this is primarily due to the circular character and not due to the notch.

Another big step toward real geometry and loading are the families of flat and curved biaxial specimens under static and dynamic load (Fig. 2.1.1-1, lower part). The performance of these tests is expensive and requires special testing equipment. To limit the expenses, tests will be done at room temperature, only.

For each of the 24 test families discussed above, the specimen shape is the same, but the specimen size is varied. For the most important test family, the flat specimens with a hole at room temperature under static load, the most extended size variation are considered. As indicated in Fig. 2.1.1-3, the smallest specimen has a thickness of 4 mm, the largest has a thickness of 200 mm which is about the wall thickness of a reactor pressure vessel. For the test families of circular specimens with notch very extended size variations are considered, too; the smallest diameter is 3 mm, the largest 150 mm.

A complete list of all the tests including the number of tests with nominal identical parameters is presented in chapter 2.1.2 and 2.1.3.

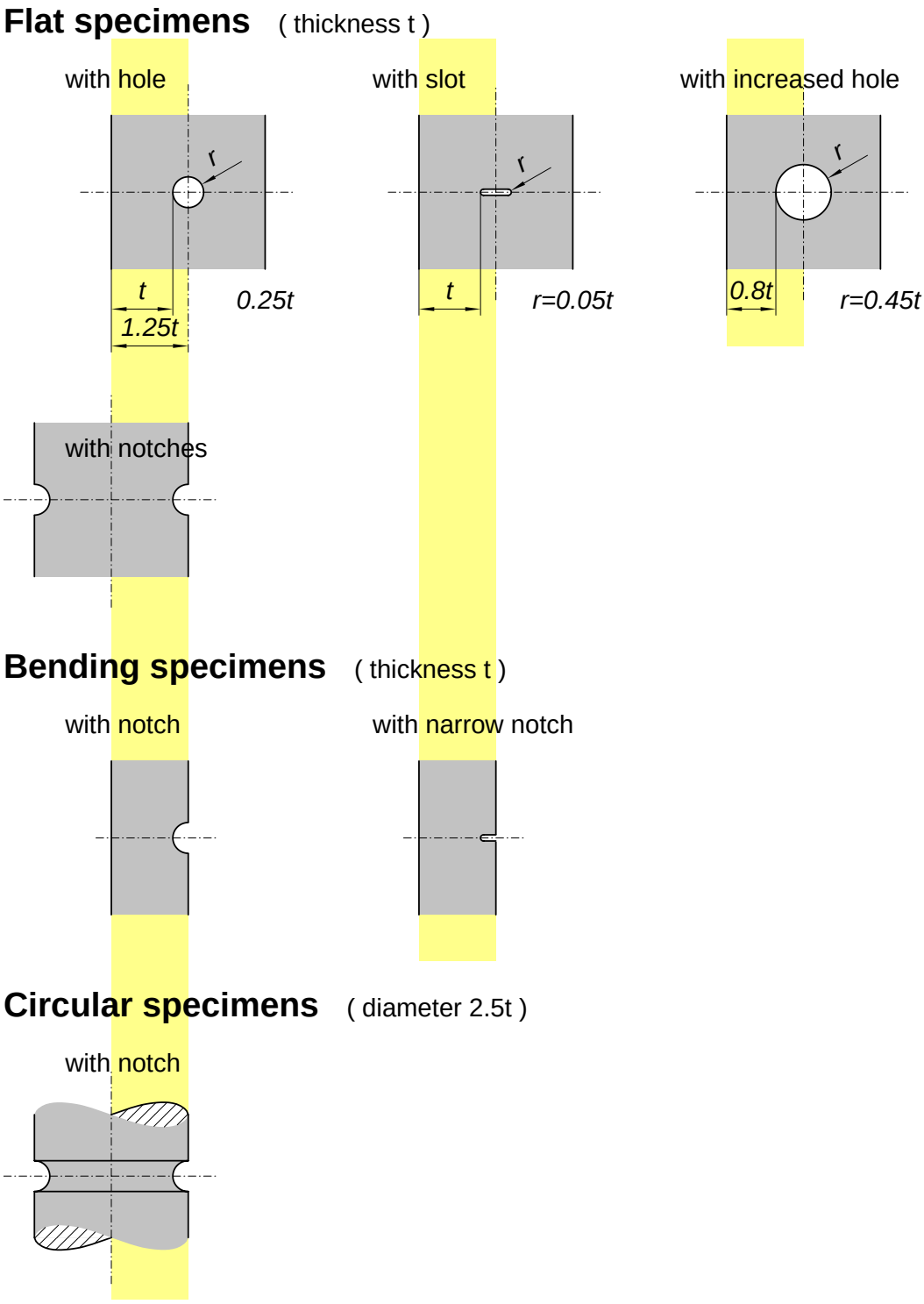

Fig. 2.1.1-2: Variations of the specimen shapes following a certain pattern

Fig. 2.1.1-3: Flat specimens with a hole.
The smallest specimen has a thickness of 4 mm,
the largest a thickness of 200 mm

2.1.1.2 Manufacturing of the specimens

In order to exclude the interference with other phenomena like variations of the mechanical properties of the material, all specimens are manufactured from material of the cylindrical section of the unused reactor pressure vessel Biblis C consisting of the material 22NiMoCr37. In addition, the mechanical material properties will be carefully monitored by a large number of material qualification test. In order to minimize the influence of remaining variations of the material properties, the (unshaped) specimens belonging to one test family will be taken from the same region of the cylindrical section of the reactor pressure vessel.

FZK will deliver the unshaped specimens, the partners doing the tests are responsible for manufacturing the specimens. There is one exception: VTT performing the biaxial tests with curved specimens under static load will receive the machined specimens from FZK.

Manufacturing tolerances of the specimens are given such that the effects on the results can be expected to be in the one-percent region; for the very small specimens this requirement could not always be met. Manufacturing processes for the specimens will be chosen such that surface hardening is minimized in sensitive regions (hole and notch surfaces). Therefore the partners agreed to manufacture the small specimens in the same shop. Small holes or notches will be produced using either new and very sharp cutting tools or by electro erosion.

2.1.2 Uniaxial tests

In the following tables the partner is mentioned who performs the test. The digit below indicates the number of nominal identical tests planned, the digit in parenthesis indicates deviations of the number of tests which have been really carried out.

2.1.2.1 Tension tests under static load

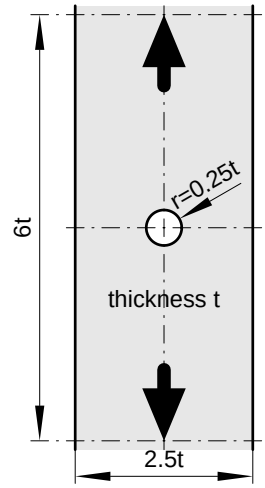

Flat specimen with hole, static load

temperature	thickness t				
	4 mm	20 mm	40 mm	80 mm	200 mm
R.T.	FZK 5	FZK/MPA 2,2(2,3)	FZK/MPA 1	MPA 1	FZK/MPA 1
400˚C	EMPA 5(6)	EMPA 2	FZK/MPA 1	MPA 1	
850˚C	EMPA 3	EMPA 2		MPA 1	

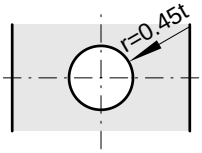

Flat specimen with increased hole, static load

R.T.	FZK 5	FZK 2(3)		MPA 1	

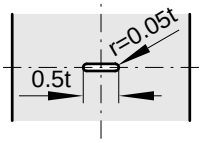

Flat specimen with slot, static load

R.T.	FZK 5(6)	FZK 2(3)		MPA 1	

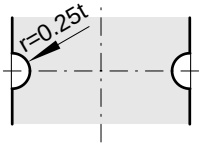

Flat specimen with notches, static load

R.T.	FZK 5(6)	FZK 2(3)		MPA 1	
400˚C	EMPA 5(6)	EMPA 2			

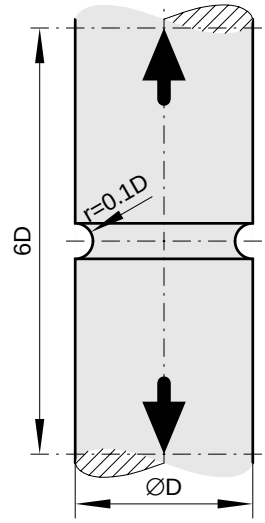

Circular specimen with notch, static load

temperature	diameter D			
	3 mm	9 mm	20 mm	150 mm
R.T.	FZK/JRC 5(5,4)	FZK (4)	MPA 2	MPA 1
400˚C	EMPA/JRC 5(6,4)	EMPA (4)	MPA 2	MPA 1
850˚C	EMPA/JRC 5(6,3)	EMPA (4)	MPA 2(4)	MPA 1

2.1.2.2 Bending tests

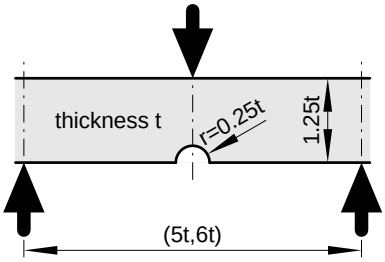

Bending specimen with notch, static load

temperature	thickness t				
	4 mm	20 mm	40 mm	80 mm	200 mm
R.T.	EMPA 5(3)	EMPA 2		EMPA 1	

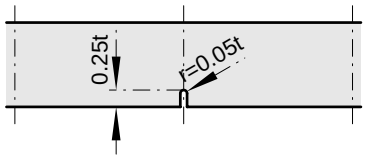

Bending specimen with narrow notch, static load

R.T.	EMPA 5(4)	EMPA 2		EMPA 1(2)	

2.1.2.3 Tension tests under dynamic load

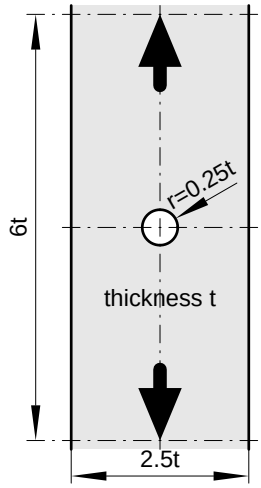

Flat specimen with hole, dynamic load

temperature	thickness t				
	4 mm	20 mm	40 mm	80 mm	200 mm
R.T.	JRC 3(4)	JRC 3(2)			
400˚C	JRC 3(2)	JRC 3(2)			
850˚C	JRC 3	JRC 3(2)			

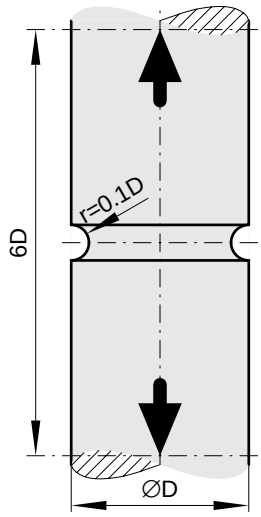

Circular specimen with notch, dynamic load

temperature	diameter D			
	3 mm	9 mm	20 mm	150 mm
R.T.	JRC 3(4)		JRC 2	
400˚C	JRC 3(4)		JRC 2	
850˚C	JRC 3		JRC (2)	

2.1.3 Biaxial tests

2.1.3.1 Tests with curved biaxial specimens under static load

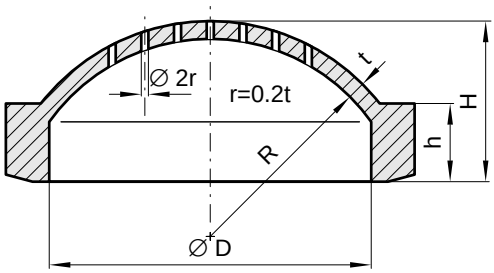

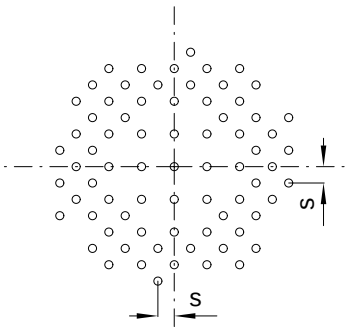

Curved biaxial specimen without hole, static load

temperature	thickness t	
	5 mm	25 mm
R.T.	VTT 3	VTT 1

Curved biaxial specimen with holes, static load

R.T.	VTT 3	VTT 1

[mm]	R	D	H	h	s
t=5	*55.6*	*90.6*	*45.2*	*22*	*4.6*
t=25	*278*	*453*	*226*	*110*	*23*

2.1.3.2 Tests with curved biaxial specimens under dynamic load

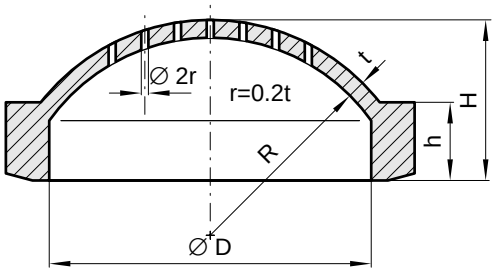

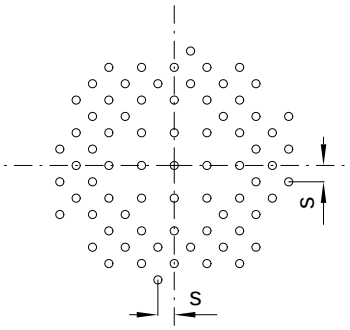

Curved biaxial specimen without hole, dynamic load

temperature	thickness t	
	5 mm	25 mm
R.T.	FZK 3(4)	FZK 2

Curved biaxial specimen with holes, dynamic load

R.T.	FZK 3	FZK 2

[mm]	R	D	H	h	s
t=5	*55.6*	*90.6*	*45.2*	*22*	*4.6*
t=25	*278*	*453*	*226*	*110*	*23*

2.1.3.3 Tests with flat biaxial specimens under dynamic load

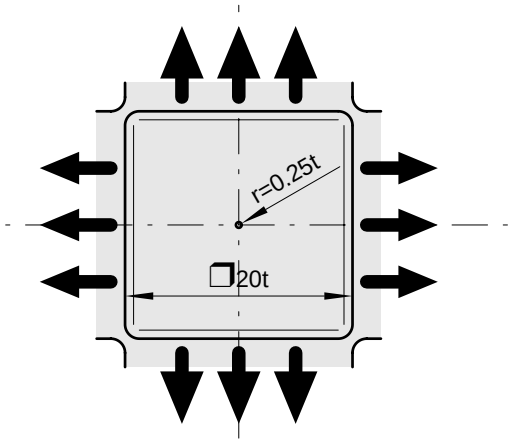

Flat biaxial specimen without hole, dynamic load

temperature	thickness t	
	4 mm	8 mm
R.T.	JRC 2	

Flat biaxial specimen with holes, dynamic load

R.T.	JRC 2	JRC 2(0)

The strain distributions obtained are not equi-biaxial. Displacements are applied only in one direction (in the drawing it is the vertical direction indicated by bigger arrows), while displacements are suppressed by appropriate clamping devices in the other direction (smaller arrows).

2.2 Planned theoretical work

Within LISSAC several theoretical models will be developed or available models will be examined. The aim is to

- predict size effects on failure strains and deformation behaviour.
- explain the theoretical background of the size effect.

The large number of different approaches is necessary since no established models are currently known which are able to describe the experimental observed size effects. Of course, it cannot be expected that all examined models will succeed in describing the experimental findings. Furthermore some of the theoretical models are considered to address only special effects and not to yield general predictions.

2.2.1 Gradient models

Gradient enriched plasticity and damage models will be examined whether they are able to describe the experimentally observed size effects in deformation and failure. These theories enhance classical models by integral- or gradient-terms of state variables and introduce additional material parameters which can be associated with internal length scales characteristic for the material.

The objective of this theoretical work is the development, analysis and application of such models; this implies an evaluation of their theoretical consistency and an assessment of their qualitative and quantitative properties as well as their ability to interpret experimentally observed size effects.

The following work is planned within LISSAC project:

- Employ gradient models for plasticity introduced by Aifantis and co-workers and also Fleck and co-workers. Furthermore generalize internal variable models (damage) with diffusive transport, analyze the relative importance of gradient terms and calibrate the models in terms of gradient coefficients and associated boundary conditions using solutions of simple loading configurations, parameter calculations and available experimental data on size effects; assess an available numerical scheme to solve non-classical boundary value problems related to the experimental part of the program. Due to the lack of time and material parameters the physical origin of the gradient terms could not be clarified by using microscopic arguments and macroscopic self-consistent models.
- Characterize computationally with the finite element method the ductile failure process using gradient plasticity models and develop a non-local damage model (modified Gurson model). Identify the corresponding material parameters and qualify the models using available experiments.
- Develop a thermodynamically consistent plasticity and gradient enhanced damage model (extension of the energy equivalent hypothesis of Sidoroff et al.) for large deformations; identify restrictions on the structure of this gradient damage model within a continuum thermo-mechanics setting.

2.2.2 Stochastic models

Models and methodologies which account for the heterogeneity evolution in plastic flow or damage should be improved or developed in this work package. The failure strains observed in the experiments including the scatter should be predicted. The results should be used to interpret the experimental findings.
The following work is planned within LISSAC project:

- Extend a damage model by evolution equations for higher order statistical moments of the void density. These moments should be treated as spatially correlated. Instead of the planned Gurson model a modified Lemaitre approach is used. A stochastic term is added to the flow function to describe the material behaviour. During the duration of the project it has be realised that this approach was not able to predict the experimental findings and so an interpretation of the experimental results was not possible.
- The formulation of a slightly more general stochastic model for void nucleation and growth and the comparison with the Gurson model and the gradient approach to damage could not be realized due to personal problems.
- Perform a numerical simulation of the stochastic grain structures using the Vornoi tessellation method. Investigate the influence of various stress profiles.

2.2.3 Local approach models

Local approach models in the classical sense use also aspects of the discrete nature of material (Intrinsic length scales such as distance and/or size of inclusions, grain size, etc.) for material characterization. Further, the numerical discretisation (e.g. FEM) is coupled to these intrinsic length scales.

Also more conventional elasto-plastic damage models which are not related to intrinsic length scales (size invariant models) should be utilized to simulate the experiments of the project.
The following work is planned within LISSAC project:

- Determine the material parameters of the elastic-plastic Rousselier damage model from test of small standard laboratory specimens; extend the model to simulate dynamic tests; assess quality of numerical simulations for differently sized specimens by comparison with experimental results of the project. The visco-plastic material law for the high temperature cases could not be used due to the lack of high temperature material characterisation.
- Incorporate a continuum damage model into a general purpose finite element program, determine constitutive parameters using small standard laboratory specimens and use available software, apply the model to other experiments. In the project the Gurson-Tvergaard-Needleman model is used as continuum damage model but the achieved results are not satisfactory. Due to this the gradient model in cooperation with the Gurson approach developed in WP6 is used for this task.
- Compare the results of the different models with the experiments.

2.3 Planned evaluation and applications

Where possible, forces (divided by characteristic specimen cross sections) versus characteristic deformations will be measured for all tests performed. In addition, appropriate post test examinations will be performed to determine the failure strains which, is a key issue of the current project.

However, reliable procedure to measure the failure strains during or after the experiments are not available. Therefore the development of such procedures is an essential part of the current project.

The results are expected to show possible size effects on the maximum stress in the specimens.

More important are the results for the failure strains. The most interesting questions are listed below:

What is the order of magnitude of the failure strains?
What is the size effect on the failure strain?
What is the effect of the specimen shape on the failure strain?
What is the scatter of the results?
What are the failure modes to be expected?

To answer these questions, also findings from theoretical models will be considered. In addition, suitable statistical analyses will be performed.

Based on all these results, it is intended to propose limit strains for severe accident conditions.

To demonstrate the applicability and the benefit of the results, sample calculations for selected severe accident loads will be presented. It is planned to address the support structure as well as the upper head of the reactor pressure vessel.

3 RESULTS

3.1 Experimental results

3.1.1 Preparation of the specimens

3.1.1.1 Arrangement of the specimens within the given material from the pressure vessel Biblis C

The arrangement of the unshaped specimens for the different test families within the cylindrical section of the pressure vessel Biblis C is shown in Fig. 3.1.1-1. The specimens of each test family are marked by a particular colour as indicated in the upper part of the figure. The arrangement shown in the lower part of the figure is done in such a way that specimens belonging to the same test family are grouped closely together. In this way the inevitable variations, of the material properties of the specimens within one test family are minimized.

The detailed arrangement of the unshaped specimens within the segment 1 of the cylindrical section of the pressure vessel is shown in Fig. 3.1.1-2. The segment 2 is not used for LISSAC specimens. The arrangement of the unshaped specimens within the segments 2 to 6 is shown in Figs. 3.1.1-3 to 3.1.1-6. Note that the unshaped specimens are identified by a two letter code, for instance AI, AJ, …, BA, … .

The arrangement of the specimens within the wall thickness of the cylindrical section is indicated in the lower part of the figures. As can be seen, the smaller specimens are located in a preferred layer within the wall. Its distance from the outside surface of the vessel is a quarter of the wall thickness. For this layer the material strength is about the same as the mean value of the strength over the wall thickness. (At the outer layers the strength is somewhat higher at the middle layer it is somewhat lower – quantitative information in the next subchapter). Thus also the arrangement of the specimens within the wall thickness of the vessel will help to reduce the effect of variations of the material properties.

By the way, specimens located in the preferred layer are marked by the additional digit 1, for instance AL1, AJ1, …; specimens located in other layers are marked by other digits. If several small specimens have the same two letter code and are located in the same layer, they will be distinguished by a fourth letter, for instance AI1A, AI1B, … . A complete list of all specimens as well as information about their shapes and test families may be found in chapter 3.1.4.3.

In order to control the material homogeneity, a large number of material blocks QA, QB, … etc. were reserved as indicate in the previous figures. The blocks were cut in slices as shown in Fig. 3.1.1-7. The slices QA1, QB1, etc. belong to the preferred layer within the wall thickness; the slices QB2, QB3, … QB7 belong to other layers. In a last step the slices are cut in pieces A, B, …, P which can be used to manufacture specimens for standard tension and Charpy impact tests. They will be referred as material qualification tests in contrast to the tests belonging to test families introduced before.

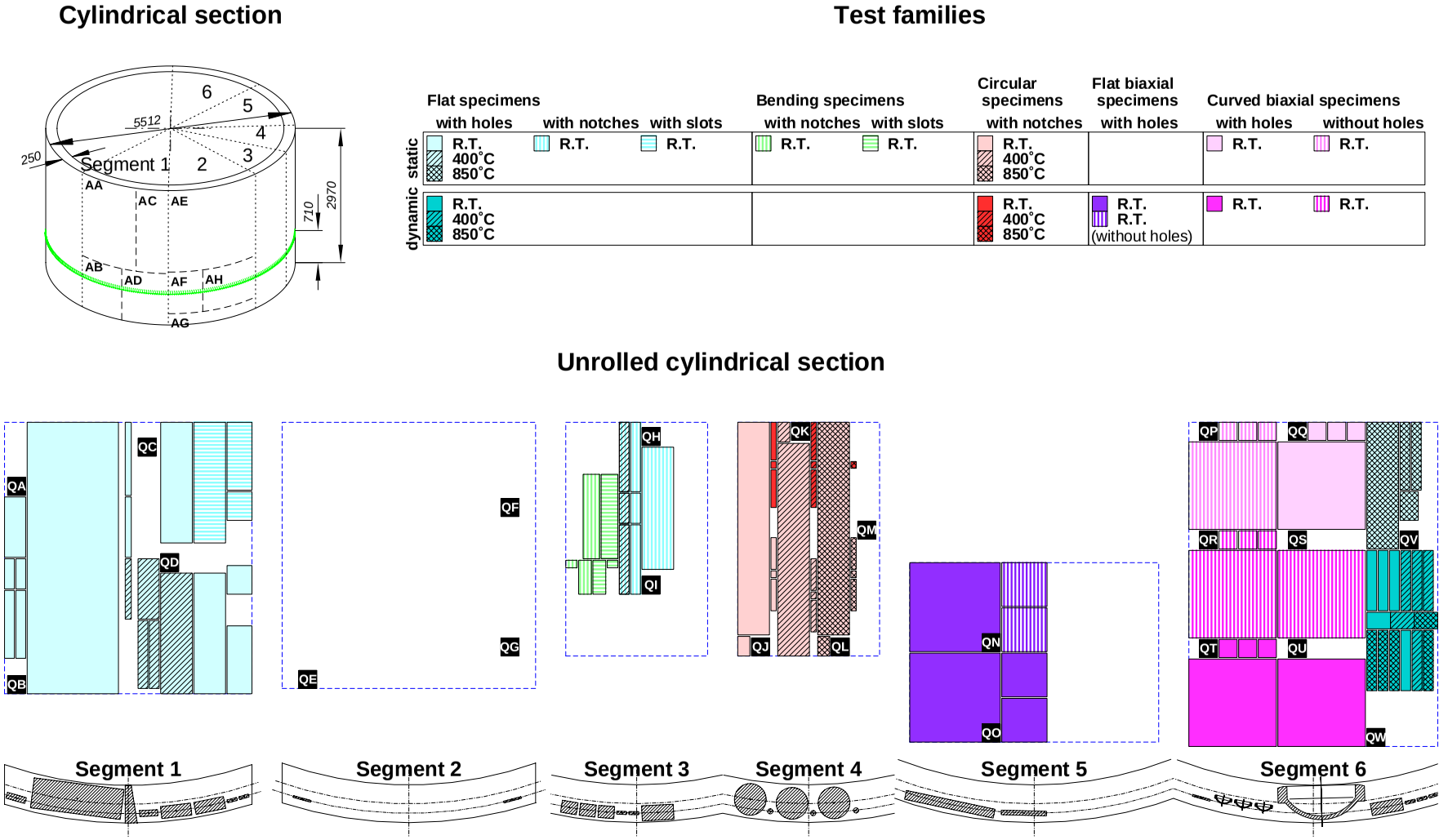

Fig. 3.1.1-1: Specimens of the different test families located in the cylindrical section of the reactor pressure vessel Biblis C

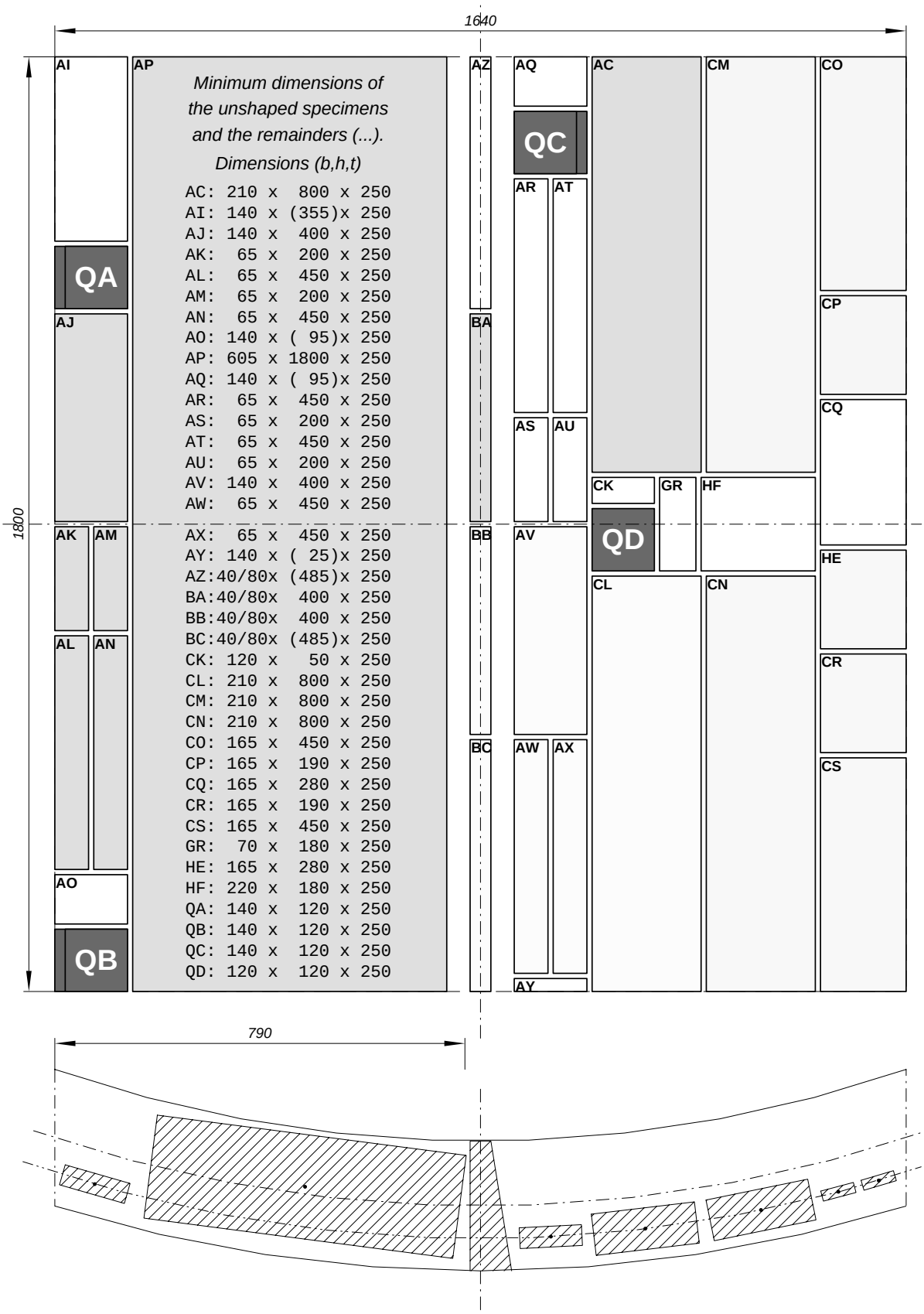

Fig. 3.1.1-2: Segment 1 of the cylindrical section

Minimum dimensions of the unshaped specimens and the remainders (...).

Dimensions (b,h,t)

```
CA: 110 x  560 x 250
CT:  75 x   50 x 250
CU:  75 x (165)x 250
CV:  85 x  225 x 250
CW: 110 x  560 x 250
CX:  85 x  225 x 250
CY:  70 x   50 x 250
CZ:  70 x (165)x 250
DA:  65 x  460 x 250
DB:  65 x  200 x 250
DC:  65 x  460 x 250
DD:  85 x  460 x 250
DE:  85 x  200 x 250
DF:  85 x  460 x 250
DG: 120 x ( 25)x 250
DH: 210 x  810 x 250
DI: 120 x ( 25)x 250
DJ:(220)x 1140 x 250
DK: 715 x  400 x 250
GS:  80 x  155 x 250
GT:  80 x  155 x 250
GZ:(220)x  400 x 250
HA: 105 x  560 x 250
HB: 345 x  335 x 250
QH: 120 x  120 x 250
QI: 120 x  120 x 250
```

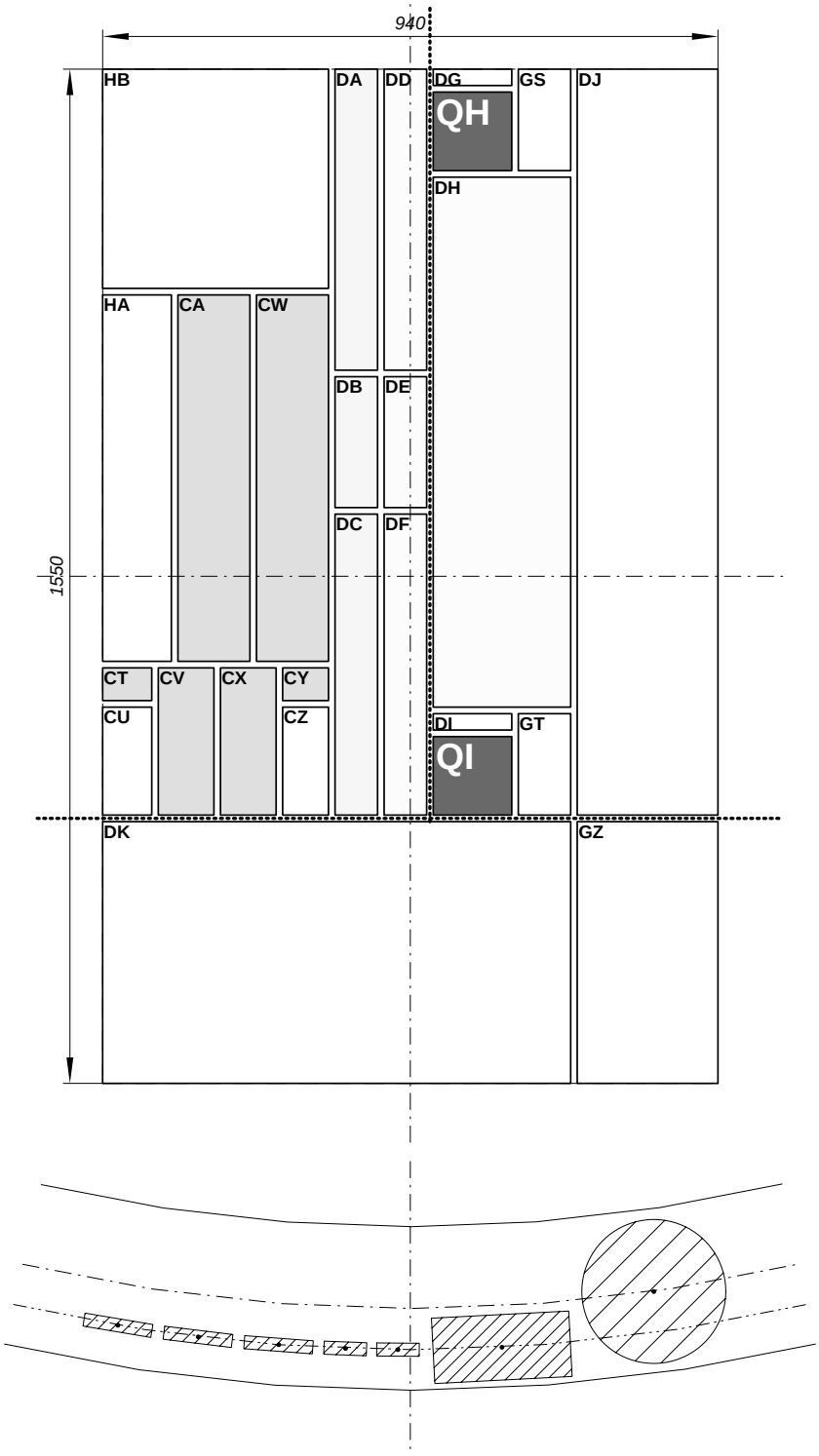

Fig. 3.1.1-3: Segment 3 of the cylindrical section

Minimum dimensions of the unshaped specimens and the remainders (...).

Dimensions (b,h,t)

```
BX:  35 x  180 x 250
BY:  35 x  320 x 250
BZ:  35 x   55 x 250
CC: 210 x 1410 x 250
DL:  80 x  130 x 250
DM:  35 x  250 x 250
DN:  35 x   45 x 250
DO:  35 x  250 x 250
DP:  35 x  210 x 250
DQ:  35 x   45 x 250
DR:  35 x  210 x 250
DS:  35 x (290)x 250
DT: 210 x 1410 x 250
DU:  80 x  130 x 250
DV:  35 x  250 x 250
DW:  35 x   45 x 250
DX:  35 x  250 x 250
DY:  35 x  210 x 250
DZ:  35 x   45 x 250
EA:  35 x  210 x 250
EB:  35 x (150)x 250
EC: 210 x 1410 x 250
ED:  80 x  130 x 250
EE:  35 x  250 x 250
EF:  35 x   45 x 250
EG:  35 x  250 x 250
EH:  35 x  210 x 250
EI:  35 x   45 x 250
EJ:  35 x  210 x 250
EK:  35 x (290)x 250
EL:(220)x 1550 x 250
HC:  35 x   55 x 250
HD:  35 x   55 x 250
QJ: 120 x  130 x 250
QK: 120 x  130 x 250
QL: 120 x  130 x 250
QM: 120 x  120 x 250
```

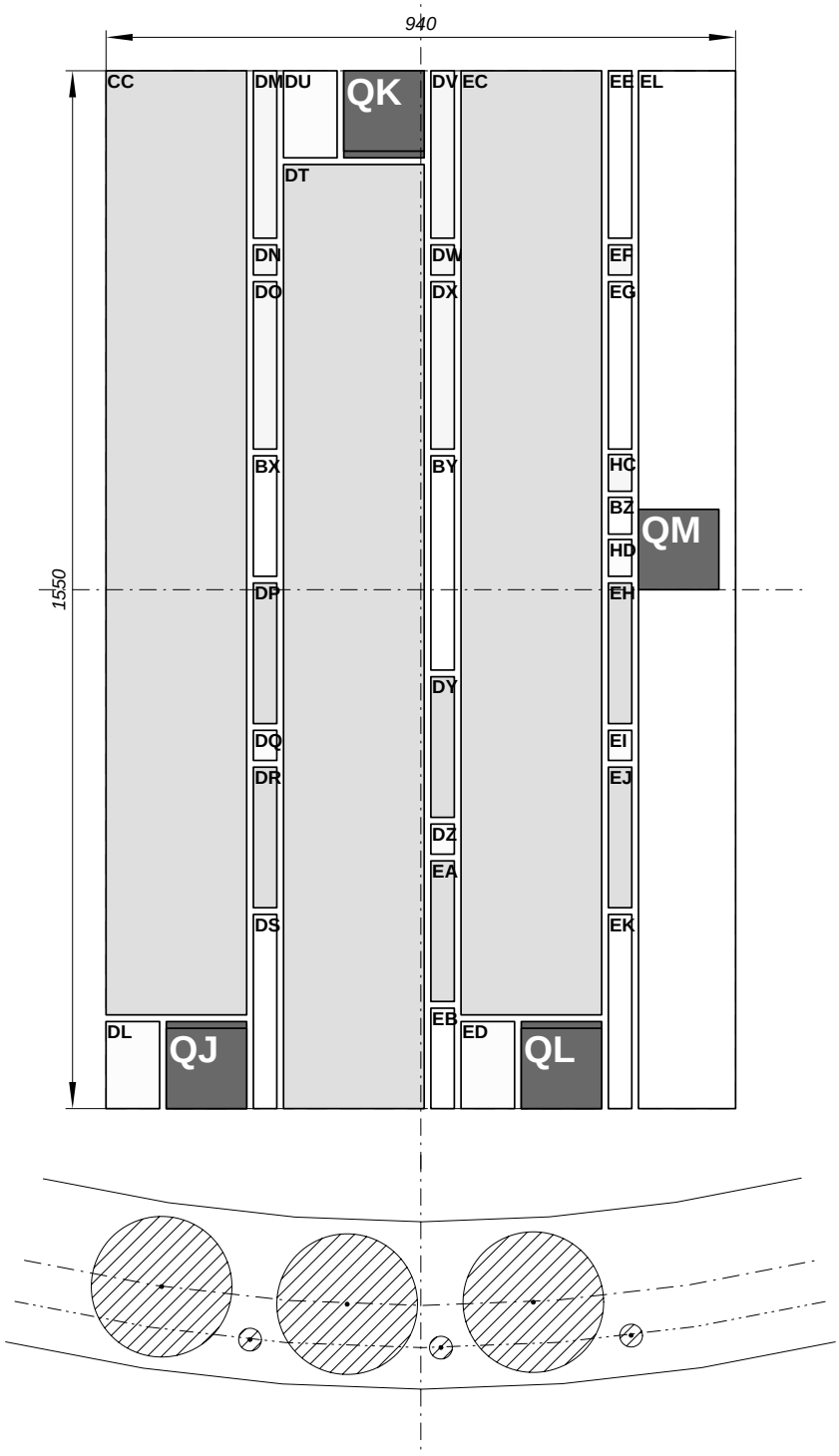

Fig. 3.1.1-4: Segment 4 of the cylindrical section

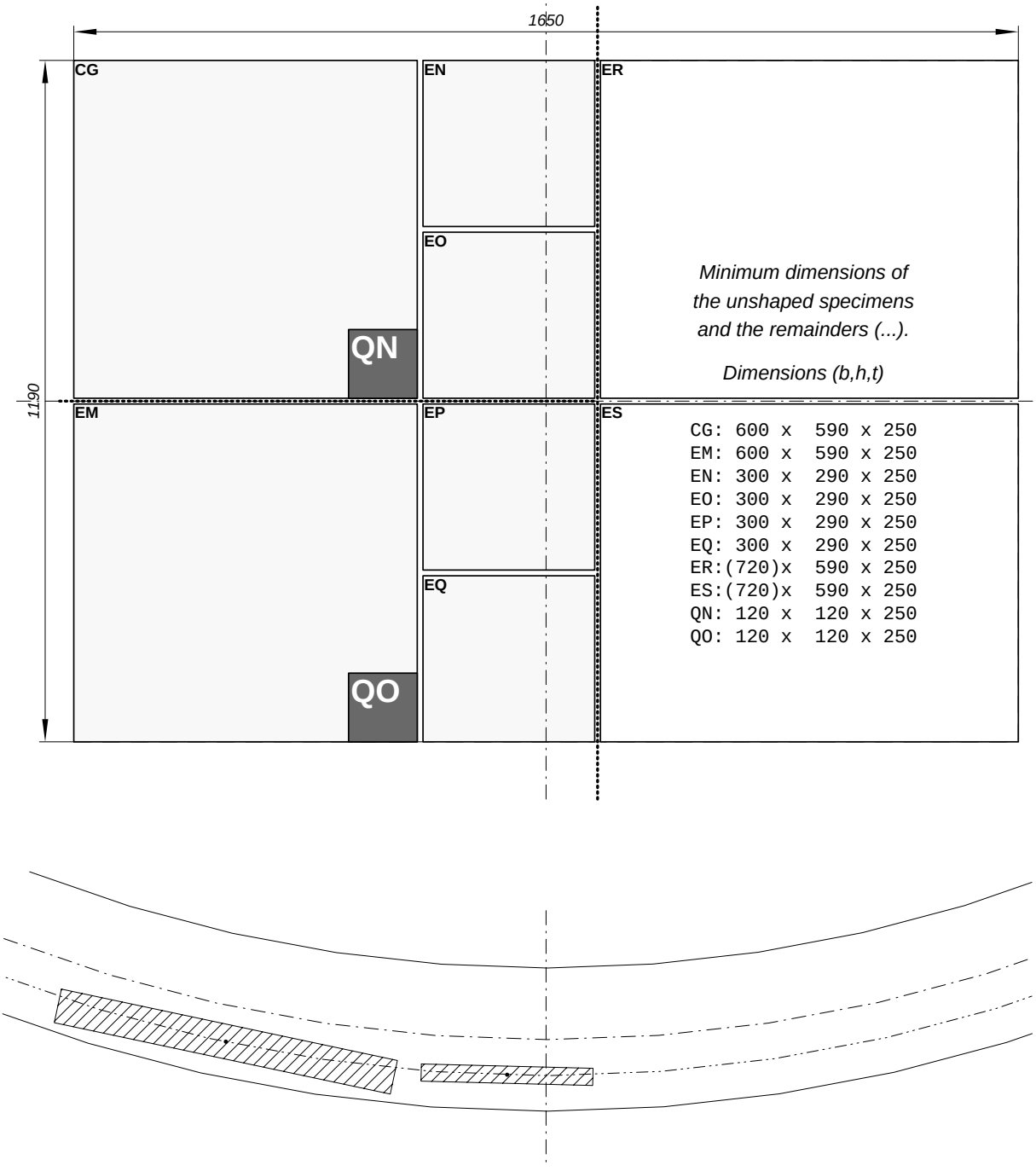

Fig. 3.1.1-5: Segment 5 of the cylindrical section

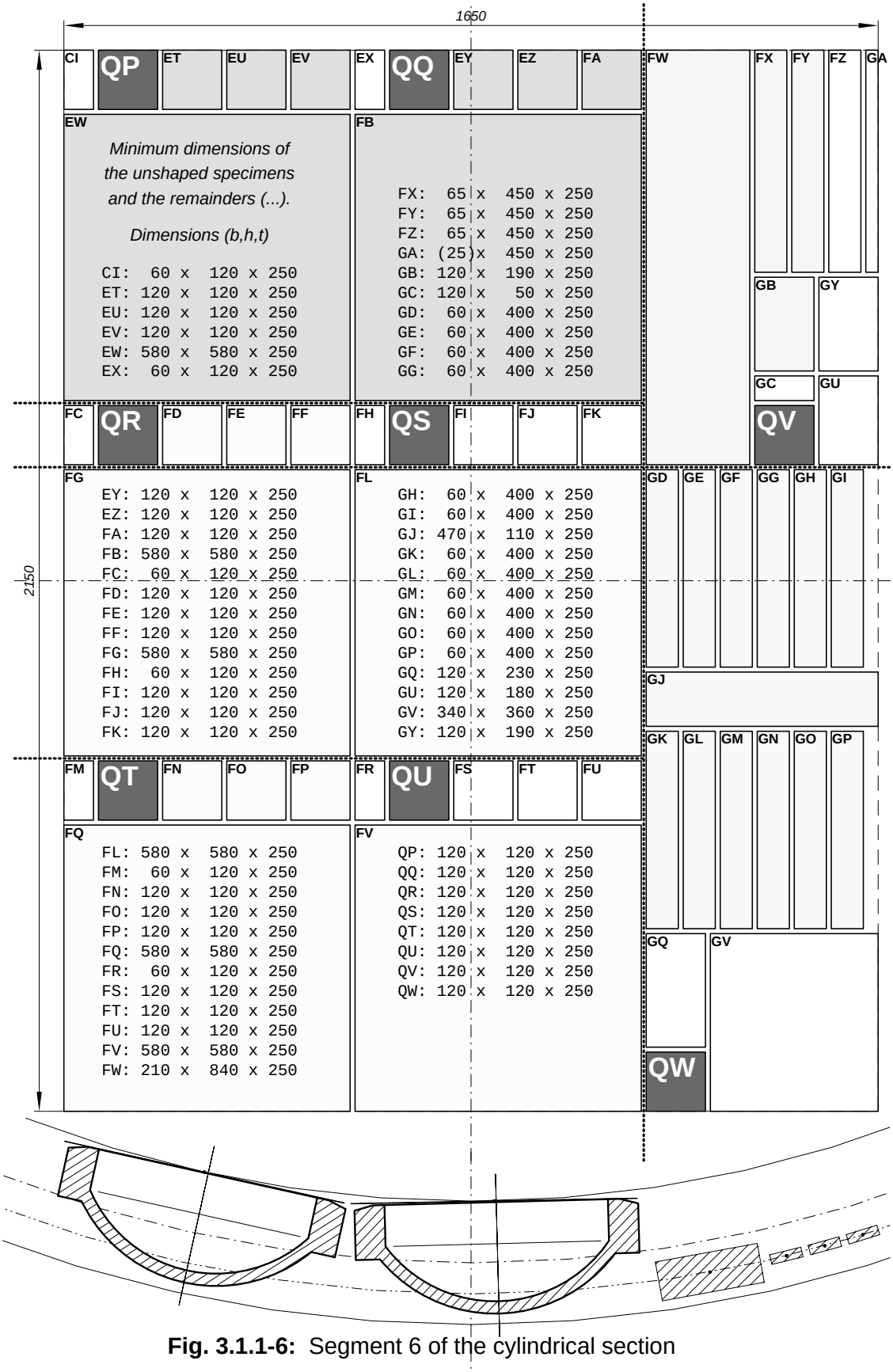

Fig. 3.1.1-6: Segment 6 of the cylindrical section

For standard quality tests the slice No.1, for instance **QA1***, will be used*

For extended quality tests additional slices will be defined, max. 15 slices.

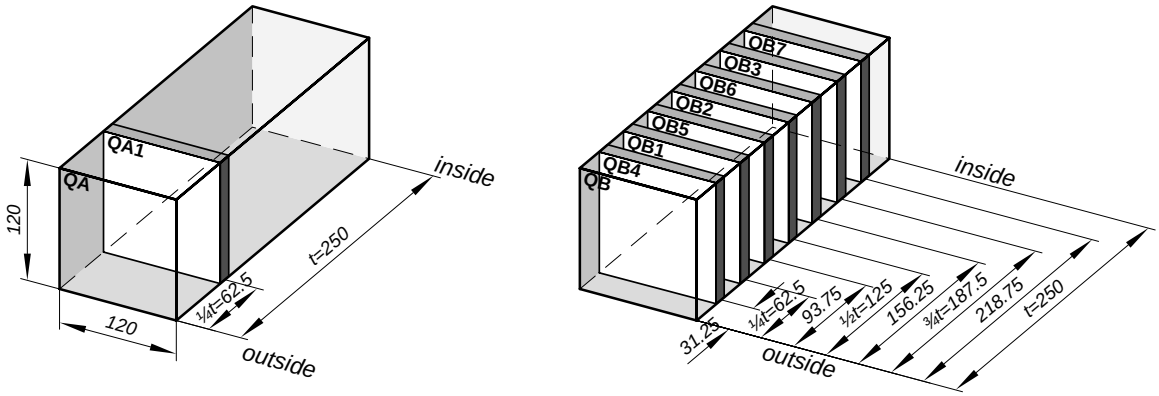

Minimum dimensions of the unshaped specimens

Dimensions (b,h,t)

```
A-D: 12 x 58 x 12
E-L: 58 x 12 x 12
M-P: 12 x 58 x 12
```

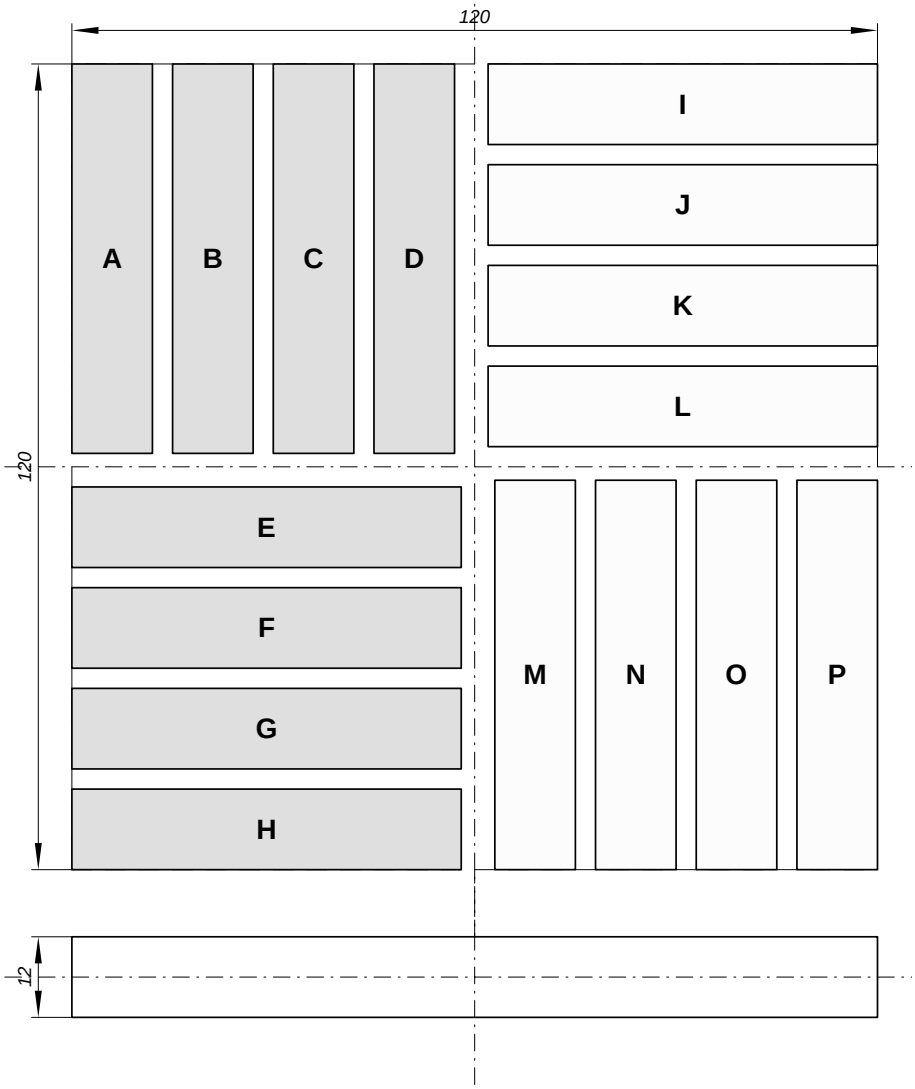

Fig. 3.1.1-7: Material blocks for the material qualification tests

3.1.1.2 Material qualification tests

To control the material homogeneity, first Charpy impact tests have been carried out which provide integral information about material strength, ductility and dynamic effects. In one series of tests specimens were taken from several blocks all over the relevant segments of the cylindrical section of the reactor pressure vessel, however only from the preferred layer 1. In this way variations of the mechanical material properties over the cylindrical surface can be studied. Furthermore it was distinguished between specimens in circumferential and axial direction. From the results shown in Fig. 3.1.1-8 one can conclude that significant variations over the cylindrical surface do not occur. Furthermore the direction of the specimens have only small influence.

In another series of tests specimens were taken from only one block, but considering several layers (slices) all over the wall thickness. Thus profiles of the mechanical material behaviour over the wall thickness can be obtained. Again from Fig. 3.1.1-9 one can conclude that the profile is almost uniform and that the direction of the specimens do not play an essential role.

However one can also see that the scatter of the results (the different symbols refer to different nominell identical tests) is rather high and impairs precise statements.

Therefore a large number of standard tensile tests have been carried out for many slices of the material blocks. In addition, also many carbon content analyses have been carried out in order to provide some kind of control, since the tensile strength is known to be related to the carbon content. The results are listed in the attached table.

As indicated in Fig. 3.1.1-7, the specimens A, B, C, D are located in circumferential, the specimens E, F, G, H are located in axial direction. After the results had documented the isotropic behaviour of the material, the direction of the specimens was no longer of interest and instead of the letters A, B, … the digits 1 and 2 were introduced to identify the specimens.

The yield stress, the ultimate stress, the elongation at failure and the reduction of area listed in the attached table confirm that the material is quite homogeneous and that the scatter of the material strength is smaller than the scatter obtained by the Charpy impact tests.

In the middle of the wall thickness the yield stress is about 6 %, the more important ultimate stress is about 2.5 % lower than at the inner and outer surface. The lowest strength occurs for the blocks QH and QJ. There the yield stress is about 4.5 %, the ultimate stress is about 3 % lower than the mean values.

Thus it can be concluded that the variation of the mechanical material properties is rather low. This is a good basis to investigate the influence of specimen size and shape on the material behaviour.

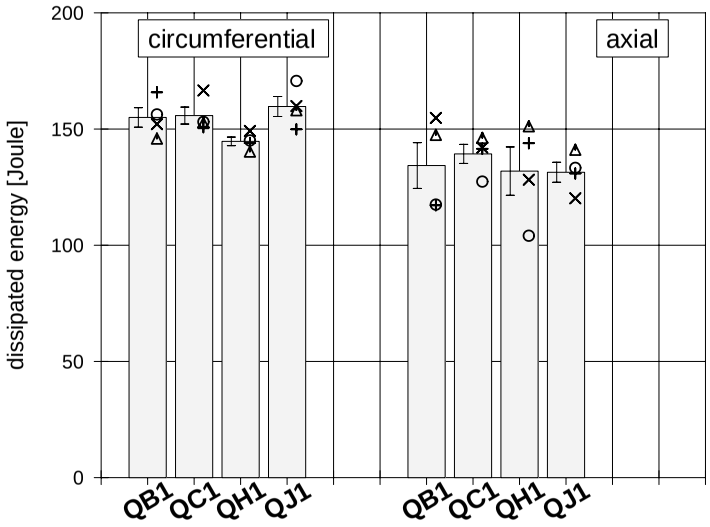

Fig. 3.1.1-8: Charpy impact tests for several blocks over the cylindrical section of the pressure vessel

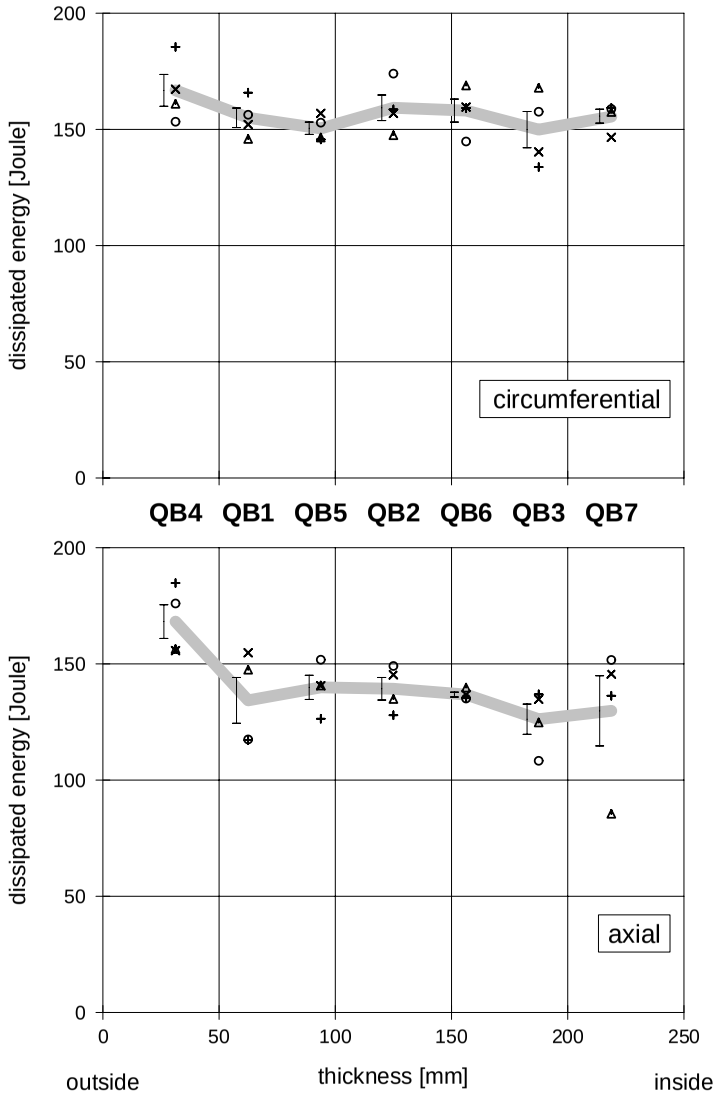

Fig. 3.1.1-9: Charpy impact tests for specimens over the wall thickness of the pressure vessel

Slice reference	Distance from the out-side (mm)	Specimen reference	Carbon content	Y.S. 0,2% (MPa)	U.T.S (MPa)	E (%)	R. of A. (%)
QA4	31	1	0,214	446	593	25,0	75,0
		2	0,214	443	591	26,0	73,0
QA1	63	1	0,214	433	586	26,0	73,0
		2	0,214	435	589	26,0	75,0
QA5	94	1	0,215	429	584	26,0	75,0
		2	0,215	429	584	29,0	75,0
QA2	125	1	0,220	423	582	26,0	77,0
		2	0,220	423	584	24,0	75,0
QA6	156	1	0,221	422	588	28,0	75,0
		2	0,221	429	584	26,0	73,0
QA3	188	1	0,226	441	597	26,0	75,0
		2	0,226	441	598	24,0	73,0
QA7	219	1	0,247	463	620	22,0	73,0
		2	0,247	470	627	24,0	73,0
QB4	31	C	0,213	449	596	26,0	73,0
	31	D	0,222	445	596	25,0	73,0
	31	E	0,216	446	595	27,0	73,0
	31	F	0,216	444	596	27,0	73,0
QB1	61	A		431	590	27,0	73,0
	61	B		437	591	27,0	73,0
	61	C	0,217	436	592	26,0	73,0
	61	D	0,218	438	592	26,0	73,0
	61	E	0,215	435	590	26,0	75,0
	61	F	0,213	443	593	25,0	73,0
	61	G		429	589	26,0	75,0
	61	H		438	589	26,0	75,0
QB5	94	C	0,215	424	583	24,0	71,0
	94	D	0,215	422	583	24,0	71,0
	94	E	0,219	430	587	26,0	73,0
	94	F	0,219	433	585	24,0	73,0
QB2	125	C	0,215	417	584	24,0	71,0
	125	D	0,221	422	585	28,0	71,0
	125	E	0,217	422	586	23,0	73,0
	125	F	0,215	422	586	24,0	75,0
QB6	156	C	0,216	428	587	26,0	71,0
	156	D	0,216	424	589	27,0	73,0
	156	E	0,223	429	587	26,0	73,0
	156	F	0,224	426	586	25,0	75,0
QB3	188	C	0,223	442	598	26,0	73,0
	188	D	0,226	440	601	26,0	73,0
	188	E	0,230	444	599	28,0	73,0
	188	F	0,227	437	597	26,0	73,0
QB7	219	C	0,228	454	605	23,0	73,0
	219	D	0,237	452	608	26,0	71,0
	219	E	0,228	443	603	24,0	75,0
	219	F	0,228	449	604	25,0	75,0

Slice reference	Distance from the outside	Specimen reference	Car-bon con-	Y.S. 0,2% (MPa)	U.T.S (MPa)	E (%)	R. of A. (%)
QC4	31	1	0,215	450	599	27,0	73,0
		2	0,215	449	594	26,0	73,0
QC1	63	A		438	591	25,0	71,0
	63	B		441	596	24,0	73,0
	63	C	0,214	435	595	27,0	73,0
	63	D	0,212	440	595	26,0	73,0
	63	E	0,215	438	593	27,0	73,0
	63	F	0,212	438	591	24,0	75,0
	63	G		444	596	25,0	73,0
	63	H		438	590	24,0	73,0
QC5	94	1	0,215	436	589	26,0	73,0
		2	0,215	427	589	26,0	73,0
QC7	219	1	0,246	465	624	22,0	73,0
		2	0,246	468	622	23,0	71,0
QD1	63	1	0,213	437	588	26,0	75,0
		2	0,213	435	588	26,0	73,0
QD12	110	1	0,218	430	586	26,0	73,0
		2	0,218	426	587	26,0	73,0
QD7	219	1	0,224	448	602	27,0	75,0
		2	0,224	428	600	25,0	73,0
QE1	63	A	0,212	441	592	30,0	73,0
		H	0,212	437	592	29,0	74,0
QG1	63	A	0,212	432	587	27,0	73,0
		H	0,212	427	588	26,0	73,0
QH1	63	C	0,215	418	575	24,0	71,0
	63	D	0,214	413	575	29,0	75,0
	63	E	0,227	412	571	26,0	73,0
	63	F	0,218	415	574	26,0	75,0
QJ1	63	C	0,216	410	570	27,0	73,0
	63	D	0,213	411	575	27,0	73,0
	63	E	0,212	413	570	26,0	71,0
	63	F	0,216	415	576	26,0	73,0
QL1	63	A	0,215	421	583	23,0	73,0
		H	0,215	430	592	26,0	73,0
QL2	125	A	0,213	419	583	24,0	67,0
		H	0,213	425	584	27,0	72,0
QS4	31	1	0,214	442	586	27,0	75,0
		2	0,214	428	585	27,0	77,0
QS1	63	1	0,214	427	579	28,0	75,0
		2	0,214	430	583	26,0	73,0
QS5	94	1	0,215	423	582	26,0	75,0
		2	0,215	418	577	27,0	75,0
QV1	63	A	0,213	427	584	27,0	71,0
		H	0,213	428	584	26,0	74,0
		Mean	0,219	434	590	25,8	73,3
		Min	0,212	410	570	22,0	67,0
		Max	0,247	470	627	30,0	77,0
		Stdv	0,008	13	11	1,5	1,5
		Number of values	82	90	90	90	90

3.1.2 Uniaxial tests

3.1.2.1 Tension tests under static load

Depending on specimen size and the temperature quite different testing machines have been used.

Figures 3.1.2-1 and 3.1.2-2 show the 100 MN machine and measuring equipment (MPA) for the biggest specimen (Flat specimen, 200 mm thickness).

Figure 3.1.2-3 shows a smaller machine (FZK) with an optical measurement system which allows the determination of strain fields at the specimen surfaces using the object grating method.

Fig. 3.1.2-4 shows the measuring devices (EMPA) for tests at elevated temperatures. In order to reduce oxidation, inert atmosphere was used for the smallest specimens (circular specimens of 3 mm diameter) at 850 °C.

For all tests the cross head speed was prescribed such that the mean strain rate related to the gauge lengths of the specimens was about $10^{-3}s^{-1}$.

More details about the tests and an extensive description of the results may be found in SAM-LISSAC-D024, -D031 and -D032.

Some of the measured load deformation relations will be presented in Figs. 3.1.2-5 to 3.1.2-14. The nominal stress at the ordinate is defined as the tension force divided by the smallest initial cross section of the specimen. The hole or notch opening at the abscissa is defined as the increase of the hole or notch in tension direction divided by the initial value. Note that the ends of the curves are usually due to the special properties of the test- and measurement facility (for instance, the stiffness of the tension machine, the measuring range, etc.); the ends do not describe specimen failure. Note furthermore that for tests with nominal identical parameters only one curve is shown. The deviations of the other curves is usually less than $\pm$ 1 %. In two cases the deviations were $\pm$ 5 %.

The maximum nominal stresses for the flat specimens of 20 mm thickness tested at 400 °C (Figs. 3.1.2-10 and 3.1.2-11) turned out to be about 10 % higher than the maximum nominal stress for other (smaller and larger) specimens of the corresponding test families. Detailed inquires about these deviations revealed that the heating time for the above mentioned specimens was about 2 hours. The heating time for the much smaller specimens of 4 mm thickness was also about 2 hours, but the heating time for the larger specimens was at least 8 hours. Therefore the flat specimen AW1 of 20 mm thickness with hole was additionally tested at 400 °C, but with a heating time of 8 hours. The results show that the maximum nominal stress is now less than 4 % higher than the corresponding values from other specimens (Fig. 3.1.2-10, dashed line). Thus it can be concluded that the deviations for the above mentioned specimens are likely to be caused by micro structural changes, the deviations are certainly not a size effect.

In the table of chapter 3.1.4.3 it will be indicated that the extension of the heating time from 2 hours to 8 hours caused also an increase of the failure strain.

Furthermore the maximum nominal stresses for all the specimens with holes or notches are a little bit higher than the corresponding stresses for smooth specimens. This effect is well known. It is due to the higher triaxiality of the stresses in the specimens with holes or notches which hinder necking processes.

The maximum nominal stresses for 850 °C shown in Figs. 3.1.2-13 and 3.1.2-14 seem to be size dependent, but in the opposite way as might be expected: The maximum stresses increase with increasing specimen size. There is one exception:

The tests with the small circular specimens of 3 mm diameter where the maximum stress is relatively high. However considering the experience with the sensitivity to heating processes just discussed, one might conclude that also in this case such effects may have influenced the results. For instance, diffusion processes at the specimen surfaces could have a degrading effect which increases for decreasing specimen size, except the small specimens of 4 mm thickness and 3 mm diameter, where the tests were essentially performed in an inert atmosphere. On the other hand, however, rather high maximum stresses were only obtained for the specimens of 3 mm diameter.

During the test of the large specimen with hole the crack could be seen first inside the hole in the middle of the wall-thickness. With slightly increasing load the crack propagated quickly to the flat surfaces of the specimen. Finally it propagated to the outer contour of the specimen.

Of special interest are the results from the object grating method mentioned above. It needs the preparation of the specimens with either a regular (deterministic) or a random (stochastic) pattern. For the preparation with a random pattern the specimen surface is sprayed by an antireflection white coloured ground paint and in a second step by a black coloured paint producing a random speckles pattern. A prepared specimen ready to use is shown in Fig. 3.1.2-15.

During the test the random speckles pattern on the surface is viewed by two CCD cameras with a triangular arrangement. The deformation of this pattern under increasing load is recorded by the cameras and after the test the data are evaluated by using digital image processing. The main problem of the evaluation is to match identical surface points related to different deformation states of the object. This is done with a 2D adaptive area based matching algorithm. Using the result the strains are calculated in a last step.

In Fig. 3.1.2-16 the resulting axial strain fields are shown at the surface for a flat specimen with hole having a wall thickness of 4 mm and for a specimen belonging to the same family having a wall thickness of 20 mm, respectively, just at the instant when a crack can be observed. The hole openings are 75 % and 61 %, respectively, at this instant. The maximum axial strains at the specimen surface are 88 % and 73 %, respectively. These results indicate a certain size effect on the deformation at failure. More extensive evaluations and discussions are presented in chapter 3.1.4 and 3.3.

From all the photographs of the broken specimens shown in SAM-LISSAC-D024, -D031 and -D032 only a few have been selected.

Figure 3.1.2-17 shows a typical fracture surface for a flat specimen with hole. Note the normal fracture zone close to the hole where the cracking has started and the shear fracture zone caused during the later phase of the failure process. Figure 3.1.2-18 shows the fracture of circular specimens with notches at room temperature, 400 °C and 850 °C. Note that in parallel to the main crack additional cracks have been initiated which, however, did not propagate very far.

These additional cracks might be one of the reasons why the measured displacements of markings applied in the notches of the circular specimens of 20 mm and 150 mm diameter led to unrealistic local (axial) failure strains up to more than 200 %. (SAM-LISSAC-D024, Figs. 57 and 58)

Fig. 3.1.2-1: Tensile testing machine of 100 MN (MPA) used for the flat specimen of 200 mm wall thickness

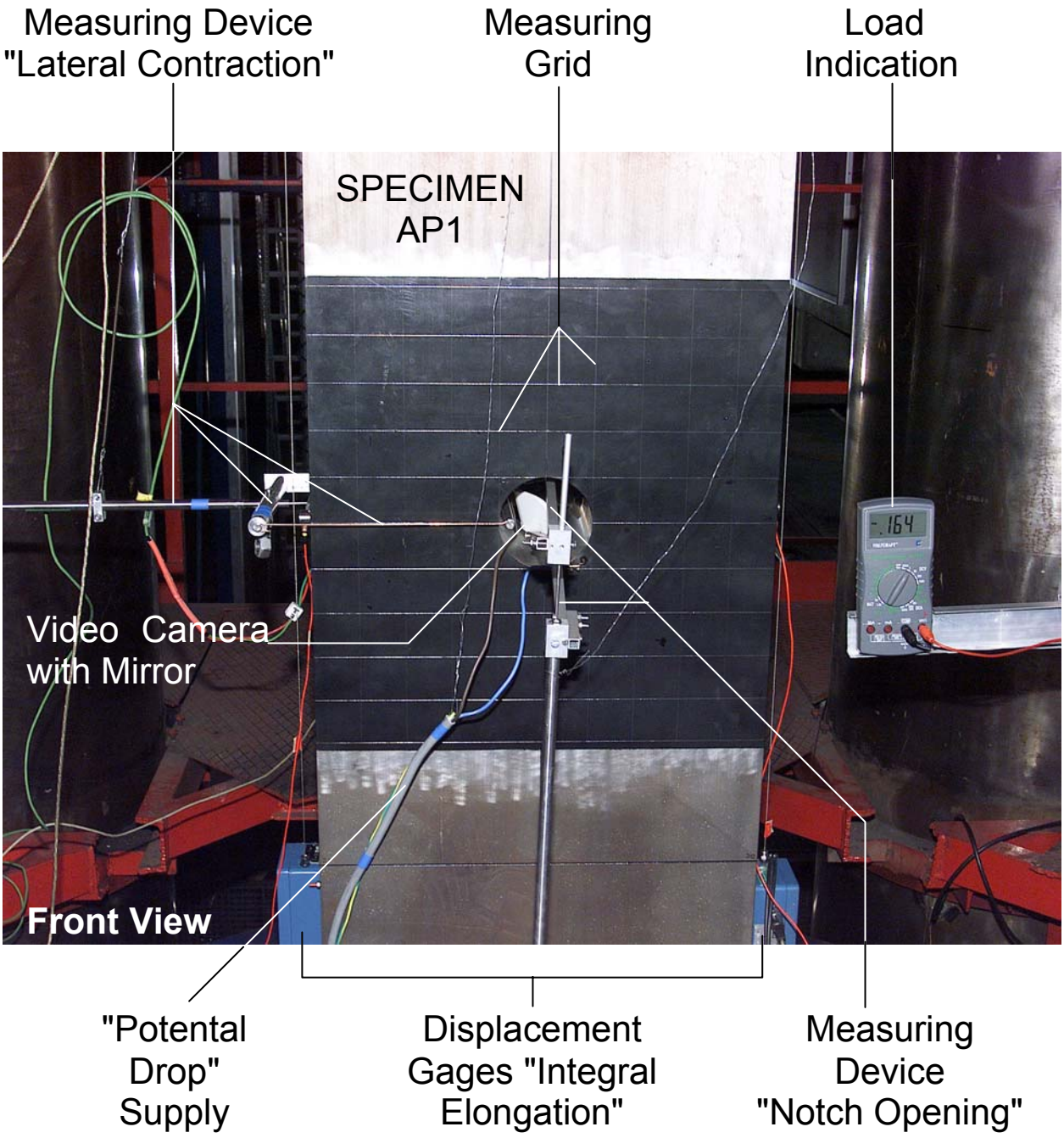

Fig. 3.1.2-2: Measuring equipment (MPA) for the flat specimen of 200 mm wall thickness

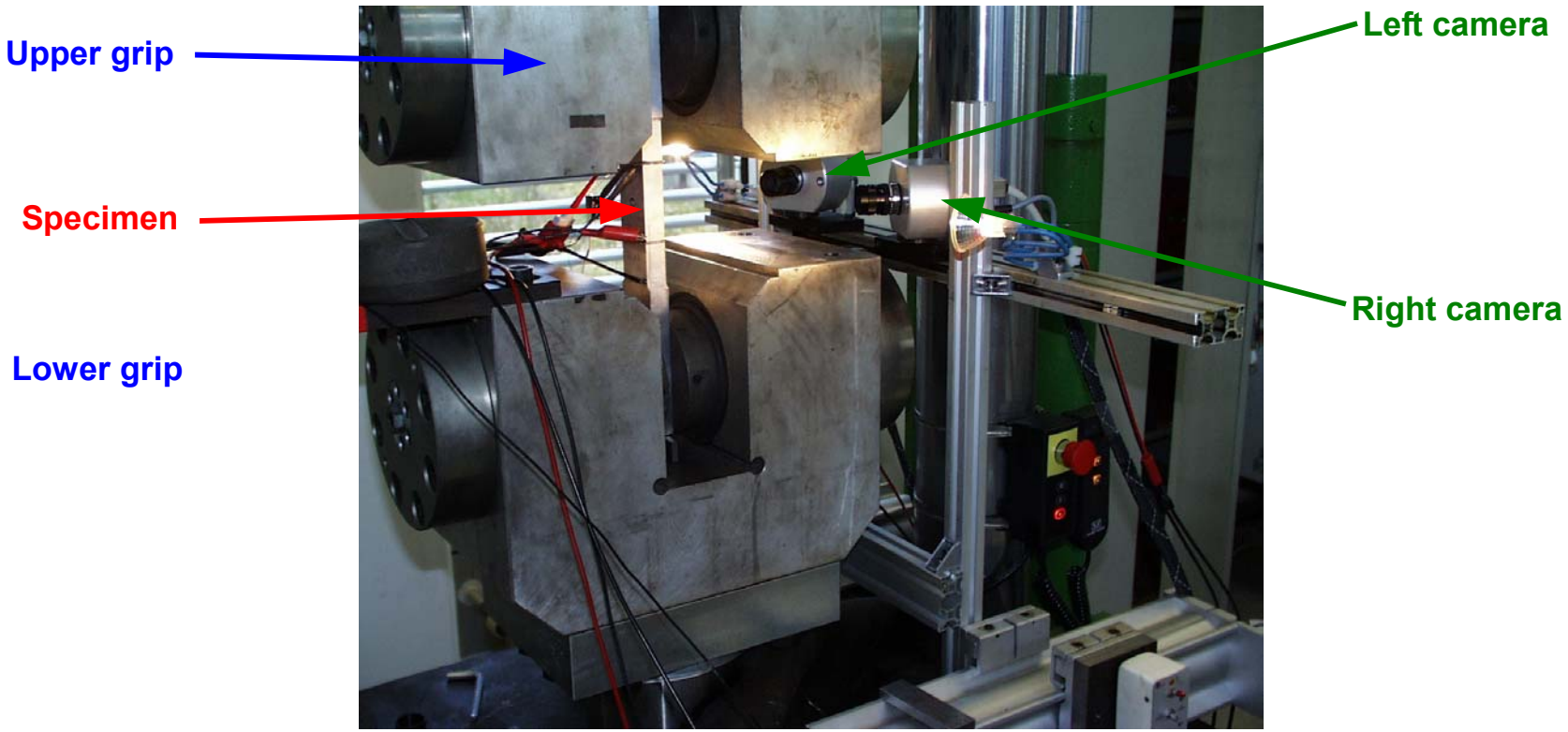

Fig. 3.1.2-3: Servo-hydraulic testing machine and optical measurement system (FZK)

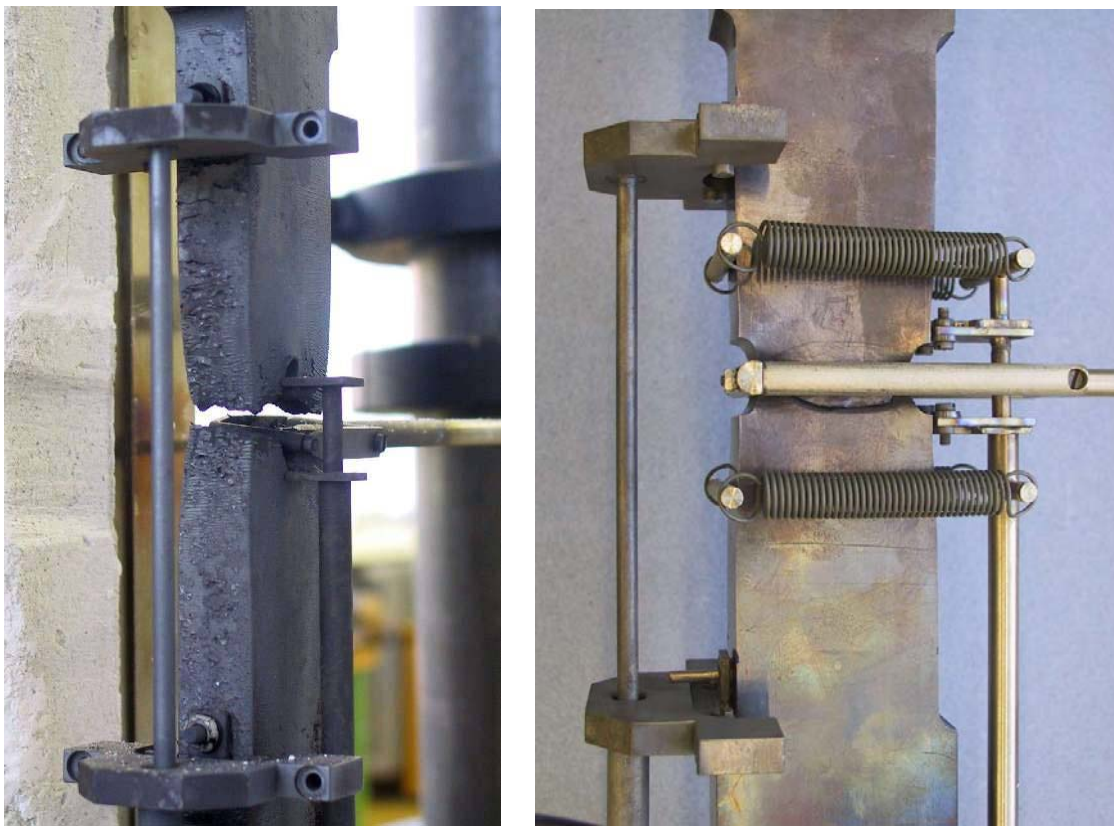

Deformation measurement on flat specimens of 20 mm wall thickness

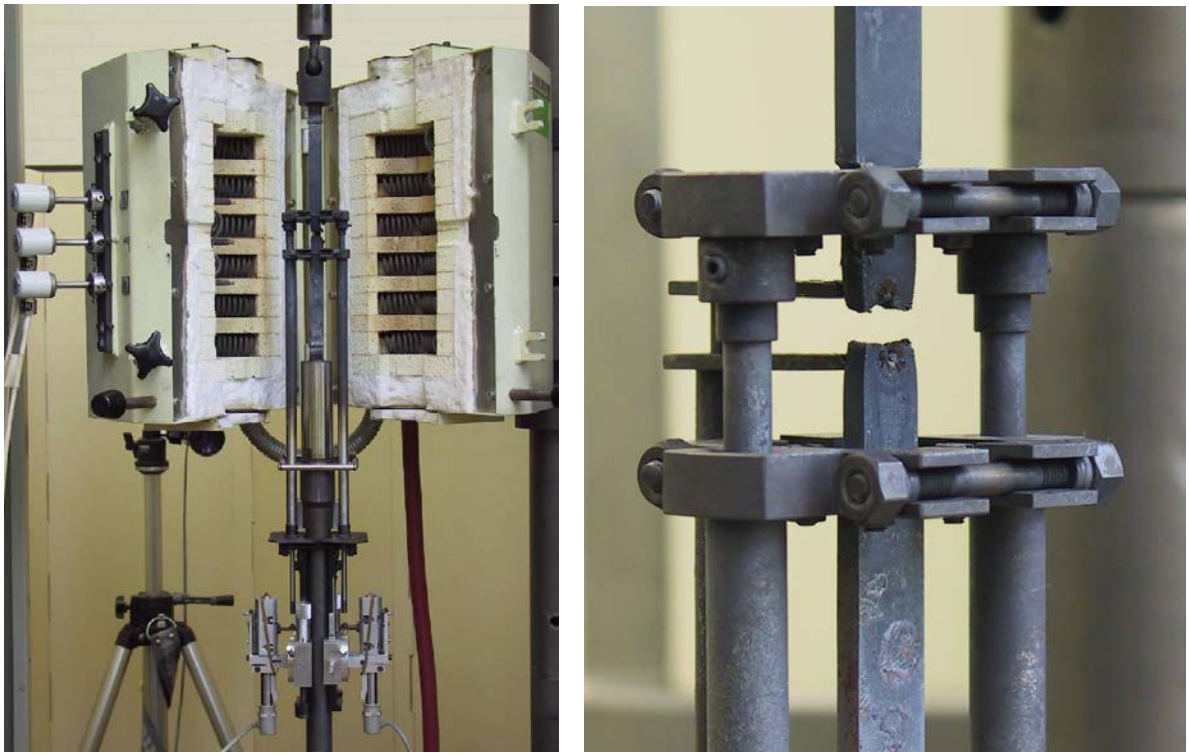

Heating facility and measurement on flat specimens of 4 mm wall thickness at 850 °C

Fig. 3.1.2-4: Measuring devices (EMPA) for tests at elevated temperatures

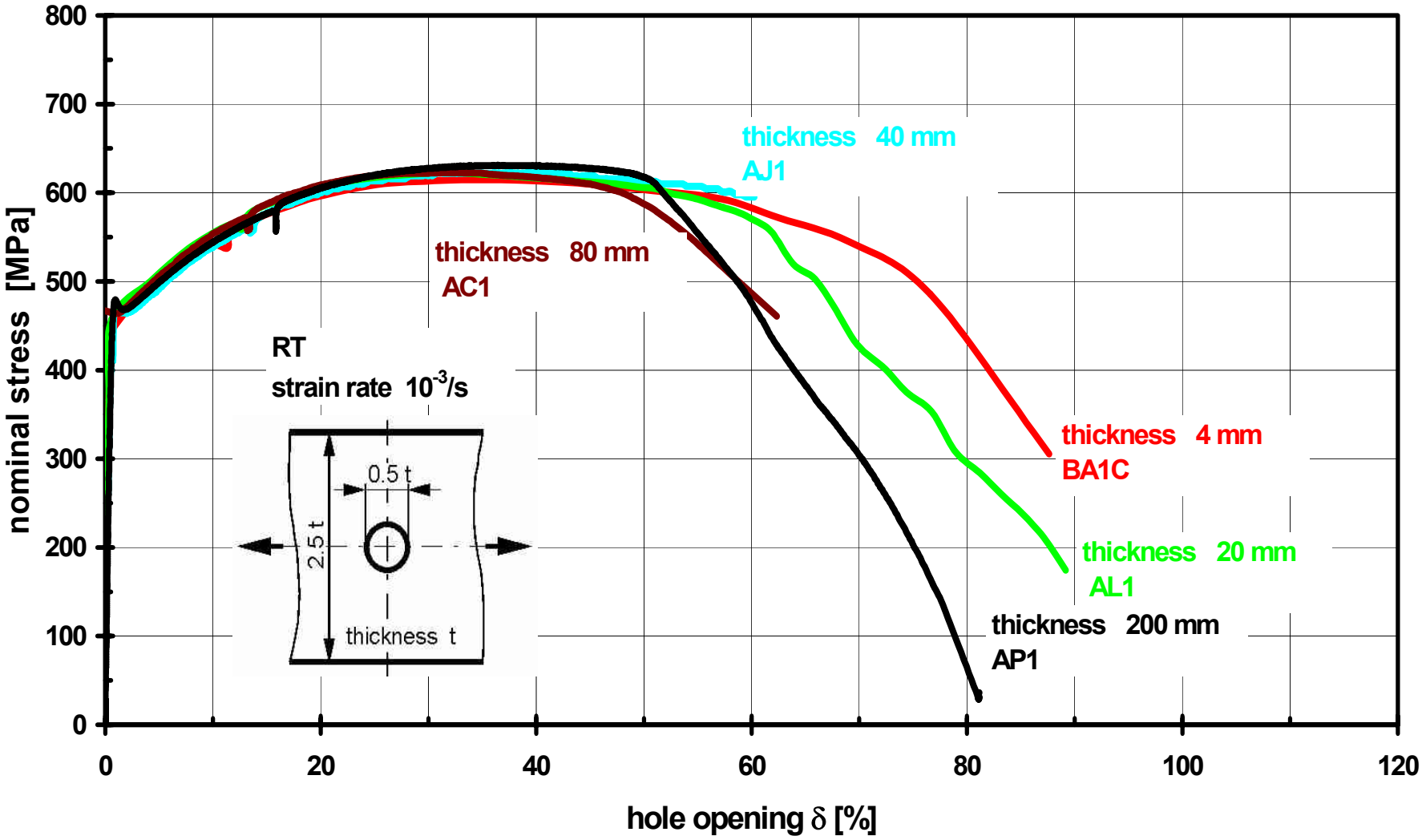

Fig. 3.1.2-5: Nominal stress vs. hole opening for the test family of flat specimens with hole, static load, RT

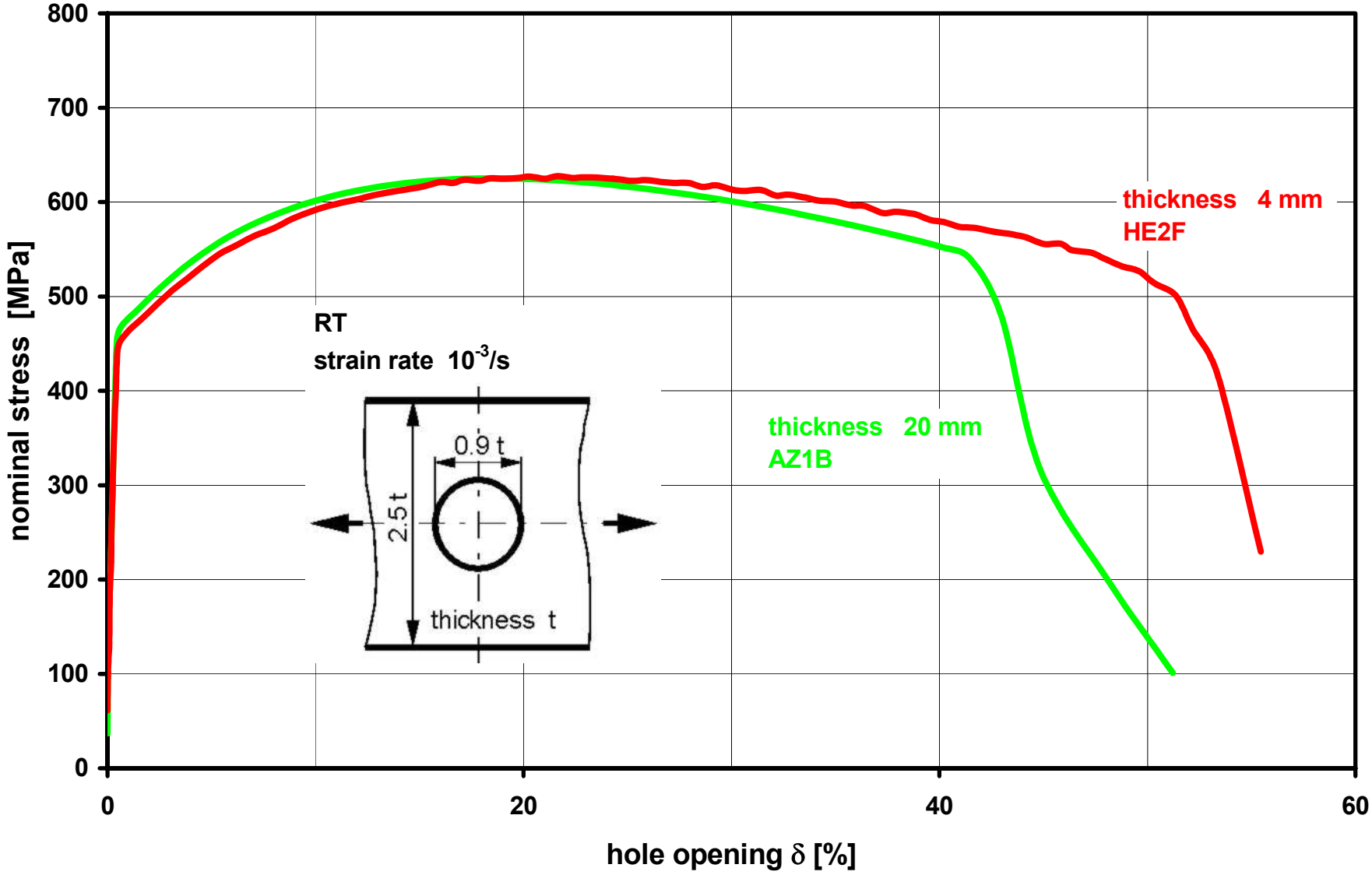

Fig. 3.1.2-6: Nominal stress vs. hole opening for the test family of flat specimens with increased hole, static load, RT

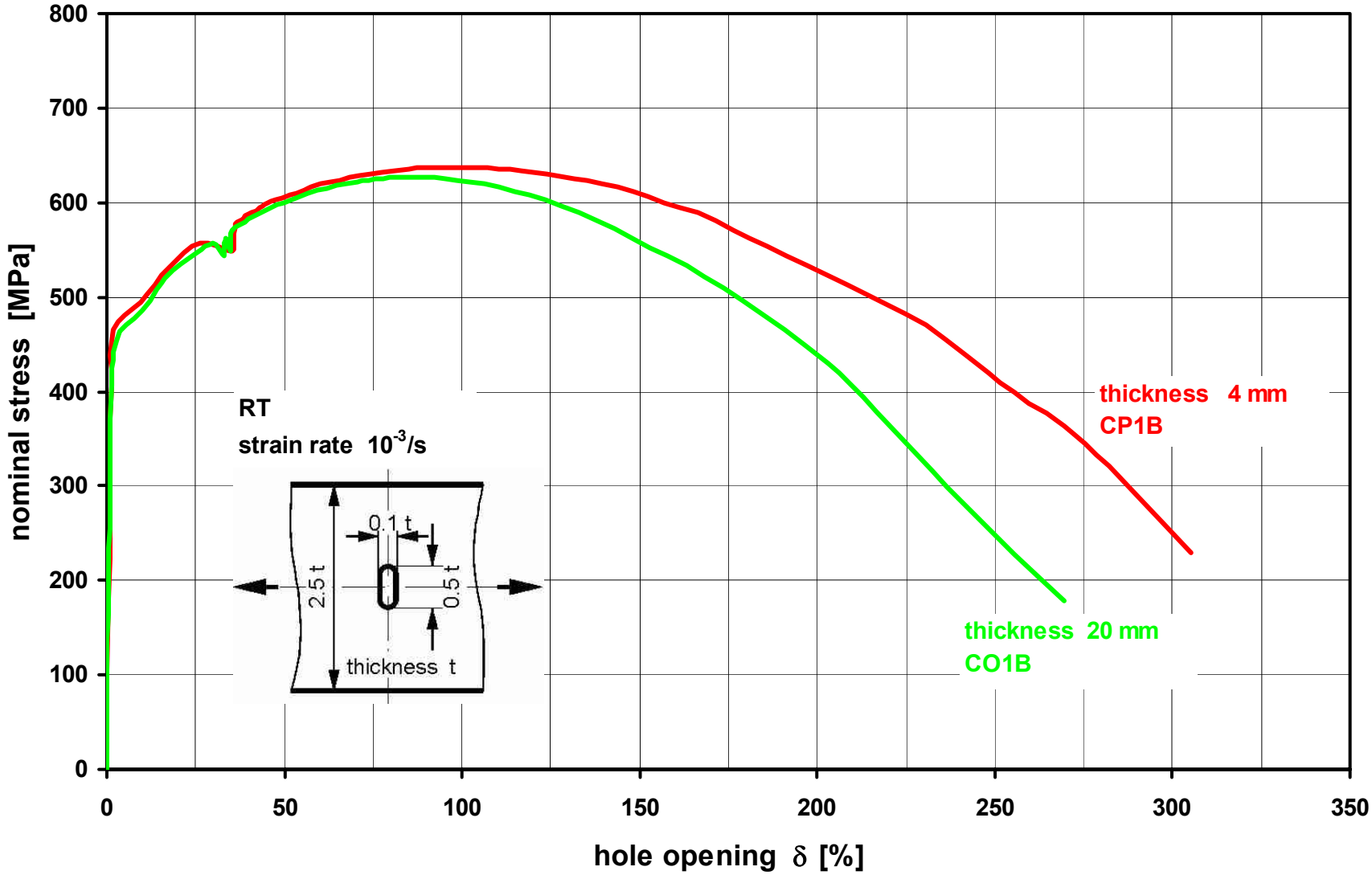

Fig. 3.1.2-7: Nominal stress vs. hole opening for the test family of flat specimens with slot, static load, RT

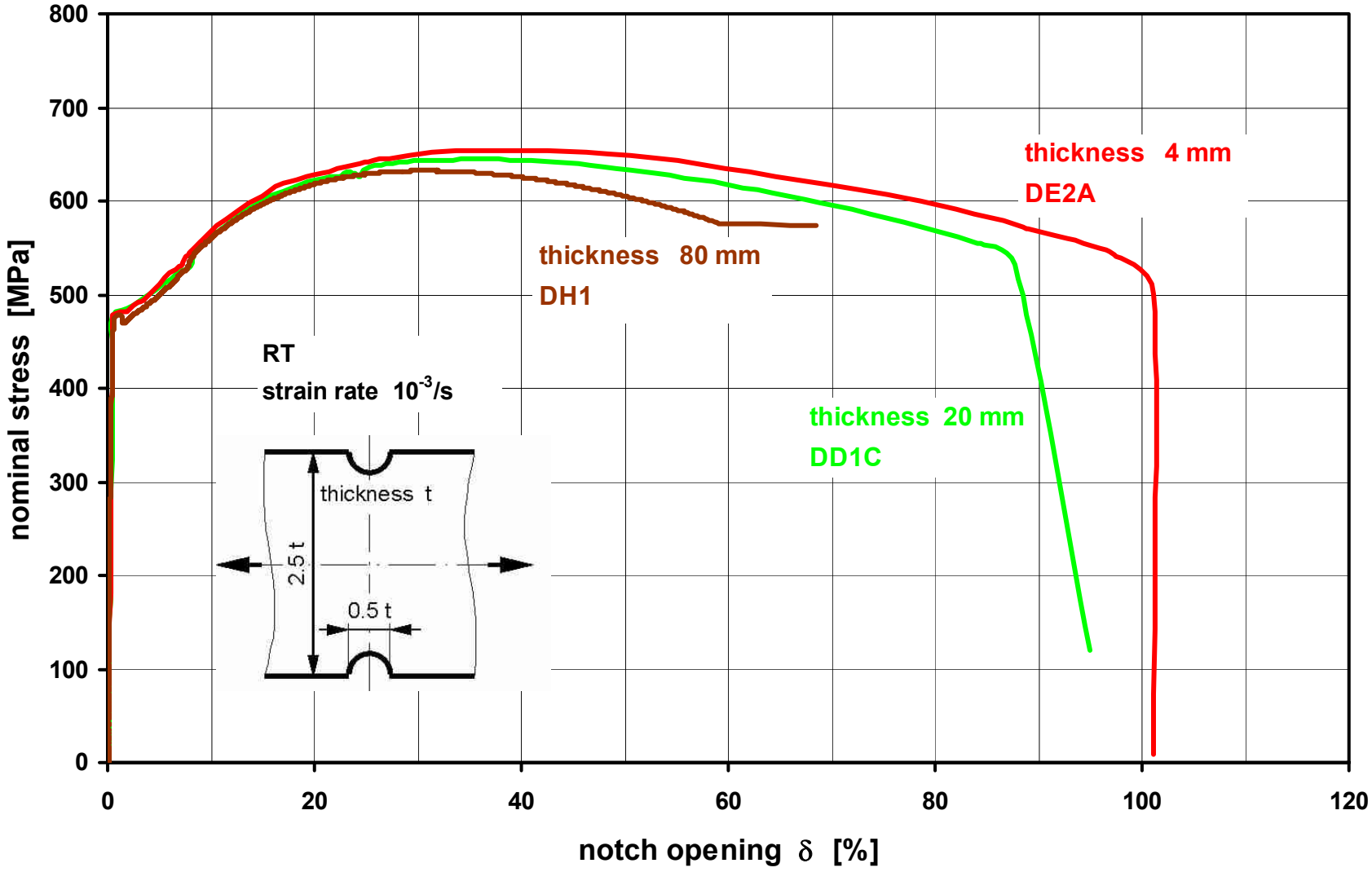

Fig. 3.1.2-8: Nominal stress vs. notch opening for the test family of flat specimens with notches, static load, RT

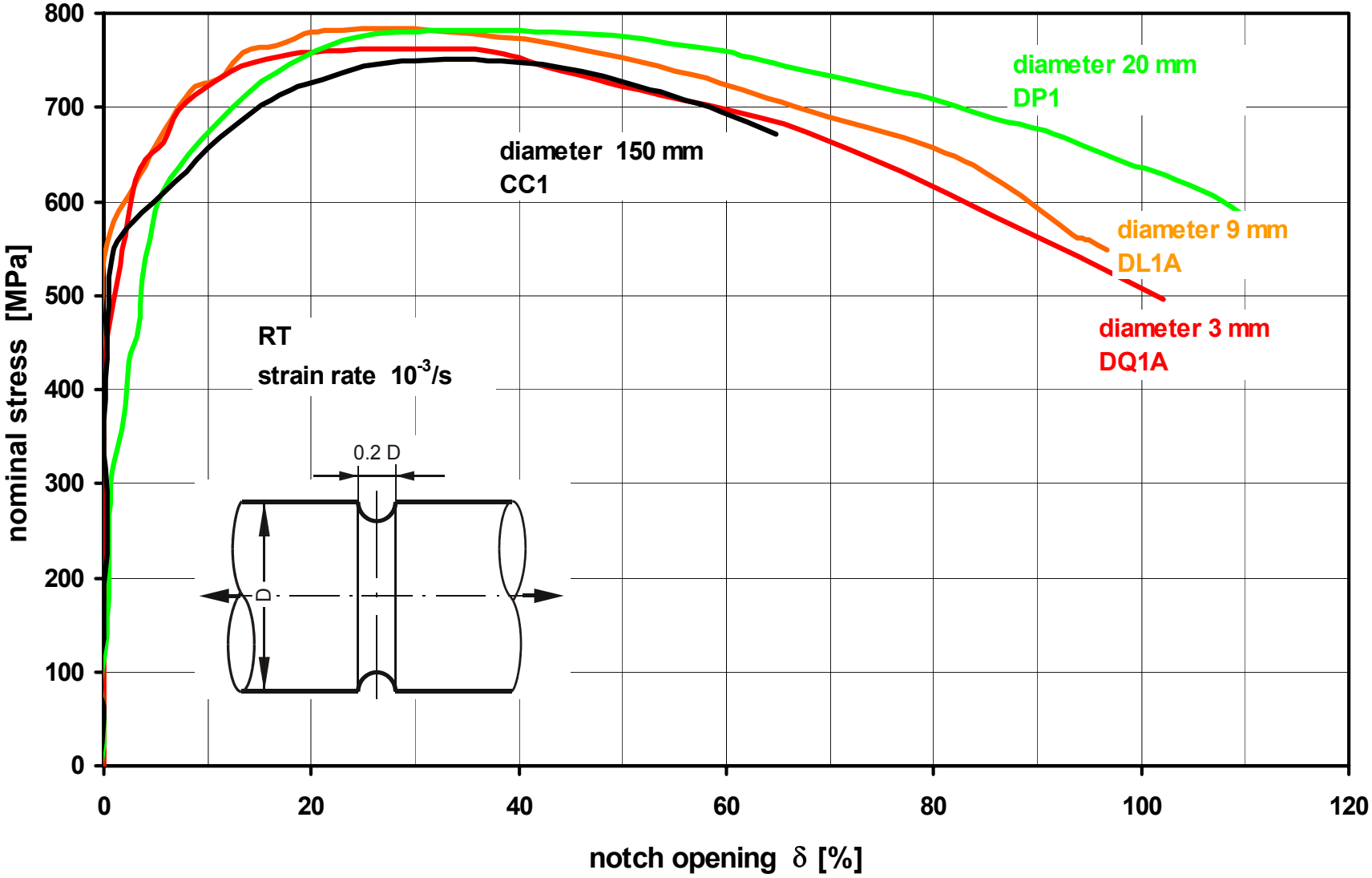

Fig. 3.1.2-9: Nominal stress vs. notch opening for the test family of circular specimens with circumferential notch, static load, RT

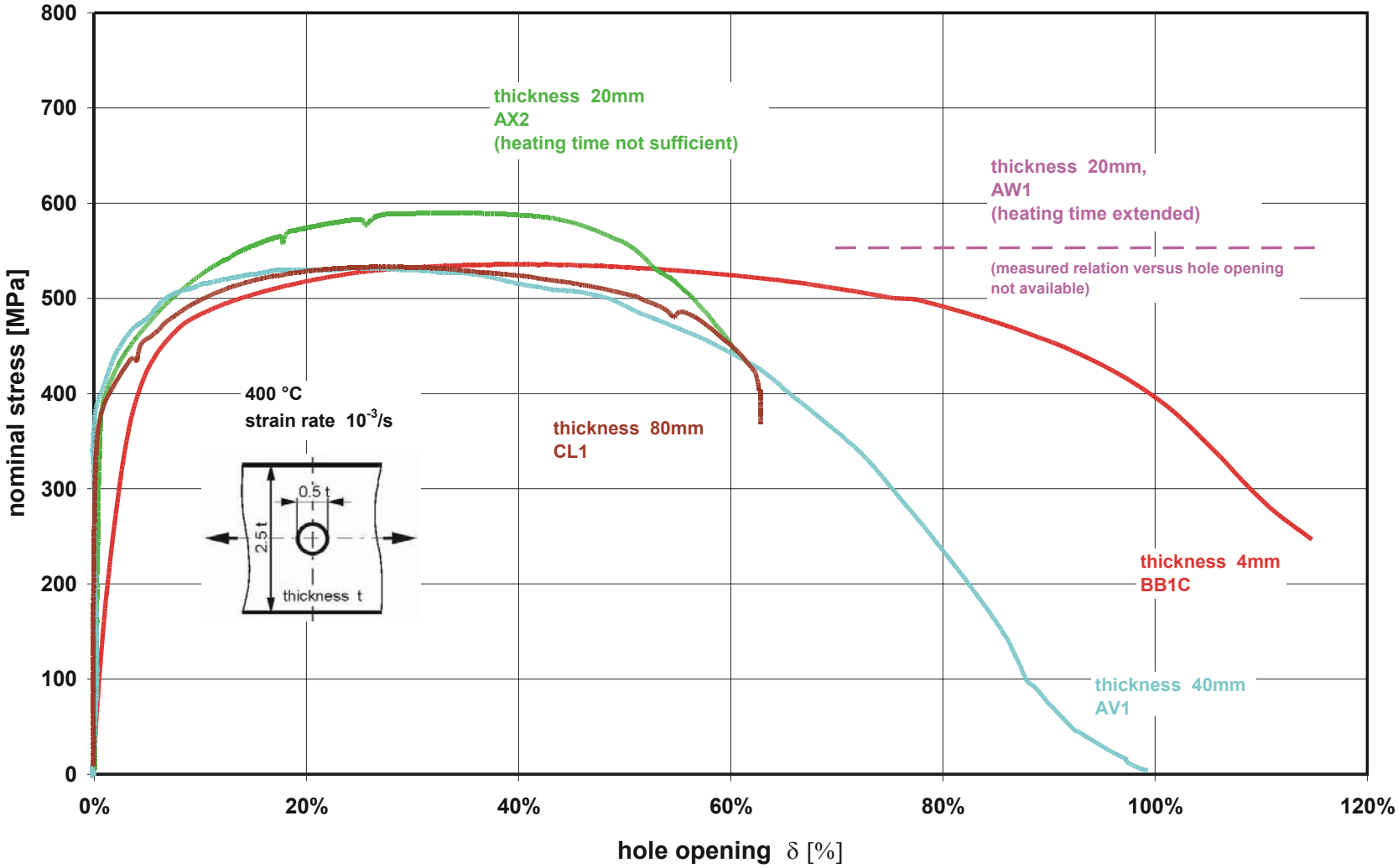

Fig. 3.1.2-10: Nominal stress vs. hole opening for the test family of flat specimens with hole, static load, 400 °C

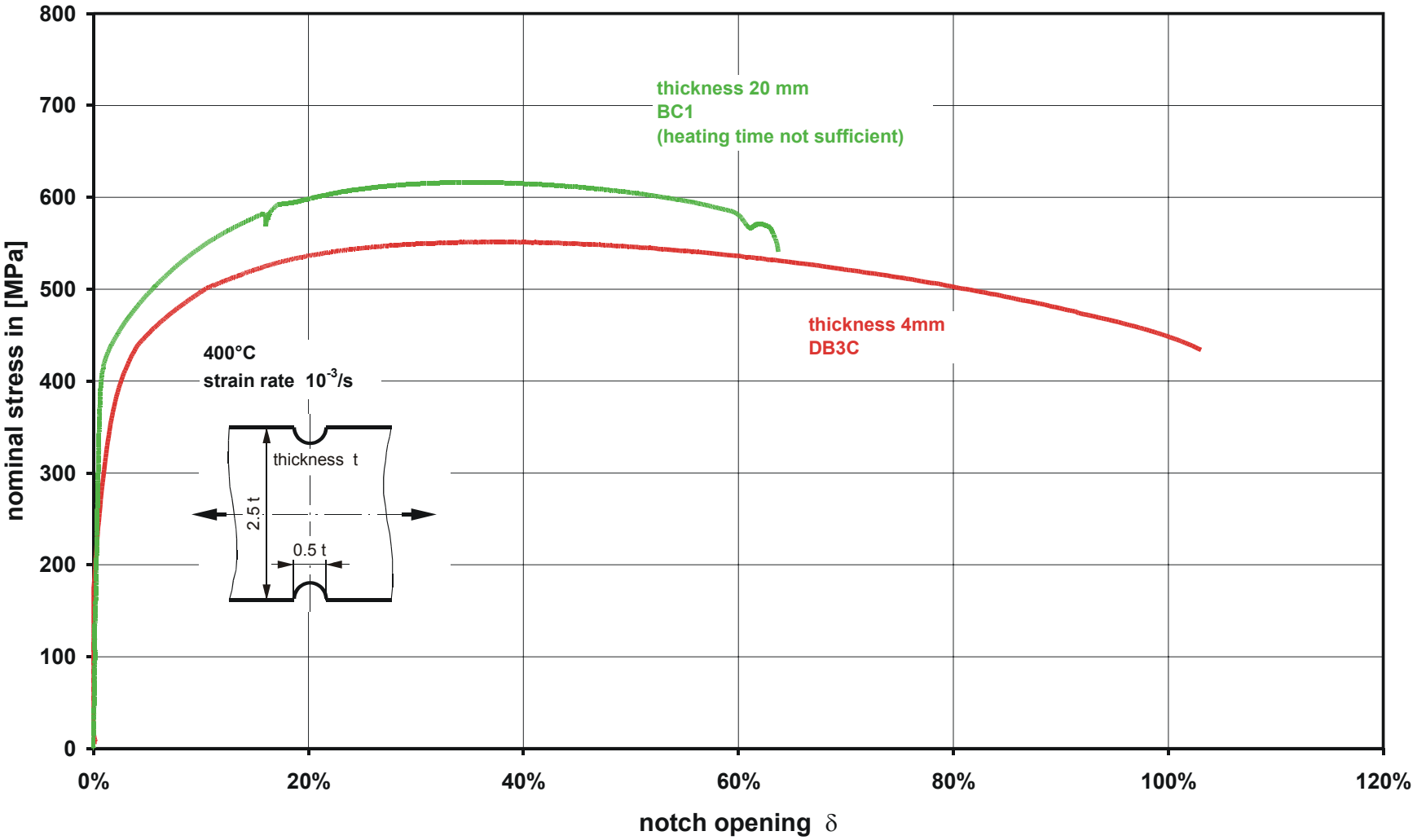

Fig. 3.1.2-11: Nominal stress vs. notch opening for the test family of flat specimens with notches, static load, 400 °C

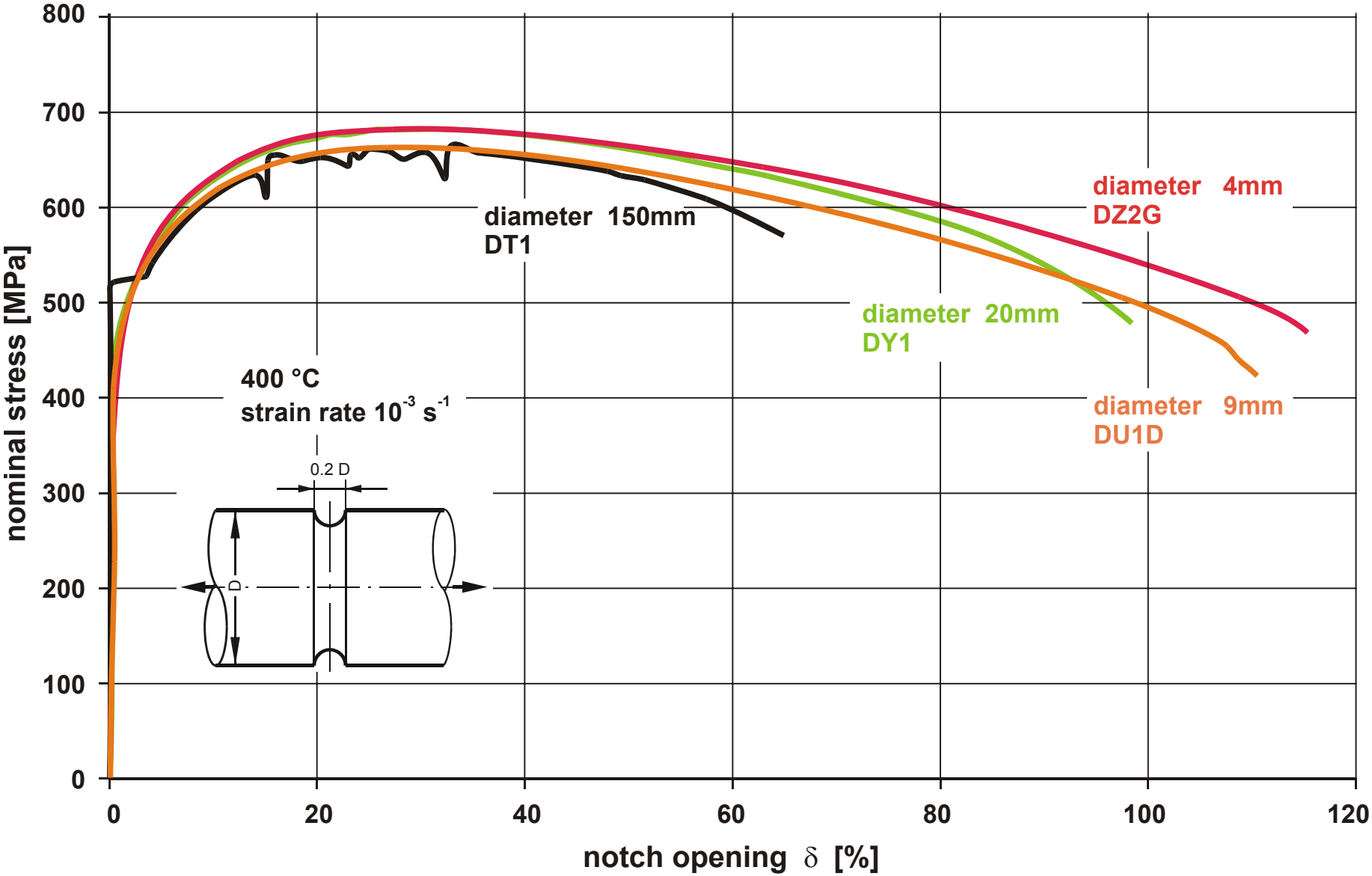

Fig. 3.1.2-12: Nominal stress vs. notch opening for the test family of circular specimens with notch, static load ,400 °C

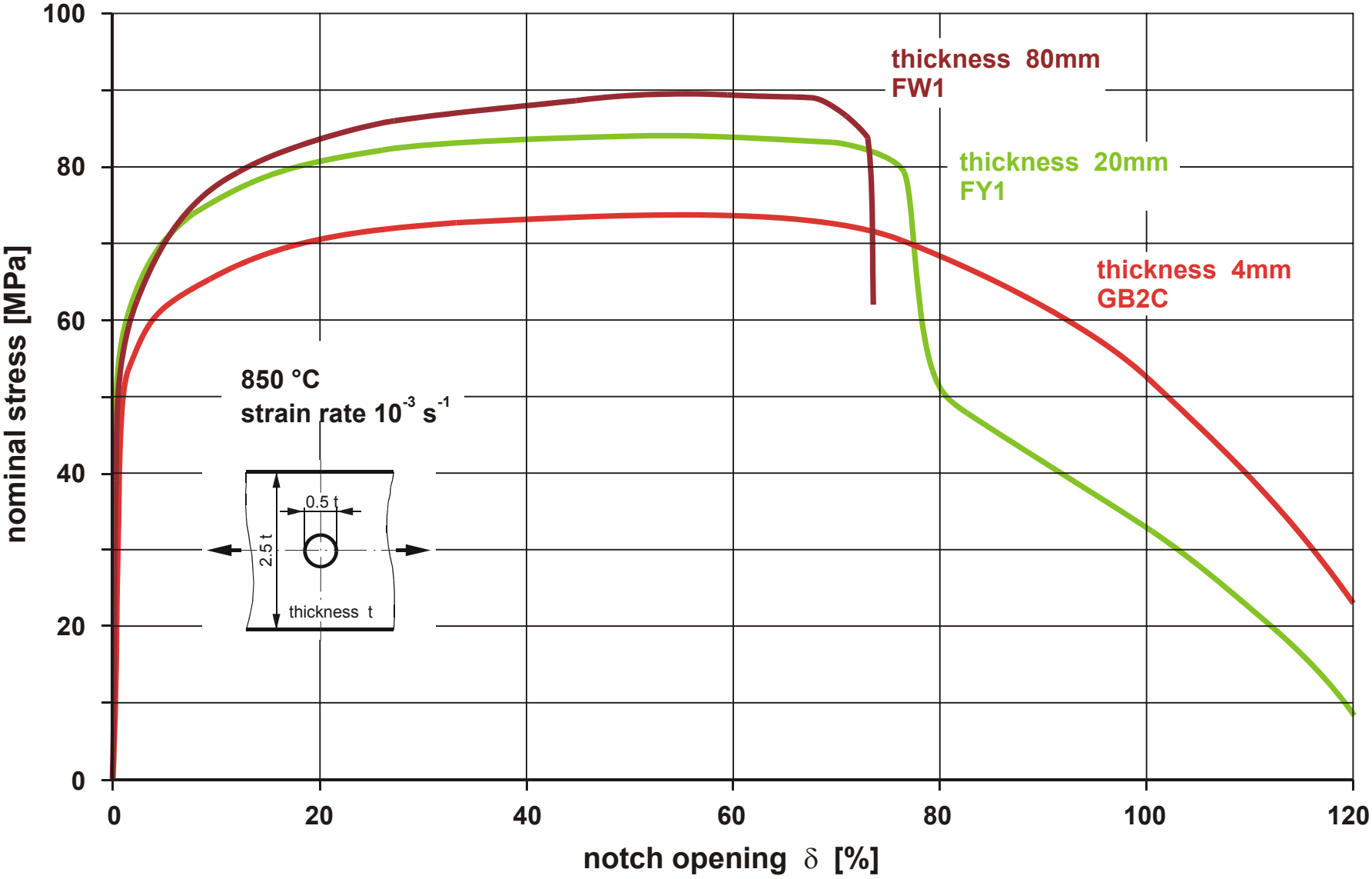

Fig. 3.1.2-13: Nominal stress vs. hole opening fort he test family of flat specimens with hole, static load, 850 °C

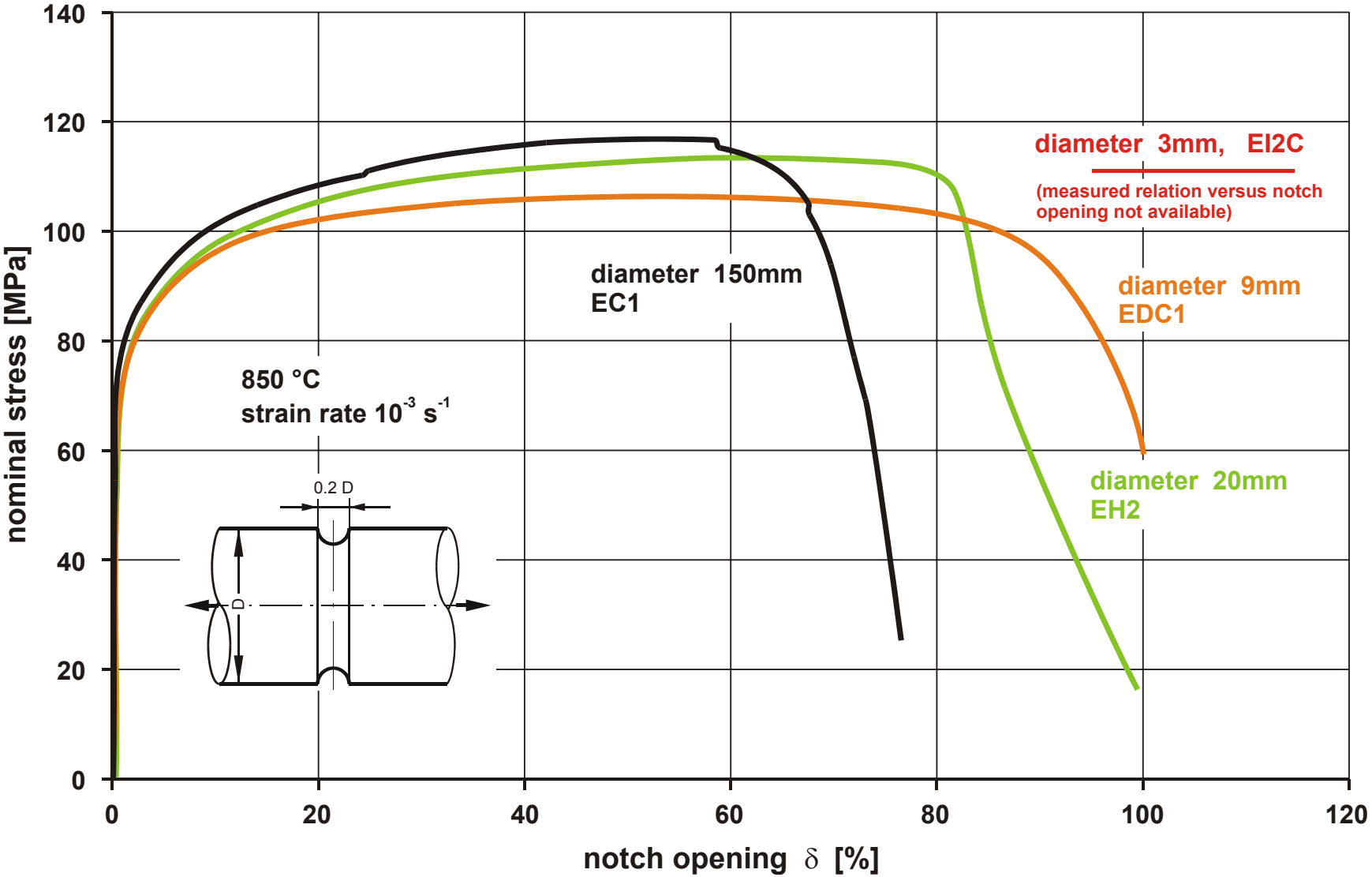

Fig. 3.1.2-14: Nominal stress vs. notch opening for the test family of circular specimens with notch, static load, 850 °C

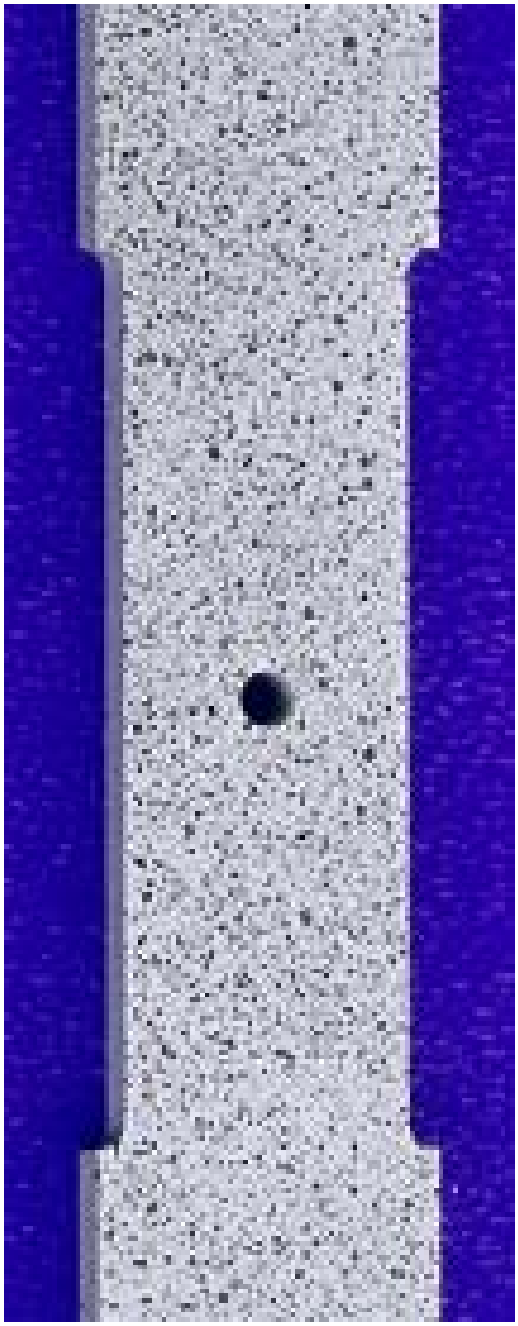

Fig. 3.1.2-15: Surface of a flat specimen prepared with a random speckles pattern for applying the object grating method

Thickness = 4 mm

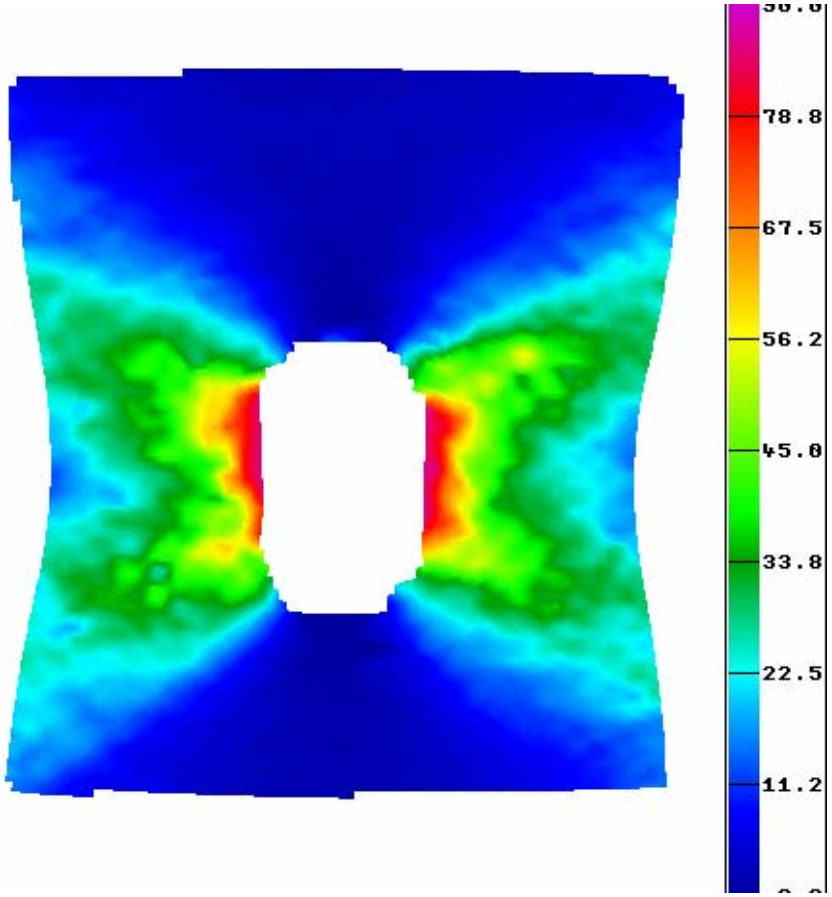

Hole opening 75 %
Max. axial strain at the specimen surface 88 %

Thickness = 20 mm

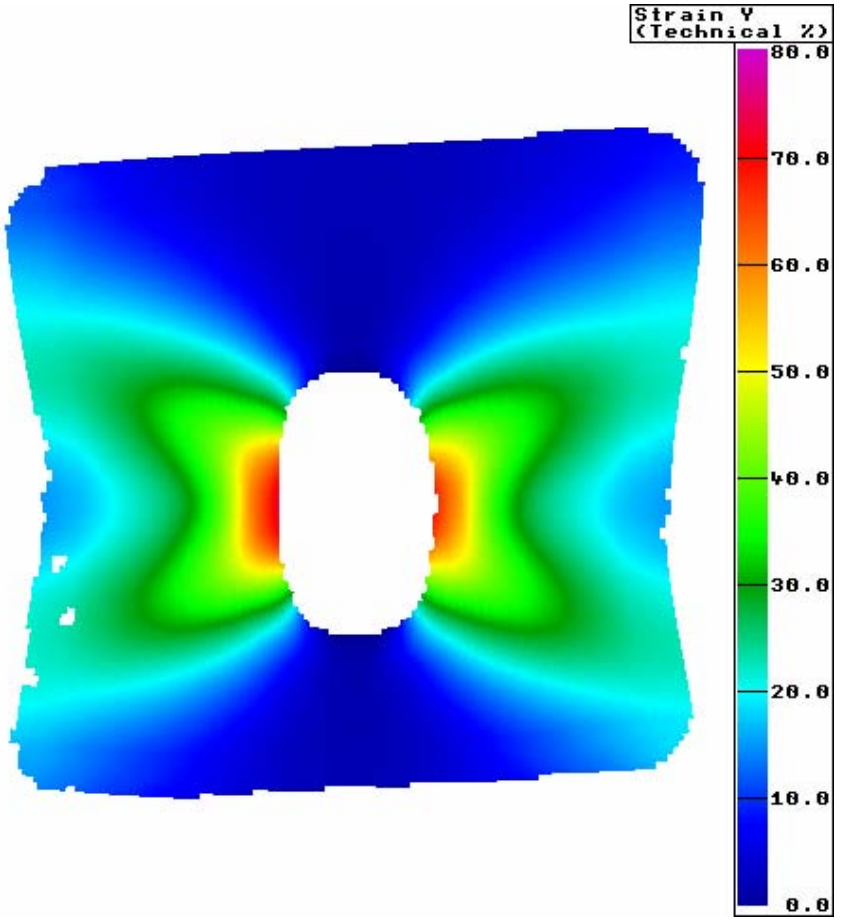

Hole opening 61 %
Max. axial strain at the specimen surface 73 %

Fig. 3.1.2-16: Axial strain fields at the surfaces of a flat specimen of 4 mm and 20 mm wall thickness, respectively, at the instant when a crack can be observed

Fig. 3.1.2-17: Fracture surface for a flat specimen with hole, 80 mm wall thickness, tested at 400 °C

RT

400 °C

850 °C

Fig. 3.1.2-18: Fracture of circular specimens of 150 mm diameter tested at different temperatures

3.1.2.2 Bending tests

The testing machine (EMPA) with a specimen is shown in Fig. 3.1.2-19. In a first set of tests the distance between the support rollers was chosen to be 5 times the specimen thickness; but for the largest specimen the maximum bending force exceeded the capacity of the testing machine. Therefore in a second set of tests the distance between the support rollers was increased to 6 times the specimen thickness.

The cross head speeds were 0.4 mm/min for the small specimens of 4 mm thickness, 1.2 mm/min for the medium size specimens of 20 mm thickness and 2.0 mm/min for the large specimens of 80 mm thickness. The resulting maximum local strain rates turn out to be considerably smaller (factor 5 to 20) than the corresponding strain rates for the tension tests.

More details about the tests and an extensive description of the results may be found in SAM-LISSAC-D032.

Here only some of the measured load-deformation relations for the tests with the increased distance between the support rollers will be presented in Figs. 3.1.2-20 and 3.1.2-21. The nominal stress at the ordinate is defined as the bending force divided by the smallest initial cross section of the specimen. The notch opening is defined as the increase of the notch measured from edge to edge, divided by the initial value. Note that for tests with nominal identical parameters only one curve is shown. The deviation of the other curves is less than $\pm$ 1.5 %.

For the specimens with wide notches (Fig. 3.1.2-20) the maximum bending which the facility allowed was not sufficient to initiate a visible crack. Only for the specimens with narrow notches (Fig. 3.1.2-21) such cracks could be obtained. They occurred in the middle of the specimen thickness. At this instant the test was stopped. Figure 3.1.2-22 shows a microstructure analysis for the notch of a small specimen with two initiating cracks; Figure 3.1.2-23 shows a photograph of the notch of a big specimen with initiating cracks.

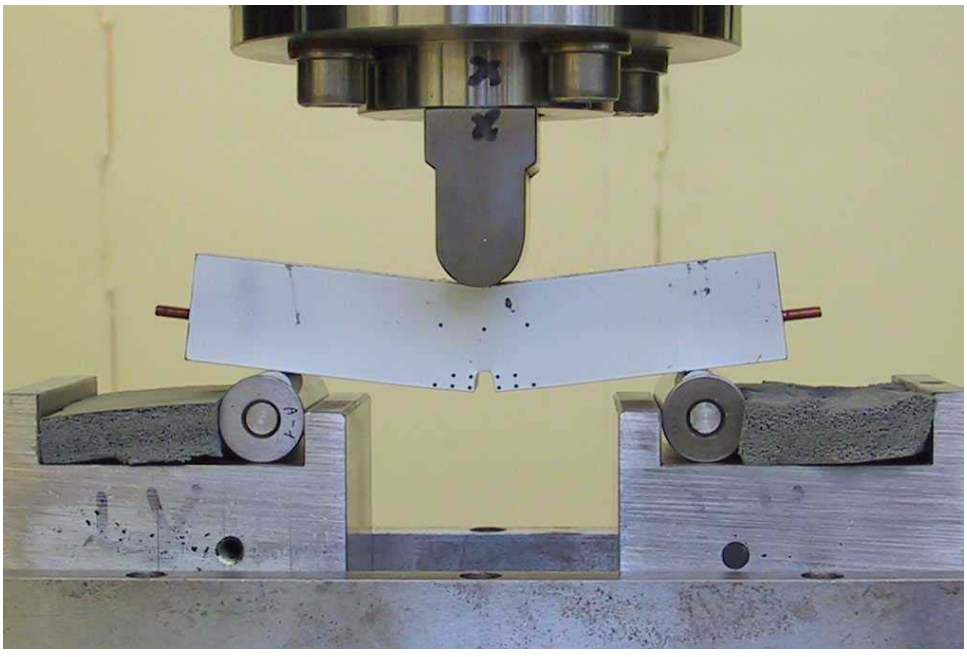

Fig. 3.1.2-19: Testing machine (EMPA) with a bending specimen

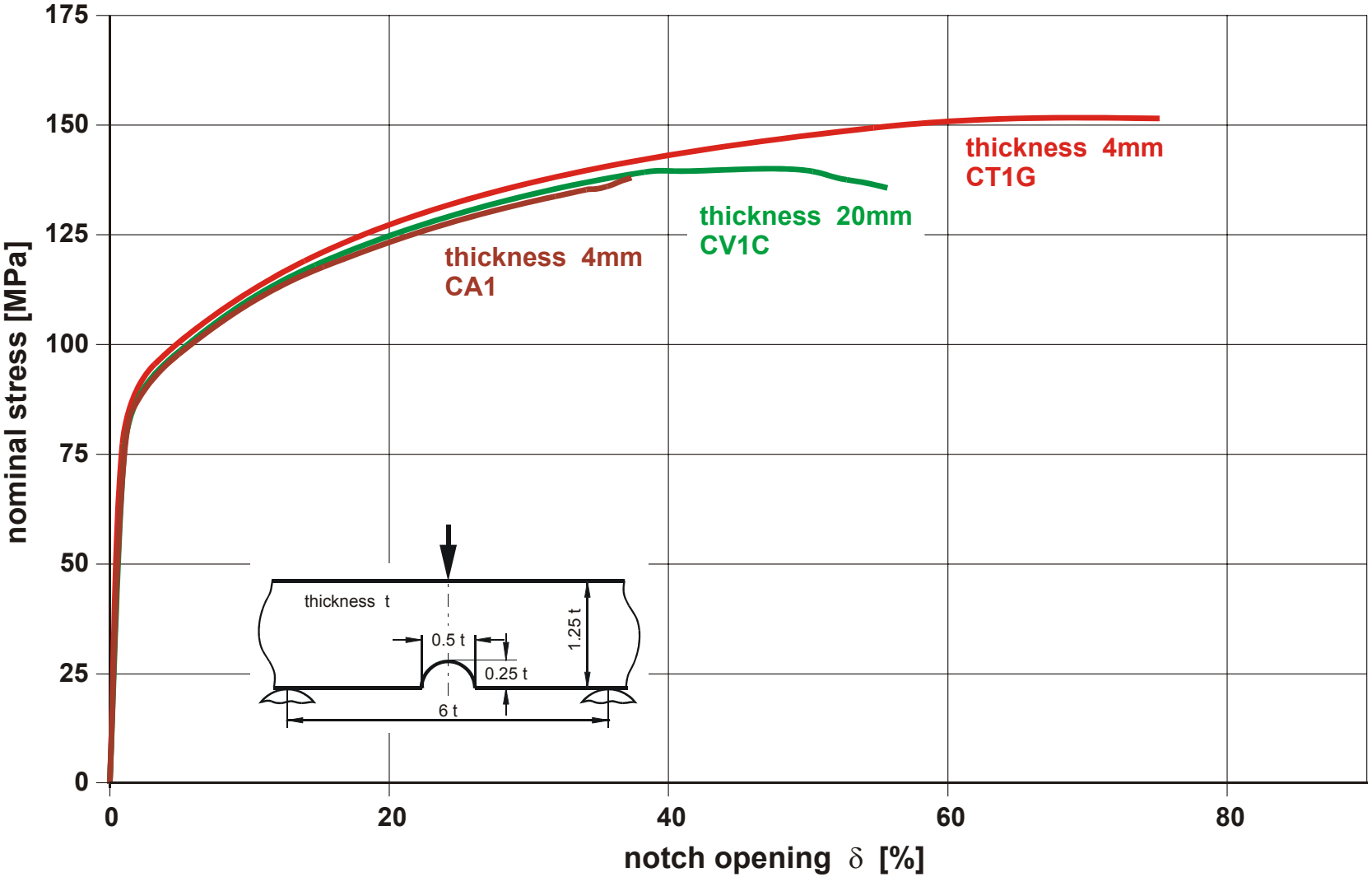

Fig. 3.1.2-20: Nominal stress vs. notch opening for bending specimens with wide notches

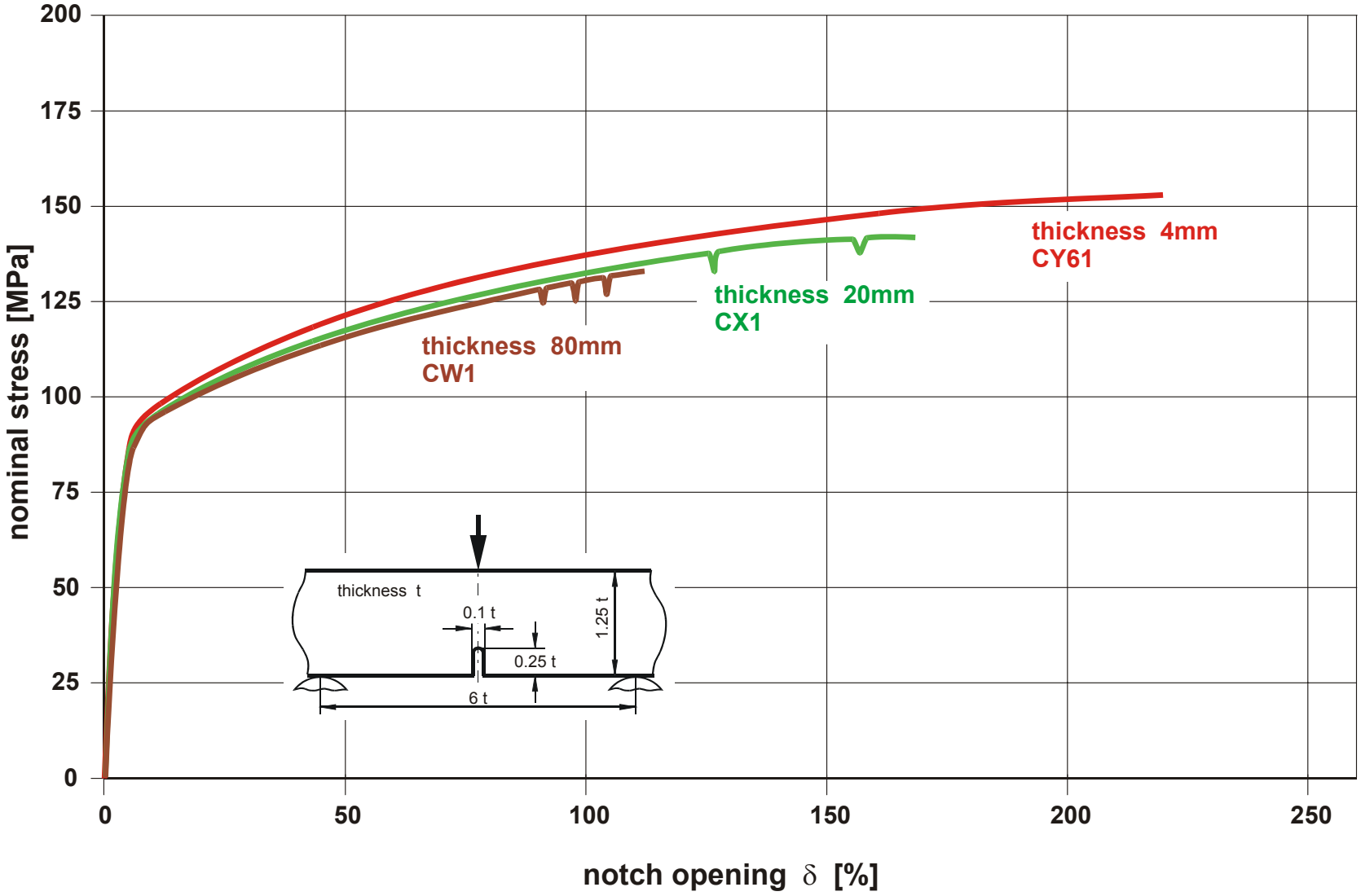

Fig. 3.1.2-21: Nominal stress vs. notch opening for bending specimens with narrow notches

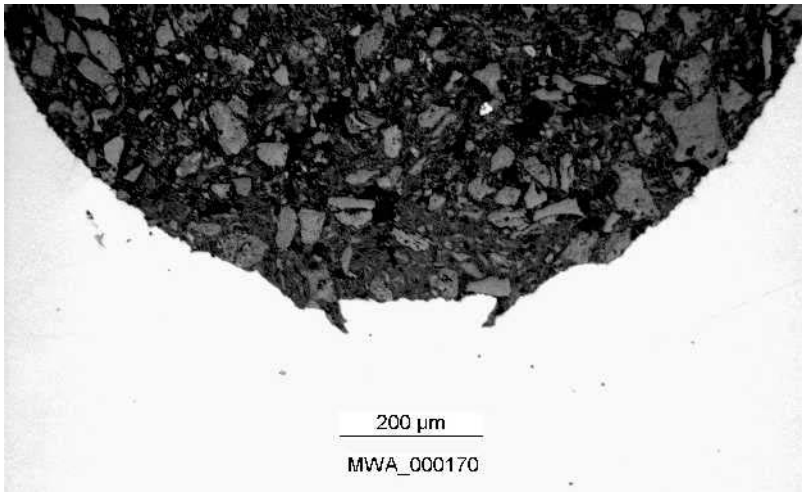

Fig. 3.1.2-22: Microstructure analysis for the notch of a small bending specimen with two initiating cracks

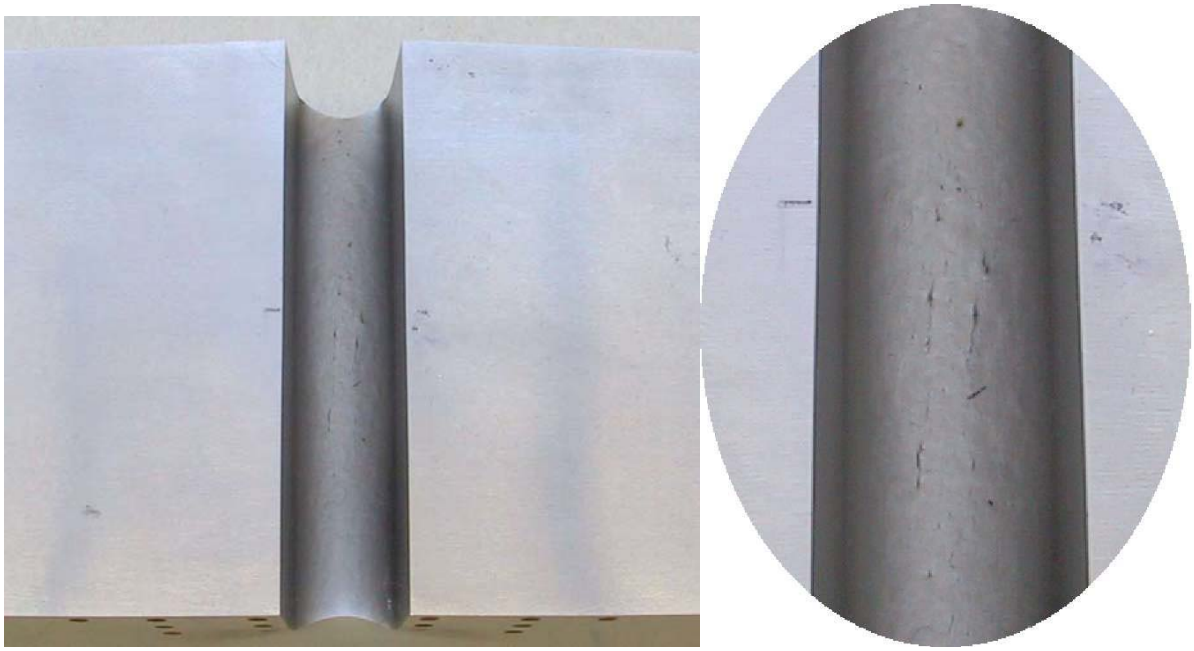

Fig. 3.1.2-23: Notch of a big bending specimen with initiating cracks

3.1.2.3 Tension tests under dynamic load

The dynamic tests are carried out with a modified split Hopkinson bar technique. The principle of this technique as well as the facility used (JRC) is shown in Fig. 3.1.2-24. The strain rates which have been realized are between 100 s^{-1} and 400 s^{-1}. A more detailed description as well as complete information about the results is documented in SAM-LISSAC-D034.

Here only selected information about the results will be presented in Figs. 3.1.2-25 to 3.1.2-30. Again, the nominal stress at the ordinate is defined as the tension force divided by the smallest initial cross section of the specimen. However, in contrast to the static tests, a continual measurement of the hole or notch opening was not possible. Instead the elongation of the gauge length of the specimens was recorded and this parameter divided by the initial gauge length is used as abscissa.

Therefore the figures describing the results of the dynamic tests cannot be compared directly with the figures from the static tests presented in chapter 3.1.2.1. However in the figures for the dynamic tests the corresponding maximum nominal stresses from the static tests were mentioned. It turns out that at room temperature the stresses versus elongation obtained under dynamic conditions are somewhat higher than under static conditions. This effect is well known. However, for 400 °C the tendency is opposite, which is remarkable. Again for 850 °C the dynamic stresses are considerably higher than the static stresses. Some curves exhibit rapid and excessive oscillations at the beginning. These are primarily due to experimental shortcomings (longer time for specimen to attain equilibrium), and secondarily to changes in the yielding behaviour of the material under impact loading.

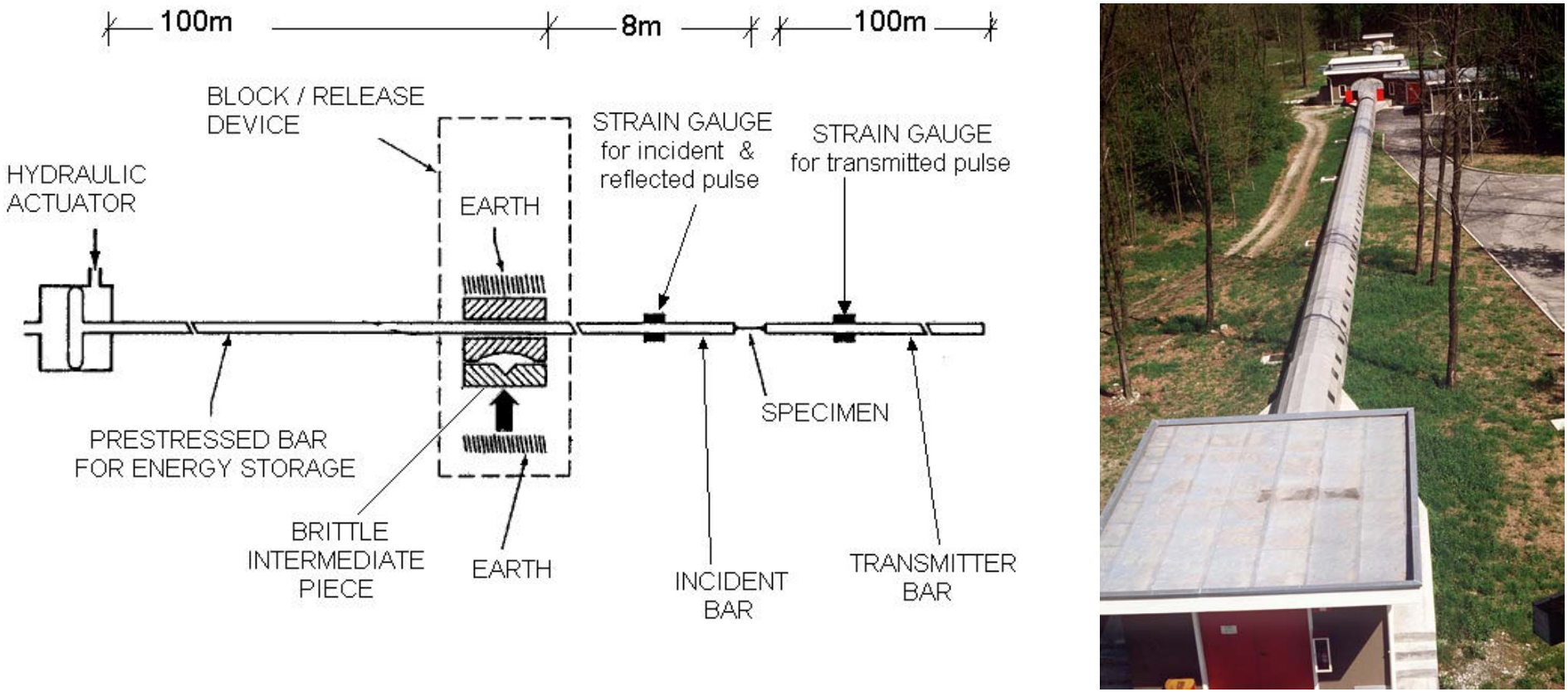

Fig. 3.1.2-24: (a) Principle of functioning and dimensions of the large Hopkinson bar at the Large Dynamic Test Facility (LDTF) of the JRC-Ispra. (b) External view of the LDTF.

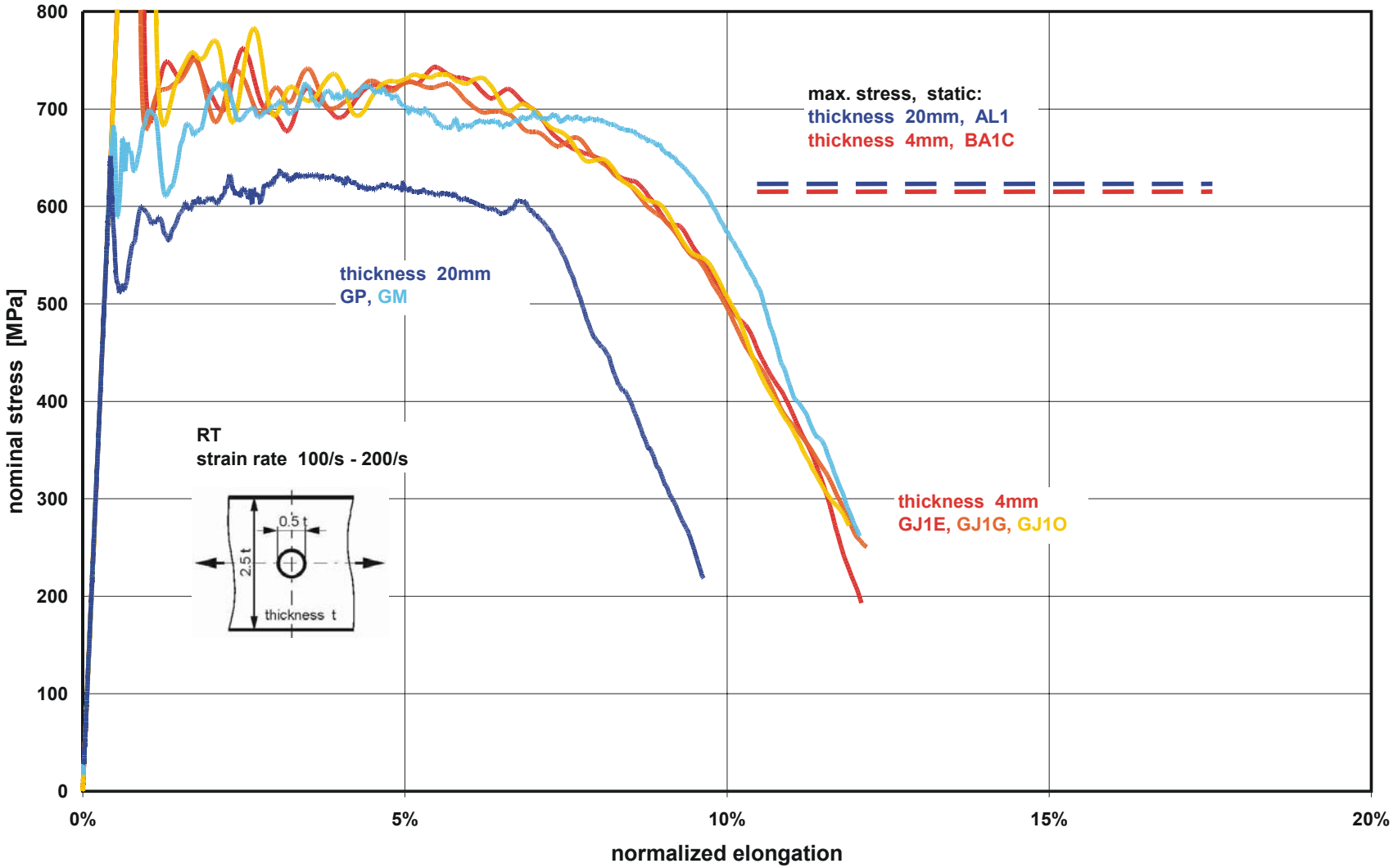

Fig. 3.1.2-25: Nominal stress vs. normalized elongation for the test family of flat specimens with hole, dynamic load, RT.

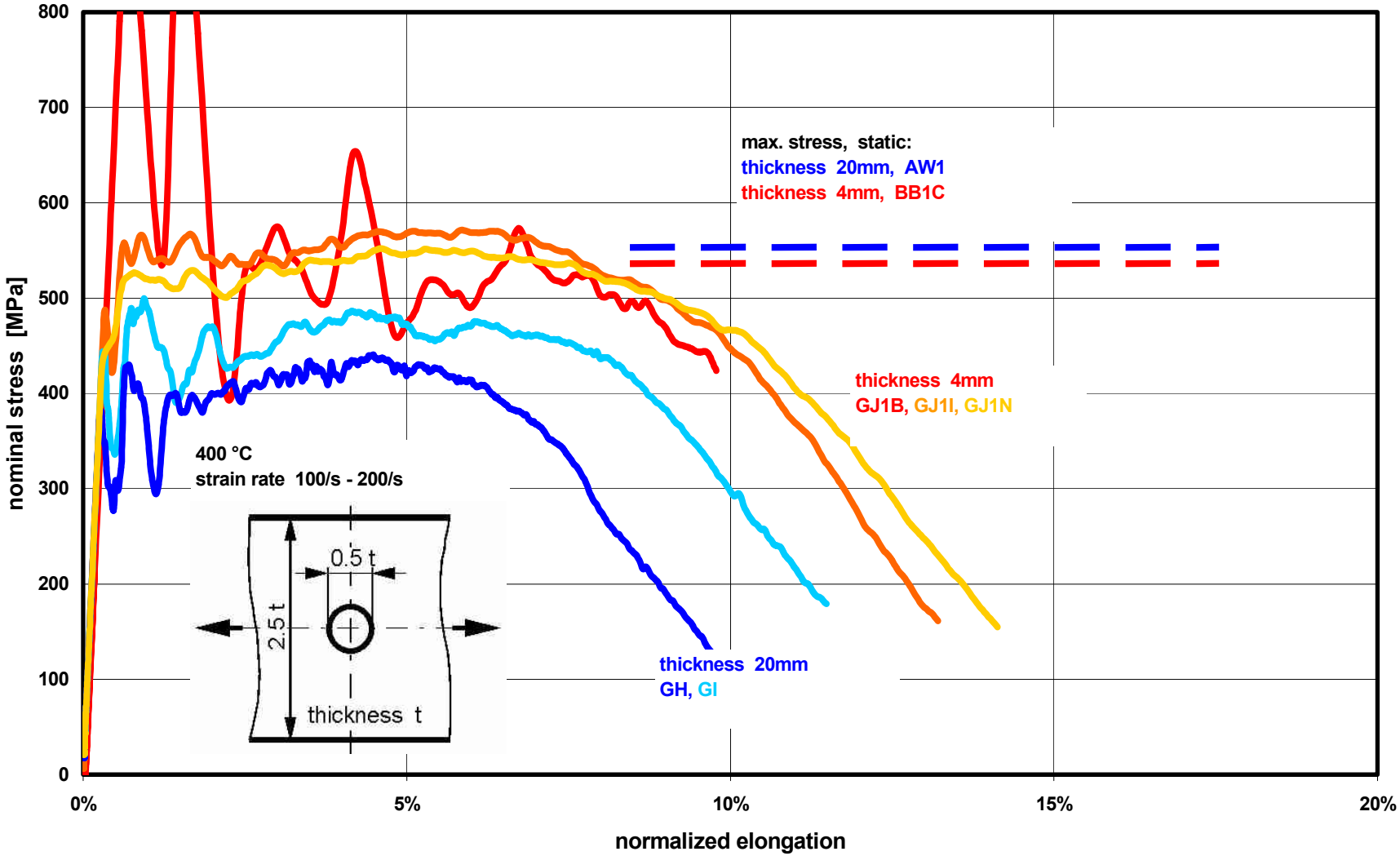

Fig. 3.1.2-26: Normal stress vs. normalized elongation for the test family of flat specimens with hole, dynamic load, 400 °C.

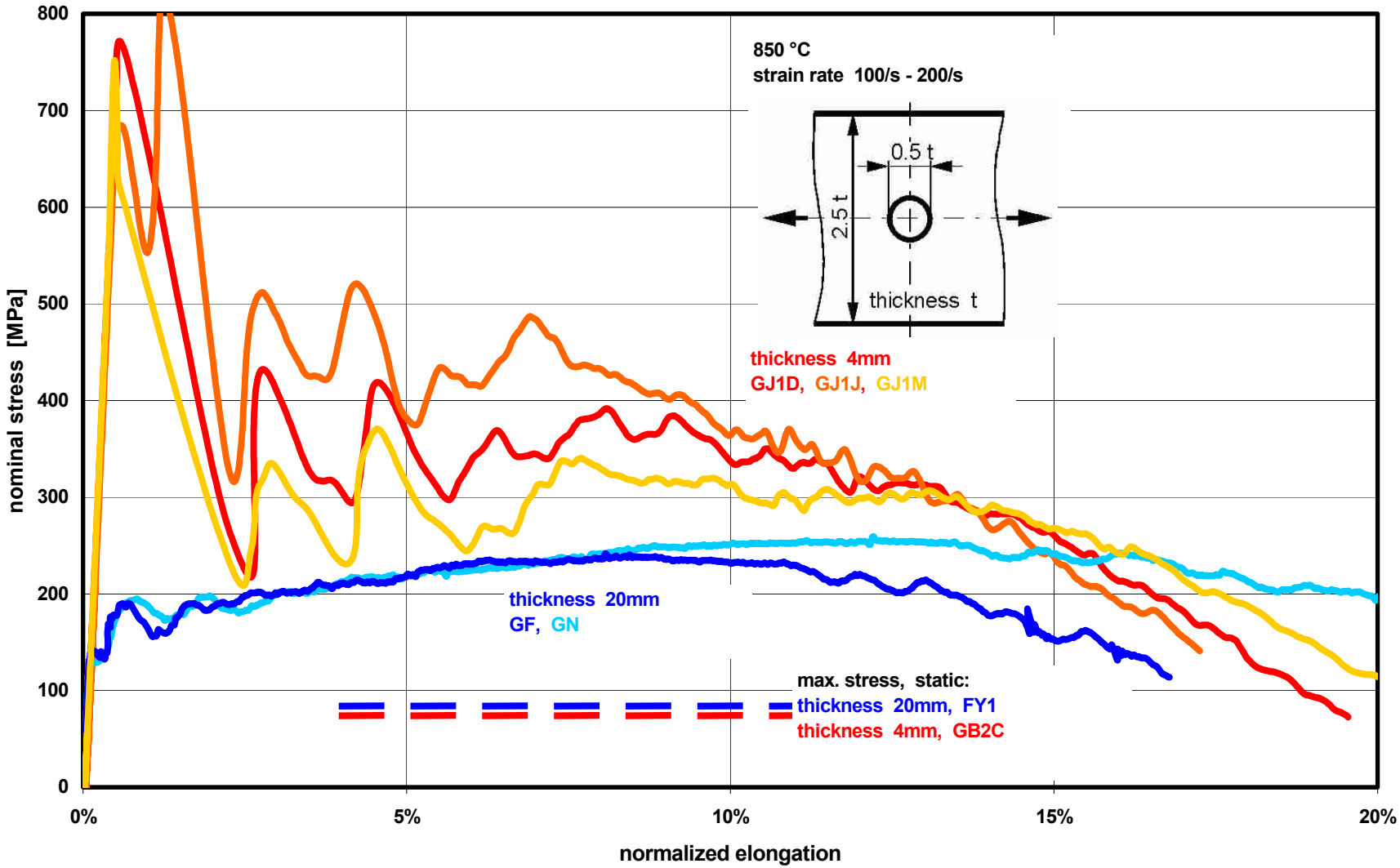

Fig. 3.1.2-27: Normal stress vs. normalized elongation for the test family of flat specimens with hole, dynamic load, 850 °C.

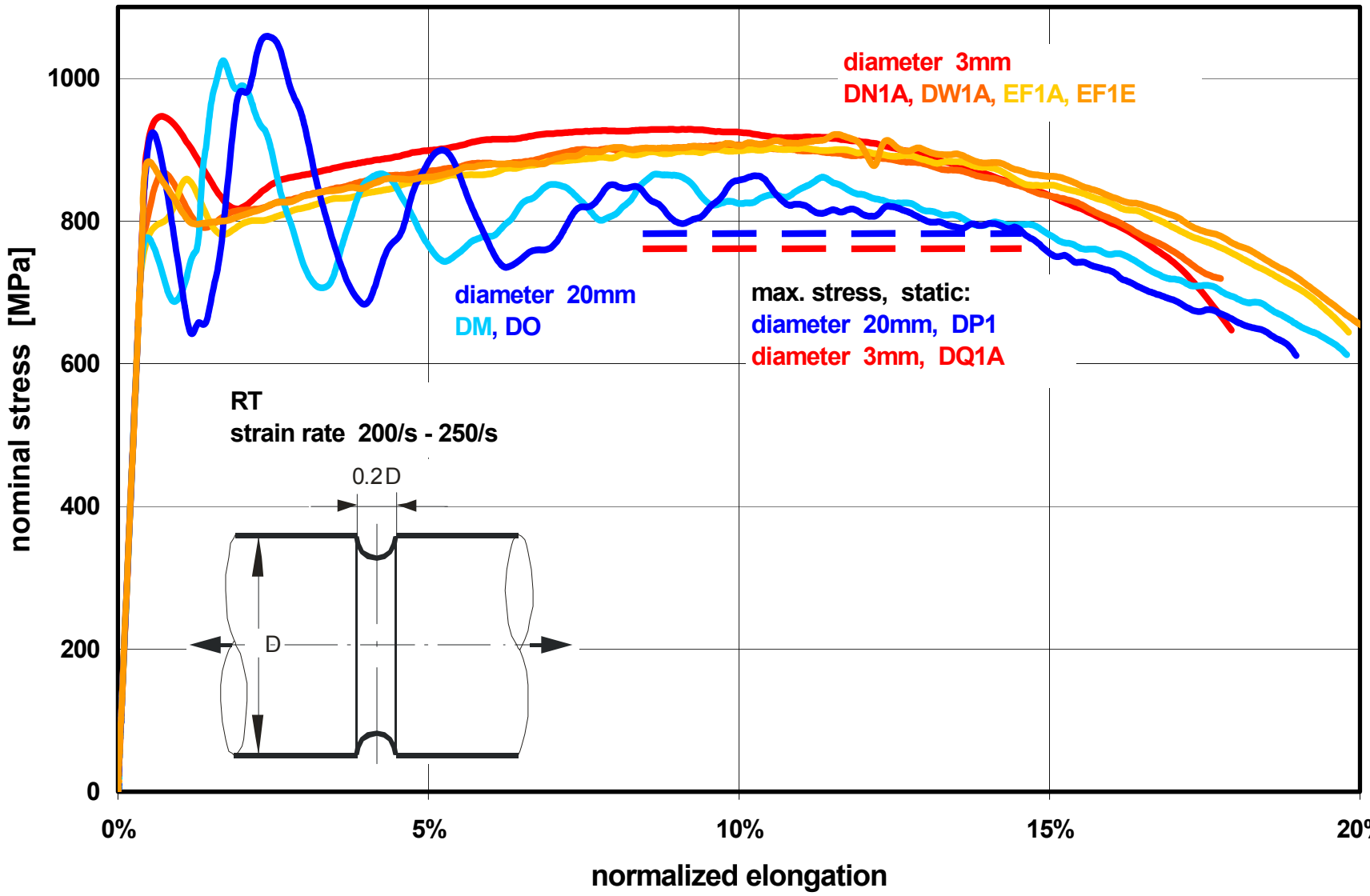

Fig. 3.1.2-28: Normal stress vs. normalized elongation for the test family of circular specimens with notch, dynamic load, RT

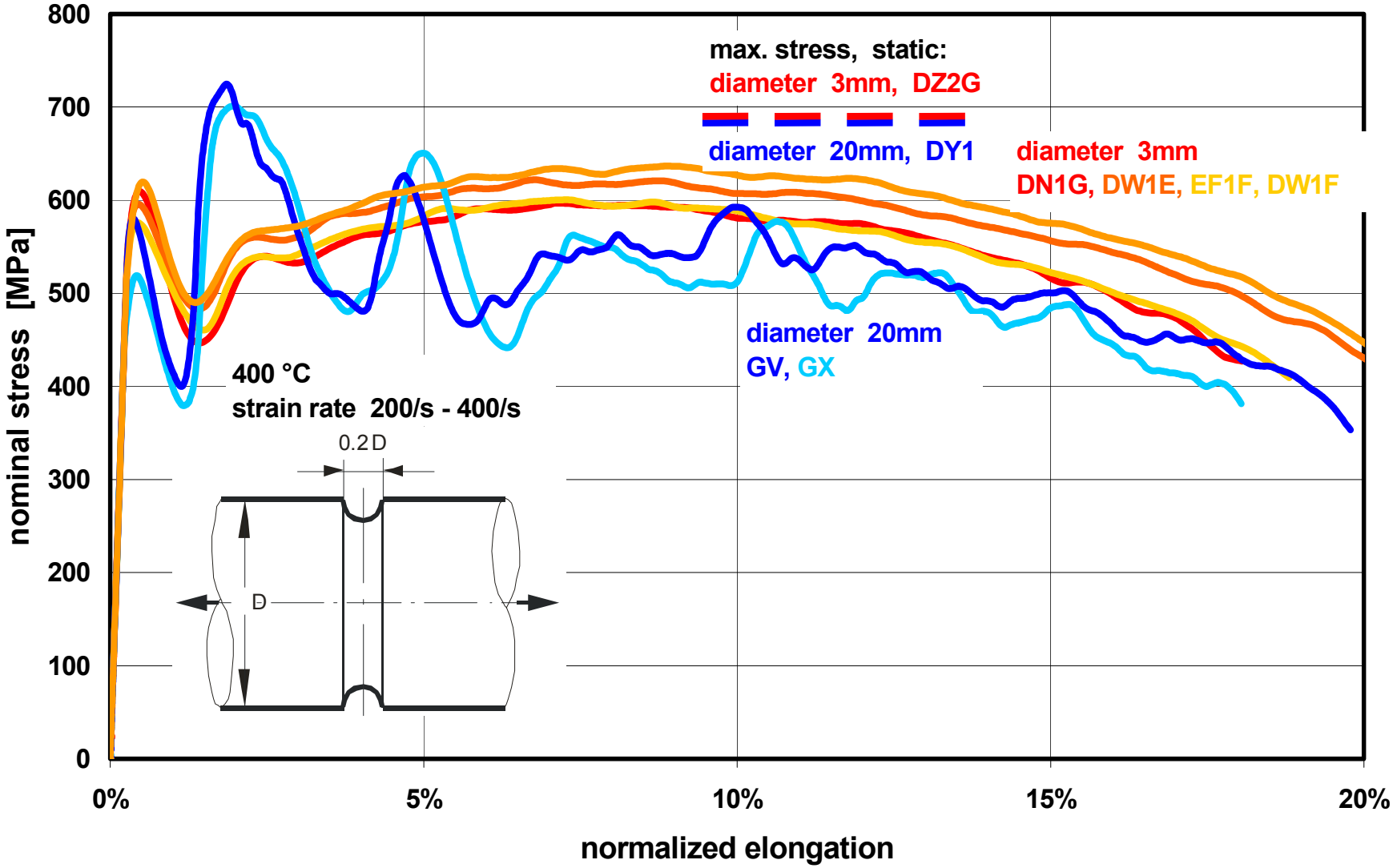

Fig. 3.1.2-29: Normal stress vs. normalized elongation for the test family of circular specimens with notch, dynamic load, 400 °C

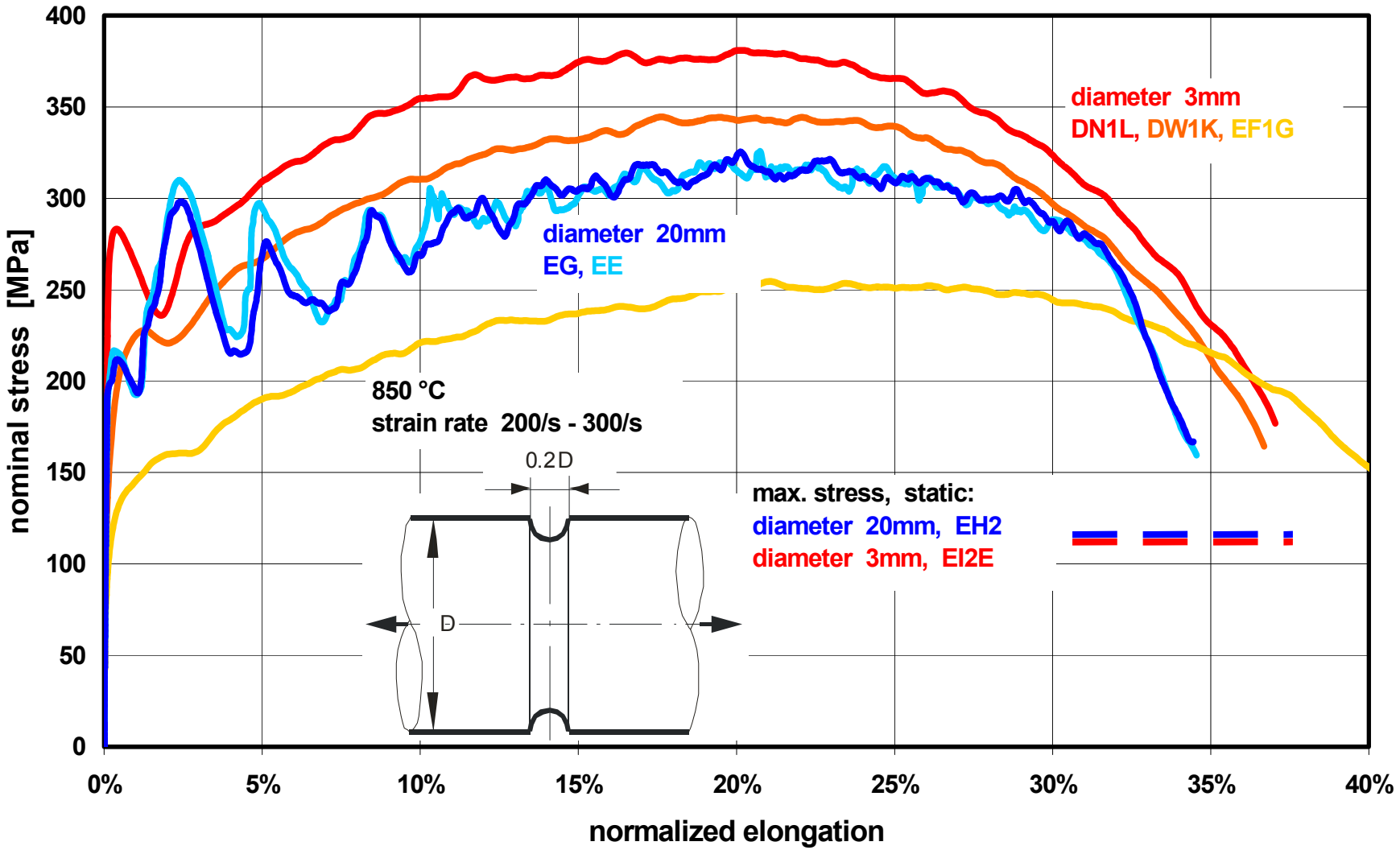

Fig. 3.1.2-30: Normal stress vs. normalized elongation for the test family of circular specimens with notch, dynamic load, 850 °C

3.1.3 Biaxial tests

3.1.3.1 Tests with curved biaxial specimens under static load

Special facilities had to be designed and manufactured (VTT) for both, the small specimens with a diameter of about 100 mm and the large specimens with a diameter of about 500 mm. A simplified drawing of the facilities is shown in Fig. 3.1.3-1. The load is applied by a liquid with slowly increasing pressure up to a value of about 1200 bar, where failure is expected. During the test the pressure and the resulting vertical displacement are measured.

To make sure that the facility is able to carry the pressure load without excessive deformations causing leakages, quite detailed finite element calculations were performed for the facility for the small specimens as indicated in Fig. 3.1.3-2. The dimensions of the facility for the large specimens were simply obtained my multiplication with the factor five.

A special problem occurred for the specimens with holes. In order to seal these holes, a sealing liner had to be added. Again, the dimensions of the liner for the large specimens are five times the dimensions of the liner for the small specimens.

There was only exception. The O-ring for the liner was not scaled up accordingly. Rather the thickness of the O-ring for the liner and consequently the nut in the liner for the large specimen (Fig. 3.1.3-3, detail B) was too small in comparison to the liner for the small specimen. Thus the stiffness of the nut region of the liner for the larger specimen was somewhat higher than the stiffness which would have resulted from exact scaling up. During the tests this small deviation from similarity will have a rather significant consequence.

The tests with some essential parameters and results are listed in the following tables. More information in SAM-LISSAC-D030.

Tests of specimens without holes:

specimen	size	liner	max. pressure [bar]	max. displ. of the dome [%]	max. amount of strain in thickness direction [%]
ET1	small	-	1150	66.9	63.2
EU1	small	-	1160	69.1	58.0
EV1	small	yes	1260	34.8	-
EW	large	-	1150	85.4	58.4

Tests of specimens with holes:

specimen	size	liner	max. pressure [bar]	max. displ. of the dome [%]
EY1	small	yes	1050	28.3
EZ1	small	yes	1110	27.9
FA1	small	yes	1090	28.4
FB	large	yes	1170	17.3 *

* for this test failure could not be reached

In addition, Fig. 3.1.3-4 shows the vertical displacement of the dome divided by the initial height of the dome versus pressure. It is remarkable that for the specimens without holes the relative deformations and pressures are almost independent of the specimen size. In other words, there is almost no size effect. The results for the test EV1 without holes cannot be included in this comparison, since for this test a liner was added to estimate its effect on the failure behaviour. It increased the stiffness of the dome, but it changed the mechanical behaviour so that the test ended before the deformation capacity of the specimen was fully used.

For all the specimens with holes a liner was added. However for the small specimens the liner was weakened in the nut region. Therefore it could carry only a small part of load. For the large specimen the liner was not weakened in the nut region very much and therefore it was able to carry a larger part of the load. As a result, in Fig. 3.1.3-4 the curves for the small specimens with holes and the large specimen with holes are different. Furthermore the test with the large specimen ended at liner failure.

The above findings are an interesting lecture in similarity of structural behaviour. Sometimes very small deviations of the design may result in quite different responses.

Figures 3.1.3-5 to 3.1.3-7 show different types of failure. Of special interest is the failure of the large specimen EW without holes. Although the pressurizing liquid is almost incompressible a larger part of the specimen was teared off completely and hurled against the ground.

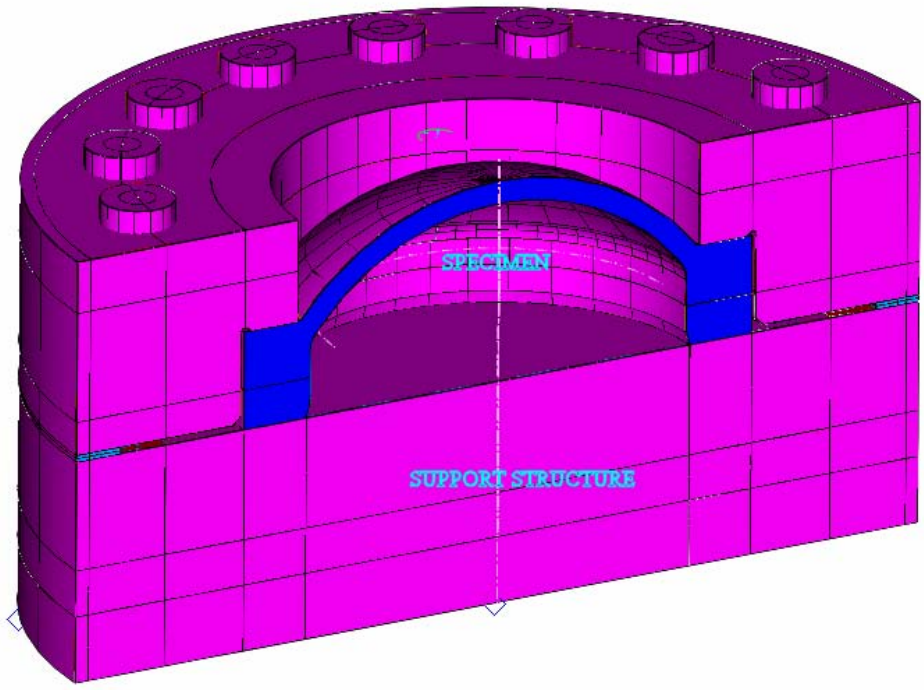

Fig. 3.1.3-1: Test facility for the curved biaxial specimens under dynamic load

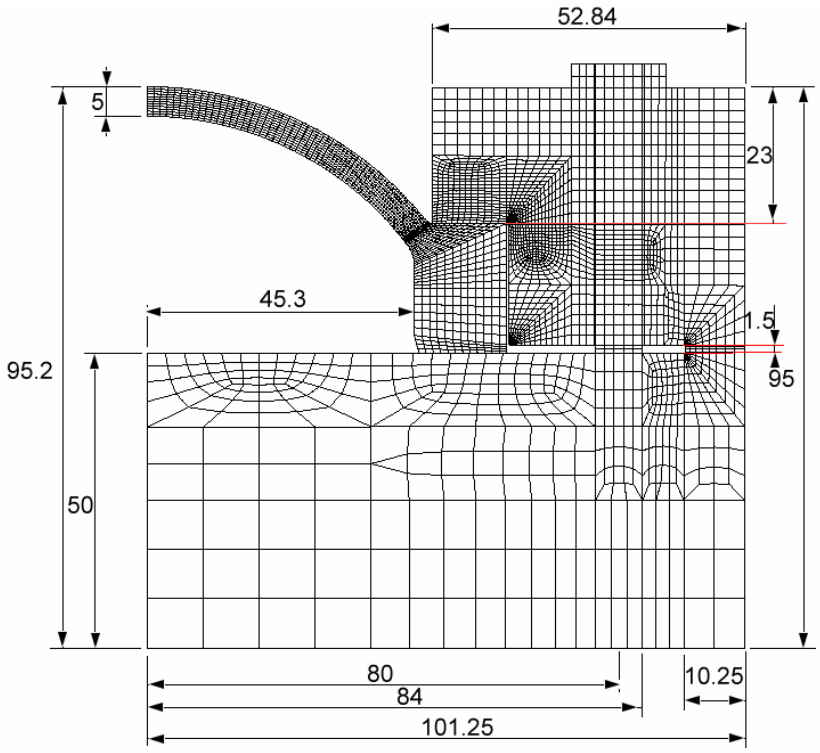

Fig. 3.1.3-2: Finite element model for analysis of the test facility

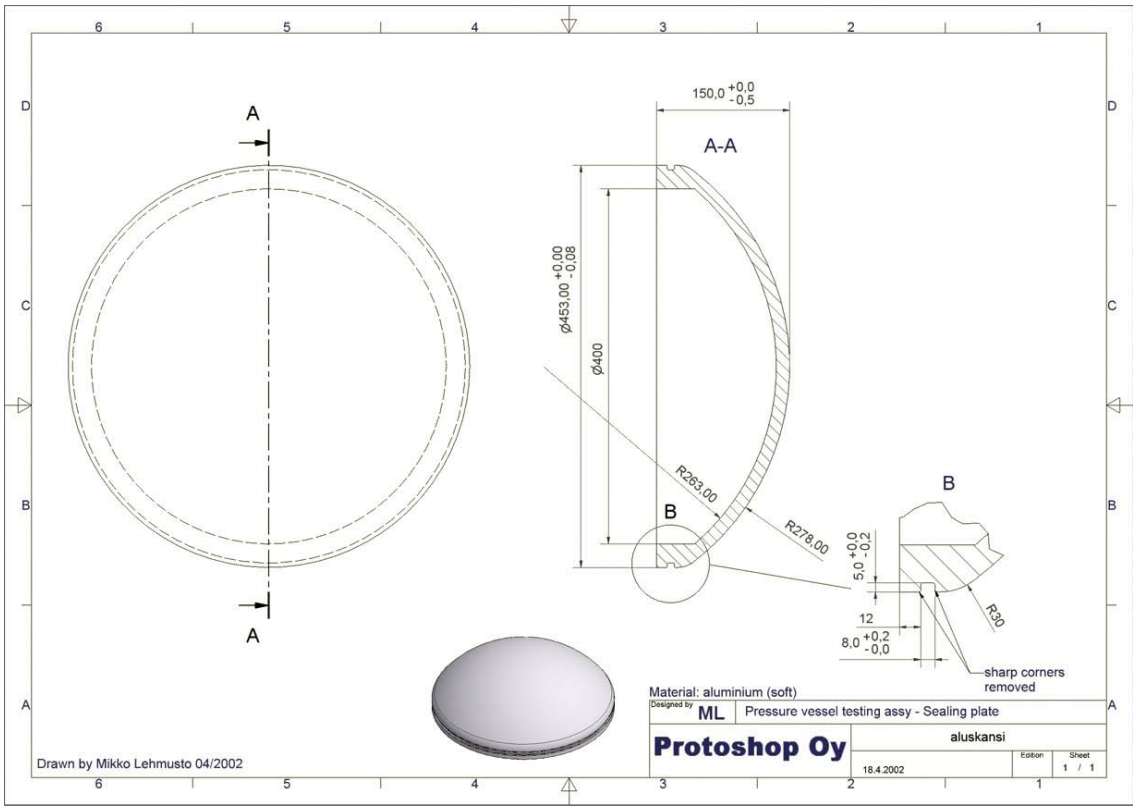

Fig. 3.1.3-3: Design of the sealing liner for the large specimen

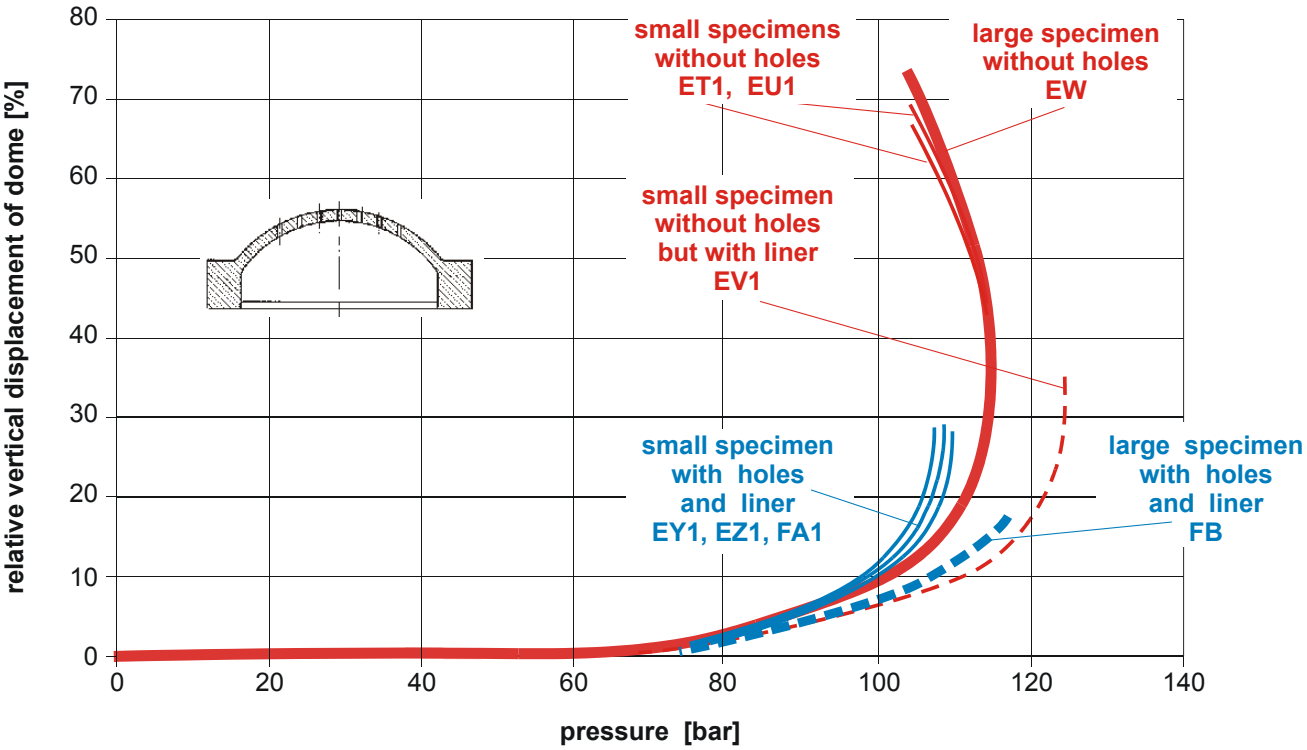

Fig. 3.1.3-4: Vertical displacement of the specimen dome divided by the initial height of the dome versus pressure

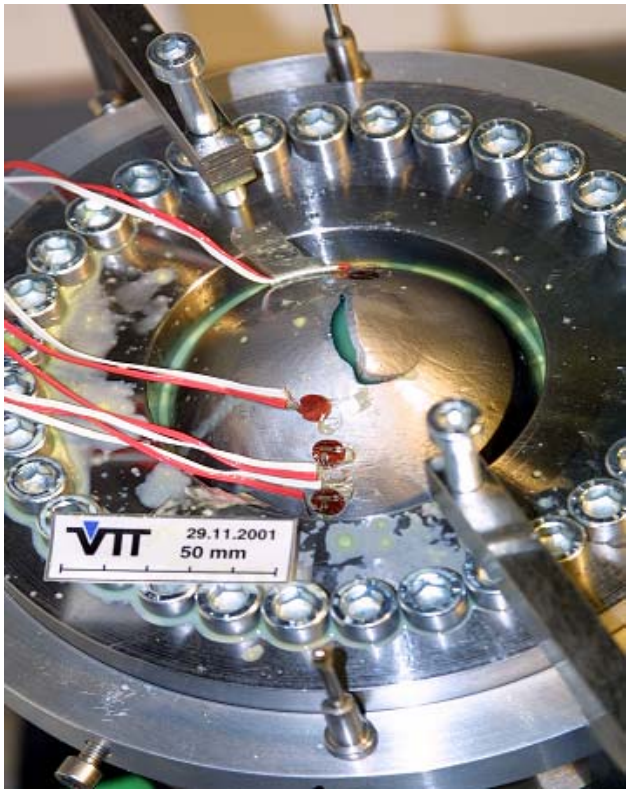

Fig. 3.1.3-5: Failure of the small specimen EU1

Fig. 3.1.3-6: Failure of the large specimen EW.
A large part of the specimen was completely teared off.

Fig. 3.1.3-7: Failure of the small specimen EZ1 and deformation of the liner

3.1.3.2 Tests with curved biaxial specimens under dynamic load

The impact facility VERDY (FZK) was adapted to perform the tests with the small specimens, as shown in Fig. 3.1.3-8. The specimen is located in the lower part of the facility with the dome in downward direction. The dynamic load is caused by a lead mass accelerated downwards and hitting the specimen.

The impact facility IVAN (FZK) was adapted for the tests with the large specimens, Fig. 3.1.3-9. Now the specimen is located in the upper part of the facility and the dynamic load is caused by a lead mass accelerated upwards.

The problem was to choose the amount, the shape and the impact velocity of the lead mass in such a way that, limited cracking occurs in the specimens. As shown in the following tables, this could not be achieved for all of the tests. In a few cases no cracking occurred. Consequently for these cases in the next chapter instead of the strain causing failure, a lower strain will be determined where the specimens remain intact. More information about the tests and the results is given in SAMLISSAC-D028.

Tests of specimens without holes:

specimen	size	impact mass [kg]	impact velocity [m/s]	max. displ. of the dome [%]	max. amount of strain in thickness direction [%]
FD1	small			*	45.7
FE1	small	1.2	161.9		57.4
FF1	small	1.2	155.5	41.9	58.4
BO1	small				47.6
FG	large	153	150.4	38.3	55.0
FL	large	152.6	152.2	*	57.7

***** For these tests failure did not occur.

Test of specimen with holes:

specimen	size	impact mass [kg]	impact velocity [m/s]	max. displ. of the dome [%]
FN1	small			*
FO1	small	0.96	105.2	21.2
FP1	small	0.96	96.3	21.2 *
FQ	large	122.6	108.1	^{o}
FV	large	122.6	100.5	20.6

***** For these tests failure did not occur.

^{o} In this case failure with excessive deformation occurred.

Figures 3.1.3-10 to 3.1.3-13 show different types of failure. For the specimens without holes usually shear type of fracture occurs with sudden changes of the slope of the fracture surface (Fig. 3.1.3-11). For the specimens with holes the deformation of the lead mass and its penetration into the holes is very impressive (Fig. 3.1.3-12).

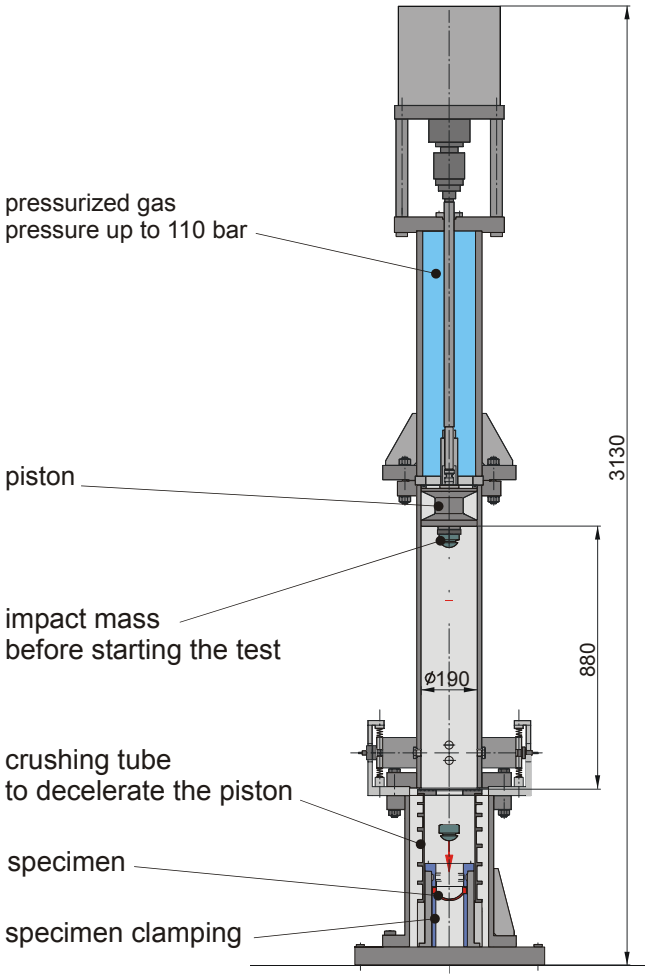

Fig. 3.1.3-8: Impact facility VERDY for the tests with the small specimens

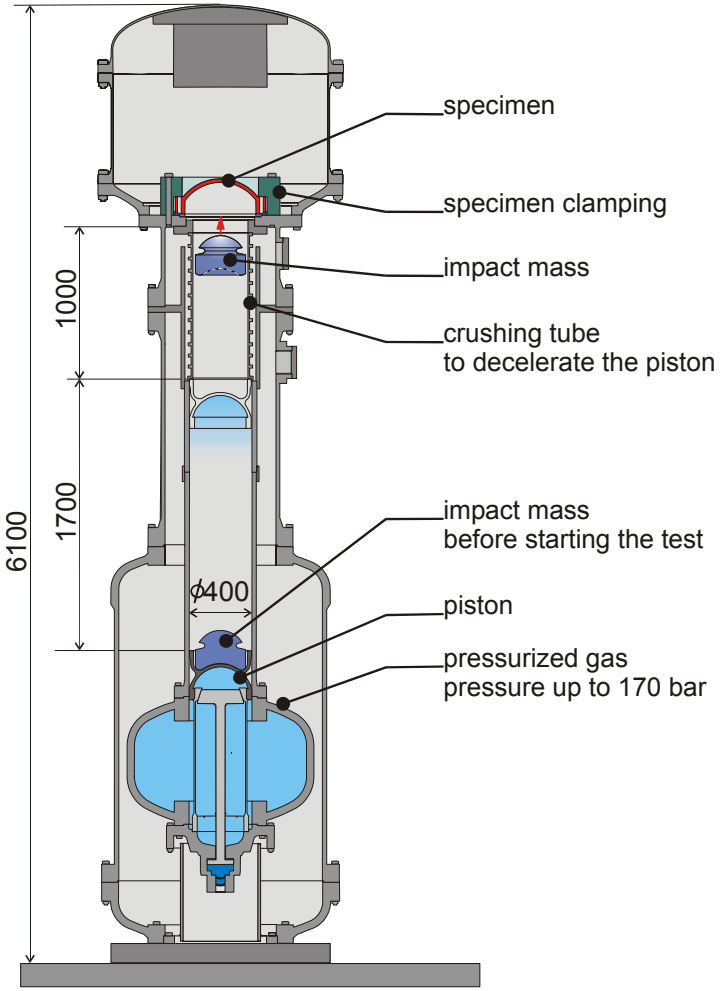

Fig. 3.1.3-9: Impact facility IVAN for the tests with the large specimens

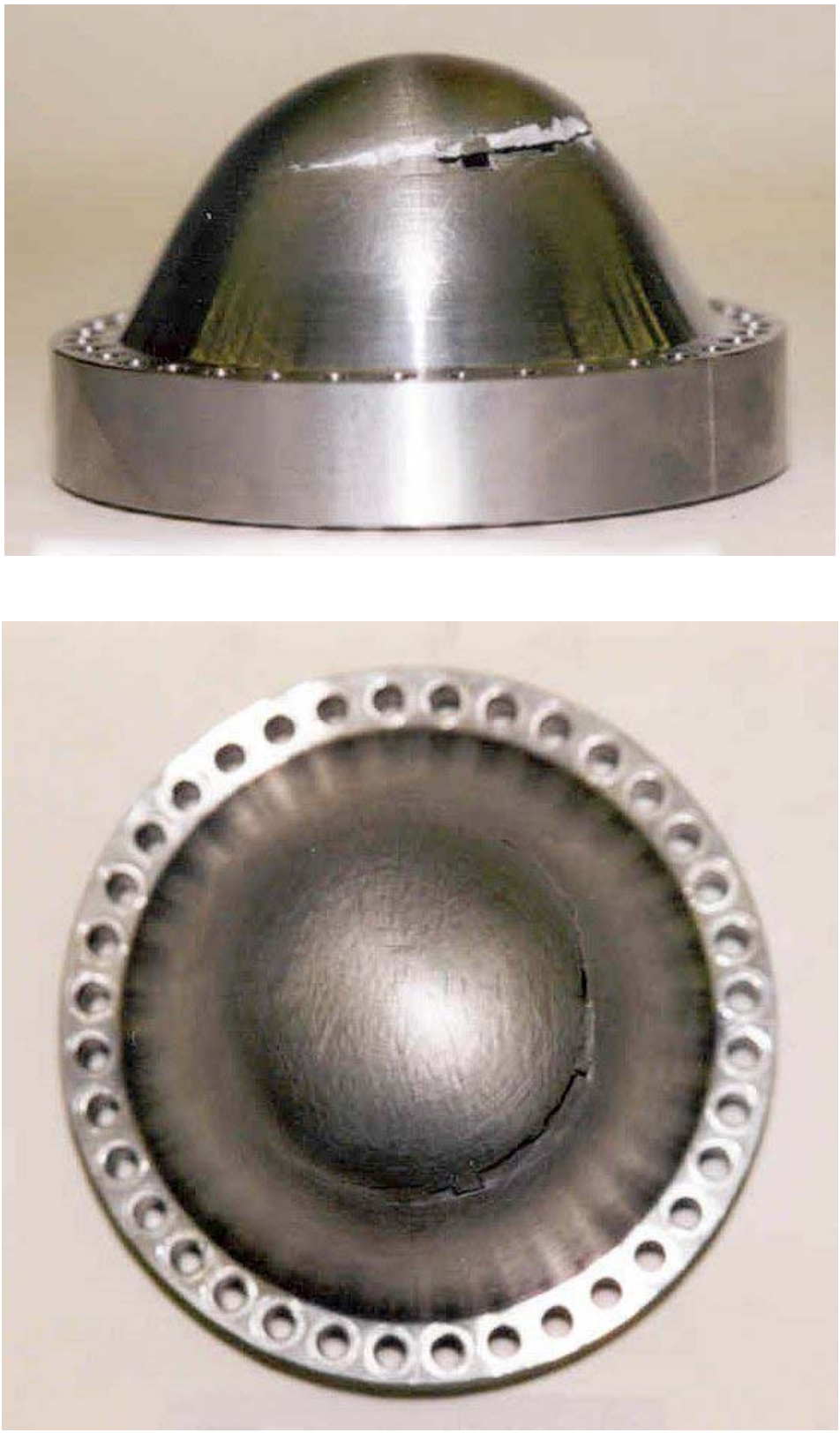

Fig. 3.1.3-10: Failure of the small specimen FF1

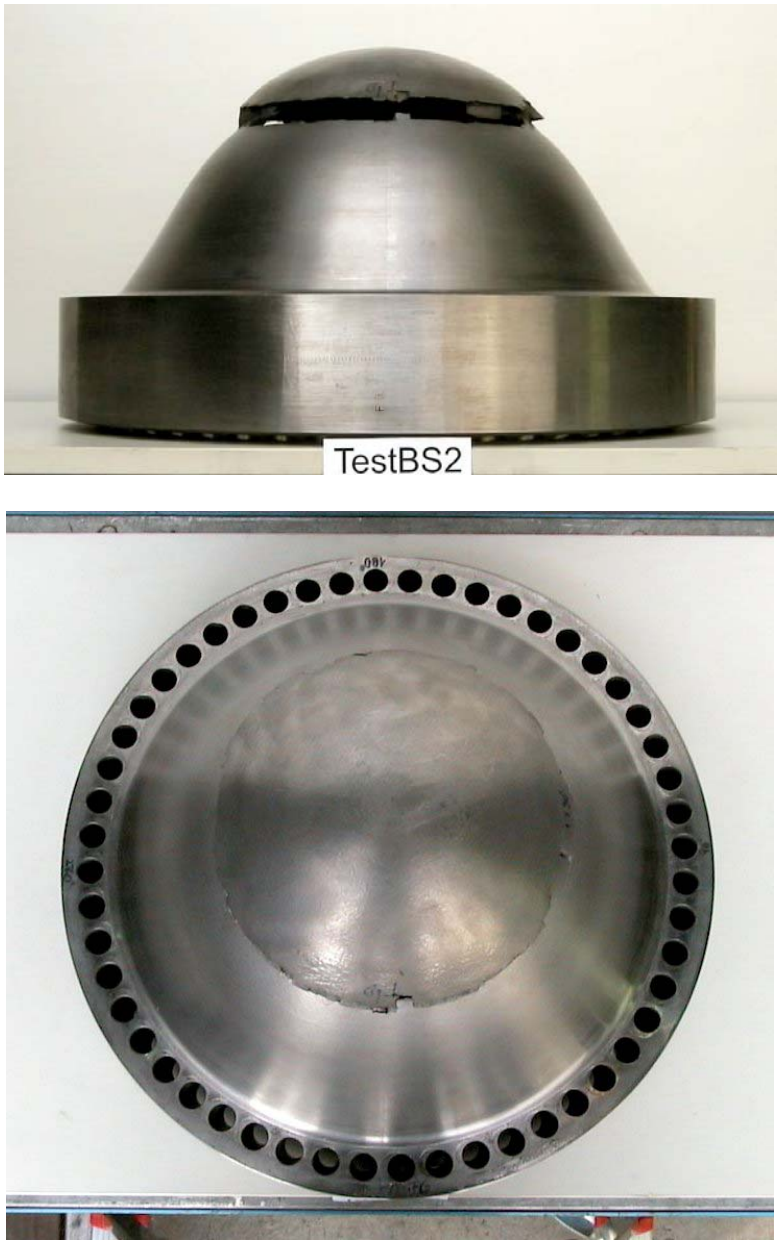

Fig. 3.1.3-11: Failure of the large specimen FG

Fig. 3.1.3-12: Failure of the small specimen FO1 and lead mass before and after the impact

180°

90°

Fig. 3.1.3-13: Failure of the large specimen FV

3.1.3.3 Tests with flat biaxial specimens under dynamic load

Biaxial specimens, as shown in Fig. 3.1.3-14, have been constructed. They are of cruciform type, with a finger-like frame holding the central gauge region. Finite element pre-calculations have shown that these specimens produce a fairly uniform strain field, and have a satisfactory behaviour even after yielding. Tests with specimens without and with hole have been performed. The dynamic tensile load is applied along the direction of the Hopkinson bars. The deformation along the transverse direction is constrained to vanish through a special device attached to the specimen and preventing transverse contraction. In the specimen shown, the uniform area is 80x80 mm^2, its thickness is 4mm, and the hole diameter is 2mm.

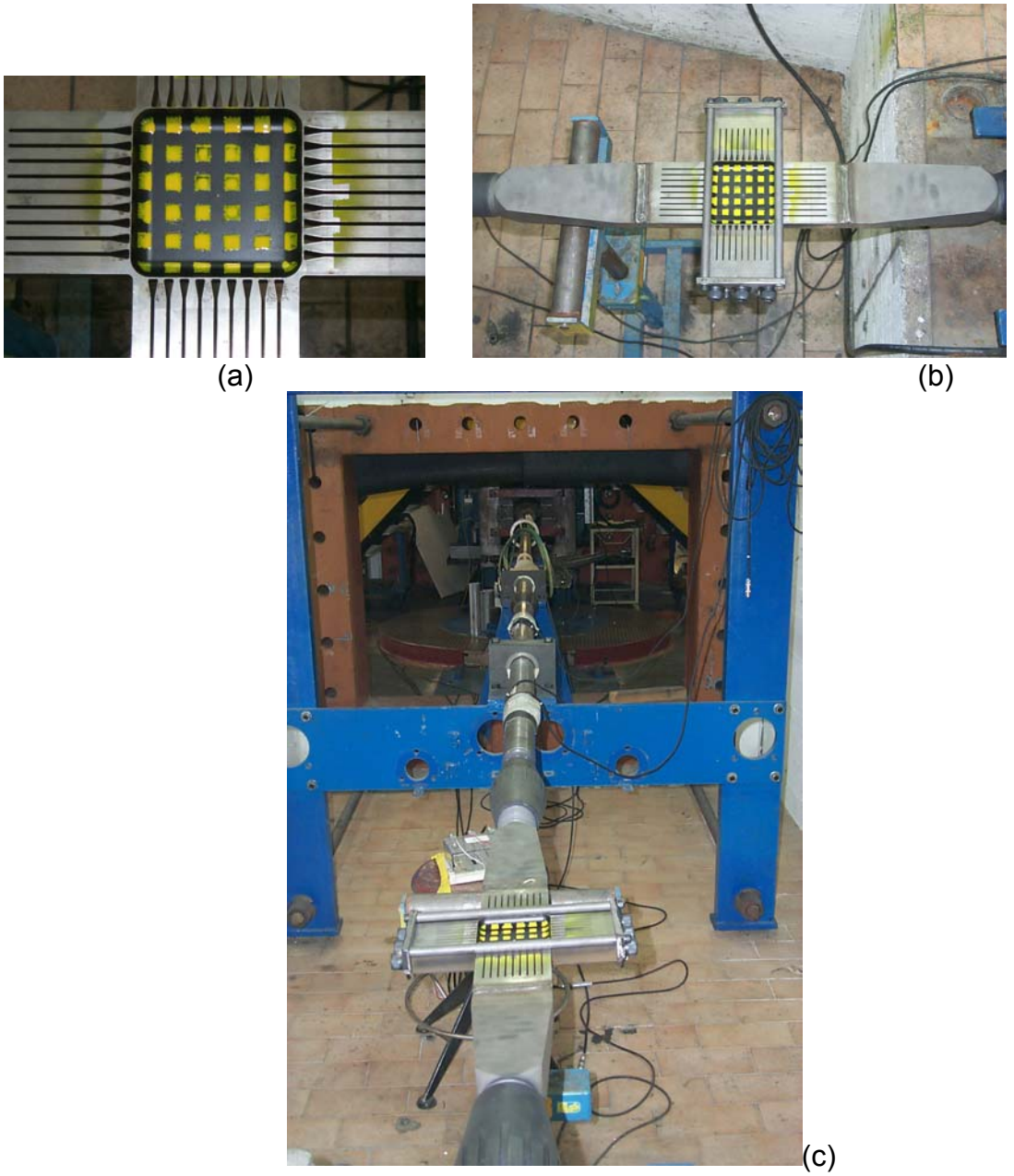

(a) (b) (c)

Fig. 3.1.3-14: (a) Details of gauge area of flat biaxial specimen with hole;
(b) Specimen with holding arms and device for preventing transverse contraction;
(c) Specimen mounted between the incident and the transmitter bars of the LDTF.

Figure 3.1.3-15 shows the specimen EP without hole before and after the test. The locally reduced thickness of the specimen has been measured after the test. The resulting values (in millimetres) are marked in the photograph of the specimen taken before the test. With the initial specimen thickness of 4 mm, the maximum amount of the (linear) strain in thickness direction is -43.8 %. For the specimen EN, which is of the same type, the strain in thickness direction amounts to -52.5%.

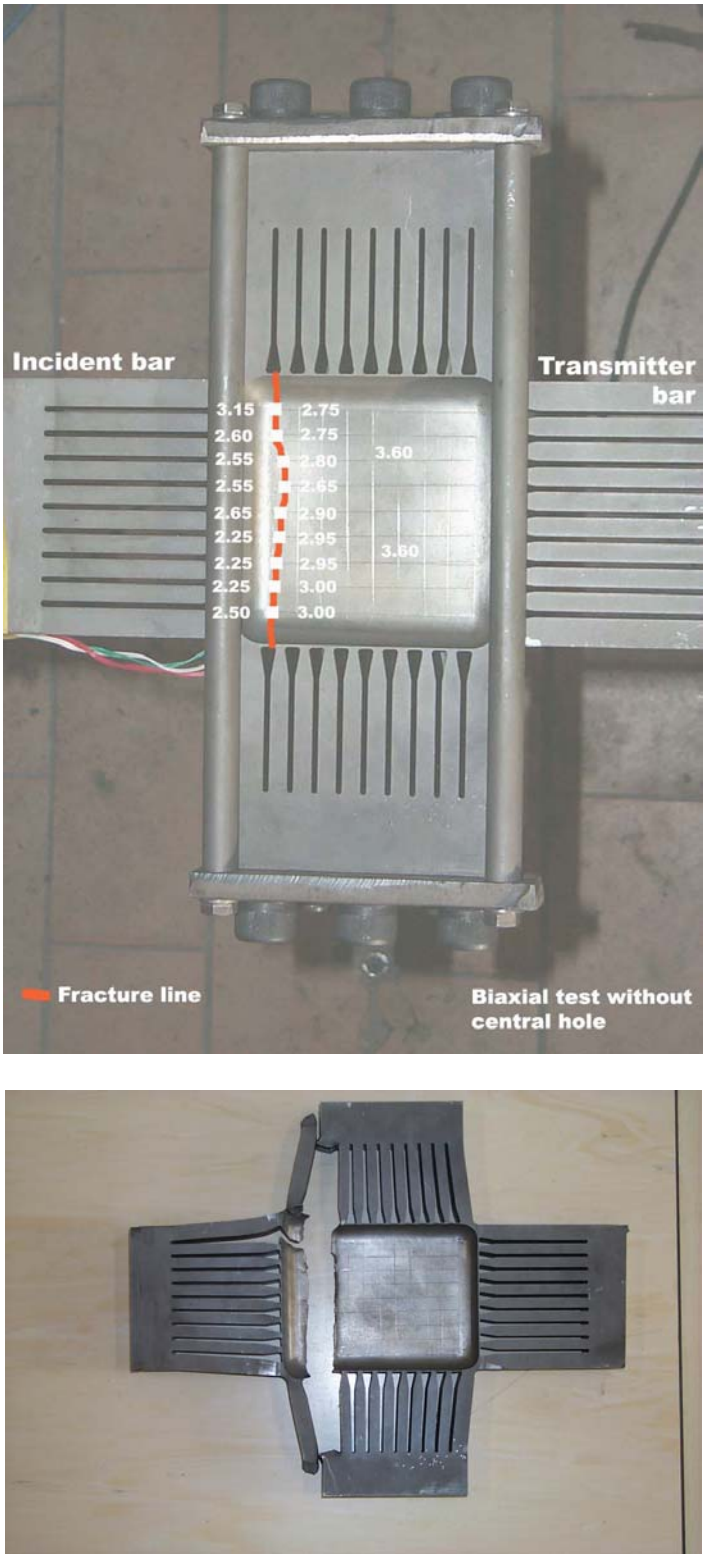

Fig. 3.1.3-15: Specimen EP without hole before and after the test

Figure 3.1.3-16 shows the specimen EO with hole before and after the test. Again, the locally reduced thickness of the specimen has been measured after the test and the values are marked in the photograph taken before the test. The initial uniform thickness of the gauge area was ~4.0mm

The reconstruction of the conditions just before failure showed that the hole had an elliptic shape with a large diameter of 4.44 mm and a small diameter of 2.82 mm.

The results for the specimen EQ were similar. Before failure the hole had an elliptic shape with a large diameter of 3.92 mm and a small diameter of 2.73 mm.

However it should be mentioned that for these specimens the accuracy of the vanishing gap method described in chapter 3.1.4.2 may hardly be reached.

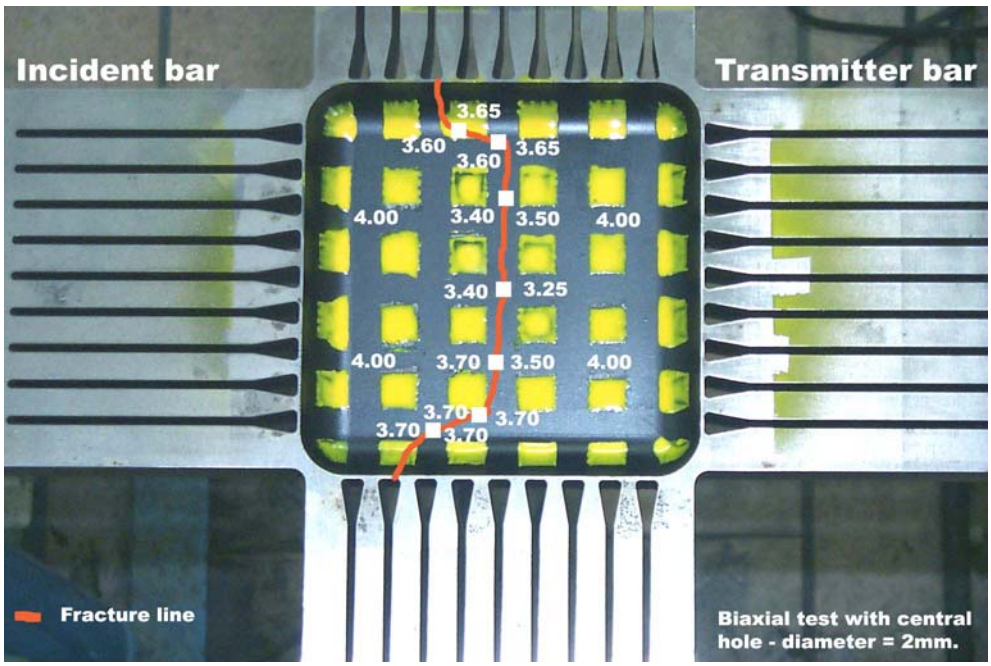

* as seen below, fracture goes through the central hole

Fig. 3.1.3-16: Specimen EO with hole before and after the test

3.1.4 Determination of the failure strains

3.1.4.1 Definition of the local failure strain

Failure is assumed to occur when a crack has reached a size which is detectable by the methods described later. The further crack propagation is not of interest here, since during this phase the remaining load carrying capacity of structures is not very reliable. It is difficult to predict and may rapidly decrease.

The local failure strain is defined as the maximum true equivalent strain (maximum logarithmic equivalent strain) reached at this instant when a crack is just detectable, however before this crack causes major strain redistributions. Thus in theoretical models describing the strain fields, fracture mechanics approaches with singularities at the crack tip must not be considered.

Usually the local failure strain occurs at the specimen surface (hole or notch surface). It should be mentioned, however, that the crack may be initiated at another position in the interior of the specimen usually with a somewhat smaller equivalent strain but with a higher triaxiality of the stress tensor.

The experiments carried out within the LISSAC project will show that the local failure strain defined above as an equivalent strain (second invariant of the strain tensor) is almost independent of the shape of the specimen. This means, failure is mainly controlled by the equivalent strain. Other quantities characterizing the strain and stress field (other invariants of the strain tensor and the invariants of the stress tensor, for instance) have not a significant influence.

However, it should be pointed out, that for specimens and loads causing other strain and stress distributions than investigated here (higher triaxiality of the stress tensor) this may not be true. This has to be considered in the later chapters where conclusions are made and the applicability of the results is discussed.

3.1.4.2 Methods to determine the local failure strain

The direct measurement of the local failure strain, i. e. the maximum equivalent strain at the instant when a crack can be just detected, is very difficult. For the LISSAC specimens with holes or notches, for instance, the maximum strain has a quite local character, it occurs at the curved surface of the hole or notch (inside the hole, for instance) and it reaches high values (often more than 100 %). Thus strain gauges can be hardly used. The application of markings and post test measurements of the increased distances between these markings is only possible for large specimens. Even in this case the interpretation of the result is difficult as discussed in subchapter 3.1.2.1. Also the application of a grid at the plane surface of a flat specimen with a hole or notches cannot really yield the maximum strain which occurs at the curved surface of the hole or notch. (But for large specimens the grid can be used to determine the strain distribution close to maximum).

Therefore indirect methods to determine the local failure strain have been developed within the LISSAC project. They are based on post test geometrical measurements at the broken specimens. The aim is to obtain a characteristic deformation δ of the specimen when a crack is just detectable. Then based on this deformation the related strain fields in the specimen can be reconstructed using theoretical models such as finite element models, for instance. The maximum equivalent strain obtained in this way is the local failure strain ε.

In the following sub-chapters the different types of LISSAC specimens will be addressed and the appropriate indirect methods to determine the local failure strain will be described.

3.1.4.2.1 Tension specimens with a hole or with notches

For these specimens used in many LISSAC test families, the so-called “vanishing gap method” will be applied. In Fig. 3.1.4-1 the method is illustrated for a flat specimen with a hole. The broken parts of the specimen are (virtually) moved together such that the gap between the fracture surfaces vanishes. To reach this condition most of the fracture zones of the broken specimen must overlap (Fig. 3.1.4-1c). It is assumed that the configuration obtained in this way represents the shape of the specimen when the crack has started to develop and is just detectable. The location of this starting crack is the position where the fracture surfaces contact each other.

It is well known that the starting crack will be always perpendicular to the tension stress (normal fracture). Therefore during the search for the position of the starting crack only elements of the fracture surfaces must be considered which are approximately perpendicular to the direction of the tension stress. The relative vertical hole increase, the so-called hole opening at this instant, is defined as the characteristic deformation δ.

This reconstruction would be correct, if during the process of crack propagation the deformed surfaces of the hole did not suffer further shape changes. A detailed discussion of this fact may be found in subchapter 3.1.4.4.1.

The major problem, however, is that in reality the broken parts of the specimens cannot overlap (because two bodies cannot occupy the same space). To overcome this problem the following procedures are applied.

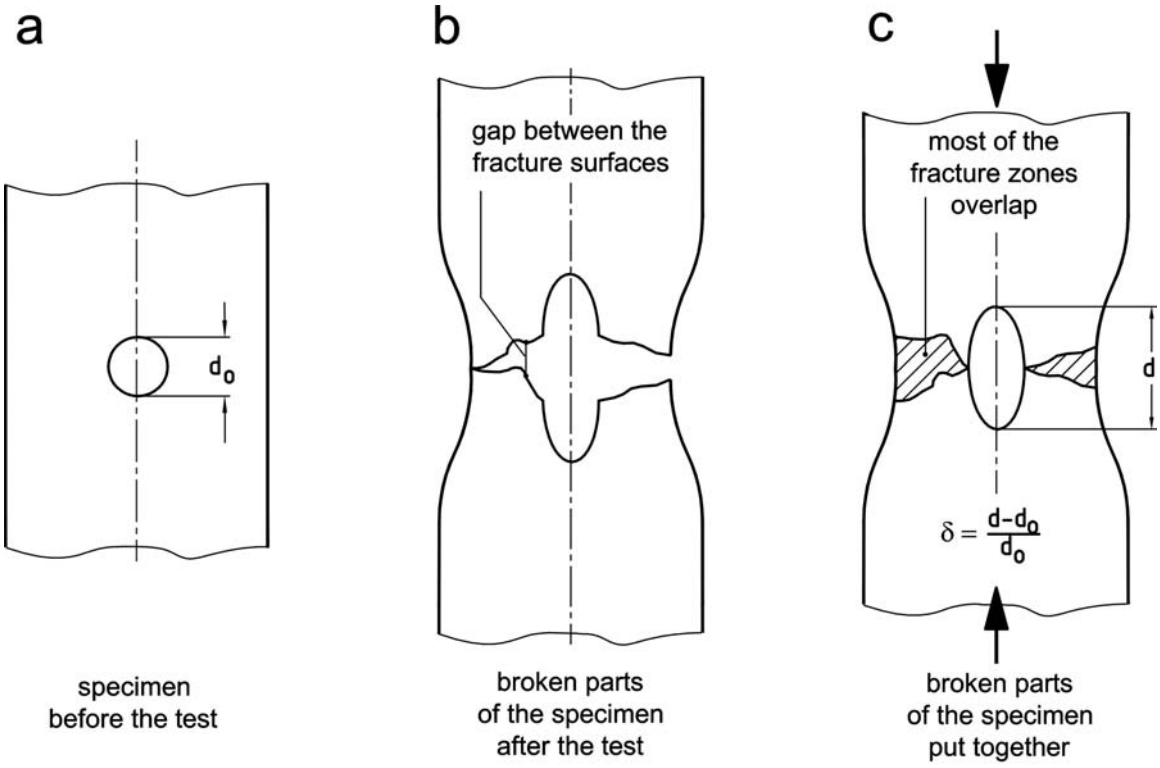

Fig. 3.1.4-1 Principle of the vanishing gap method

For *tension specimens of medium size* with a wall thickness of 20 mm, for instance, the

vanishing gap method
using a three-dimensional measuring machine **(1a)**

is applied. Here the geometry of the fracture surfaces of the broken parts of the specimen is scanned by a mechanical probe as illustrated in Fig. 3.1.4-2 and the relative hole or notch opening δ is calculated.

For specimens of small size the visual control of the scanning process would not allow sufficient accuracy. Thus for *flat tension specimens of small size* the

vanishing gap method
using optical triangulation **(1b)**

is applied. Different fringe pattern are projected and the resulting pictures of the fracture surfaces are taken by a CCD camera and processed to obtain a three-dimensional image. Using these data the characteristic deformation δ can be calculated.

For *tension specimens of large size* transportation and handling at the measuring machine would be expensive. In this case the

vanishing gap method
inserting plastic material into the gap between the fracture surfaces **(1c)**

turned out to be appropriate. This technique and suitable plastic material is well known in dentistry. The geometry of the resulting mock-up of the gap can be easily measured and again the relative hole or notch opening δ can be calculated.

If the broken parts of circular tension specimen are put together as close as possible, the remaining gap between the fracture surfaces is relatively small. Thus for *small circular tension specimens* the

vanishing gap method
based on direct measurement of the notch opening **(1d)**

is applied. The small width of the gap between the fracture surfaces is assessed and subtracted for calculation of the relative notch opening δ. For circular specimens often additional cracks can be observed which have not propagated through the whole cross-section (see Fig. 3.1.2-18, for instance). The widths of the gaps due to these cracks are assessed and subtracted, too.

Fig. 3.1.4-2: Fracture surfaces of the broken parts of a specimen to be scanned by the mechanical probe of a three dimensional measuring machine.

As indicated above the relative hole or notch opening δ is used to reconstruct the complete strain fields in the specimen. For each family of tension tests one specimen is selected, the tension force is increased monotonically step by step and finite element calculations are carried out for each step. To describe the material properties the elastic-plastic stress-strain diagrams determined in section 3.1.1 are used. Both, the strain fields and the hole or notch opening versus load are obtained. After elimination of the load the strain fields versus the hole or notch opening can be obtained. Thus the strain fields and especially the maximum equivalent strain, which represents the local failure strain, is known for each hole or notch opening δ determined above.

Figure 3.1.4-3 shows the finite element models and Fig. 3.1.4-4 the stress-strain diagrams used for the calculations. Figures 3.1.4-5 to 3.1.4-7 show the maximum equivalent strain representing the local failure strain versus the hole or notch opening. In addition, also the strain components contributing to the maximum equivalent strain are indicated. More detailed information about the strain fields can be found in SAM-LISSAC-D027.

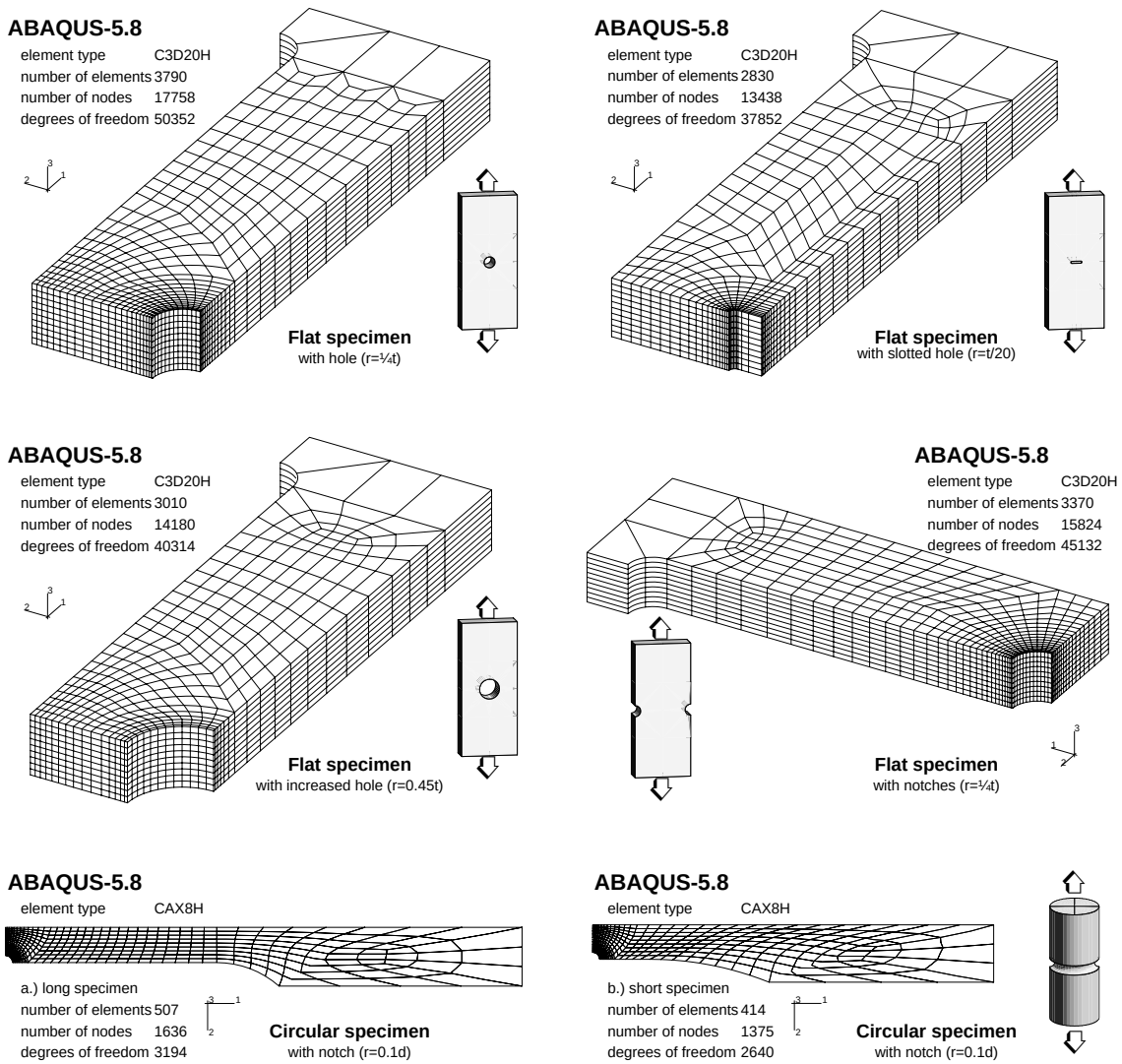

Fig. 3.1.4-3: Finite element models used to calculate the strain distributions.

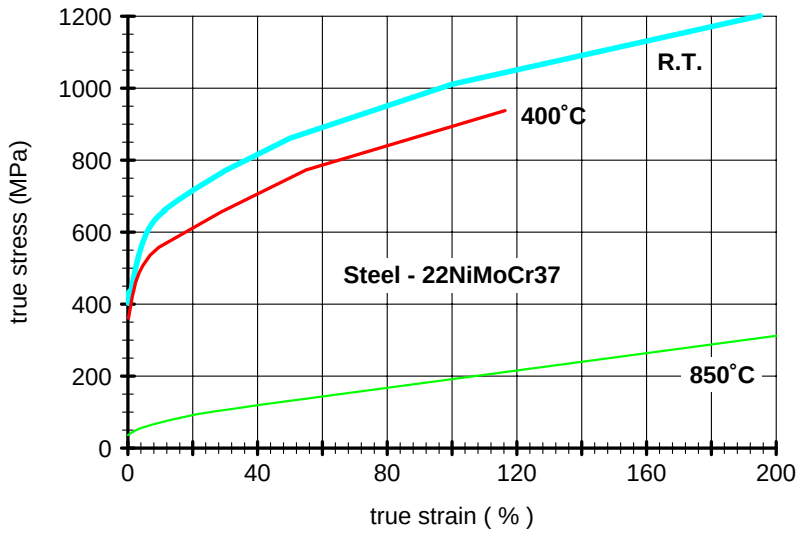

Fig. 3.1.4-4: Stress-strain diagrams used to calculate the strain distributions.

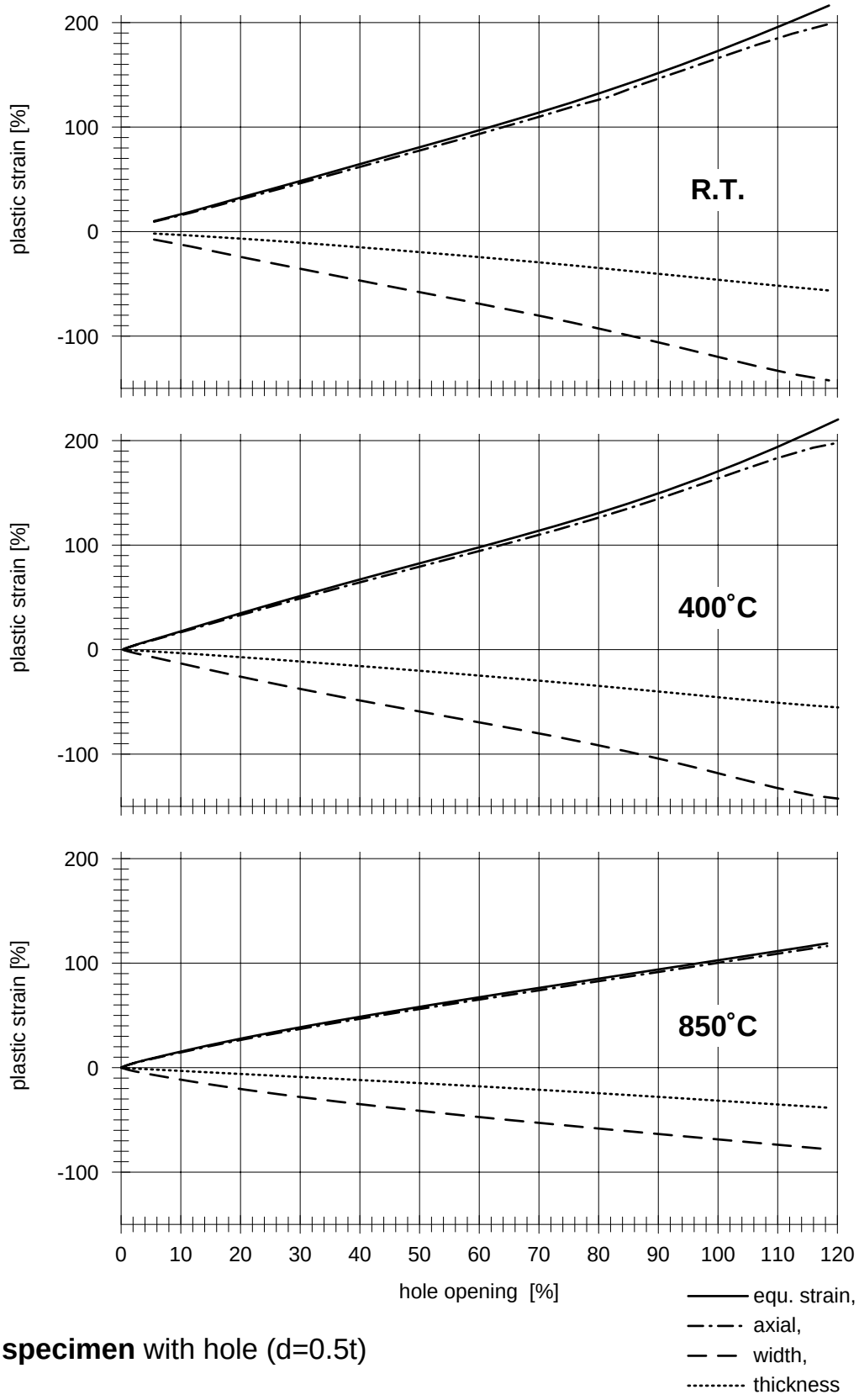

Flat specimen with hole (d=0.5t)

Fig. 3.1.4-5: Maximum equivalent strain and related strain components versus hole opening for the families of flat specimens with hole.

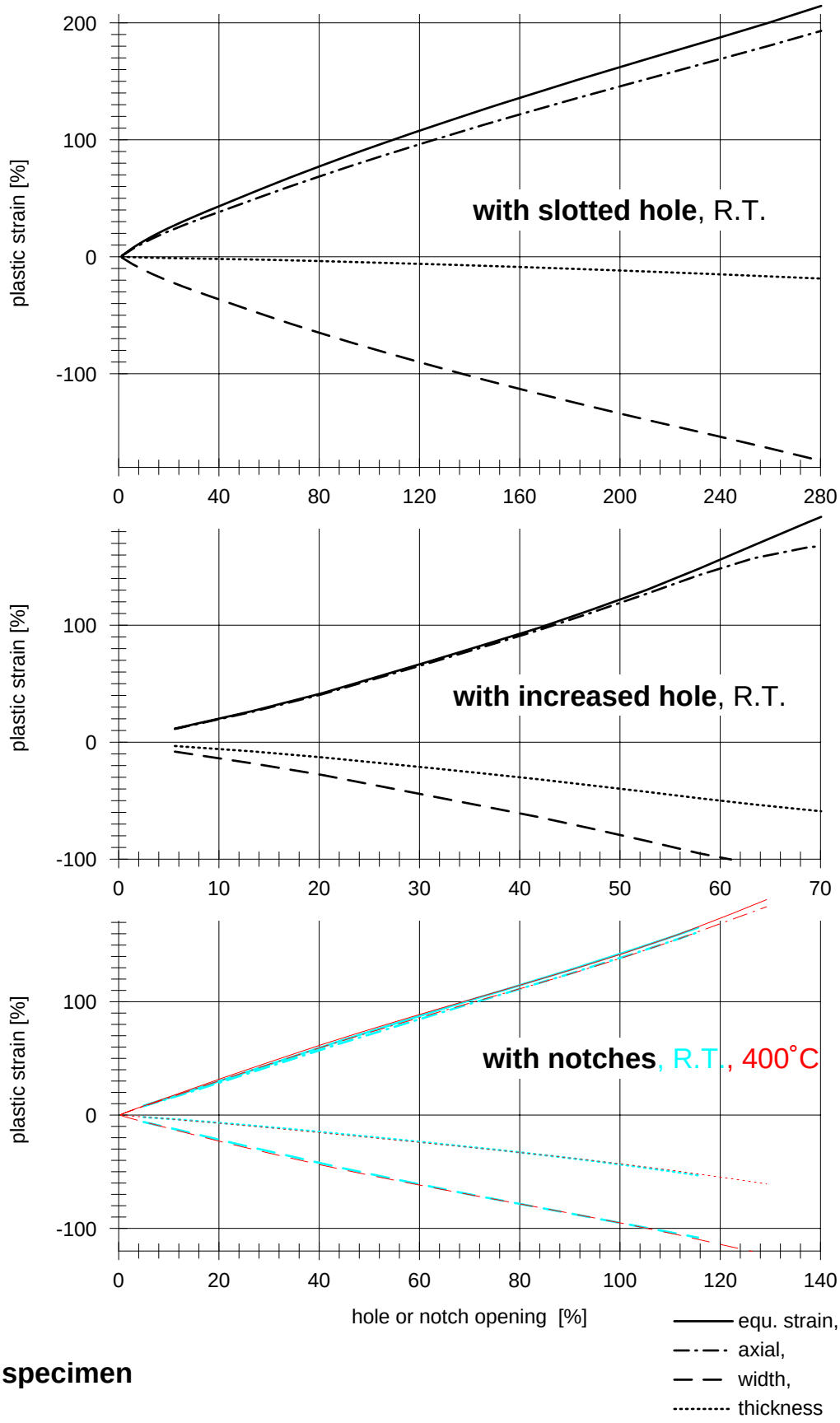

Flat specimen

Fig. 3.1.4-6: Maximum equivalent strain and related strain components versus hole or notch opening for the families of flat specimens with slots, increased holes and notches.

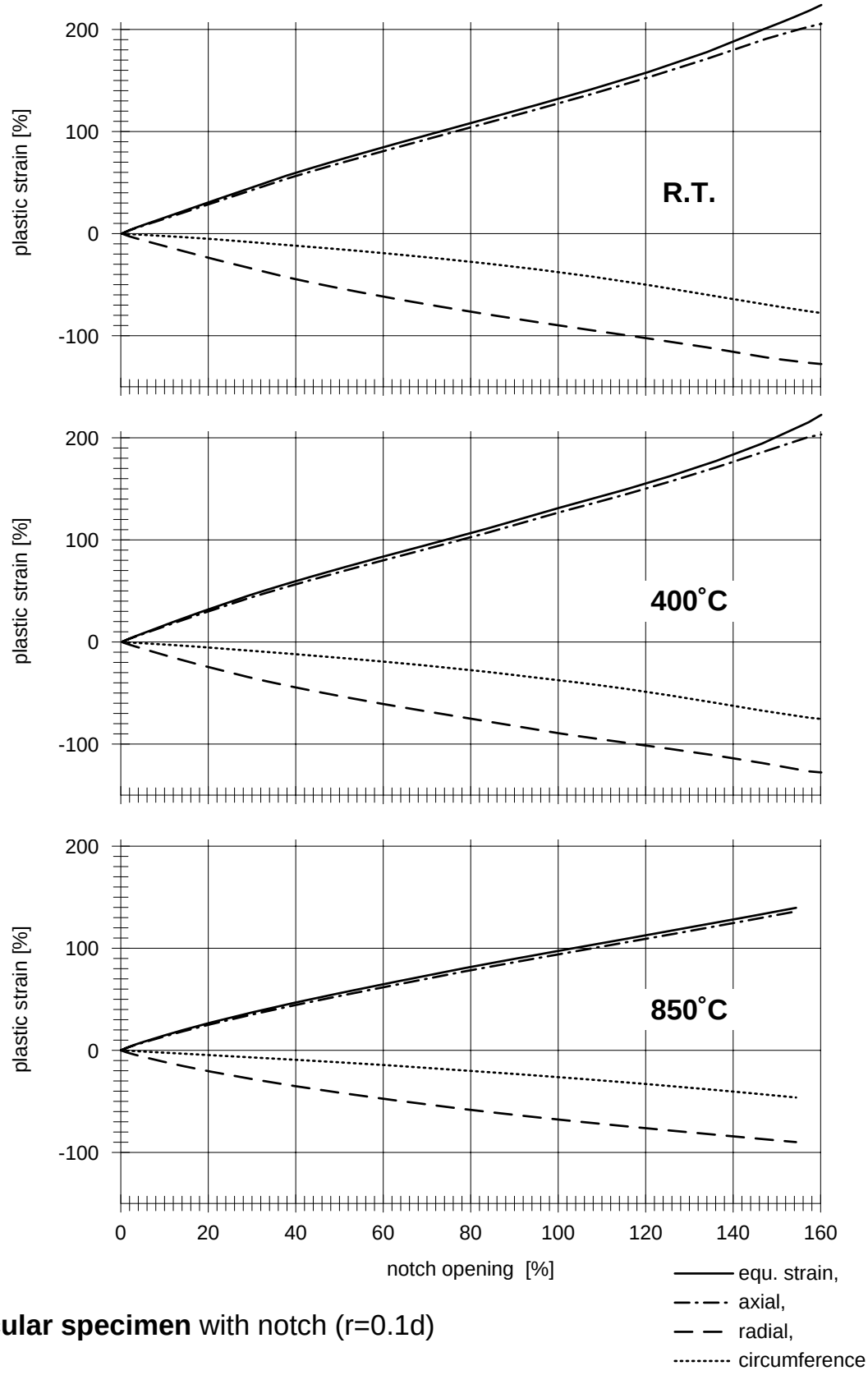

Circular specimen with notch (r=0.1d)

Fig. 3.1.4-7: Maximum equivalent strain and related strain components versus notch opening for the families of circular specimens with notch.

3.1.4.2.2 Circular tension specimens without notches

These specimens were primarily used to check the material homogeneity and to determine the reference stress-strain-diagrams. Thus these specimens do not belong to any test family. Nevertheless it was tried to determine their local failure strain, too.

For these specimens usually necking before fracture is quite strong, but the necking radius is assumed to be relatively large. In this case the strain fields in the smallest cross section will be relatively uniform and the

cross section reduction method **(2)**

seems to be suitable to solve the problem. The relative cross section reduction which can be easily measured at the broken specimen represents the characteristic deformation δ .

The maximum equivalent strain can be calculated by simple formulae derived in SAM-LISSAC-D025, chapter 3. The radial strain in the smallest cross section is

$$\varepsilon_R = -1+\sqrt{1-\delta}$$

and the maximum equivalent strain which represents the failure strain is

$$\varepsilon = \ln\left[1+\frac{2}{3}\left|\frac{(1+\varepsilon_R)^3}{(1-\varepsilon_R)^2}\right|\right]$$

3.1.4.2.3 Curved biaxial specimens

For curved biaxial specimens without and with holes the so-called

forging die method **(3)**

has been developed within a previous research program]. A three-dimensional finite element model of the specimen is used as shown in Fig. 3.1.4-8. To reduce the number of elements symmetry conditions are considered and therefore only 1/8 of the shell has been modelled. The measured displacements for selected points of the deformed specimen are used to form the contact surface of a “forging die”. This means, not only one characteristic deformation of the specimen, but several values are considered.

In the deformed specimen cracks should have just started. If in the experiment cracks have already propagated, the measured displacements have to be corrected to describe the earlier state.

Finally the finite element model is pressed against the rigid surface of the forging die, as shown in Fig. 3.1.4-8b. This means, a so-called “contact problem” has to be solved to obtain the related strain fields including the maximum equivalent strain which is the required failure strain.

Sometimes an appropriate correction to describe the state where cracks have just started is difficult. For specimens with holes an additional check is possible by comparing the hole increases measured after the test with the corresponding value obtained from the finite element calculations.

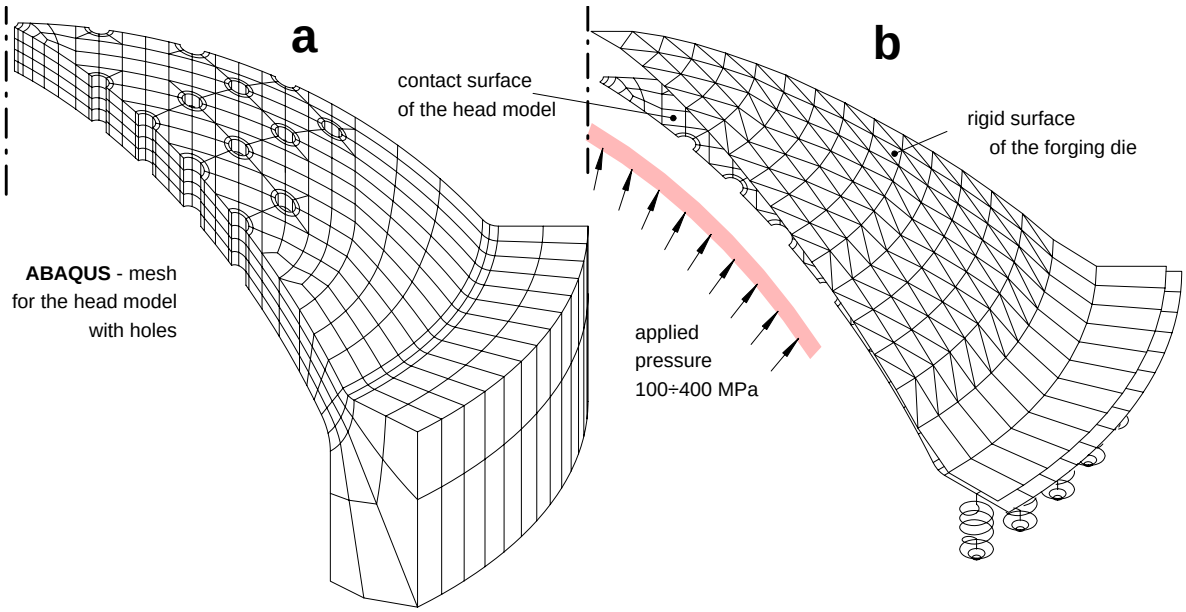

Fig. 3.1.4-8: Determination of the strain distribution using the forging die method.

The pressure applied to press the finite element model against the forging die was between 100 and 400 MPa depending on the prescribed displacements (prescribed curvature of the forging die). A pressure increase beyond this value had only negligible influence on the result.

3.1.4.2.4 Flat or curved biaxial specimens without holes under uniform load.

For these specimens usually the local necking before fracture is relatively small. Therefore the failure strain is about the same as the maximum equivalent strain close to the fracture zone and thus the

thickness reduction method **(4)**

can be applied. The minimum strain in thickness direction close to the fracture zone which can be easily measured at the broken specimen represents the characteristic deformation δ. Note that this strain is negative. The maximum equivalent strain which is approximately the local failure strain ε can be calculated by a simple formula derived in SAM-LISSAC-D025, chapter 5.

$$\varepsilon = \ln\left[1+\frac{2}{3}\left|\sqrt{\frac{1}{1+\delta}-(1+\delta)}\right|\right]$$

3.1.4.2.5 Bending specimens with notch

For these specimens

visual inspection during testing **(5)**

was possible. So the test can be stopped when a crack becomes visible and the relative notch opening, which is defined as the characteristic deformation δ, can be determined directly. Then using this deformation the related strain fields and the maximum equivalent strain can be calculated in a similar same way as described in subchapter 3.1.4.2.1.

Figure 3.1.4-9 shows the deformed finite element model used for the specimens with narrow notch. Furthermore this figure shows the maximum equivalent strain representing the failure strain ε versus the notch opening for both, the specimen with standard notch and the specimen with narrow notch. Again, more details can be found in SAM-LISSAC-D027.

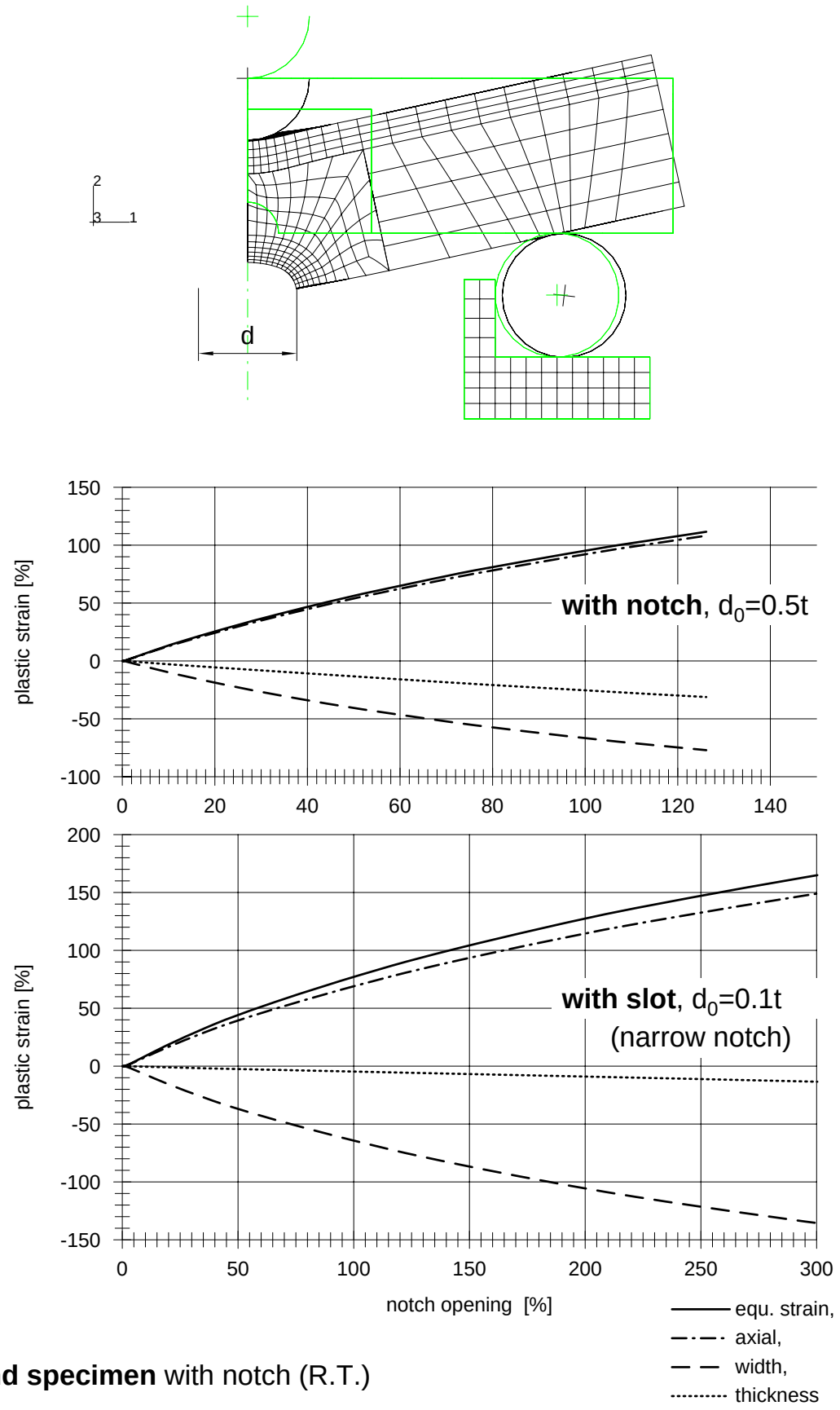

Fig. 3.1.4-9: Finite element model as well as the failure strain and the related strain components for the bending specimens

3.1.4.3 Results for the local failure strains

For most specimens the determination of the characteristic deformation δ and the failure strain ε was straight forward. In the following tables the values obtained are deeply coloured.

For some specimens the determination of δ and ε has been repeated under slightly different conditions or using different methods. Here the most appropriate values have been selected. In the tables only these values are deeply coloured.

For some circular specimens of 3 mm diameter it turned out that the manufacturing of the notch was not correct. The depth of the notch varied between 0.300 and 0.332 mm which covers a range of about 10 %. The correct value would have been 0.3 mm. There were also doubts about the surface quality of the notch. Perhaps the cutting tool was defective causing uncontrolled surface hardening. Thus the results should be considered with caution and in the tables the values for δ and ε are lightly coloured.

For a few specimens failure did not occur. Here δ and ε are related to the maximum deformation reached and not to failure. In the tables these values are also lightly coloured.

For some other specimens which are not members of a test family the values for δ and ε have been determined, too. However in the tables these values are not coloured.

Specimens without values for δ and ε have not been manufactured or the tests have not been done or evaluated. However it should be pointed out that in summary more tests were done than committed in the annex to the LISSAC contract. This can be checked in the attached tables where the number of the committed tests is also mentioned. The very few tests which had to be cancelled were replaced by other tests introduced to solve unforeseen problems.

For the flat biaxial specimens without hole under dynamic load one experimental results became available very late, the other result is still missing. Therefore in the following tables the late result is lightly coloured; in the diagram of Fig. 3.3.1-4 it could not be included. To determine the failure strain ε, the method 4 had to be modified to account for the fact that the dynamic tensile load is applied only in one direction of the flat specimen while the strain is approximately suppressed in the other direction. The resulting failure strain of 53.7 % agrees very well with the failure strains between 52.8 % and 56.4 % for the curved biaxial specimens without hole under dynamic load.

Also for the flat biaxial specimens with hole under dynamic load the results were too late in order to be included in the diagram of Fig. 3.3.1-4. For the some reason the failure strain could be assessed only roughly. Based on the increased elliptical circumference of the hole the mean values of the equivalent strain at failure along this circumference could be determined to 71 % and 67 %. The maximum local strains at failure are higher than these values. Based on other experiments under similar conditions a local failure strain between 100 % and 150 % should be expected.

Flat specimen with hole, static load, R.T.

specimen code	partner	thickness/ diam. [mm]	radius of hole/ notch [mm]	tests com-mitted	δ [%]	ε [%]	method applied	δ [%]	ε [%]
BA1A	FZK	4	1		87	145	1b		
BA1B	FZK	4	1		87	145	1b	86 *	143 *
BA1C	FZK	4	1						
BA1D	FZK	4	1						
BA2A	FZK	4	1		85	140	1b		
BA2B	FZK	4	1	**5**	79	130	1b	76 *	125 *
BA2C	FZK	4	1						
BA2D	FZK	4	1						
BA3A	FZK	4	1		87	145	1b	86 +	143 +
BA3B	FZK	4	1						
BA3C	FZK	4	1						
BA3D	FZK	4	1						
AL1	FZK	20	5		66,3	105	1a		
AN1	FZK	20	5		62,3	100	1a		
AK1	FZK/MPA	20	5	**4**	62	100	1a		
AK2	FZK/MPA	20	5		68	108	1a		
AM1	FZK	20	5						
AR1	FZK	20	5		65,3	104	1a		
AJ1	FZK/MPA	40	10	**1**	60	95	1a		
AC1	MPA	80	20	**1**	52	85	1c		
AP1	FZK/MPA	200	50	**1**	44	70	1c		

\+ lateral correlation corrected, 0.12 mm

* lateral correlation corrected, 0.08 mm

Flat specimen with increased hole, static load, R.T.

specimen code	partner	thickness/ diam. [mm]	radius of hole/ notch [mm]	tests com-mitted	δ [%]	ε [%]	method applied	δ [%]	ε [%]
HE1B	FZK	4	1,8						
HE1C	FZK	4	1,8						
HE1D	FZK	4	1,8						
HE1E	FZK	4	1,8						
HE1F	FZK	4	1,8						
HE2B	FZK	4	1,8	**5**					
HE2C	FZK	4	1,8		57	145	1b	58 +	150 +
HE2D	FZK	4	1,8		53	130	1b		
HE2E	FZK	4	1,8		54	135	1b		
HE2F	FZK	4	1,8		50	121	1b	51 *	124 *
HE2G	FZK	4	1,8		54	135	1b		
AZ1B	FZK	20	9		47,2	114	1a		
CS1B	FZK	20	9	**2**	45,11	105	1a		
CS1C	FZK	20	9		45,11	105	1a		
CN1	MPA	80	36	**1**	40	95	1c		

\+ lateral correlation corrected, 0.08 mm

* lateral correlation corrected, 0.05 mm

Flat specimen with slot, static load, R.T.

specimen code	partner	thickness/ diam. [mm]	radius of hole/ notch [mm]	tests com-mitted	δ [%]	ε [%]	method applied
CP1B	FZK	4	0,2		150	130	1b
CP1C	FZK	4	0,2		160	135	1b
CP1D	FZK	4	0,2		240	185	1b
CP1E	FZK	4	0,2		205	165	1b
CP1F	FZK	4	0,2		190	155	1b
CP2B	FZK	4	0,2	**5**	220	175	1b
CP2C	FZK	4	0,2				
CP2D	FZK	4	0,2				
CP2E	FZK	4	0,2				
CP2F	FZK	4	0,2				
AZ1A	FZK	20	1		136	119	1a
CO1B	FZK	20	1	**2**	128	115	1a
CO1C	FZK	20	1		138	120	1a
CM1	MPA	80	4	**1**	120	107	1c

Flat specimen with notches, static load, R.T.

specimen code	partner	thickness/ diam. [mm]	radius of hole/ notch [mm]	tests com-mitted	δ [%]	ε [%]	method applied	δ [%]	ε [%]
DE1A	FZK	4	1						
DE1B	FZK	4	1		80	113	1b		
DE1C	FZK	4	1		110	155	1b	110 *	155 *
DE1D	FZK	4	1						
DE2A	FZK	4	1		105	150	1b	110 +	155 +
DE2B	FZK	4	1		105	150	1b		
DE2C	FZK	4	1	**5**	110	155	1b		
DE2D	FZK	4	1		105	150	1b		
DE3A	FZK	4	1						
DE3B	FZK	4	1						
DE3C	FZK	4	1						
DE3D	FZK	4	1						
BC1B	FZK	20	5		82,1	117	1a		
DD1C	FZK	20	5	**2**	102,3	145	1a		
DF1A	FZK	20	5		93,1	133	1a		
DH1	MPA	80	20	**1**	65	70	1c		

\+ lateral correlation corrected, 0.02 mm

* lateral correlation corrected, 0.05 mm

Bending specimen with notch, static load, R.T.

specimen code	partner	thickness/ diam. [mm]	radius of hole/ notch [mm]	tests com-mitted	δ [%]	ε [%]	method applied
CT1A	EMPA	4	1				
CT1B	EMPA	4	1		89 #	87 #	5
CT1C	EMPA	4	1				
CT1D	EMPA	4	1				
CT1E	EMPA	4	1				
CT1F	EMPA	4	1	**5**			
Ct1G	EMPA	4	1		75 #	78 #	5
CT1H	EMPA	4	1				
CT1I	EMPA	4	1				
CT1J	EMPA	4	1		77 #	80 #	5
CV1A	EMPA	20	5		56 #	62 #	5
CV1B	EMPA	20	5	**2**			
CV1C	EMPA	20	5		57 #	63 #	5
CA1	EMPA	80	20	**1**	38 #	45 #	5

\# no failure

Bending specimen with narrow notch, static load, R.T.

specimen code	partner	thickness/ diam. [mm]	radius of hole/ notch [mm]	tests com-mitted	δ [%]	ε [%]	method applied
CY1A	EMPA	4	0,2				
CY1B	EMPA	4	0,2				
CY1C	EMPA	4	0,2				
CY1D	EMPA	4	0,2		250	147	5
CY1E	EMPA	4	0,2		260	151	5
CY1F	EMPA	4	0,2	**5**	230	140	5
CY1G	EMPA	4	0,2				
CY1H	EMPA	4	0,2		245	145	5
CY1I	EMPA	4	0,2				
CY1J	EMPA	4	0,2				
CX1A	EMPA	20	1		154	106	5
CX1B	EMPA	20	1	**2**			
CX1C	EMPA	20	1		165	111	5
CW1	EMPA	80	4	**1**	104	80	5
CB	EMPA	80	4		84 #	67 #	5

\# no failure

Circular specimen with notch, static load, R.T.

specimen code	partner	thickness/ diam. [mm]	radius of hole/ notch [mm]	tests commit-ted	δ [%]	ε [%]	method applied	ε [%]	δ [%]	ε [%]
DN1C	JRC	3	0,3		72,8	100	1d	113 +	64,1 *	90 *
DW1H	JRC	3	0,3	**0**	89,3	119	1d	135 +	80,6 *	109 *
EF1B	JRC	3	0,3		87,3	117	1d	133 +	78,7 *	107 *
EF1H	JRC	3	0,3		100,7	134	1d	152 +	92 *	124 *
DQ1A	FZK	3	0,3		124	163	1d		123,3 &	162 &
DQ1B	FZK	3	0,3							
DQ1C	FZK	3	0,3							
DQ1D	FZK	3	0,3							
DQ1E	FZK	3	0,3							
DQ1F	FZK	3	0,3							
DQ1G	FZK	3	0,3							
DQ1H	FZK	3	0,3							
DQ2A	FZK	3	0,3		123	162	1d		127,5 &	167 &
DQ2B	FZK	3	0,3		125	164	1d		125 &	164 &
DQ2C	FZK	3	0,3	**5**	125	164	1d		125,6 &	165 &
DQ2D	FZK	3	0,3							
DQ2E	FZK	3	0,3							
DQ2F	FZK	3	0,3							
DQ2G	FZK	3	0,3							
DQ2H	FZK	3	0,3							
DQ3A	FZK	3	0,3							
DQ3B	FZK	3	0,3							
DQ3C	FZK	3	0,3							
DQ3D	FZK	3	0,3							
DQ3E	FZK	3	0,3							
DQ3F	FZK	3	0,3		126	166	1d		120,8 &	159 &
DQ3G	FZK	3	0,3							
DQ3H	FZK	3	0,3							
DL1A	FZK	9	0,9		109	144	1d			
DL1B	FZK	9	0,9		108	142	1d			
DL1C	FZK	9	0,9	**3**	104	137	1d			
DL1D	FZK	9	0,9		111	146	1d			
DL1E	FZK	9	0,9							
DP1	MPA	20	2	**2**	86	114	1c			
DR1	MPA	20	2		86	114	1c			
CC1	MPA	150	15	**1**	65	90,4	1c			

\+ for the evaluation the notch depth was increased from 0.3 to 0.325 mm

* the specimens were machined to reduce the gap opening

& measurement repeated by another person

Curved biaxial specimen without holes, statîc load, R.T.

specimen code	partner	thickness/ diam. [mm]	radius of hole/ notch [mm]	tests commit-ted	δ [%]	ε [%]	method applied	ε [%]	method applied
ET1	VTT	5	∞	□	-63,2	62	4	72	3
EU1	VTT	5	∞	**3**	-58	56	4		
EV1	VTT	5	∞	□		**&**			
EW	VTT	25	∞	**1**	-58,4	56,6	4		

& test difficult to interprete

Curved biaxial specimen with holes, static load, R.T.

specimen code	partner	thickness/ diam. [mm]	radius of hole/ notch [mm]	tests commit-ted	δ [%]	ε [%]	method applied
EY1	VTT	5	1			126	3
EZ1	VTT	5	1	**3**		136	3
FA1	VTT	5	1			**&**	
FB	VTT	25	5	**1**		32 #	

& test difficult to interprete

no failure

smooth circular specimen, static load, R.T.

(not member of a test family)

specimen code	partner	thickness/ diam. [mm]+C47	radius of hole/ notch [mm]	tests com-mitted	δ [%]	ε [%]	method applied
GR1F	EMPA	5	∞	□	72	112	2
GR1G	EMPA	5	∞	□	70	106	2
GR1H	EMPA	5	∞	□	71	109	2
GR1I	EMPA	5	∞	□	71	109	2
GR1J	EMPA	5	∞	□	71	109	2
GR12F	EMPA	5	∞	□	71	109	2
GR12G	EMPA	5	∞	□	73	115	2
GR12H	EMPA	5	∞	**0**	71	109	2
GR12I	EMPA	5	∞	□	73	115	2
GR12J	EMPA	5	∞	□	68	100	2
GR7F	EMPA	5	∞	□	71	109	2
GR7G	EMPA	5	∞	□	71	109	2
GR7H	EMPA	5	∞	□	71	109	2
GR7I	EMPA	5	∞	□	69	103	2
GR7J	EMPA	5	∞	□	71	109	2

Flat specimen with hole, static load, 400°C

specimen code	partner	thickness/ diam. [mm]	radius of hole/ notch [mm]	tests com-mitted	δ [%]	ε [%]	method applied
BB1A	EMPA	4	1		70	114	1b
BB1B	EMPA	4	1		73	119	1b
BB1C	EMPA	4	1		72	118	1b
BB1D	EMPA	4	1		79	129	1b
BB1E	EMPA	4	1		77	126	1b
BB1F	EMPA	4	1		93	156	1b
BB1G	EMPA	4	1				
BB1H	EMPA	4	1	**5**			
BB1I	EMPA	4	1				
BB1J	EMPA	4	1				
BB1K	EMPA	4	1				
BB1L	EMPA	4	1				
BB1M	EMPA	4	1				
BB1N	EMPA	4	1				
AW1	EMPA	20	5		61,2 *	99 *	
AX1	EMPA	20	5	**2**	52,7	85	1a
AX3	EMPA	20	5		44,6	75	1a
AV1	MPA	40	10	**1**	53	86	1c
CL1	MPA	80	20	**1**	63	99	1c

* This test has been carried out later. The heating time was about 8 hours.
For the tests AX1 and AX3 the heating time was only about 2 hours, which turned out to be not sufficient

Flat specimen with notches, static load, 400°C

specimen code	partner	thickness/ diam. [mm]	radius of hole/ notch [mm]	tests com-mitted	δ [%]	ε [%]	method applied
DB1A	EMPA	4	1				
DB1B	EMPA	4	1				
DB1C	EMPA	4	1				
DB2A	EMPA	4	1				
DB2B	EMPA	4	1		120	172	1b
DB2C	EMPA	4	1		100	142	1b
DB3A	EMPA	4	1	**5**	112	161	1b
DB3B	EMPA	4	1		101	144	1b
DB3C	EMPA	4	1		92	133	1b
DB4A	EMPA	4	1		118	169	1b
DB4B	EMPA	4	1				
DB4C	EMPA	4	1				
BC1A	EMPA	20	5		77,2	111	1a
DA1	EMPA	20	5	**2**			
DA3	EMPA	20	5				
DC1	EMPA	20	5		65,1	96	1a

Circular specimen with notch, static load, 400°C

specimen code	partner	thickness/ diam. [mm]	radius of hole/ notch [mm]	tests com-mitted	δ [%]	ε [%]	method applied	ε [%]	δ [%]	ε [%]
DN1K	JRC	3	0,3		140,5	185	1d	194 +	140,5 *	185 *
DW1I	JRC	3	0,3	**0**	106,1	139	1d	146 +	106,1 *	139 *
DW1D	JRC	3	0,3		115,2	150	1d	157 +	115,2 *	150 *
EF1I	JRC	3	0,3		124,3	161	1d	169 +	124,3 *	161 *
DZ1A	EMPA	3	0,3							
DZ1B	EMPA	3	0,3							
DZ1C	EMPA	3	0,3							
DZ1D	EMPA	3	0,3							
DZ1E	EMPA	3	0,3							
DZ1F	EMPA	3	0,3							
DZ1G	EMPA	3	0,3							
DZ1H	EMPA	3	0,3							
DZ2A	EMPA	3	0,3							
DZ2B	EMPA	3	0,3							
DZ2C	EMPA	3	0,3							
DZ2D	EMPA	3	0,3	**5**						
DZ2E	EMPA	3	0,3		106	138	1d			
DZ2F	EMPA	3	0,3		116	151	1d			
DZ2G	EMPA	3	0,3		128	166	1d			
DZ2H	EMPA	3	0,3							
DZ3A	EMPA	3	0,3		127	164	1d			
DZ3B	EMPA	3	0,3		117	152	1d			
DZ3C	EMPA	3	0,3		133	174	1d			
DZ3D	EMPA	3	0,3							
DZ3E	EMPA	3	0,3							
DZ3F	EMPA	3	0,3							
DZ3G	EMPA	3	0,3							
DZ3H	EMPA	3	0,3							
DU1A	EMPA	9	0,9							
DU1B	EMPA	9	0,9		110	144	1d			
DU1C	EMPA	9	0,9	**3**	97	129	1d			
DU1D	EMPA	9	0,9		116	151	1d			
DU1E	EMPA	9	0,9		106	138	1d			
DY1	MPA	20	2	**2**	93	123	1c			
EA1	MPA	20	2		88	116	1c			
DT1	MPA	150	15	**1**	65	90	1c			

\+ for the evaluation the notch depth was increased from 0.3 to 0.310 mm

* the specimens were machined to reduce the gap opening

Flat specimen with hole, static load, 850°C

specimen code	partner	thickness/ diam. [mm]	radius of hole/ notch [mm]	tests com-mitted	δ [%]	ε [%]	method applied	δ [%]	ε [%]
GB1A	EMPA	4	1						
GB1B	EMPA	4	1						
GB1C	EMPA	4	1						
GB1D	EMPA	4	1						
GB1E	EMPA	4	1						
GB1F	EMPA	4	1						
GB2A	EMPA	4	1	**3**					
GB2B	EMPA	4	1						
GB2C	EMPA	4	1		65	73	1b	69 &	75 &
GB2D	EMPA	4	1		64	72	1b	71 &	78 &
GB2E	EMPA	4	1		58	66	1b	65 &	73 &
GB2F	EMPA	4	1						
FX1	EMPA	20	5	**2**	72,1	79	1a		
FY1	EMPA	20	5		75,8	83	1a		
FW1	MPA	80	20	**1**	70	75	1c		

& microscope with higher resolution to define the normal fracture zone

Circular specimen with notch, static load, 850°C

specimen code	partner	thickness/ diam. [mm]	radius of hole/ notch [mm]	tests com-mitted	δ [%]	ε [%]	method applied	ε [%]	δ [%]	ε [%]
DN1D	JRC	3	0,3		47,4	54	1d	61 +	45,3 *	52 *
DW1J	JRC	3	0,3	**0**	55,9	62	1d	70 +	53,9 *	60 *
EF1J	JRC	3	0,3		46,8	53	1d	60 +	44,8 *	51 *
EI1A	EMPA	3	0,3							
EI1B	EMPA	3	0,3							
EI1C	EMPA	3	0,3							
EI1D	EMPA	3	0,3							
EI1E	EMPA	3	0,3							
EI1F	EMPA	3	0,3		106	102	1d			
EI1G	EMPA	3	0,3							
EI1H	EMPA	3	0,3							
EI2A	EMPA	3	0,3							
EI2B	EMPA	3	0,3							
EI2C	EMPA	3	0,3		95	94	1d			
EI2D	EMPA	3	0,3		85	85	1d			
EI2E	EMPA	3	0,3	**5**	83	84	1d			
EI2F	EMPA	3	0,3		81	82	1d			
EI2G	EMPA	3	0,3		88	88	1d			
EI2H	EMPA	3	0,3							
EI3A	EMPA	3	0,3							
EI3B	EMPA	3	0,3							
EI3C	EMPA	3	0,3							
EI3D	EMPA	3	0,3							
EI3E	EMPA	3	0,3							
Ei3F	EMPA	3	0,3							
EI3G	EMPA	3	0,3							
EI3H	EMPA	3	0,3							
ED1A	EMPA	9	0,9							
ED1B	EMPA	9	0,9		91	90	1d			
ED1C	EMPA	9	0,9	**3**	95	94	1d			
ED1D	EMPA	9	0,9		87	87	1d			
ED1E	EMPA	9	0,9		95	94	1d			
EH1	MPA	20	2		76	78	1c			
EH2	MPA	20	2	**2**	85	85	1c			
EJ1	MPA	20	2		82	83	1c			
EJ2	MPA	20	2		85	85	1c			
EC1	MPA	150	15	**1**	74	76	1c			

\+ for the evaluation the notch depth was increased from 0.3 to 0.325 mm

* the specimens were machined to reduce the gap opening

Flat specimen with hole, dynamic load, R.T.

specimen code	partner	thickness/ diam. [mm]	radius of hole/ notch [mm]	tests committed	δ [%]	ε [%]	method applied
GJ1A	JRC	4	1				
GJ1E	JRC	4	1		83	139	1b
GJ1G	JRC	4	1	**3**	85	142	1b
GJ1I	JRC	4	1		90	151	1b
GJ1O	JRC	4	1		81	134	1b
GD1	JRC	20	5				
GE1	JRC	20	5	**3**			
GM1	JRC	20	5		75	124	1a
GP1	JRC	20	5		74	122	1a

Circular specimen with notch, dynamic load, R.T.

specimen code	partner	thickness/ diam. [mm]	radius of hole/ notch [mm]	tests committed	δ [%]	ε [%]	method applied	ε [%]	δ [%]	ε [%]	method applied
DN1A	JRC	3	0,3		79,1	105	1d	119 +	64,1 *	85 *	
DW1A	JRC	3	0,3		74,2	95	1d	107 +	59,2 *	80 *	
EF1A	JRC	3	0,3		81,4	105	1d	119 +	66,4 *	90 *	
EF1E	JRC	3	0,3	**3**	91,6	120	1d	136 +	76,6 *	95 *	
DN1B	JRC	3	0,3								
DN1E	JRC	3	0,3								
DN1F	JRC	3	0,3								
DN1H	JRC	3	0,3								
DM1	JRC	20	2	**2**	103	135	1d		98	129	1a
DO1	JRC	20	2		89	119	1d		92,5	123	1a

\+ for the evaluation the notch depth was increased from 0.3 to 0.325 mm

* the specimens were machined to reduce the gap opening

Flat biaxial specimen without hole, dynamic load, R.T.

specimen code	partner	thickness/ diam. [mm]	radius of hole/ notch [mm]	tests committed	δ [%]	ε [%]	method applied
EP1	JRC	4	∞	**2**	-43.8	53.7	4 *
EN1	JRC	4	∞		-52,5	67,4	4 *

* the method 4 had to be modified; the results were too late for further consideration.

Flat biaxial specimen with hole, dynamic load, R.T.

(Tests of 8 mm specimens cancelled)

specimen code	partner	thickness/ diam. [mm]	radius of hole/ notch [mm]	tests committed	δ [%]	ε [%]	method applied
EO1	JRC	4	1	**2**		180	+
EQ1	JRC	4	1			146	+
CG1	JRC	8	2	**2**			
EM1	JRC	8	2				

\+ only a rough assessment of **ε** was possible; the results were too late for further considerations

Curved biaxial specimen without holes, dynamic load, R.T.

specimen code	partner	thickness/ diam. [mm]	radius of hole notch [mm]	tests committed	δ [%]	ε [%]	method applied	ε [%]	method applied
FD1	FZK	5	∞	□	-45,7 #	43,5 #	4		
FE1	FZK	5	∞	**3**	-57,4	55,4	4		
FF1	FZK	5	∞	□	-58,4	56,4	4	61,7	3
BO1	FZK	5	∞	□	-47,6 #	45,2 #	4		
FG	FZK	25	∞	**2**	-54,98	52,8	4		
FL	FZK	25	∞	□	-57,65	55,6	4		

\# no failure

Curved biaxial specimen with holes, dynamic load, R.T.

specimen code	partner	thickness/ diam. [mm]+C47	radius of hole/ notch [mm]	tests committed	δ [%]	ε [%]	method applied
FN1	FZK	5	1			65 #	3
FO1	FZK	5	1	**3**		117	3
FP1	FZK	5	1			54 #	3
FQ	FZK	25	5	**2**		&	
FV	FZK	25	5			115,5	3

\# no failure

& excessive deformation after failure

Flat specimen with hole, dynamic load, 400°C

specimen code	partner	thickness/ diam. [mm]	radius of hole/ notch [mm]	tests committed	δ [%]	ε [%]	method applied
GJ1B	JRC	4	1		87	144	1b
GJ1C	JRC	4	1				
GJ1F	JRC	4	1	**3**			
GJ1H	JRC	4	1				
GJ1N	JRC	4	1		92	154	1b
GG1	JRC	20	5				
GH1	JRC	20	5	**3**	53	89	1a
GI1	JRC	20	5		76,5	126	1a
GO1	JRC	20	5				

Circular specimen with notch, dynamic load, 400°C

specimen code	partner	thickness/ diam. [mm]	radius of hole/ notch [mm]	tests committed	δ [%]	ε [%]	method applied	ε [%]
DW1E	JRC	3	0,3		114,3	147	1d	154 +
DW1F	JRC	3	0,3		116,9	155	1d	163 +
EF1F	JRC	3	0,3		98,7	123	1d	129 +
DN1G	JRC	3	0,3		113,2	145	1d	152 +
DW1B	JRC	3	0,3	**3**				
DW1C	JRC	3	0,3					
DW1D	JRC	3	0,3					
DW1E	JRC	3	0,3					
DW1F	JRC	3	0,3					
DV1	JRC	20	2	**2**	103	135	1d	
DX1	JRC	20	2		105	137	1d	

\+ for the evaluation the notch depth was increased from 0.3 to 0.310 mm

Circular specimen with notch, dynamic load, 600°C

(not member of a test family)

specimen code	partner	thickness/ diam. [mm]	radius of hole/ notch [mm]	tests committed	δ [%]	ε [%]	method applied
DW1G	JRC	3	0,3	**0**	172,5	255 #	1d

\# calculation done for 400° C

Circular specimen with notch, dynamic load, 800°C

(not member of a test family)

specimen code	partner	thickness/ diam. [mm]	radius of hole/ notch [mm]	tests com-mitted	δ [%]	ε [%]	method applied
DN1I	JRC	3	0,3	**0**	185,3	163 #	1d

calculation done for 850° C

Flat specimen with hole, dynamic load, 850°C

specimen code	partner	thickness/ diam. [mm]	radius of hole/ notch [mm]	tests com-mitted	δ [%]	ε [%]	method applied	δ [%]	ε [%]
GJ1D	JRC	4	1		115	116	1b	132 &	132 &
GJ1J	JRC	4	1		135	134	1b	146 &	146 &
GJ1K	JRC	4	1	**3**					
GJ1L	JRC	4	1						
GJ1M	JRC	4	1		117	118	1b	139 &	139 &
GF1	JRC	20	5		153	150	1a		
GK1	JRC	20	5						
GL1	JRC	20	5	**2**					
GN1	JRC	20	5		151,7	149	1a		

& microscope with higher resolution to define the normal fracture zone

Circular specimen with notch, dynamic load, 850°C

specimen code	partner	thickness/ diam. [mm]	radius of hole/ notch [mm]	tests com-mitted	δ [%]	ε [%]	method applied	ε [%]
DN1L	JRC	3	0,3					
DW1K	JRC	3	0,3		175,3	155	1d	163 +
EF1C	JRC	3	0,3	**3**				
EF1D	JRC	3	0,3					
EF1G	JRC	3	0,3		207,5	180	1d	189 +
EE1	JRC	20	2	**0**	180	160	1d	
EG1	JRC	20	2		175	155	1d	

+ for the evaluation the notch depth was increased from 0.3 to 0.310 mm

3.1.4.4 Comments on the accuracy of the local failure strains

3.1.4.4.1 Tension specimens with a hole or with notches investigated by the vanishing gap method

As already mentioned, the reconstruction of the strain fields at failure assumes that during the process of crack propagation the deformed surfaces of the hole or notches do not suffer further shape changes. Basic consideration of the stress redistribution caused by a propagating crack (no tension stress normal to the fracture surfaces) support this assumption. In addition, observations made during some of the tests with the optical measurement system (Fig. 3.1.2-3) indicated that during the process of crack propagation the contour of the holes in the middle of the specimens remains constant. Small changes of the contour which might not be detectable with the optical measurement can be assessed to cause a relative error of the local failure strain of less than $\pm$ 5 %.

Another source of errors are lateral displacements sometimes occurring during the crack propagation process as indicated in Fig. 3.1.4-10a. It is assumed that initially when the crack is still small, these lateral displacements are small, too, and can be neglected. Thus, if the broken parts are put together in order to apply the vanishing gap method, lateral displacements are omitted as indicated in Fig. 3.1.4-10b. Nevertheless, uncertainties of the lateral correlation of the broken parts have to be considered. This was especially a problem for the flat tension specimens with 4 mm thickness. Therefore in some cases indicated in the tables of chapter 3.1.4.3 the lateral correlation was varied (corrected) allowing lateral displacements up to 3 % of the specimen thickness. The resulting relative errors of the failure strain were up to about $\pm$ 4 %. For tension specimens of larger thicknesses or different shapes this error is assumed to be the same (although one should expect that it is smaller).

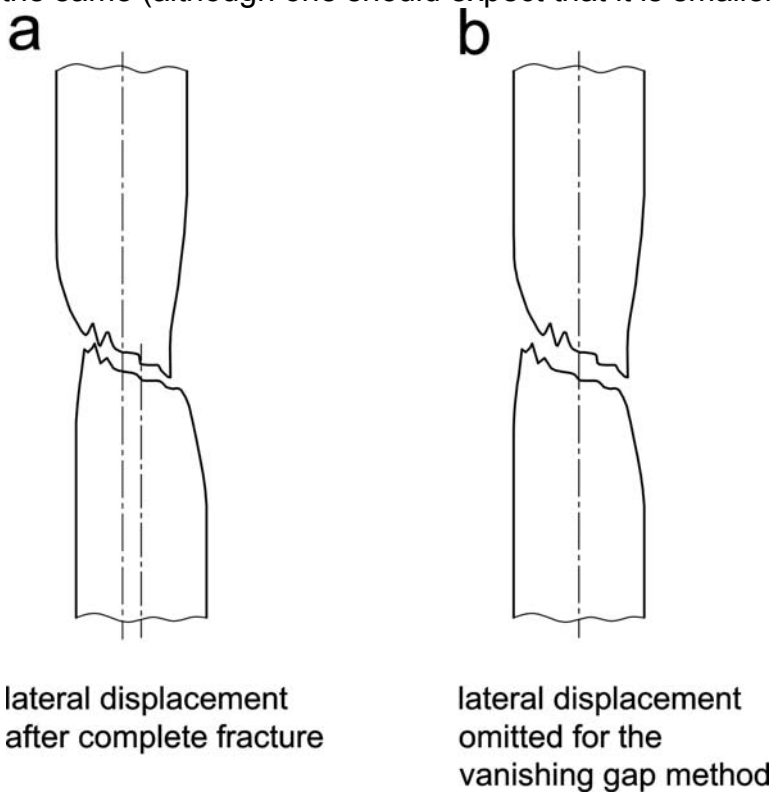

Fig. 3.1.4-10: Lateral displacements of tension specimens

Measuring errors of axial displacements using the three-dimensional measuring machine have been assessed to ± 0.1 mm. The resulting relative error of the local failure strain is about ± 1 %. Corresponding measuring errors using optical triangulation (small flat tension specimens) or inserting plastic material into the gap between the fracture surfaces (big tension specimens) are assumed to have the same effect on the local failure strain.

However, measuring errors of the axial displacements, using the vanishing gap method with direct measurement of the notch opening, which was applied for the circular tension specimens of 3 mm diameter, have a larger effect on the local failure strain. Here the most difficult problem was to assess the maximum width of the gap between the fracture surfaces and the widths of the possible gaps of other cracks which did not propagate through the hole cross section of the specimens. These gaps had to be subtracted from the measured notch opening. Even with the microscope the resulting error of the notch opening is about ± 0.1 mm. Considering that the initial notch width is only 0.6 mm, which during the test increases to about 1.5 mm, the resulting relative error of the local failure strain is about ± 10 %.

To check this error, some of the measurements have been repeated by another person. This resulted in relative deviations for the local failure strain of about + 3 % and − 5 %. Thus the above assessment of the accuracy seems to be reasonable (or slightly conservative).

A final source of errors is the reconstruction of the strain fields at failure by finite element calculations. The finite element discretizations used (Fig. 3.1.4-3) should allow suitable spatial resolutions and therefore the resulting error is assumed to be negligible. Uncertainties of the description of the constitutive equations by the stress-strain diagrams (Fig. 3.1.4-4) may have more influence. Considering the difference between the stress strain diagrams at room temperature and at 400 °C and considering the related, quite moderate differences of the plastic strains versus the hole or notch opening (Figs. 3.1.4-5 to 3.1.4-7), it can be concluded that the resulting relative error of the failure strain could be up to ± 5 %.

In order to summarize the particular errors discussed above one has to consider the quadratic error propagation rule. For all the tension specimens – except the circular specimens of 3 mm diameter – the application of the vanishing gap method causes a relative error of the failure strain of about ± **8 %**. For the circular specimens of 3 mm diameter the relative error is about ± **13 %**.

A more integral check of the accuracy of the vanishing gap method is possible by using the results from the object grating method presented in Fig. 3.1.2-16.

For a flat specimen of 4 mm thickness the object grating method yielded a hole opening at failure of **75 %** and a maximum axial strain at the specimen surface of 88 %. Based on this hole opening finite element calculations yield a corresponding axial strain of 92.5 % and a failure strain (maximum equivalent strain in the middle of the specimen thickness) of **124 %**. In comparison to this the results of the vanishing gap method presented in chapter 3.1.4.3 quote hole openings between **79 %** and **87 %** resulting in failure strains between **130 %** and **145 %**.

For a flat specimen of 20 mm thickness the object grating method yielded a hole opening of **61 %** and an axial strain of 73 %; finite element calculations yield an axial strain of 72.5 % and a failure strain of **98 %**. In comparison the results of the vanishing gap method quote hole openings between **62 %** and **68 %** resulting in failure strains between **100 %** and **108 %**.

Based on these comparisons one can conclude, that the error assessments described before seem to be reasonable. In general, the values from the object grating method are somewhat smaller than the values from the vanishing gap method. This systematic deviation can be explained by the somewhat different definition of failure. With the object grating method very small cracks are detectable and these cracks define failure. With the vanishing gap method the cracks must be a little bit larger to be detected and consequently the related failure strains are somewhat larger, too.

3.1.4.4.2 Curved biaxial specimens investigated by the forging die method

An assessment of the accuracy of this method was done within another research project [34]. The strains determined with this method deviated from the strains determined by the displacements of marking points applied at the specimens only moderately up to ± **10 %**.

As an additional control within the LISSAC project, the evaluations for the specimens FO1 and FV tested under dynamic load were extended. The application of the forging die method yielded maximum equivalent strains of 117 % and 115.5 %, respectively. The measurement of increased hole circumferences yielded corresponding mean values of the equivalent strain around the most critical holes of 100 % and 97 %, respectively. Thus the maximum values obtained by the forging die method seem to be reasonable.

3.1.4.4.3 Flat or curved biaxial specimens without holes investigated by the thickness reduction method

One source of uncertainty is the measurement of the minimum strain in thickness direction close to the fracture surface. If one approaches the fracture surface, the strain in thickness direction decreases (the amount increases). However very close to the fracture surface the measurement is impaired by the shear type of fracture resulting in very local asymmetric necking effects. The resulting relative error for the local failure strain can be assessed to ± 5 %.

Another error is due to the assumptions in the theoretical model described in SAM-LISSAC-D025, chapter 5. An assessment of this error is hardly possible; guesses may also yield ± 5 %.

Finally it should be considered that the thickness reduction method yields the maximum mean value across the wall thickness. The maximum peak value, probably at the outer or inner surface of the specimen, will be somewhat higher. This has been confirmed by the evaluation of the specimen FF1 tested under dynamic load. The thickness reduction method leads to a maximum equivalent strain of 56.4 %, the forging die method able to determine the peak value across the wall thickness yields a peak value of 61.7 %.

In summary the relative error for the failure strain is suggested to vary between **-5 %** and **+10 %**.

3.1.4.4.4 Bending specimens investigated by visual inspection during testing

With this method the process to detect the initial crack is quite simple. Nevertheless the recognition of the initial crack is connected with some uncertainty. The resulting relative error for the local failure strain can be assessed to $\pm$ 5 %.

Furthermore the size of the initial crack defining specimen failure can be expected to be smaller than for the other methods, where a visual inspection of the crack during the test was not possible. (The same was true for the object grating method mentioned in subchapter 3.1.4.4.2 in comparison to the other methods). Thus the failure strains determined with the current method will be probably somewhat smaller than the failure strains obtained with the other methods. This systematic deviation will be addressed again in chapter 3.3.1. The relative value could be as much as -10 %.

The error due to the reconstruction of the strain fields at failure by finite element calculations should be similar to the corresponding error discussed in subchapter 3.1.4.4.1. There the resulting relative effect on the failure strain was assessed to $\pm$ 5 %.

If the systematic deviation is suppressed in order to obtain results comparable with the other assessments, in summary the relative error for the failure strain could be **+10 %.**

3.2 Theoretical results

3.2.1 Gradient models

3.2.1.1 Damage enhanced flow theory of gradient plasticity

3.2.1.1.1 Theory

Higher-order strain gradient theories are able to model phenomena that cannot be captured by standard elasticity and plasticity theories, which do not involve an internal length scale in their constitutive equations. Size effects, strain localization and patterning are representative examples of such phenomena. This advantage of gradient theories is due to the involvement of an internal length scale in the constitutive material description through the gradient coefficients.

The present work documented in [1] uses the flow theory of gradient plasticity proposed by Aifantis and co-workers [2-6]. It is implemented within an element-free Galerkin (EFG) framework in order to solve 2D and 3D boundary-value problems considering finite deformations. In this gradient theory the usual constitutive relations of classical plasticity are modified by including the Laplacian of the hardening parameter into the standard expression for the yield condition. To account for void nucleation, void growth and crack initiation, the above framework has been extended to include also a damage mechanics model proposed by Lämmer and Tsakmakis [7] as a generalization of Dhar et al. [8] damage approach. Material failure (microcrack initiation) can be determined by employing the most common engineering criteria: (a) a local failure strain criterion, (b) a local failure stress criterion, and (c) a local failure damage criterion.

The most common damage variable D is identified as the effective area reduction caused by discontinuities in the form of microcracks and microvoids. In the present work, however, we employ another scalar damage variable X related to D as

$$X = \frac{D}{1-D} \;\Rightarrow\; 1-D = \frac{1}{1+X}$$

where X is monotonically increasing with D and takes values within the range 0 (undamaged material, i.e. $D = 0$) and $+\infty$ (completely damaged material, i.e. $D = 1$). Thus, X is not bounded which avoids numerical integration problems [9].

Damage evolution is assumed to obey the following law

$$\dot{D} = a_o \dot{\hat{\varepsilon}}^p_{eq} + (a_1 + a_2 D)\frac{(-Y)^n}{(1-D)^q}\dot{\hat{\varepsilon}}^p_{eq}; \quad -Y = \frac{\hat{\tau}^2_{eq}}{2E(1-D)^2}\left[\frac{2(1+\nu)}{3} + 3(1-2\nu)\frac{\hat{\tau}^2_m}{\hat{\tau}^2_{eq}}\right],$$

where a_o, a_1, a_2, n, q are non-negative material parameters and $(-Y)$ is the elastic damage energy release rate. This law was studied by Lämmer and Tsakmakis [7] as a generalization of the damage model of Dhar et al. [8] where $n = 1$ and $q = 0$. The first term, which is independent of $(-Y)$, accounts for damage evolution due to void nucleation, while the second term, which depends on $(-Y)$, represents the damage evolution due to void growth.

One of the simplest forms of flow theory of gradient plasticity is based on the gradient modification of the standard expression for the flow stress $\hat{\tau}_{eq} = \kappa(\hat{\gamma})$ to include the Laplacian of the hardening parameter in Eulerian coordinates $\nabla^2_x \hat{\gamma}$. The corresponding form of the gradient-dependent yield condition reads

$$f = \hat{\tau}_{eq} - \left[\kappa(\hat{\gamma}) + c(\hat{\gamma}) \nabla_x^2 \hat{\gamma} \right] = 0.$$

Then, by including also damage effects, i.e.

$$f = \hat{\tau}_{eq}(1+X) - \left[\kappa(\hat{\gamma}) + c(\hat{\gamma}) \nabla_x^2 \hat{\gamma} \right] = 0,$$

a more generalized theory can be developed, where $c(\hat{\gamma})$ is the phenomenological gradient coefficient, which, in general, depends on the hardening parameter $\hat{\gamma}$. Furthermore, the equivalent stress $\hat{\tau}_{eq}$ is the usual von Mises measure defined as $\hat{\tau}_{eq} = \sqrt{3\hat{\boldsymbol{\tau}}' \cdot \hat{\boldsymbol{\tau}}' / 2}$, where $\hat{\boldsymbol{\tau}}'$ denotes the deviatoric part of the Kirchhoff stress tensor $\hat{\boldsymbol{\tau}}$ in the corotational configuration.

Instead of using a finite element formulation, the element-free Galerkin (EFG) method is employed herein. It is a meshless method that bases on a moving least squares principle for the formulation of the shape functions [10, 11].

3.2.1.1.2 Determination of material depending parameters

For the homogeneous part of the flow stress $\kappa(\hat{\gamma})$ one may use the experimentally true stress – strain curve. In contrast to other methods a modified elongation of the true stress strain curve is used which fits well the tensile engineering stress – strain curve, in combination with the gradient model as shown in the next section.

$$\kappa(\hat{\gamma}) = \begin{cases} A_1 \exp\left[-A_2 \hat{\gamma}^m \exp\left(A_3 \hat{\gamma}\right)\right] + A_4 \hat{\gamma}^p + \sigma_y, & \hat{\gamma} \le \hat{\gamma}_u \\ \dfrac{1}{2}\left\{k_u + k_u(\hat{\gamma} - \hat{\gamma}_u) + A_1 \exp\left[-A_2 \hat{\gamma}^m \exp\left(A_3 \hat{\gamma}\right)\right] + A_4 \hat{\gamma}^p + \sigma_y\right\}, & \hat{\gamma}_u < \hat{\gamma} \le 1 \\ \dfrac{1}{2}\left\{k_u + k_u(\hat{\gamma} - \hat{\gamma}_u) + k_o \hat{\gamma}^N\right\}, & \hat{\gamma} > 1 \end{cases},$$

where the parameters used to accomplish the fitting (using the least square method) are σ_y = 441 MPa (initial yield stress), A_1 = 175.682 MPa, A_2 = $2.365 \cdot 10^{-3}$, A_3 = 5.932, A_4 = 497.808 MPa, m = – 1.65, p = 0.896, k_o = 1010.8 MPa, N = 0.3025, $\hat{\gamma}_u$ = 0.138 and k_u = 677.8 MPa. The used true stress strain curve (marked as " used by AUT") is shown in Fig. 3.2.1.1-1 in comparison to the curve used by the other partners (marked as " given by MPA").

Concerning the elastic material parameters, the values E = 231000 MPa and ν = 0.2 are used. Moreover, the value c = –110.25 N is employed for the Laplacian coefficient unless otherwise stated. This value corresponds to a phenomenological internal length $l = \sqrt{-c / k_u}$ = 0.403 mm.

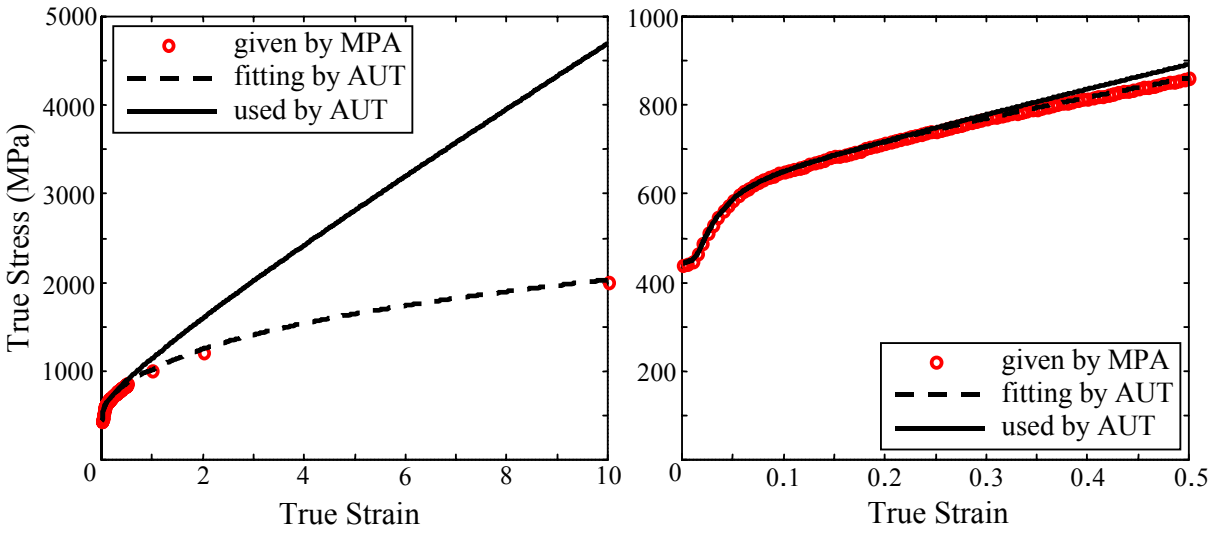

Fig. 3.2.1.1-1: Comparison of the true stress – strain curve used by the partners (MPA curve) with that used by AUT.

3.2.1.1.3 Results

Cylindrical tensile specimens

Consider a cylindrical specimen of diameter D_o and length $L = 5D_o$ which is subjected to tensile loading, as shown in Fig. 3.2.1.1-2.

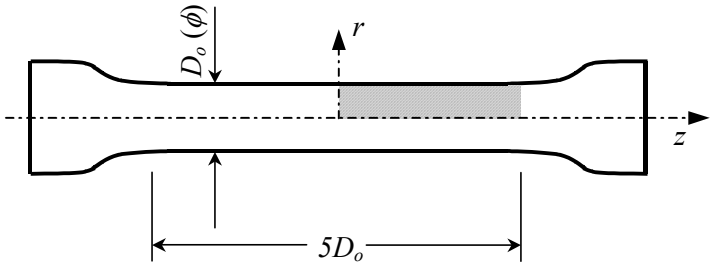

Fig. 3.2.1.1-2: Cylindrical tensile specimen.

Axisymmetric loading conditions are assumed. Because of symmetry, only one quarter of the cylinder is considered. A geometric imperfection is introduced at the symmetry cross-section. In particular, the specimen radius within a distance of $0.08D_o$ from the symmetry section is 5 % smaller than the overall radius.
The nodal distribution of the EFG discretization employed is depicted in Fig. 3.2.1.1-3.

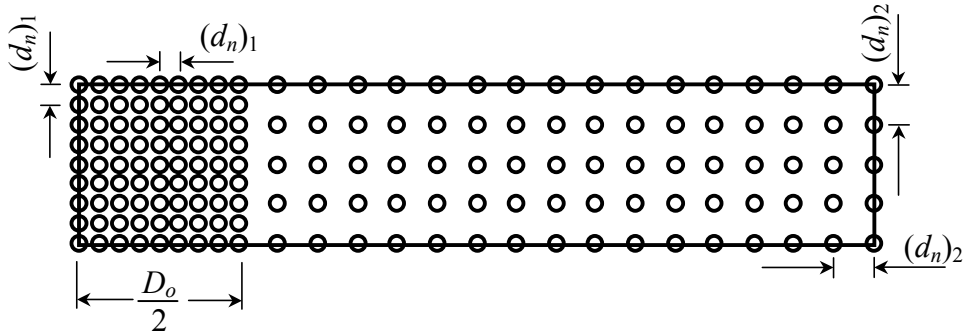

Fig. 3.2.1.1-3: EFG nodal distribution in a quarter of the tensile specimen.

Then, the validity of the used homogeneous equivalent stress – strain responses given is investigated with standard plasticity ($c \equiv 0$) without damage

$(a_o \equiv 0, a_1 \equiv 0, a_2 \equiv 0, n \equiv 0, q \equiv 0)$. The computed engineering stress – strain graph is compared with the experimental results, Fig. 3.2.1.1-4. As shown, the prediction corresponds well with the experimental results.

In order to study size effects, three geometrically similar specimens with D_o = 5, 15 and 50 mm (see Fig. 3.2.1.1-2) were considered. Gradient plasticity ($c = -110.25$ N) without damage $(a_o \equiv 0, a_1 \equiv 0, a_2 \equiv 0, n \equiv 0, q \equiv 0)$ is assumed. The obtained engineering stress vs. engineering strain and engineering stress vs. diameter reduction graphs are depicted in Fig. 3.2.1.1-4.

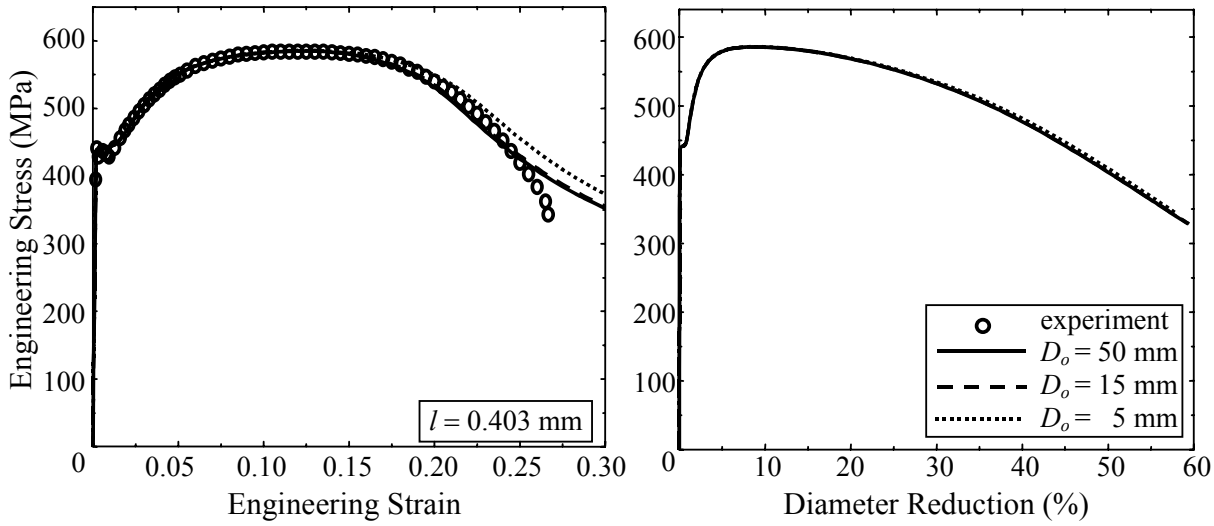

Fig. 3.2.1.1-4: Size effect on the engineering stress at the symmetry cross-section for geometrically similar tensile specimens without damage.

As was expected, the pre-necking behaviour is not influenced by the specimen size due to the absence of strain gradients. On the other hand, at any engineering strain in the post-necking regime, the engineering stress decreases with specimen size. However, the relation between engineering stress and diameter reduction at the symmetry cross-section (which is a measure of the maximum strain) exhibits a negligible size effect. Furthermore, in the present case, the relation between the maximum principal Almansi-Hamel strain $\underset{\sim}{\boldsymbol{e}} = (\boldsymbol{I} - \boldsymbol{F}^{-\mathrm{T}}\boldsymbol{F}^{-1})/2$, and the maximum equivalent plastic strain $(\hat{\varepsilon}^p_{eq})_{\max}$, displays no size influence. Then it follows that the engineering stress at fracture is not size-dependent if a local failure strain criterion is adopted. The respective engineering strain, however, decreases with specimen size.

If we assume a local failure stress criterion instead of a strain criterion, then plastic strain at fracture can decrease or increase with specimen size depending on the critical stress τ_c value used for the maximum principal Kirchhoff stress.

Repeating the above computations using the non-zero damage parameters n = 1, $a_o = 10^{-4}$, $a_1 = 10^{-4}\,\mathrm{MPa}^{-1}$ and $a_2 = 1\,\mathrm{MPa}^{-1}$, the results depicted in Fig. 3.2.1.1-5 are obtained. Concerning the size influence the aforementioned remarks are also evident in the present example. Moreover, a local failure damage criterion D_c is considered. According to literature [8,12] a value of $D_c = 0.05$ is chosen.

As shown in Fig. 3.2.1.1-6, increasing the specimen size results in smaller engineering stresses at failure, while the respective engineering strains and maximum plastic strains increase. This trend is qualitatively opposite to that experimentally observed within the LISSAC project for various non-uniform geometries.

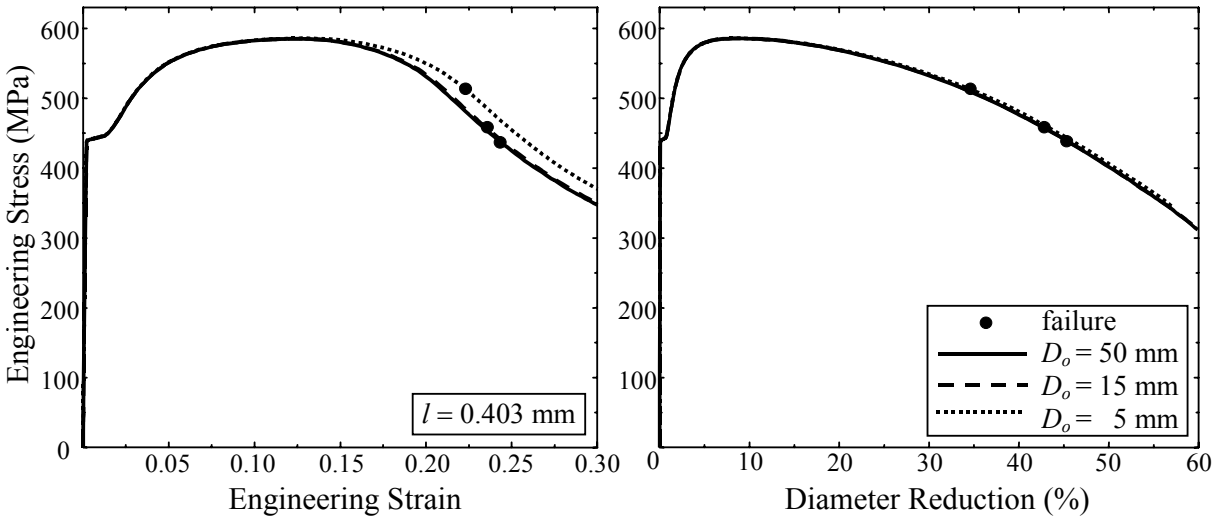

Fig. 3.2.1.1-5: Size effect on the engineering stress for geometrically similar tensile specimens with a critical damage failure criterion $D_c = 0.05$.

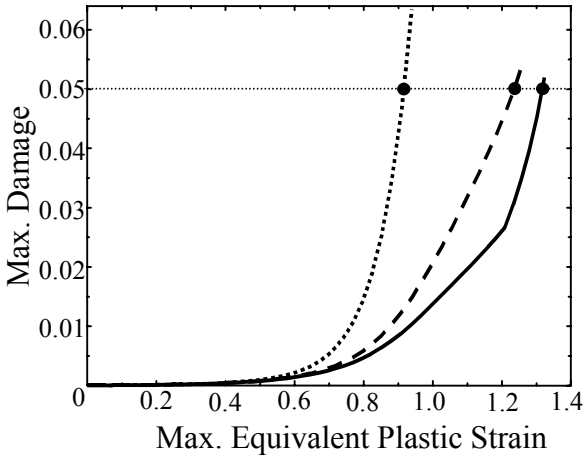

Fig. 3.2.1.1.6: Size effect on the maximum damage value for geometrically similar tensile specimens with a critical damage failure criterion $D_c = 0.05$.

Cylindrical tensile specimens with a notch

Consider a cylindrical specimen of diameter D_o and length $L = 6D_o$, which has a central semicircular notch and is subjected to tensile loading, as shown in Fig. 3.2.1.1-7.

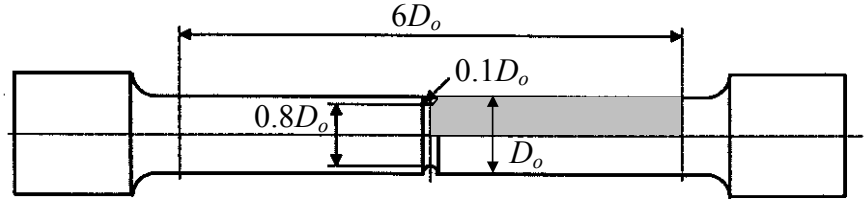

Fig. 3.2.1.1-7: Cylindrical tensile specimen with a notch.

Axisymmetric loading conditions are again assumed and thus, the 3D problem is reduced to 2D.

Analyses with and without damage inclusion are performed also for the present problem using the same values for the material parameters. Among the specimens tested experimentally in LISSAC, three geometrically similar specimens with D_o = 9, 20 and 150 mm are considered herein to study size effects. The computed results for the no damage inclusion case are depicted in Fig. 3.2.1.1-8, where the engineering stress is defined as the load over the net section area and the engineering strain equals the elongation over the specimen length. As shown, the pre-necking behaviour is hardly influenced by the specimen size due to the relatively small internal length (l//0.8D_o = 0.056 for the smallest specimen) combined with the small strain gradients (compared to those arisen in the post-necking regime). As in the case of the unnotched tensile specimens, at any engineering strain in the post-necking regime, the engineering stress decreases with specimen size. Comparison of the computed engineering stress – strain predictions with the respective experimental data reveals an overestimation of the engineering stress mainly in the post-necking regime, as illustrated in Fig. 3.2.1.1-8.

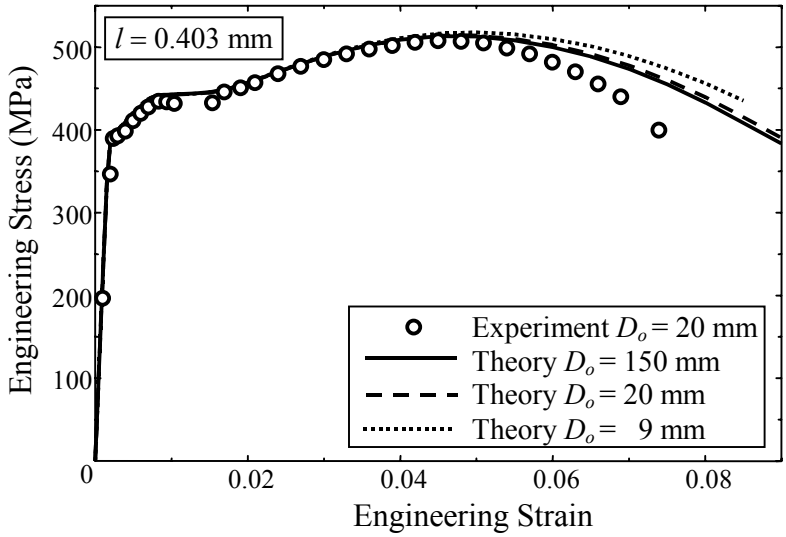

Fig. 3.2.1.1-8: Size effect on the engineering stress for geometrically similar notched specimens and comparison of the experimental results with the theoretical predictions without damage.

A local failure stress criterion or a local failure strain criterion can be adopted to account for fracture (nucleation of a crack) in the present non-damage case. The two criteria lead to qualitatively contrary size effects. In particular, plastic strain at fracture increases with specimen size when a local failure stress criterion is used, while it decreases when a local failure strain criterion is employed. The latter is in agreement with the experimental data obtained within LISSAC.

The foregoing computations are repeated for the case of damage inclusion using the same damage parameters as before. The corresponding results are depicted in Fig. 3.2.1.1-9. As observed, the aforementioned remarks concerning the non-damage case are still valid. Moreover, larger specimens have lower values of engineering stress at fracture, while all the corresponding strain measures (i.e. engineering strain, diameter reduction, notch opening increase and maximum plastic strain) increase with specimen size. As already mentioned, the latter trend is opposite to that observed experimentally in the LISSAC project.

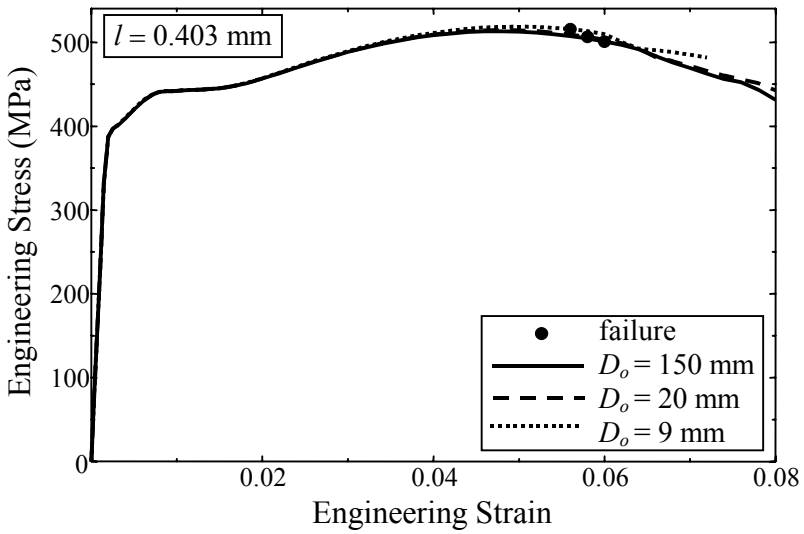

Fig. 3.2.1.1-9: Size effect on the engineering stress for geometrically similar notched specimens with a critical damage failure criterion $D_c = 0.05$.

Flat specimens with a central hole

Consider a flat specimen with a central hole, which is subjected in uniaxial tension as shown in Fig. 3.2.1.1-10.

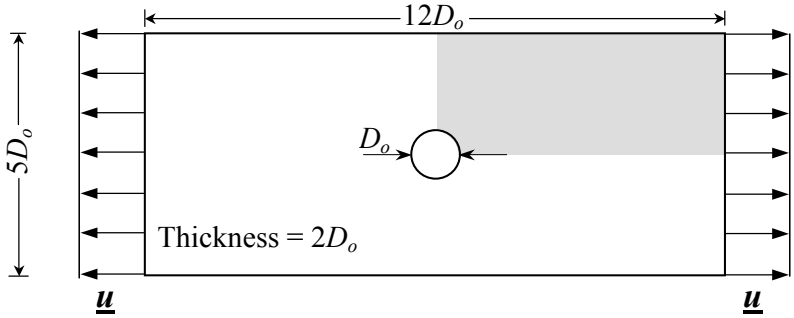

Fig. 3.2.1.1-10: Flat specimen with a central hole.

In the present case, 3D rather than 2D analysis is performed. Because of symmetry, only one eighth of the specimen is considered.

Among the specimens tested experimentally in LISSAC, three geometrically similar specimens with Do = 2, 20 and 100 mm are considered to study size effects herein. The computed results for the case of damage inclusion are depicted in Figs. 3.2.1.1-11, where material parameters are assumed identical to those used for the round bars. Also, the engineering stress is defined as the load over the net section area, the engineering strain equals the elongation over the specimen length, and the hole opening is normalized with the initial hole radius.

As in the notched specimens, the pre-necking behaviour is hardly influenced by the specimen size due to the relatively small internal length (l/2Do = 0.1 for the smallest specimen) combined with the small strain gradients (compared to those arisen in the post-necking regime). Moreover, the results for the two larger specimens are identical, i.e. the size influence vanishes. This also stems from the small internal length compared to the specimens dimensions (l/2Do = 0.01 for Do =20 mm and l/2Do = 0.002 for Do =100 mm). Nevertheless, there is a relatively evident size effect in the response of the smallest specimen in the post-necking regime. As before, at

fore, at any engineering strain in the post-necking regime, the engineering stress decreases with specimen size.

As in the case of notched tensile specimens, the assumptions of a local failure stress criterion or a local failure strain criterion lead to qualitatively contrary size effects, i.e. plastic strain at fracture increases with specimen size when a local failure stress criterion is used, while it decreases when a local failure strain is employed. As mentioned, the latter is in agreement with the experimental data obtained within LISSAC. On the other hand, when the local failure damage criterion $D_c = 0.05$, is adopted, smaller specimens have smaller maximum equivalent plastic strain at fracture. However, the respective engineering strain and hole opening increase with specimen size. The latter size influences are in agreement with the LISSAC experimental results.

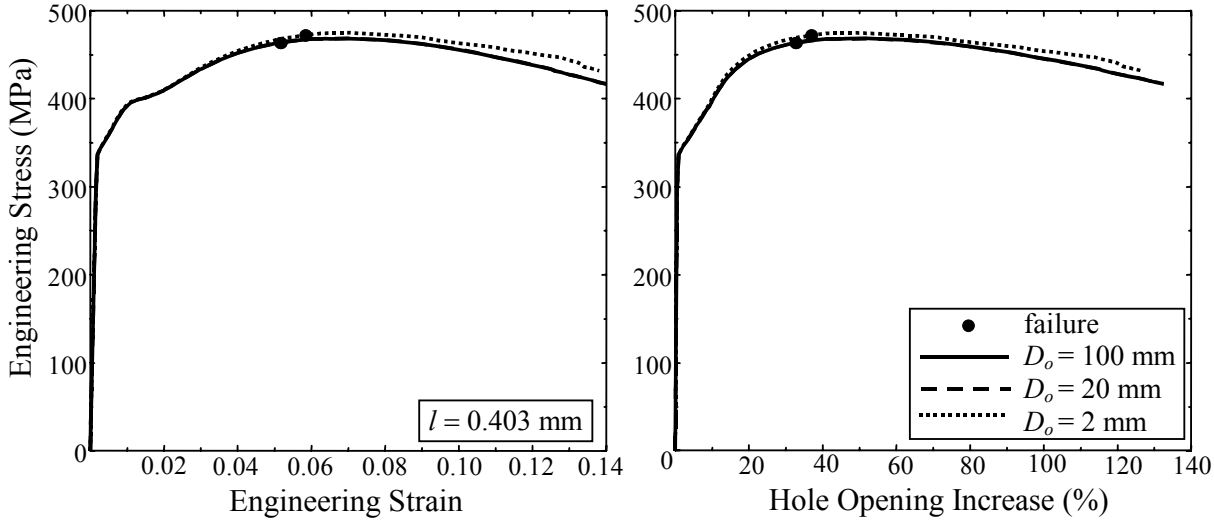

Fig. 3.2.1.1-11: Size effect on the engineering stress for geometrically similar flat specimens with a central hole using a critical damage failure criterion $D_c = 0.05$.

3.2.1.1.4 Conclusions

A flow theory of gradient plasticity enhanced with a damage mechanics model was proposed and its formulation for the solution of boundary value problems in finite deformations was developed. The element-free Galerkin method was used for the numerical implementation of this formulation.

Concerning the deformation behaviour of the simulated cylindrical unnotched specimens, the cylindrical notched specimens and the flat specimens with a central hole, the following conclusions can be drawn from these numerical investigations:

- The pre-necking behaviour is not influenced by the specimen size for unnotched tensile specimens due to the absence of strain gradients.
- The pre-necking behaviour is hardly influenced by the specimen size for notched and perforated specimens due to the relatively small internal length assumed in conjunction with the small strain gradients (compared to those arisen in the post-necking regime).

The above theoretical predictions are in qualitative agreement with the experimental results obtained in LISSAC. However, concerning the relations between

engineering stress and local strain quantities (symmetry cross-section area reduction or notch/hole opening increase), a more pronounced size effect was observed experimentally. The relatively small internal length used in the theoretical analysis could be a possible explanation for this difference. Nevertheless, the pronounced experimental size effect concerns mainly the deformation behaviour of an already cracked material, which is beyond the subject of the present work.

Concerning the failure behaviour, the following conclusions can be drawn from the aforementioned numerical investigations:

- When a local failure strain criterion is adopted, then the maximum plastic strain at fracture is not size-dependent for the unnotched specimens, while it decreases with the specimen size for notched or perforated specimens. This size effect is in agreement with the experimental trend.
- When a local failure stress criterion is adopted, then the maximum plastic strain at fracture increases with the specimen size for notched or perforated specimens, which is opposite to the experimental trend. For the unnotched specimens, the maximum plastic strain at fracture can decrease or increase with specimen size depending on the critical stress value used.
- When a local failure damage criterion $D_c = 0.05$, is adopted smaller specimens have smaller maximum equivalent plastic strains at fracture, which is contrary to the experimental trends observed in LISSAC. This difference is probably due to faster damage evolution in the smaller specimens. In particular, gradient plasticity implies that smaller specimens can sustain higher stress values, which, in collaboration with the stress-controlled damage evolution law [9], give higher damage rates.

In view of the above remarks, it is concluded that the present gradient plasticity theory can be used to interpret size effects in the deformation behaviour of the material tested in LISSAC. However, concerning size effects in failure, only a local failure strain criterion seems to give convincing predictions. A local failure damage criterion could perhaps give acceptable results if the above framework is modified by adding a plastic potential associated with damage in the yield condition, similarly to the models of Rousselier [12] or Tvergaard and Needleman. Also the inclusion of a damage or strain gradient term in the damage evolution law could possibly solve the problem.

3.2.1.2 A nonlocal damage model for elastoplastic materials based on gradient plasticity theory

Experimental and theoretical studies have shown that size effects in structure deformations and failure become significant as soon as strain gradients are high in relation to the microstructure. To give an accurate prediction for the failure of structures with high strain gradients these gradients are introduced in the constitutive equations. A detailed description is given in [1].

3.2.1.2.1 Theory

Classical continuum models suffer from pathological mesh dependence in strain-softening materials. The reason is that in this case the critical condition for localization coincides with the condition for loss of ellipticity of the governing differential equations. The difficulty of mathematical model reflects the absence of internal length scales in the governing equations.

Aifantis [2] suggested a simple form of plasticity depending on plastic strain gradients which is termed gradient plasticity theory. In this theory, the scalar variable, i.e. the Laplacian of the equivalent plastic strain is included into the usual yield condition and constitutive equation. So the difficulties exhibited by the classical plasticity can be eliminated when the material enters the softening regime. Using the gradient terms, it is possible to determine the shear band width and to perform mesh independent finite element calculations.

The simplest form of gradient plasticity is based on the gradient modification of the expression for the flow stress $\overline{\sigma} = \sigma(\overline{\varepsilon}^{p})$ to include the Laplacian of the equivalent plastic strain, i.e. $\nabla^2\overline{\varepsilon}^{p}$.

$$\sigma_y(\overline{\varepsilon}^{p}, \nabla^2\overline{\varepsilon}^{p}) = \sigma_y(\overline{\varepsilon}^{p}) - g\nabla^2\overline{\varepsilon}^{p}$$

The corresponding form of the yield equation can be written as

$$\Phi(\sigma_y(\overline{\varepsilon}^{p}, \nabla^2\overline{\varepsilon}^{p})) = \Phi(\sigma_y(\overline{\varepsilon}^{p})) - g\nabla^2\overline{\varepsilon}^{p}$$

where $\Phi(\sigma_y(\overline{\varepsilon}^{p}))$ is the classical J2 yield stress measure, $\overline{\varepsilon}^{p}$ is the equivalent plastic strain and g is a positive coefficient with the dimension of force.

If the gradient plasticity theory is used in pure bending to explain size effects and only the Laplacien of plastic strain is introduced into the flow stress, no size effect can be achieved due to $\nabla^2\overline{\varepsilon}^{p} = 0$. For this reason, in the work of size effects analysis by Aifantis, the first-order derivate , $\left|\nabla\overline{\varepsilon}^{p}\right|$, is included. Then flow stress and constitutive equation can be written as:

$$\sigma_y(\overline{\varepsilon}^{p}, \left|\nabla\overline{\varepsilon}^{p}\right|, \nabla^2\overline{\varepsilon}^{p}) = \sigma_y(\overline{\varepsilon}^{p}) + g_1\left|\nabla\overline{\varepsilon}^{p}\right| - g\nabla^2\overline{\varepsilon}^{p}$$

$$\Phi(\sigma_y(\overline{\varepsilon}^{p}, \left|\nabla\overline{\varepsilon}^{p}\right|, \nabla^2\overline{\varepsilon}^{p})) = \Phi(\sigma_y(\overline{\varepsilon}^{p})) + g_1\left|\nabla\overline{\varepsilon}^{p}\right| - g\nabla^2\overline{\varepsilon}^{p}$$

In the Gurson Tveergard Needleman (GTN) model one only considers that the material failure process is modelled by nucleation, growth and coalescence of the

micro voids. The conventional constitutive relation, which is originally suitable for the macroscopic analysis, is assumed to be valid for the matrix material in microscopic scale. It is an obvious shortcoming in the model.

Nonlocal forms of the GTN model in which the delocalization is related to the damage parameter were developed by Leblond [3], Tvergaard and Needleman [4] et al. In their work the porosity is treated nonlocally by averaging the actual porosity value in an assumed neighboring region. Ramaswamy and Aravas [5] suggested a gradient treatment of the porosity of the GTN model. In their study, effects of void diffusion, interaction and coalescence have been considered. The first and second derivatives of the porosity enter the evolution equation. Variations of the porosity are controlled by a diffusion equation. All these efforts are assuming that the material length is only related to damage development which may be certainly contradictory to the known experimental observation of size effects in plasticity.

Due to existence of voids, the strain field of the porous material is inhomogeneous. In the microscopic level the strain concentrates around the voids. According to recent knowledge, the matrix at microscopic level may have significantly different features from that at the macroscopic cases. Discussions about intrinsic material length make it necessary to introduce a material length into constitutive equation of the matrix. From the view point of gradient plasticity the strain variations may significantly change the matrix strength. In this work, we postulate the matrix strength depending on the strain field. The gradient plasticity is introduced into the matrix material to consider the micromechanisms by voids.

In the frame of gradient plasticity, the yield condition is expressed as

$$\Phi\left(q,p,f,\sigma_y\right)=\frac{q^2}{\sigma_y^2\left(\bar{\varepsilon}^p,\nabla^2\bar{\varepsilon}^p\right)}+2q_1 f\cosh\left(\frac{3q_2 p}{2\sigma_y\left(\bar{\varepsilon}^p,\nabla^2\bar{\varepsilon}^p\right)}\right)-\left(1+q_1^2 f^2\right)=0$$

In the equation above the actual stress of matrix, $\sigma_y\left(\bar{\varepsilon}^p,\nabla^2\bar{\varepsilon}^p\right)$, is a function of gradients of plastic strains, represented by $\nabla^2\bar{\varepsilon}^p$. The first order strain gradient $\left|\nabla\bar{\varepsilon}^p\right|$ is omitted, it cannot avoid the mesh dependence during damage evolution. If material failure is accompanied with high plastic strain gradients, e.g. near a crack tip, the matrix will be strengthened locally to prevent strain localization.

3.2.1.2.2 Results

Due to a rearrangement of partners no results for LISSAC are presented in this chapter. However the model is used by another partner and the results are presented in chapter 3.2.3.2.

3.2.1.2.3 Conclusions

In this work, a new algorithm of computational gradient plasticity on finite strain assumptions was formulated. Based on the new algorithm of gradient plasticity, the formulation and finite element implementation of a micro mechanical damage model by implementing gradient plasticity theory into GTN damage model was presented.

3.2.1.3 Micromorphic deformation and damage model

Constitutive equations for a micromorphic model describing size effects in elasticity are derived [1]. Also a micromorphic plasticity theory is used to model size phenomena [2, 3] in the plasticity region. The models were programmed and implemented in the finite element code ABAQUS. For plasticity only isotropic hardening is incorporated, while softening in the material response is modelled by using a scalar valued internal variable.

3.2.1.3.1 Theory

Elasticity

For describing size effects in elasticity constitutive equations for a micromorphic continua are derived:

$$\begin{aligned}\sigma_{ij} &= E_{ijpq}\varepsilon_{pq} + B_{ijpq}\beta_{pq}\\ \tau_{ij} &= A_{ijpq}\beta_{pq} + B_{pqij}\varepsilon_{pq}\\ M_{ijk} &= C_{ijkpqr}K_{pqr}\end{aligned}$$

In these equations, σ is the classical stress tensor, τ is an additional stress tensor depending on the microstructure and M represents the couple stress tensor. ε, β and K are the linearized strain and curvature tensors.

In case of isotropy the theory depends on eighteen independent coefficients. λ and μ are the classical Lamé-constants, α measures the non-symmetry of the elasticity tensor **E**. The elasticity tensors **A**, **B** of order 4 depend on 2 and the elasticity tensor **C** of order 6 depends on 11 material parameters:

$$\begin{aligned}E_{ijpq} &= \lambda\delta_{ij}\delta_{pq} + (\mu+\alpha)\delta_{ip}\delta_{jq} + (\mu-\alpha)\delta_{iq}\delta_{jp}\\ A_{ijpq} &= a_1\delta_{ij}\delta_{pq} + a_2(\delta_{ip}\delta_{jq} + \delta_{iq}\delta_{jp})\\ C_{ijkpqr} &= c_1\delta_{ij}\delta_{kp}\delta_{qr} + c_2\delta_{ij}\delta_{kq}\delta_{rp} + c_3\delta_{ij}\delta_{kr}\delta_{pq} + c_4\delta_{jk}\delta_{ip}\delta_{qr} + c_5\delta_{jk}\delta_{iq}\delta_{pr} +\\ &\quad + c_1\delta_{jk}\delta_{ir}\delta_{pq} + c_5\delta_{ik}\delta_{jp}\delta_{qr} + c_6\delta_{ki}\delta_{jq}\delta_{rp} + c_2\delta_{ki}\delta_{jr}\delta_{pq} + c_7\delta_{ip}\delta_{jq}\delta_{kr} +\\ &\quad + c_8\delta_{jp}\delta_{kq}\delta_{ir} + c_8\delta_{kp}\delta_{iq}\delta_{jr} + c_9\delta_{ip}\delta_{jr}\delta_{kq} + c_{10}\delta_{jp}\delta_{kr}\delta_{iq} + c_{11}\delta_{kp}\delta_{ir}\delta_{jq} +\\ B_{ijpq} &= b_1\delta_{ij}\delta_{pq} + b_2(\delta_{ip}\delta_{jq} + \delta_{iq}\delta_{jp})\end{aligned}$$

Plasticity

For describing size effects in plasticity a micromorphic model with scalar-valued damage is developed. The plasticity theory will be restricted to J_2-flow. Accordingly, the yield function can be written as

$$f = \frac{1}{1-d}\sqrt{p_1\boldsymbol{\sigma}^D\cdot\boldsymbol{\sigma}^D + p_2\boldsymbol{\sigma}^D\cdot(\boldsymbol{\sigma}^D)^T + q\boldsymbol{\tau}^D\cdot\boldsymbol{\tau}^D + r_7\mathbf{M}\cdot\mathbf{M}} - \frac{k}{1-d}$$

where *k* denotes the yield stress and *d* is the variable describing damage effects. σ^D and τ^D are the deviatoric stress tensors, M is the couple stress tensor and p_1, p_2, q, r_7 are material parameters. We set

$$p_1 = \frac{3}{2}$$
$$p_2 = q = 0$$

to obtain comparable results with the classical theory. The parameter r_7 is governing the nonlocality in the constitutive behaviour.

The yield stress k is defined by:

$$k = c(r + r_0) + k_0$$

c and k_0 are material parameters, while r_0 represents an initial internal strain.

A general evolution equation describing ductile damage is given by [4]:

$$\dot{d} = \alpha_0 \dot{s} + (\alpha_1 + \alpha_2 d)\frac{(-\Omega)^n}{(1-d)^q}\dot{s} \geq 0$$

with α_0, α_1, α_2, n, q being nonnegative material parameters. For the special case

$\alpha_1 = \alpha_2 = q = 0$ and $n = 1$

we obtain [5]:

$$\dot{d} = -\alpha_1 \Omega \dot{s}$$

Here, the influence of the triaxiality ratio on the damage evolution is taken into account by Ω [4]:

$\Omega := \Omega_e + \Omega_p$.

$\Omega_e := -\frac{1}{2}E_{ijpq}\varepsilon_{ij}\varepsilon_{pq} - \frac{1}{2}A_{ijpq}\beta_{ij}\beta_{pq} - \frac{1}{2}B_{ijkpqr}K_{ijk}K_{pqr} - \frac{1}{2}C_{ijpq}\varepsilon_{ij}\beta_{pq}$.

$\Omega_p := -cr^2$

3.2.1.3.2 Determination of material depending parameters

The theory includes 26 material parameters. Parameter studies by using FE calculations suggest that only 8 parameters suffice to model general size-effects (Tab. 3.2.1.3.1).

	parameter	dimension	
elasticity	λ	[N/mm²]	classical elasticity constants
	μ	[N/mm²]	(Lamé constants)
	α	[N/mm²]	non-symmetry of the elasticity tensor **E**
	c_7	[N]	nonlocal elasticity parameter
plasticity	b	[-]	isotropic hardening
	c	[N/mm²]	(b = 17 N/mm², c = 4100 N/mm²)
	r_7	[1/mm²]	additional parameter of yield function
damage	α_1	[-]	scalar-valued damage (α_1= 0.1)

Tab. 3.2.1.3.1: Material parameters

Due to the lack of methods for determining the non classical material parameters the needed constants can not be adapted to LISSAC material. The influence of the parameters will be discussed in the following sections.

3.2.1.3.3 Results

The LISSAC specimen (Fig. 3.2.1.3-1) has been modelled in two dimensions assuming plane strain.

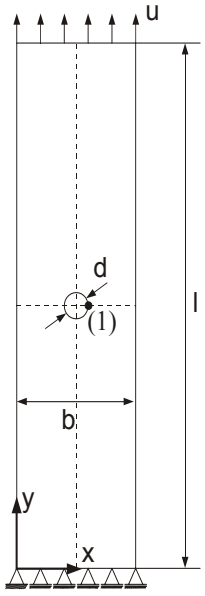

	parameter *n* [-]	length *l* [mm]	diameter *d* [mm]	width *b* [mm]
specimen 1	1	6	0,5	2,5
specimen 4	4	24	2	10
specimen 20	20	120	10	50
specimen 200	200	1200	100	500

Fig. 3.2.1.3-1: Flat specimen with round hole

Size effects in elasticity

The non classical material parameters of the theory α and c_7 are unknown and their identification is by no means straightforward from experiment. Therefore, at the present stage parameter studies are carried out in order to study the influence of α and c_7 .The first material constant (α) measures the antisymmetric part of the coupling between shear stress and strain. Therefore a small value compared to the Lamé-constant μ is reasonable.

The second material constant (c_7) associates the curvatures **K** (unit: 1 per length) with couple stresses **M** (unit: force per length). Therefore, c_7 has the dimension of a force. The ratio of this parameter to e. g. μ could be interpreted as the square of an intrinsic length l_c:

$$l_c := \sqrt{\frac{c_7}{\mu}}$$

This length is a material property on which the influence of couple stresses depends strongly. If the ratio of the smallest dimension of a body to l_c is large, the theory shows that the effect of couple stresses is negligible. If there are strain gradients and a dimension of a body approaches l_c, couple stresses may produce effects of appreciable magnitude.

The tension test specimen was analysed for a series of parameter variations and with different dimensions shown in Tab. 3.2.1.3.1. A measure for the size effect is the stress concentration, which is defined as maximum stress at the notch σ_y compared to the stress σ_0 of a smooth specimen.

Both parameters (α and c_7) influence the stress concentration around the circular hole of a tension-test specimen (Fig. 3.2.1.3-1).

The classical solution of our example is $\frac{\sigma_y}{\sigma_0}$=3.14 (Fig. 3.2.1.3-2). In this case, σ_y represents the stress at point (1) (Fig. 3.2.1.3-1) in y-direction of the specimen with hole and σ_0 is the stress of a smooth specimen. As $\frac{\alpha}{\mu}$ becomes large, the stress concentration factor approaches a lower limit of $\frac{\sigma_y}{\sigma_0}$=1.9.

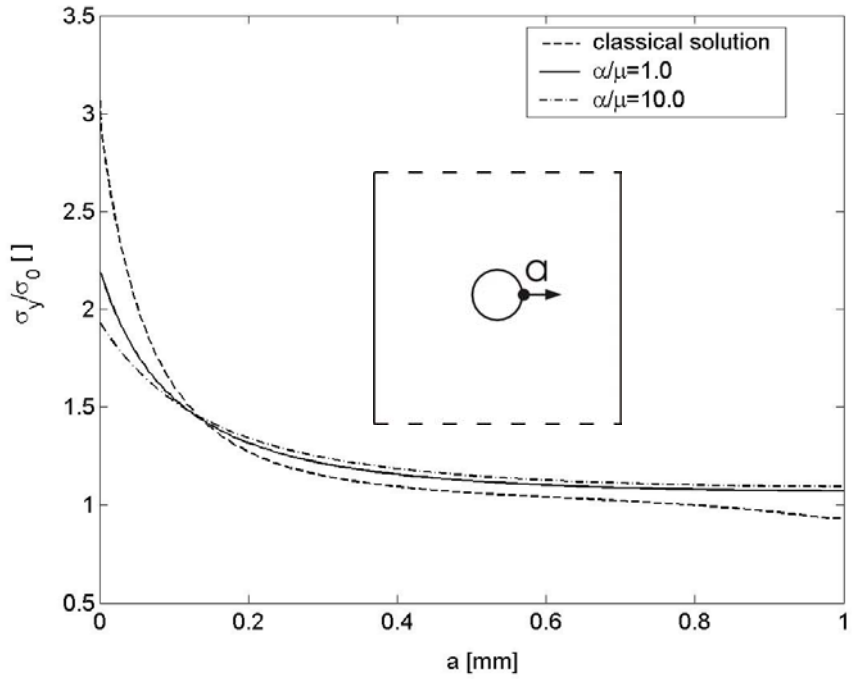

Fig. 3.2.1.3-2: Stress concentration factor versus notch distance a ($c_7 = 0.1 \cdot \mu$ mm²).

A parameter study is carried out to illustrate the influence of α and c_7 on the stress concentration factor $\frac{\sigma_y}{\sigma_0}$ of the tension test specimen. Parameter α parametrically was chosen as $\mu/100, \mu/10, \mu$ and $\mu \cdot 10$. Parameter c_7 , which has a dimension of area compared to μ was varied within the range of 8 decades. The results show that the stress concentration factor decreases strongly with increasing α (depending on $\frac{c_7}{\mu}$). No size effects are measured if α is very small.

In a second study the specimen was analysed for a series of parameter variations and with four different dimensions, which differ by factors 4, 20 and 200 with respect to the first specimen (Fig. 3.2.1.3-1). It can be demonstrated that increasing the overall dimensions by a factor n results in the same change in stress concentration as changing the material parameter c_7 by a factor n². This proves that the theory is able to predict size-effects in the elastic range.

In a final example the physical dimensions of the specimen are varied by a factor *n*=0.0001, 0.01, …, 400, 10000. A characteristical dimension l_m of the specimen is introduced as:

$$l_m := 2d = 0.4b$$

The internal length is chosen as:

$$l_c := 0.31623\text{mm})$$

It can be observed that the internal length is a material property on which the influence of couple stresses depends strongly. If the ratio of the characteristic dimension of a specimen l_m is large compared to l_c the nonlocal effects are negligible. If

the dimension of the specimen approaches the internal length, couple stresses produce effects of appreciable magnitude.
These parameter studies indicate that the results approach asymptotically the classical limit for small values of α and c_7. If c_7 is very large, the results tend asymptotically to a second limit.

A major influence of the parameter α on the stress concentration factor is observed. If α is very small compared to μ, the size effect is limited to a few percent. In case of $\alpha/\mu = 10$ the size effect is up to 35%.

Size-effect in plasticity with scalar-valued damage

The parameter is r_7 governing nonlocality in the constitutive behaviour. The effect of parameter r_7 in the yield function is illustrated in Fig. 3.2.1.3-3, while Fig. 3.2.1.3-4 displays the distribution of stress σ_y at point (1) (see Fig. 3.2.1.3-1) as a function of the global strain $\Delta l/l$.

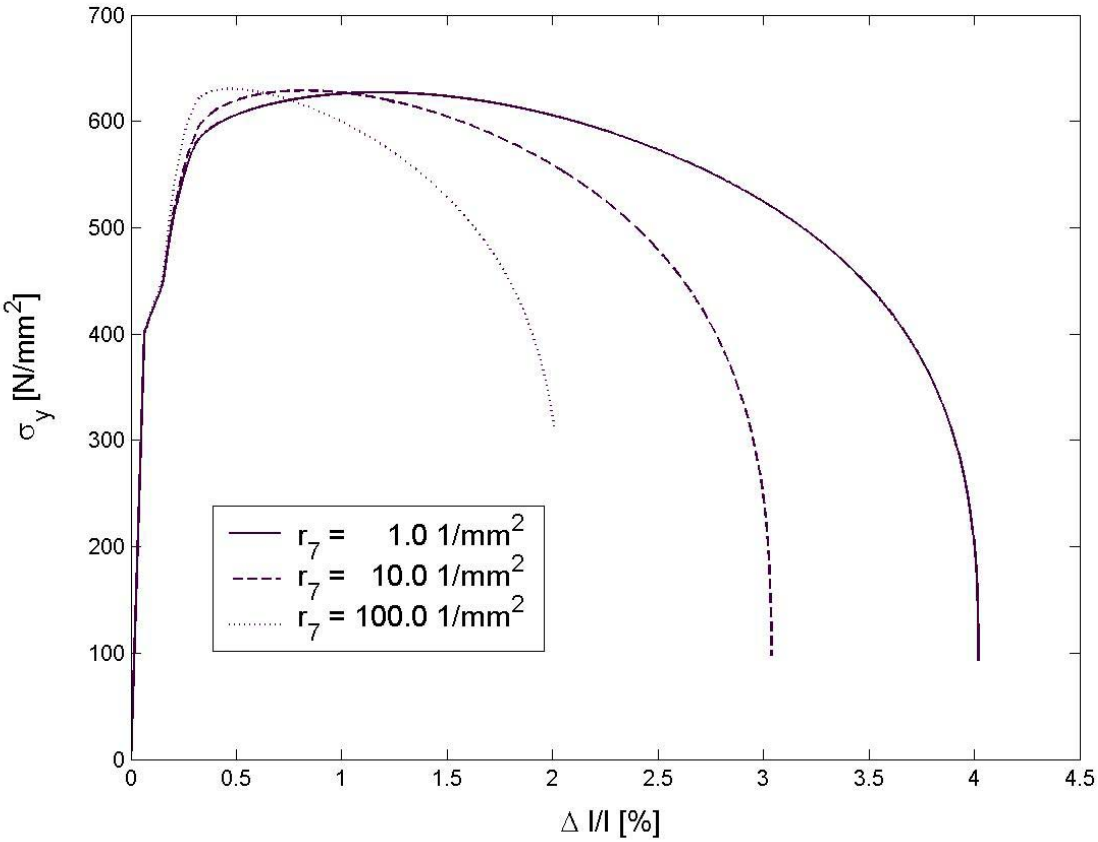

Fig. 3.2.1.3-3: σ_y at point (1) versus global strain - variation of r_7 (plasticity with scalar-valued damage)

The maximum stress of all specimen is nearly identical but the failure strain decreases by increasing the specimen's size.

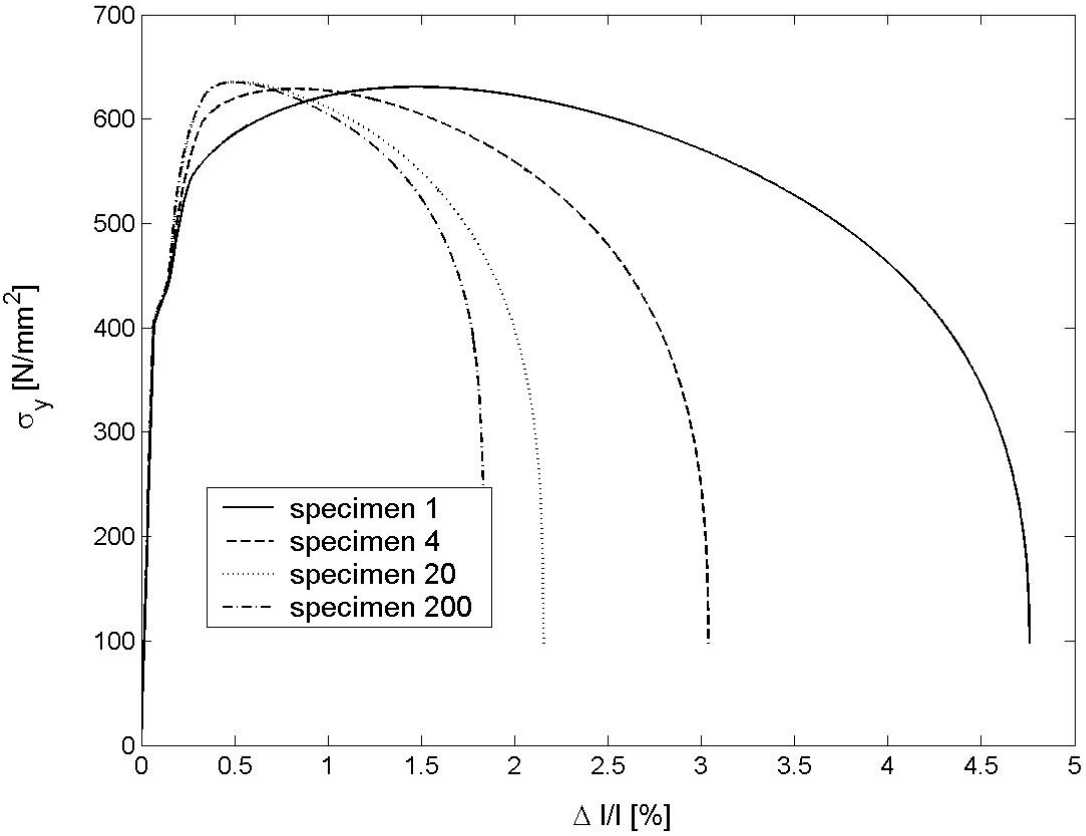

Fig. 3.2.1.3-4: σ_y at point (1) versus global strain - variation of the specimen's size (plasticity with scalar-valued damage)

3.2.1.3.4 Conclusions

The problem of size-effect has been analysed in this contribution with a micromorphic theory which includes scalar-valued damage and a material related length l_c. Concerning the theoretical derivations and the results from the elastic and plastic simulations the following conclusions can be drawn:

- The non classical material parameters of the theory are unknown and their identification is by no means straightforward from experiment. Due to this problem the parameters cannot be determined for the LISSAC material and only qualitatively results can be achieved.
- The micromorphic theories for elasticity are able to predict size effects in dependence of the choosen material parameters. The parameter studies indicate that the results approach asymptotically the classical solution for small values of α and c_7. If c_7 is very large, the results tend asymptotically to a second limit.
- The simulations with the micromorphic elastic plastic theory with scalar valued damage predict also size effects. Again the size effect depends on the selection of the material parameters. Due to the lack of the LISSAC material parameters a reliable statement if the theory is able to predict the experimentally observed size effect can not be made.

In this contribution some promising theories are developed and implemented in a finit element program. Future works must show if the model is able to predict quantitatively the experimental findings.

3.2.2 Stochastic models

In general the deformation and failure behaviour of specimens and components is not of a deterministic nature. To describe the observed experimental behaviour the statistical scatter should be taken into account. Therefore one objective of LISSAC is to analyse stochastic models for their capability to describe size and scatter effects in deformation and failure.

3.2.2.1 Stochastic material damage model

Here a modified Lemaitre continuum damage model (CDM) is applied and evaluated [1]. More information about stochastic material modelling may be found in [2, 3].

3.2.2.1.1 Theory

A Lemaitre damage model was modified in a way that the deterministic flow function and consistency condition were replaced by so-called Brownian processes [4]. The expectation values for the flow function and consistency condition remain so invariably compared with their deterministic counterparts. Due to the non-linearity of the material law however, the expectation values for the plastic strains and for the damage deviate from the deterministic sizes.

The used flow function Φ including damage and a stochastic term is defined as follows:

$$\Phi = \frac{\sigma_{eq}}{1-f} - r - \sigma_{yield} - \int_0^t \gamma(t')\,dB_{t'} = 0$$

Here σ_{yield} gives the yield stress and r represents the isotropic hardening of the material. The integral (Ito integral) defines the stochastic disturbance.

The constitutive equation for the evolution of the damage parameter f is given by the following equation:

$$\dot{f} = c\,\dot{\varepsilon}_{eq}^{pl}$$

were c is a material constant.

In order to avoid a second spatial integration, the background field is simulated by a weighted averaging of a spatially uncorrelated field Z_{lokal} (correlation length = 0) and a spatially completely correlated field Z_{global} (correlation length = ∞). The weighting parameter is calculated from the constant factor γ and from $L_{element}/L_C$ were $L_{element}$ is the characteristic lengths of the current finite element and L_C the internal material length. The actual damage is represented by the parameter f. Thus the Ito integral for the stochastic addition is computed as follows:

$$Z_{t+\Delta t} = Z_t + \frac{\gamma}{\frac{L_{element}}{L_c} - 1}\left\{\left[\left(\frac{L_{element}}{L_c}\right)^f - 1\right]Z_{lokal} + \left[\frac{L_{element}}{L_c} - \left(\frac{L_{element}}{L_c}\right)^f\right]Z_{global}\right\}$$

This stochastically extended Lemaitre model has been directly implemented as a material model in a standard finite element program. Thus the practical capabilities of stochastic CDMs for predicting size effects in failure and scatter has been evaluated.

3.2.2.1.2 Determination of material depending parameters

The five material parameters, the yield limit, the hardening/softening parameter, the stochastic weight and the internal material length, have been roughly tuned to the reference material curve, by an empirical procedure. The stochastic weight is a stress, which may be derived from the scatter observed for the initial yield stress. It amounts to about 2 %. The internal material length is simply set to the dominating microscopic length, the distance of inclusions in the virgin material. It is assumed to be about 0.1 mm. The other parameters are set by a manual try and correct procedure.

3.2.2.1.3 Results

The size effect evaluations have had to be performed for specimen geometries with rather non-homogeneous stress/strain fields. The specimen family of flat specimens with a hole has been chosen for this purpose. However, accounting for the expensive computational efforts a reduced special grid has been developed (as shown in Fig. 3.2.2.1-1.

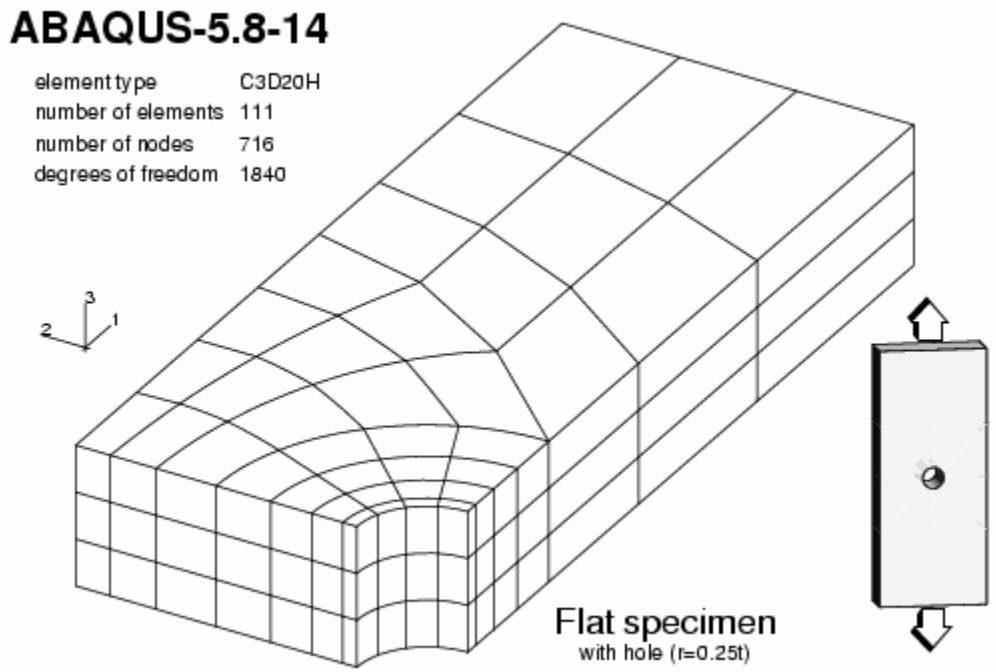

Fig. 3.2.2.1-1: Special finite element grid for the flat specimen with hole to apply the stochastic model

The results for three different specimen sizes are depicted in Fig. 3.2.2.1-2. For simplicity the different sizes are modelled by changing the internal length instead of adapting the mesh size. To have a pronounced size effect, the stochastic weight has been set to a relatively high value. However, the results do not show a systematic

size dependency. Rather the scatter dominates. Adapting the stochastic weight to a more realistic value will even decrease the systematic influence. This will result in a situation, where the large numerical errors induced by the weakening of the convergence criteria will deteriorate the results.

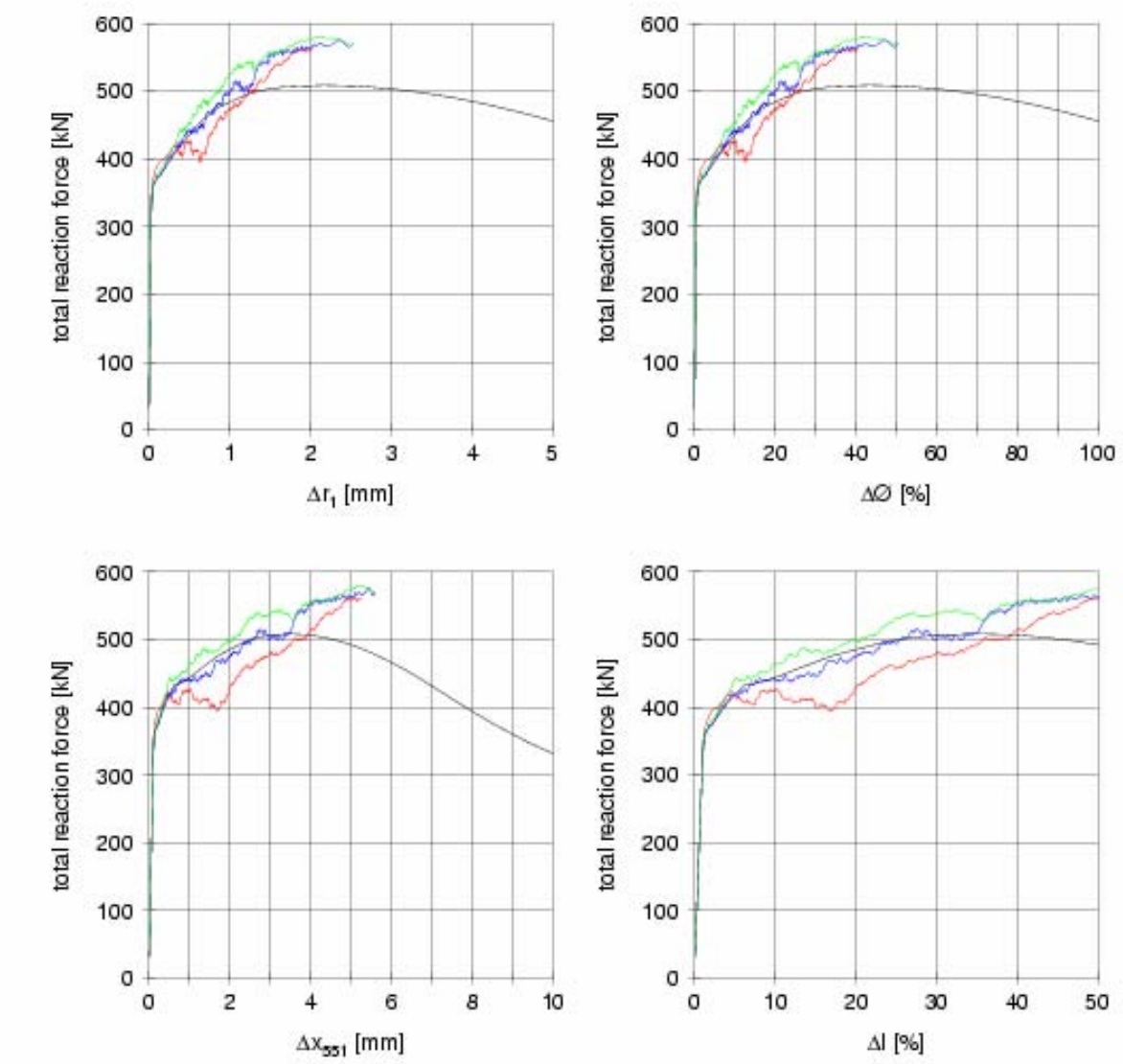

Fig. 3.2.2.1-2: Results for different sizes of flat specimens with holes;
black: deterministic
blue: 0.2 mm thickness of the specimen
red: 20 mm thickness of the specimen
green: 200 mm thickness of the specimen

To evaluate the influence of the intentionally introduced stochastic scatter, repeated calculations were done for the middle size (20 mm thickness). The results are summarized in the force/displacement diagram, Fig. 3.2.2.1-3.

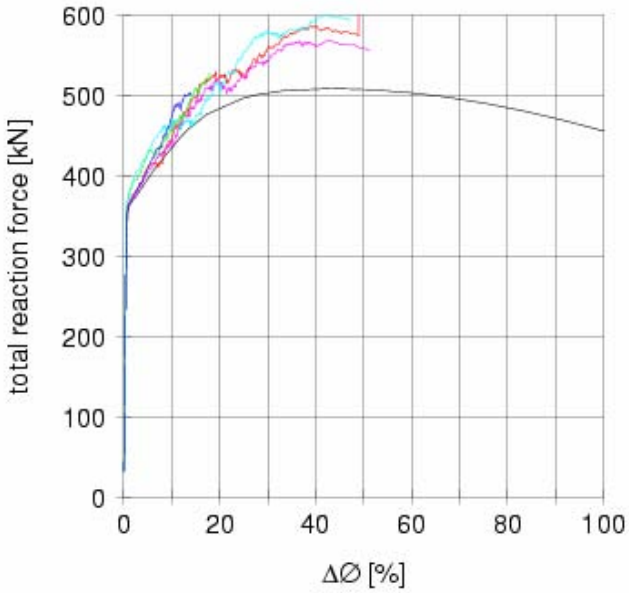

Fig. 3.2.2.1-3: Comparison of repeated calculations for the flat specimen with hole, 20 mm thickness

The comparison of these results with the results for the different specimen sizes demonstrates the dominating influence of the scatter hiding possible small systematic size effect. However one can conclude that large size effects can hardly be expected from this stochastic model. The comparison also indicates, that the equivalence of integration in time and space does not allow to derive expectation values from a reasonable small number of repeated calculations.

3.2.2.1.4 Conclusions

The stochastically extended Lemaitre model has been directly implemented as a material model in a standard finite element program. Thus the practical capabilities of stochastic CDM for predicting size effects in failure and scatter have been evaluated. The simulations done within this task lead to the following conclusions:

- The model is able to predict a scattering effect.

- The proposed model is not suitable for predicting size effects because of the dominating influence of the scatter hiding any systematic size effect. This is partly due to some restrictions of the straightforward implementation:
  - The simple weights had to be replaced by a more non-linear influence function for the stochastic background field.
  - Commercially available finite element codes do not allow tuning the integration scheme to improve the implementation deficiencies. Proper functioning would require an expensive specific finite element code development.

- However, the essential of the stochastic approach is that the physical mechanism behind the size effect in failure obtained in the experimental programme can hardly be explained by stochastic phenomena. It seems to be of a different nature.

3.2.2.2 Elastic-plastic behaviour of polycrystalline aggregates with stochastic arrangement of grains

The elastic-plastic behaviour of polycrystalline aggregates with stochastic arrangement of grains was simulated using a computational approach, which combines the most important mesoscale features and compatibility with conventional continuum mechanics. A detailed description is given in [1].

3.2.2.2.1 Theory

The main idea of the used approach to model elastic plastic behaviour of polycrystalline aggregates was to divide the continuum (e.g., polycrystalline aggregate) into a set of sub-continua – grains. Each grain was simulated as a randomly oriented anisotropic monocrystal. The overall behaviour of the aggregate is then sought through the combined response of the randomly shaped and oriented grains.

The model covers the following main phases of the deformation: (1) elastic deformation; (2) rate-independent plastic deformation (at low temperatures); and (3) potential for generalization towards rate-dependent plasticity (creep) and initialization of microcracks at the inclusions/voids. The analysis was limited to 2D models.

An overview of the constitutive model [2,3] used to obtain results is described in this section. The basic idea of the constitutive model is as follows:

- The random grain structure (in a plane) is modeled with Voronoi tessellation.
- Each grain is assumed to be anisotropically elastic with random orientation of crystal lattice.
- Plasticity model assumes plastic deformation by simple shear on the specified set of slip planes. The slip planes are essentially defined by the random orientations of crystal lattice, which differ among the grains.

Voronoi Tessellation

The concept of Voronoi tessellation has recently been extensively used in materials science, especially to model random microstructures like aggregates of grains in polycrystals, patterns of intergranular cracks and composites. A Voronoi tessellation represents a cell structure constructed from a Poisson point process by introducing planar cell walls perpendicular to lines connecting neighboring points.

Elasticity

The LISSAC material shows a body-centered cubic crystal (α-Fe) with rather pronounced orthotropic elasticity. Each monocrystal (grain) is assumed to behave as continuum. Constitutive relations in linear elasticity are given by the generalized Hooke law:

$$\sigma_{ij} = C_{ijkl} \cdot \varepsilon_{kl} .$$

σ_{ij} represents the second rank stress tensor, C_{ijkl} the fourth rank stiffness tensor and ε_{ij} the strain tensor. The inverse of the stiffness tensor is called compliance tensor D_{ijkl} and is defined as:

$$\varepsilon_{ij} = D_{ijkl} \cdot \sigma_{kl} .$$

The elastic properties (e.g., stiffness and compliance tensor) of the polycrystalline aggregate are completely defined by the properties of the monocrystals and the

interaction between the monocrystals. The standard procedure for the estimation of the overall macroscopic behaviour of interacting monocrystals is to average the stress and strain tensors over all material directions and over the volume [4].

Macroscopic stress $<\sigma_{ij}>$ and strain tensors $<\varepsilon_{kl}>$ may be used to estimate the macroscopic stiffness C^*_{ijkl} or macroscopic compliance tensor D^*_{ijkl}:

$$\left\langle \sigma_{ij} \right\rangle = C^*_{ijkl} \left\langle \varepsilon_{kl} \right\rangle, \ \left\langle \varepsilon_{kl} \right\rangle = D^*_{ijkl} \left\langle \sigma_{ij} \right\rangle .$$

Crystal plasticity

Assumption of crystal plasticity is that plastic deformation is a result of crystalline slip only. It is assumed that crystalline slip is driven by resolved shear stress $\tau^{(\alpha)}$ [5] :

$$\tau^{(\alpha)} = m_i^{(\alpha)} \cdot \sigma_{ij} \cdot s_j^{(\alpha)},$$

where the α-th slip system is defined by a combination of slip plane (determined by normal $m_i^{(\alpha)}$) and slip direction ($s_j^{(\alpha)}$) of the crystal lattice. Body-centered cubic crystal lattice has three families of slip planes: {110}, {112}, and {123} and one family of slip directions: <111>. This leads to 48 possible slip systems. Stress rate can be defined as:

$$\dot{\sigma}_{ij} = C_{ijkl} \cdot \left(\dot{\varepsilon}_{kl} - \dot{\varepsilon}^p_{kl} \right) = C_{ijkl} \cdot \left(\dot{\varepsilon}_{kl} - \sum_\alpha \frac{1}{2} \dot{\gamma}^{(\alpha)} \left(s_i^{(\alpha)} m_j^{(\alpha)} + s_j^{(\alpha)} m_i^{(\alpha)} \right) \right).$$

Rate-independent plasticity may be treated as the limit of the rate-dependent visco-plasticity [5]. The slipping rate $\dot{\gamma}^{(\alpha)}$ of the α-th slip system is determined by the corresponding resolved shear stress $\tau^{(\alpha)}$ as:

$$\dot{\gamma}^{(\alpha)} = \dot{a}^{(\alpha)} \left(\frac{\tau^{(\alpha)}}{g^{(\alpha)}} \right) \left(\left| \frac{\tau^{(\alpha)}}{g^{(\alpha)}} \right| \right)^{n-1},$$

where $\dot{a}^{(\alpha)}$ is reference strain rate, n the strain rate sensitivity parameter and $g^{(\alpha)}$ the current strain hardened state of the crystal. In the limit as n approaches infinity this power law approaches that of a rate-independent material. The current strain hardened state $g^{(\alpha)}$ can be derived from:

$$\dot{g}^{(\alpha)} = \sum_\beta h_{\alpha\beta} \dot{\gamma}^{(\beta)},$$

where $h_{\alpha\beta}$ are the slip hardening moduli. More authors dealt with hardening moduli (e.g., [5,6]), with all of them basing their work on empirical models. Pierce et al. and Asaro [6] hardening law is used in our research. Self- (index $_{\alpha\alpha}$) and latent-hardening moduli ($_{\alpha\beta}$) are defined as:

$$h_{\alpha\alpha} = h(\gamma) = h_0 \, \mathrm{sech}^2 \left| \frac{h_0 \gamma}{\tau_S - \tau_0} \right| \text{ and } h_{\alpha\beta} = q h(\gamma), \ (\alpha \neq \beta),$$

where h_0 is the initial hardening modulus, τ_0 the yield stress, which equals the initial value of current strength $g^{(\alpha)}(0)$, τ_S the break-through stress where large plastic flow initiates, γ the cumulative slip and q is the hardening factor.

Approximation of representative volume element (RVE) size

Geometrical similar specimens, which are larger than RVE, will all have the same macroscopic response, regardless their size. The size effect on macroscopic level therefore cannot be observed [7]. On the other hand, specimens smaller than RVE will show size effect. For a polycrystalline aggregate smaller then RVE the inverse macroscopic compliance tensor is not necessarily equal to the macroscopic stiffness tensor:

$$C^{*}_{ijkl} \neq \left(D^{*}_{ijkl}\right)^{-1}.$$

A condition when RVE size is achieved can be defined as [4]:

$$C^{*}_{ijkl} \cong \left(D^{*}_{ijkl}\right)^{-1}. \quad \text{or} \quad \left\langle \sigma_{eq_s} \right\rangle \cong \left\langle \sigma_{eq_d} \right\rangle. \qquad (3.2.2.2.1)$$

where indexes $_s$ and $_d$ denote stress and displacement driven boundary conditions, respectively. A relation between macroscopic equivalent stresses for both boundary conditions for a polycrystalline aggregate smaller than RVE can be written as [8]:

$$\frac{\left\langle \sigma_{eq_s} \right\rangle}{\left\langle \sigma_{eq_d} \right\rangle} = 1 + O\left(i/i_{RVE}\right), \quad (3.2.2.2.2)$$

where i_{RVE} represents the number of grains in RVE and i is the number of grains in polycrystalline aggregate smaller than the RVE. A RVE for this research is assumed to be achieved, when residuum O is smaller than 1% [9].

Correlation length

The required numerical effort could in principle be reduced if the essential inhomogenities are identified and appropriately transferred to the macroscopic models. A frequently used and promising method is to calculate the domain of influence of crystal grains [10]. The correlation length is one of the criteria for estimating statistical dependency of stress field in certain direction and enables one to estimate the domain of influence of the individual crystal grain.

The correlation length in our research is calculated from the equivalent stress field, which is determined for every Gaussian integration point of the finite element. Since stress is a 2-D variable, the vector of data for the correlation length calculation has to be extracted. The correlation length is calculated for the selected direction at the calculating point, with the length of the vector determined by the search radius.

By limiting the length of the vector of data, the information contained in the vector is limited to the search radius. Consequently the autocorrelation, covariance function and the correlation length calculated from this vector all give information on the local search radius. If the search radius is very small, the amount of information contained in the data vector could be too small for a meaningful estimation of the autocorrelation (covariance) function. On the other hand, if the search radius is large, the local nature of the calculated autocorrelation function is lost. The search radius is

therefore a compromise between these two aspects. In the presented work two different search radiuses were used, corresponding to twice the average crystal grain size (case a) and average crystal grain size (case b).

Current limitations

Currently available computational capabilities suggest limitation to 2-D analysis. The size of polycrystalline aggregates used in analysis is quite small compared to the thickness of specimen used in tensile tests. Plane strain assumption was therefore used in analyses.

The main idea followed in this report is essentially fitting a discontinuous random media into the framework of a continuum-based numerical analysis. The main assumptions are:

- the domain of the grain is adequately described as continuum and
- the discontinuous behaviour is completely assigned to the grain boundaries.

Nevertheless, the inherent conflict of continuum assumptions applied to a discontinuous random media may become very important at the boundaries of computational domain. The solutions built in the finite element software would, assuming the continuum, tend to describe either repeatable structures (e.g., symmetry, prescribed displacements in stress analysis) or free surfaces (e.g., traction in stress analysis).

It is however to be noted that the difference is levelling out with increased number of analyzed grains. Therefore, the continuum-based boundary conditions can be safely applied to a computational domain, which is isotropic at least in a statistical sense [11].

3.2.2.2.2 Determination of material depending parameters

The microstructure of the investigated pressure vessel steel (22NiMoCr3-7) is, at least in the broad sense, characterized as follows:

- Bainitic microstructure, based on α-Fe with body centered cubic (b.c.c.) crystals. α-Fe crystal cell is about 2.48 10^{-10} m long. Its volume is about 1.53 10^{-29} m^3 [12].
- Average grain size is in the order of 23 µm (0.023 mm). It therefore contains in the order of 10^{17} crystal cells and in the order of 10^4 dislocations (assuming no work hardening and average distance between dislocations in the order of 10^{-7} m [13,14])
- Average sizes of inclusions are between 5 and 10 µm with average distance between them of approximately 500 µm [14].

Material parameters for elasticity are obtained from the literature for α-Fe for body-centered cubic crystal lattice. It is assumed that small amounts of alloying elements do not change the elastic stiffness/compliance of a crystal grain significantly. The nonzero components of the stiffness tensor are c_{iiii} = 230 GPa, c_{iijj} = 135 GPa and c_{ijij} = 117 GPa.

Material parameters for plasticity also are obtained from literature for rate-independent crystal plasticity (e.g., [7]) and from results of simple tensile tests of pressure vessel steel 22NiMoCr37 [15]. The following values were used: the strain rate sensitivity parameter n = 50, the reference strain rate $\dot{a}^{(\alpha)}$ = 0.001 s^{-1}, the initial hardening modulus h_0 = 70 MPa, the break-through stress τ_S = 15.5 MPa, yield stress τ_0 = 155 MPa and hardening factor q = 1.

3.2.2.2.3 Results

Macroscopic strain/stress curves

Strain/stress curves were obtained for polycrystalline aggregates with 14, 23, 53, 110, and 212 grains with sizes varying from 0.10 mm × 0.07 mm to 0.40 mm × 0.28 mm. All polycrystalline aggregates used in analyses have an average grain size of 0.023 mm, which is in accordance with metalografic research of the selected material [14]. 30 different random orientations of crystal lattices and 2 boundary conditions (stress and displacement boundary conditions) were analyzed for each polycrystalline aggregate. The polycrystalline aggregate was loaded with biaxial loads p_1 and p_2 (= ½ p_1). Macroscopic equivalent stress $<\sigma_{eq}>$ and macroscopic equivalent strain $<\varepsilon_{eq}>$ are calculated as [4]:

$$\left\langle \sigma_{eq} \right\rangle = \frac{1}{V}\int_V \sigma_{eq}\ dV \text{ and } \left\langle \varepsilon_{eq} \right\rangle = \frac{1}{V}\int_V \varepsilon_{eq}\ dV\ ,$$

where σ_{eq} stands for equivalent stress, ε_{eq} for equivalent strain and V for volume of polycrystalline aggregate [3].

Hill's anisotropic plasticity was calibrated with results of crystal plasticity and then used to model plastic material behaviour of grains.

Examples of macroscopic strain/stress curves are available in [2]. Relationships between macroscopic equivalent (Von Mises) stress and macroscopic equivalent strain clearly show scatter of strain-stress curves due to orientations of crystal lattice. General conclusions are [3]:

- The scatter of macroscopic strain/stress curves is of comparable magnitude for both boundary conditions.
- Curves nearly coincide in elasticity.
- The scatter in plasticity is mainly due to the different yielding points of macroscopic strain/stress curves.
- The scatter (i.e., macroscopic equivalent stresses) is decreasing as the size of the polycrystalline aggregate (number of grains) increases. The scatter in plasticity for 14-grains aggregates is around ±50 MPa (around ±10%). The scatter for 53-grains aggregates is around ±25 MPa (~±5%) and for 212- grains aggregate is around ±15 MPa (~±3%).

Strain/stress fields

A crystal plasticity material model was used to more accurately show relevant mesoscopic features. One 212-grain polycrystalline aggregate with displacement boundary conditions was analyzed in full detail.

Examples of strain/stress fields are available in [2]. From evolution of equivalent stress, equivalent strain, resolved shear stress and cumulative slip one can observe [3]:

- Distinctive heterogeneity on the mesoscopic level could be observed. Very noticeable shear banding occurs in plasticity. This represents the main direction of material flow in the polycrystalline aggregate. Due to the local concentrations of material flow in shear bands, the equivalent strain within shear bands is up to 500% higher than macroscopic (i.e., average) equivalent strain. Similar concentration appears also in equivalent stress field. The differences are up to 60% compared to macroscopic equivalent stress. Local strain and stress concentra-

tions due to a grain structure might therefore contribute significantly to localized failure of material and consequently to initialization and growth of microcracks.

- Shear banding typically develops at grain boundaries (shear bands are less recognizable when passing through the grains). Shear banding appears in directions of about 50° from x-axis. The typical distance between shear bands is in the order of 1 grain size (around 0.04 mm).

Estimation of RVE size

RVE size was estimated for elasticity and plasticity. Analyses were carried out on polycrystalline aggregates with 14, 23, 53, 110 and 212 grains with sizes from 0.1 mm × 0.07 mm to 0.4 mm × 0.28 mm. 30 different random orientations of crystal lattices and 2 boundary conditions (stress and displacement boundary conditions) were analyzed for each polycrystalline aggregate. Analyses were carried out at biaxial loads p_1 = 200 MPa and p_2 = 100 MPa for elasticity and p_1 = 1000 MPa and p_2 = 500 MPa for plasticity.

Equivalent macroscopic strains and stresses are shown in Fig. 3.2.2.2-1 and 3.2.2.2-2 where d in the legend refers to displacement boundary condition, s refers to stress boundary condition and ave refers to average values (averaged over 30 different randomly orientated crystal lattices with displacement or stress boundary conditions). The number following abbreviation denotes number of grains of polycrystalline aggregates with separate values for each boundary condition. Analytical solution for elasticity for macroscopically homogenous material ($<\varepsilon_{eq}>$ = 0.0515% and $<\sigma_{eq}>$ = 96.2 MPa) is also shown in Fig. 3.2.2.2-1 obtained by continuum elasticity with material parameters: E = 210 GPa and ν = 0.29 [16].

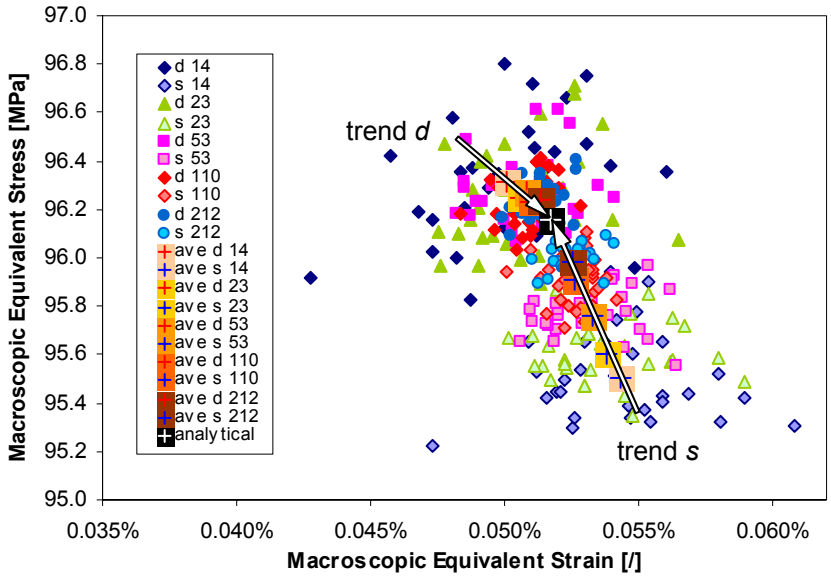

Fig. 3.2.2.2-1: Scatter of macroscopic equivalent strain/stress in elasticity

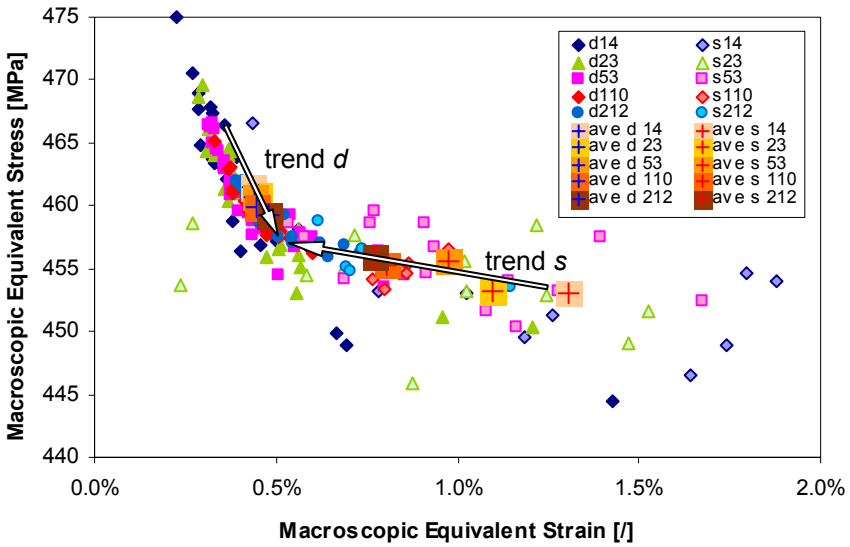

Fig. 3.2.2.2-2: Scatter of macroscopic equivalent strain/stress in plasticity

A tendency towards decrease of scatter as number of grains in the aggregates increases can be observed. Average values of macroscopic strains and stresses (for both boundary conditions) show a clear trend towards analytical solution with increasing number of grains in the aggregate.

RVE size was estimated according to eq. (3.2.2.2.2). Macroscopic equivalent stresses were taken at macroscopic equivalent strain $<\varepsilon_{eq}>$ of 0.0515 % (in elasticity) and 1% (in plasticity). Fig. 3.2.2.2-3 and 3.2.2.2-4 shows macroscopic equivalent stresses and scatter depending on number of grains in polycrystalline aggregate for displacement (denoted as d) and stress (denoted as s) driven boundary conditions. Extrapolation lines are drawn in accordance with eq. (3.2.2.2.1).

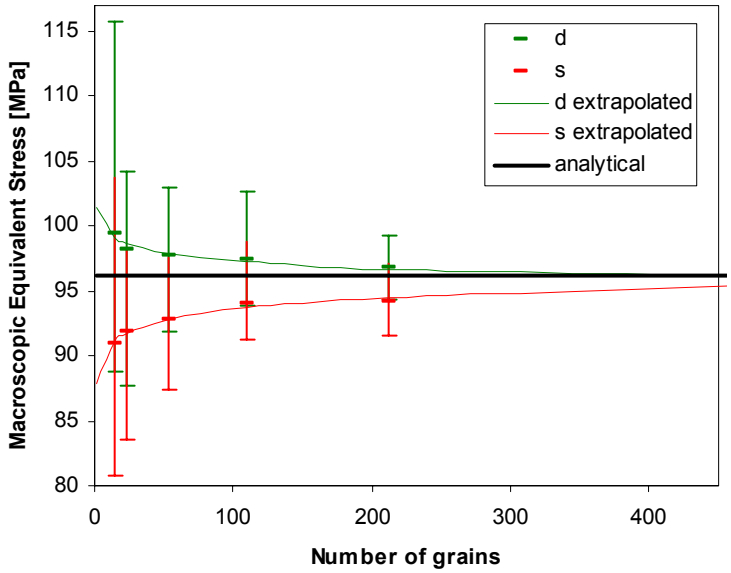

Fig. 3.2.2.2-3: Convergence of macroscopic equivalent stresses in elasticity

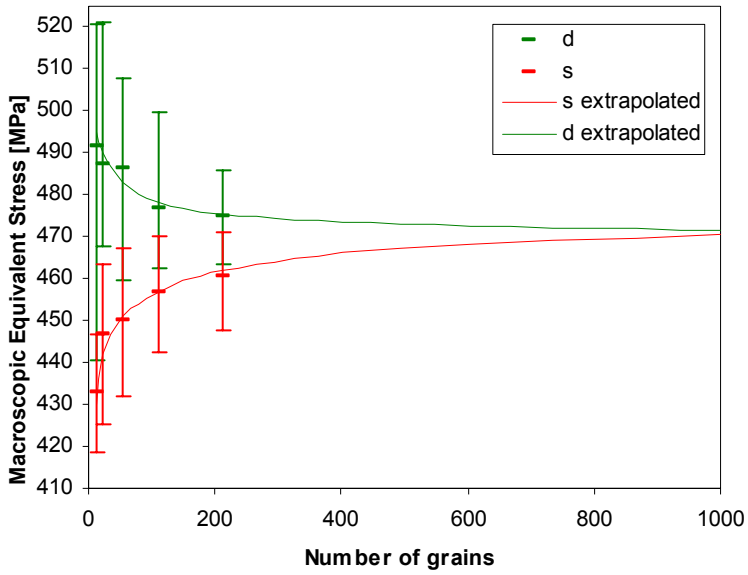

Fig. 3.2.2.2-4: Convergence of macroscopic equivalent stresses in plasticity

With residuum O for 212-grain aggregate over 2% for elasticity and 5% for plasticity, one can conclude that RVE has not been achieved. However, trend toward analytical solution and decrease of scatter with increasing number of grains is clearly visible. The RVE size in elasticity is estimated to 372 grains, which corresponds to a polycrystalline aggregate of 0.53 mm × 0.38 mm in size. This is comparable with results from literature for aluminum oxide [17]. The RVE size in plasticity is estimated to 803 grains, which corresponds to a polycrystalline aggregate of 0.78 mm × 0.55 mm in size. We considered that use of optimized material parameters would not significantly change estimates of RVE size in elasticity and plasticity.

Ductile damage may occur simultaneously with plastic strain at larger levels. It results from the nucleation of cavities due to decohesion between voids/inclusions and the matrix followed by their growth and their coalescence [18,19]. Shortest connections among voids are obvious candidates for possible void coalescence paths. Those paths, which can be described with Delaunay tessellation, can be used to describe void coalescence paths [20,21]. Since the Delaunay tessellation is the geometric dual of the Voronoi tessellation, one can imply their similar behaviour.

Average distance between voids (modelled with Delaunay tessellation) is 500 μm [14]. If we extrapolate estimates of RVE size of plasticity to damage, we can expect that RVE size for damage would demand a polycrystalline aggregate with at least 800 voids (Poisson points in the Delaunay tessellation). This would represent a window the size of 15.1 mm × 10.7 mm [3]. Coupled model (Voronoi and Delaunay tessellation) with random grains and random inclusions would therefore lead to a polycrystalline aggregate with more than 300,000 grains, which is well beyond computational capabilities at this moment.

Correlation lengths

Correlation lengths for a 212-grain polycrystalline aggregate were calculated for six calculation points on the strain-stress curve [10]. Fig. 3.2.2.2-5 and 3.2.2.2-6 show histograms of model area with regard to the correlation length for case (a) (search radius of two average grain size) and case (b) (search radius of one average grain), respectively.

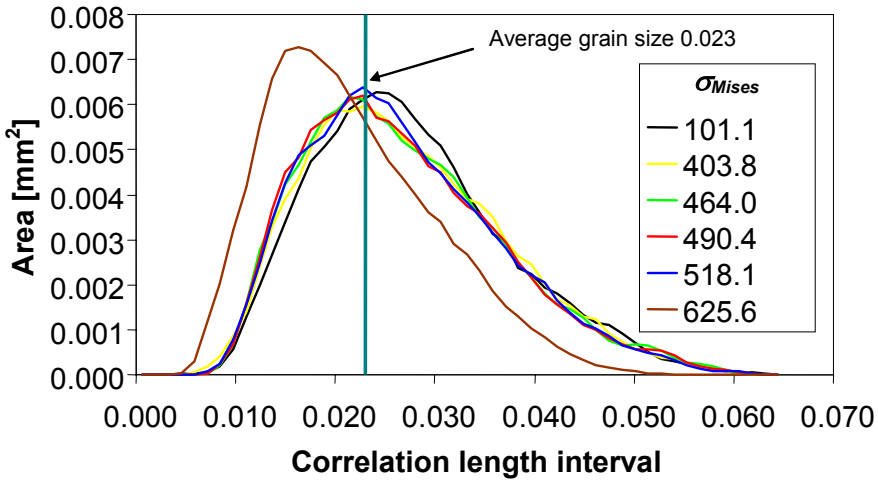

Fig. 3.2.2.2-5: Histogram of model area with regard to correlation length – case (a)

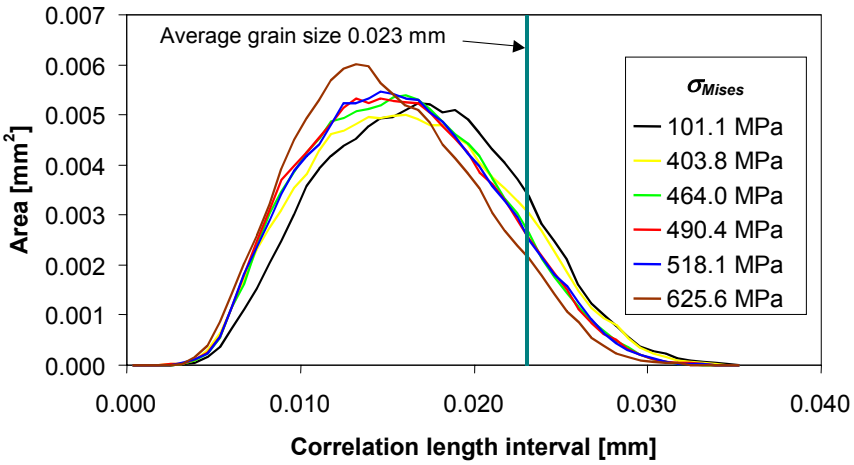

Fig. 3.2.2.2-6: Histogram of model area with regard to correlation length – case (b)

Large search radius of the case (a) enables us to observe the influence of a certain grain on a wider area of the model. On the other hand the wider the search area is, more averaging is performed when calculating correlation function and the desired local nature of the correlation function is lost. Because of that a second, smaller search radius has been introduced-case (b). Due to the smaller search radius local statistics of the stress field is obtained, however the resulting correlation lengths are therefore smaller. This will become evident in the following section.

The areas of higher correlation length values for both cases are mostly inside the grain boundaries, sometimes spreading over several grains. In a few cases the areas of higher correlation length values seem to concentrate on the grain boundaries. For the case (a) the regions of high correlation values can be seen at the model boundaries. This is due to the 2D interpolation of the Mises stresses in the border region where is a lack of data on the Mises stresses outside the model boundaries.

The average correlation length in elasticity for case (a) is 0.027 mm, which is 18 % larger than the average crystal grain size. For the case (b) the average correlation length is 0.017 mm, which is lower than the average crystal grain size. The macroscopic equivalent stresses in plasticity (calculation points 3 and above) are larger than the yield strength σ_Y. Calculation lengths for these calculation points tend to de-

crease with a higher macroscopic equivalent stress. For the calculation point 6, the average correlation length is 0.021 mm for case (a) and 0.015 mm for case (b). Both values are below the average grain size. This suggests that the equivalent stress fields in the search areas become increasingly more random as the load and the macroscopic equivalent stress increase. Thus the influence area of the finite elements and crystal grains reduces as the macroscopic equivalent stress increases.

One must point out however, that the area for which the correlation length is calculated for is limited to the search area with the radius equal to twice the average grain size (2×0.023 mm) and the average grain size (0.023 mm).

3.2.2.2.4 Conclusions

The elastic-plastic behaviour of planar polycrystalline aggregates with stochastic arrangement of grains was simulated using the computational approach, which combines the most important mesoscale features and compatibility with conventional continuum mechanics. Each grain was simulated as a randomly oriented anisotropic monocrystal (anisotropic elasticity and crystal plasticity). An averaged (macroscopic) response of the polycrystalline aggregate was then sought through the appropriate averaging procedures. Polycrystalline aggregates with different number of randomly orientated grains and different boundary conditions were loaded with biaxial loads. From the presented simulations it can be concluded:

- Obtained macroscopic strain/stress curves show large scatter, which is decreasing as the number of grains in polycrystalline aggregate increases. Distinctive heterogeneity in plasticity on the mesoscopic (grain size) level can be observed in the stress and strain fields. Local stresses were found to be up to 60% higher than macroscopic stresses. The effect is even more pronounced when dealing with strains, with local strains reaching up to 500% of macroscopic strains. Local stress/strain concentrations due to a grain structure might therefore contribute significantly to localized failure of material and consequently to initiation and growth of microcracks.
- Random grain structure might be one of the causes for size effects in polycrystalline aggregates smaller than representative volume element (RVE) size. In this report, the RVE size in elasticity is estimated to be at least 370 grains, which corresponds to a polycrystalline aggregate size of about 0.5 mm × 0.4 mm. The estimated RVE size in plasticity is at least 800 grains, which corresponds to a polycrystalline aggregate size of about 0.8 mm × 0.55 mm. These results are in accordance with the literature. Prediction is that RVE size for damage would be 15 mm × 11 mm in size.
- The range of sizes of LISSAC specimens suggests negligible influence of size effects in elasticity and plasticity, which is in accordance with the experimental part of the project. The estimated RVE size for damage however suggests that size effects could be observed within LISSAC experiments. Again, this is in accordance with results of LISSAC tests.
- The correlation length is taken as a measure of the grain domain of influence. As long as the macroscopic equivalent stresses are lower than the yield strength, the average grain domain of influence is somewhat larger than the average grain size. With the increase of the load, the average grain domain of influence decreases to about 93% of the average grain size. The correlation length depends on the observed area. Larger search radius is associated with higher correlation length values.

3.2.3 Local approach models

3.2.3.1 Rousselier damage model

The main goals of these investigations are to predict the failure strains in dependence of the different boundary conditions and to help to define reasonable limit strains[1]. For reaching these aims a damage model formulated by Rousselier was used in combination with the finite element program ADINA [2]. Selected specimens were modelled and calculated to examine the capability of the Rousselier model to describe geometry and size effects on the deformation and failure behaviour. For describing dynamic effects the Cowper and Symonds model is implemented into ADINA.

3.2.3.1.1 Theory

Common material laws for describing ductile deformation like von Mises law can not predict the limits of elasto-plastic deformation. However, in reality, deformation is generally limited by fracture processes.

In most metals and alloys second phase particles and inclusions can be observed. If ductile fracture is observed the fracture process can be divided into three phases [3,4]:

- void nucleation at particles and grain boundaries
- void growth with increasing plastic deformation
- void coalescence $\Rightarrow$ micro crack

The models for describing ductile fracture are often called damage models or due to their local formulation local approach models. Depending on the damage model one or several of the three phases of ductile fracture will be simulated numerically.

Models for describing void initiation

Void initiation during material deformation occurs by debonding of matrix and particles or by fracture of particles. In general plastic deformation is required for the initiation of the voids.

For pressure vessel steels it is found that the larger voids which are mainly responsible for ductile fracture principally initiate on manganese sulphide particles. Most of the voids initiate directly at the onset of plastic deformation. A very successful criterion for void initiation in these steels is:

$$\bar{\sigma}^{vM} \geq R_e$$

If this criterion is fulfilled the void volume is set to the so called initial void volume f_0.

Void growth models

In the calculations which are done within LISSAC project the Rousselier model is used [5]. With this approach a flow function for porous materials that means for materials containing voids is derived. For the computations the model was used in the following form:

$$\Phi = \frac{\overline{\sigma}^{vM}}{1-f} + \sigma_k \cdot D \cdot f \cdot e^{\frac{\sigma^{hyd}}{(1-f)\cdot\sigma_k}} - \sigma_y = 0$$

$f \mathrel{\widehat{=}}$ void volume

$\sigma_k, D \mathrel{\widehat{=}}$ material constants

Models for describing void coalescence

The numerous mathematical approaches reflect the complexity of this process. The most common criteria however is the critical void volume. This criteria is also used in this project.

Introduction of an internal length for describing size effects

In the theoretical framework of the damage models it is assumed that in ductile fracture the crack jumps from void to void. In finite element calculations this can be simulated by finite crack jumps from node to node or from integration point to integration point respectively. Due to this, the absolute size of the finite elements used in the damage calculation must be related very closely to the mean distance of the voids or to the mean distance of the inclusions leading to voids.

Dynamic material model

In most cases for metallic materials it can be stated that the stress strain curve is shifted to higher stresses with increasing strain rates [6,7]. For the simulation of this phenomena a material law have to be found which describes the material hardening in dependence of the strain and the strain rate.

$$\sigma = \sigma(\varepsilon, \dot{\varepsilon}, T)$$

In the LISSAC project only stress strain curves with two different strain rates are available. Due to this, only a relatively simple strain rate dependent material model with few parameters can be chosen.
A relatively good approximation for ferritic steels is given by Cowper and Symonds [8].

$$\sigma^{dyn}(\varepsilon) = \left(\sqrt[p]{\frac{\dot{\varepsilon}_{pl}}{D}} + 1 \right) \cdot \sigma(\varepsilon)$$

Within LISSAC project the Cowper and Symonds law is included in the Rousselier material subroutine to take the dynamic material hardening into account.

3.2.3.1.2 Determination of material depending parameters

The material models presented are implemented as user defined material model in a commercial finite element code. For describing the mechanical behaviour the models need material depending parameters. The determination of these parameters is discussed in this chapter.

Material dependent model parameters at room temperature

For the determination of the stress strain law for the LISSAC material, 15 tensile specimens have been tested at room temperature at EMPA [9]. The results of the tests are used to extract a mean stress strain curve. The detailed procedure is presented in a special LISSAC report [10]. For the calculations the stress strain curve from experiment **GR1H** is chosen because this curve gives the best approximation of all experiments.

For getting the true stress strain curve up to the failure point of LISSAC material the curve was fitted numerically. For the numerical fitting the geometry of the tensile specimens is modelled with finite elements. Due to symmetry only a quarter of the specimen is modelled with axis symmetric 8 nodes elements. The specimen has a small neck with a reduction of the radius of 0.01 mm in the mid plane, which is in conformity with the standards. The determinated true stress strain curve is presented in Fig. 3.2.3.1-1.

Due to the lack of metallographic data for the LISSAC material the used parameters for the Rousselier damage model the following results and assumptions are taken from literature:

- Void initiation should take place at the beginning of plastic deformation.
- The Rousselier stress σ_k is set to 445 MPa.
- The critical void volume f_c is set to 0.05.
- The characteristically length l_c is set to 0.2 mm.

The initial void volume f_0 is calibrated numerically with the help of the deformation behaviour of the standard tensile specimen. For $f_0 = 0.0003$ the finite element results represent a good approximation of the experiment.

Material dependent model parameters at 400°C

For the determination of the true stress strain curve at 400°C five experiments have been performed at ENSA. During the tests only the load and the cross head displacement have been measured. Since the elongation of the proportional section necessary for the strain calculation cannot be determined from the crosshead displacement directly, the following procedure has been used:

- From the five stress 'over all strain' (cross head displacement / proportional measurement length) curves an artificial mean curve is calculated.
- With the data from ENSA (proportional measurement length = 25 mm and proportional cross section area = 19.53 mm²) the mean load crosshead displacement curve is determined.
- The cross head displacement can be separated into the elongation of the machine (crosshead deformation and grips) and into the elongation of the whole specimen (including thread heads).
- With an iterative finite element procedure the true stress strain curve can be calculated from the total specimen elongation with a special developed numerical procedure.

The true stress strain curve achieved with this procedure is presented in Fig. 3.2.3.1-2.

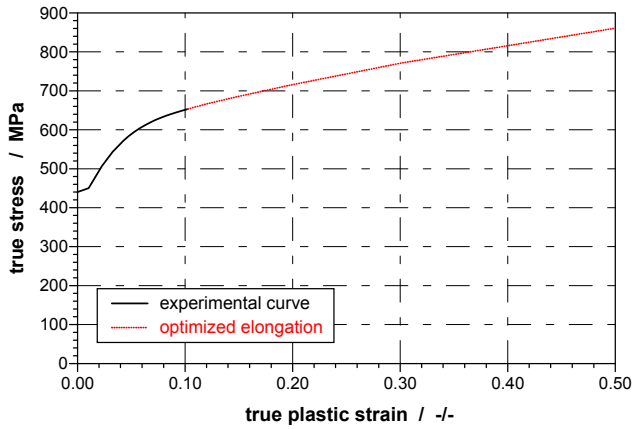

Fig. 3.2.3.1-1: elongation of the true stress strain curve, roomtemp.

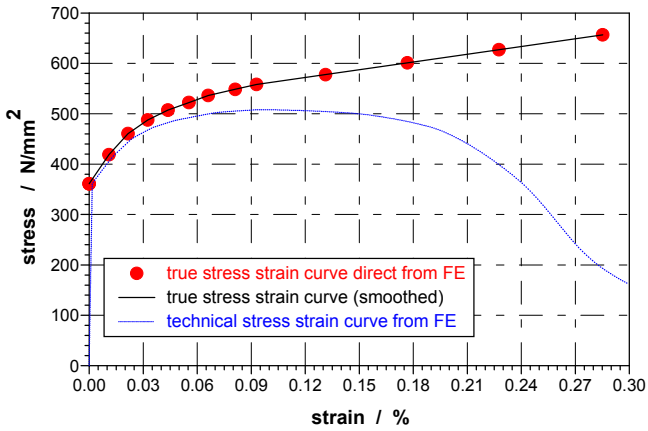

Fig. 3.2.3.1-2: technical and true stress strain curves, 400°C

For checking the computed true stress strain curve the results are compared with the curves determined at JRC/ELSA [11]. The agreement, particularly toward smaller stretches is well, Fig. 3.2.3.1-3.

Nevertheless it must be noted that the computed curve is only an approximation.

Material dependent model parameters for dynamic tests

Within LISSAC project the Cowper Symonds model is included in the Rousselier material subroutine to take the dynamic material hardening into account.

For the LISSAC material only two different strain rates are available: A quasi static curve and a curve with a strain rate of 250 s^{-1} [11]. These two curves are used to calibrate the Cowper Symonds variables p and D. The calibration gives p=6 and $D=57*10^6$. The approximated and the experimental curves for the strain rates of $1s^{-1}$ up to $250s^{-1}$ can be seen in Fig. 3.2.3.1.4.

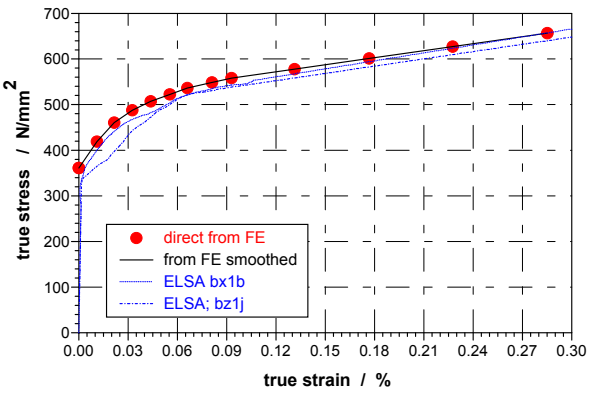

Fig. 3.2.3.1-3: experimental and numerical true stress strain curves, 400°C

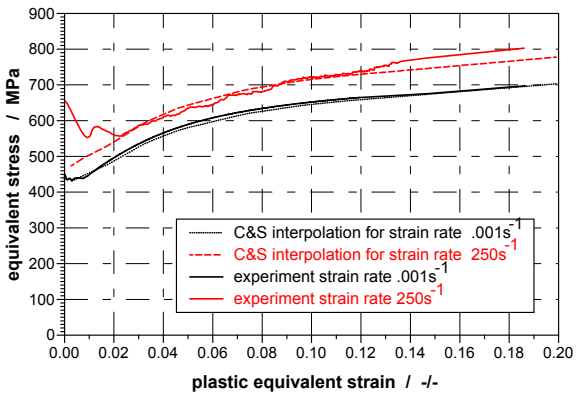

Fig. 3.2.3.1-4: experimental and approximated true stress strain curves with different strain rates, roomtemp.

3.2.3.1.3 Results

Within the LISSAC project tests have been performed for different specimen types with various sizes and loading conditions. In this chapter calculations have been done for the following cases:

Size variation:	flat specimens with hole; different sizes
Geometry variation:	flat specimen with hole; flat specimen with notches; flat specimen with increased hole, curved biaxial specimen without holes
Variation of stress triaxiality:	circular specimen with notch, circular specimen with ESIS geometry, circular specimen with increased notch depth

For simulating crack initiation and crack growth Rousselier's damage model is used. Consequently for all the calculations the same stress strain curve and the same set of damage parameters have been used.

Size variation

For the size variation the flat specimens with hole have been used. The exact geometry of the different specimens can be taken from Fig. 3.2.3.1.5. Due to symmetry only 1/8 of the specimens is modelled with 20nodes three dimensional isoparametric elements.

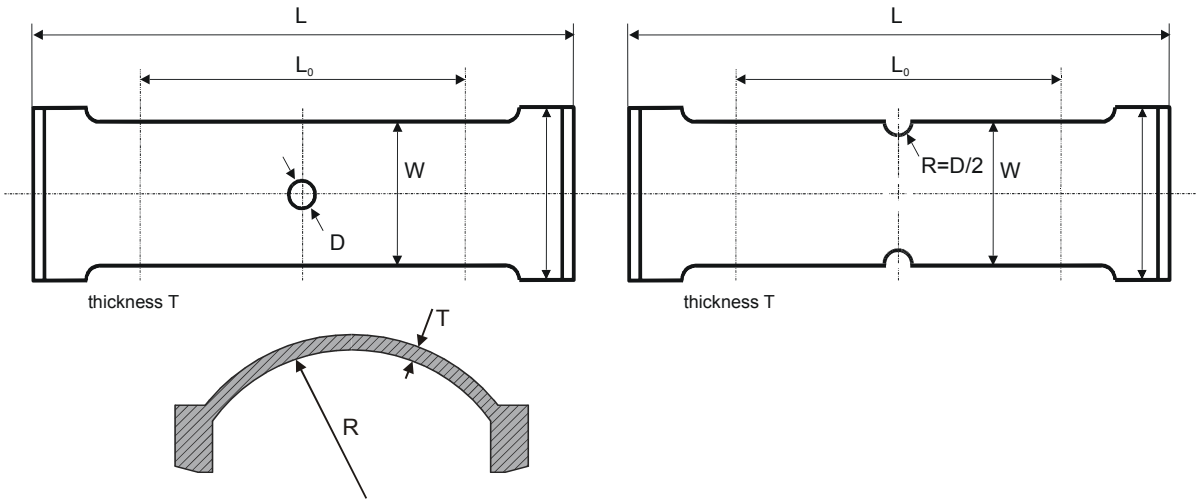

specimentype	T	W	D	L_0	R
with hole	4 mm	10 mm	2 mm	24 mm	
with hole	20 mm	50 mm	10 mm	120 mm	
with hole	40 mm	100 mm	20 mm	240 mm	
with notch	20 mm	50 mm	10 mm	120 mm	
Curved biaxial	5 mm				55.6 mm

Fig. 3.2.3.1-5: Geometry of the simulated specimens

For a better comparison between the different sizes the load is normalized with the gross section and the displacement is normalized with the measurement lengths. In Fig. 3.2.3.1-6 - 3.2.3.1-8 the stress versus the normalized hole opening is shown. When comparing the numerical results with the experimental ones it can be seen that the deformation behaviour can be described very well with the Rousselier model.

Also the loss of the load bearing capacity at the end of the experiments due to crack initiation and crack growth can be predicted well. When comparing the simulations of the different sizes with each other a clear size effect can be seen Fig. 3.2.3.1-9.

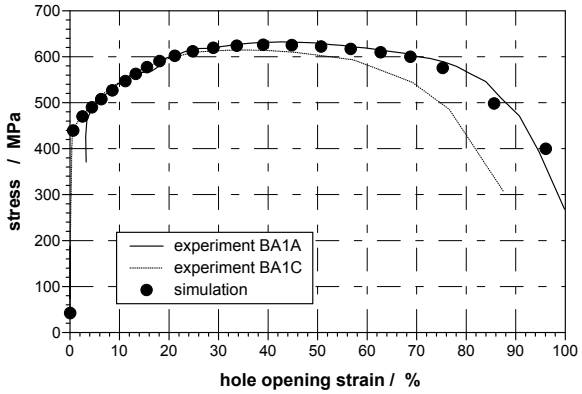

Fig. 3.2.3.1-6: experimental and simulated stress – hole opening strain of the flat specimens with the hole diameter of 2 mm

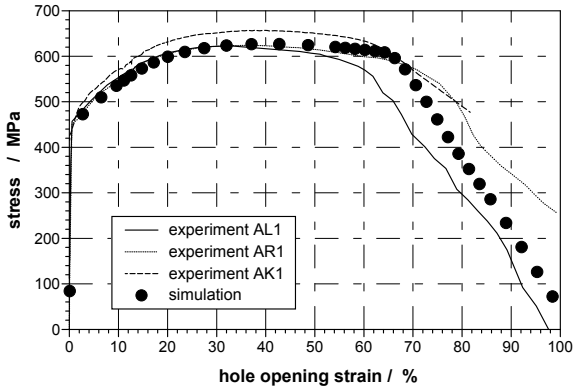

Fig. 3.2.3.1-7: experimental and simulated stress – hole opening strain of the flat specimens with the hole diameter of 10 mm

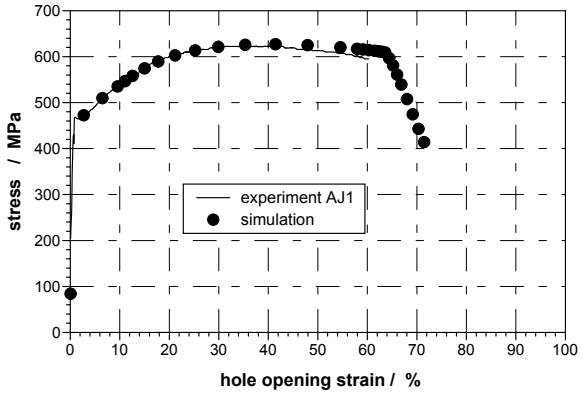

Fig. 3.2.3.1-8: experimental and simulated stress – hole opening strain of the flat specimens with the hole diameter of 20 mm

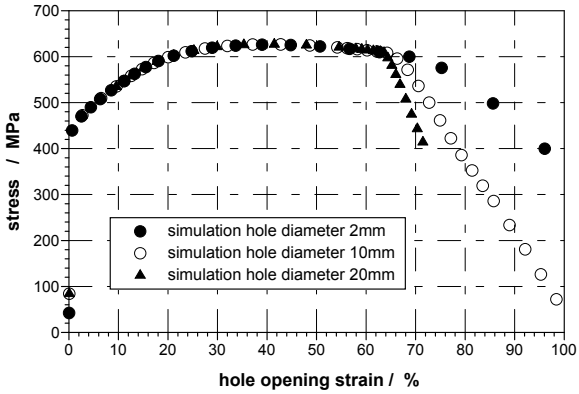

Fig. 3.2.3.1-9: simulated stress – hole opening strain behaviour of the flat specimens with different sizes

Geometry variation

For the geometry variation a flat specimen with hole (already discussed), a flat specimen with notches, a flat specimen with an increased hole and a curved biaxial loaded specimen without holes is selected. The geometries of the different specimen types can be taken from Fig. 3.2.3.1-5.

The normalized load deformation behaviour of the specimen with the notches can be predicted well until maximum load. Behind maximum load the experimental loads are slightly overestimated, Fig. 3.2.3.1-10. Nevertheless the failure point can be predicted with high accuracy.

The normalized hole opening of the specimen with the increased hole is simulated well with the model, Fig. 3.2.3.1-11.

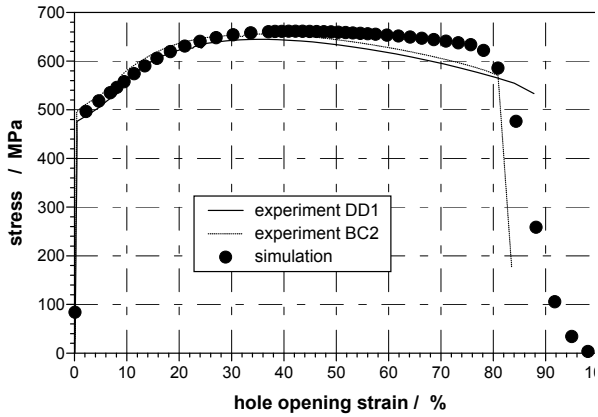

Fig. 3.2.3.1-10: experimental and simulated stress – hole opening strain of the flat specimens with the notch of 10 mm

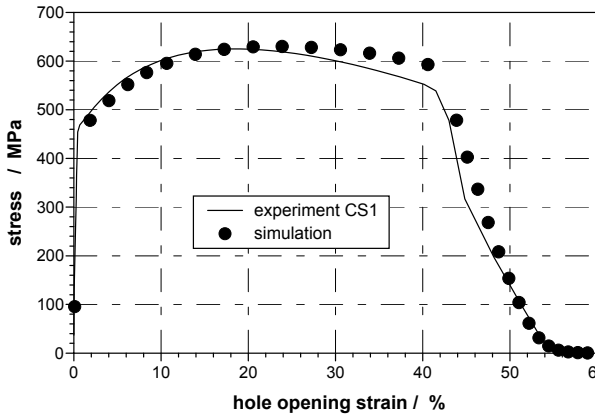

Fig. 3.2.3.1-11: experimental and simulated stress – hole opening strain of the flat specimens with the increased hole of 18 mm

The curved biaxial loaded specimen without holes represents a model of the head of a reactor pressure vessel. The head is loaded with internal pressure. In contrast to the specimens discussed above, the head has no geometrical imperfections like notches or holes. Also the head is loaded biaxial. Due to the geometry the head can be modelled with axis symmetric elements. Despite the totally different geometry and loading conditions the deformation behaviour can be predicted well with the numerical simulation, Fig. 3.2.3.1-12.

Variation of stress triaxiality

To examine the influence of the stress triaxiality different round notched tensile bars have been calculated and compared with experiments. The different geometries can be taken from Fig. 3.2.3.1-13. The elongation behaviour (deformation and fracture) of the specimen with 20mm gross diameter is predicted well with the Rousselier model, Fig. 3.2.3.1-14. Also a specimen with a slightly changed geometry suggested by the ESIS [12] for determining parameters for damage models like the Rousselier model is simulated. This specimen type is not tested within LISSAC project but in an German research project. The confermity between experiment and simulation is good, Fig. 3.2.3.1-15. Nevertheless there is an important difference between the two specimens. In all the specimens tested in LISSAC the crack initiates at the notch root or close behind it. In contrast to this observation the fracture of the ESIS specimen initiates in the centre of the specimen. These experimental findings are also observed in the simulations.

Calculated failure strains

The main task in LISSAC is to determine the failure strains. In LISSAC the failure strains are defined as follows:

- The failure strain is defined as the maximum equivalent plastic strain at crack initiation.
- The failure strain is a local parameter.
- The failure strain is always determined on the surface of the notch or hole ground, although with some samples the failure begins under the specimen surface.

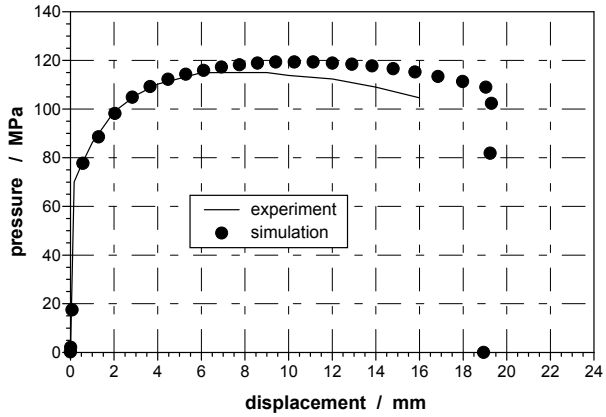

Fig. 3.2.3.1-12: experimental and simulated pressure - displacement behaviour of the curved biaxial loaded specimen

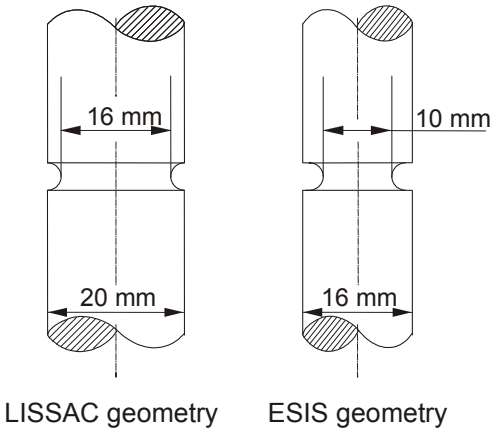

Fig. 3.2.3.1-13: geometries of the different round notched tensile bars with a notch root radius of 2mm

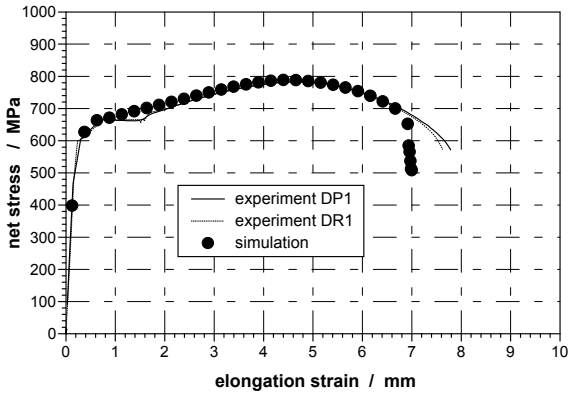

Fig. 3.2.3.1-14: experimental and simulated stress - elongation strain of the round notched tensile bar (LISSAC geometry) with 2 mm notch root radius

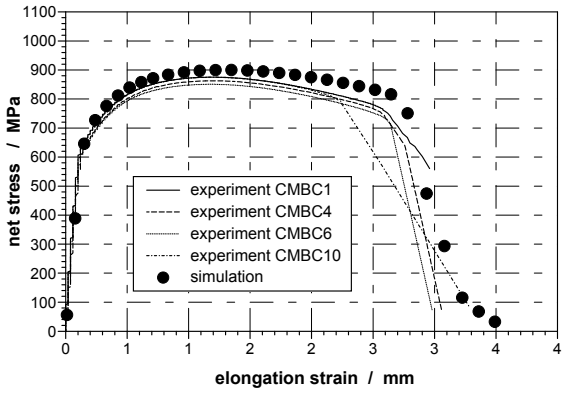

Fig. 3.2.3.1-15: experimental and simulated stress - elongation strain of the round notched tensile bar (ESIS geometry) with 2 mm notch root radius

Due to these definitions also the numerical failure strains are determined.

In Fig. 3.2.3.1-16 the experimental failure strains [13] are plotted versus the radius of the hole or notch. All the experimental results are lying in a narrow scatter band. When plotting the numerical results into the experimental scatter band it can be seen that the calculated fracture strains of the LISSAC specimens fit well in the experimental scatter band, Fig. 3.2.3.1-16. In contrast to this, the failure strain of the ESIS specimen is remarkably below the scatter band. These deviations may results from the following facts:

- The fracture in the ESIS specimen initiates in the center of the specimen; the failure strain is determined on the specimen surface in the notch ground.
- The stress triaxiality at the point of initiation is different.

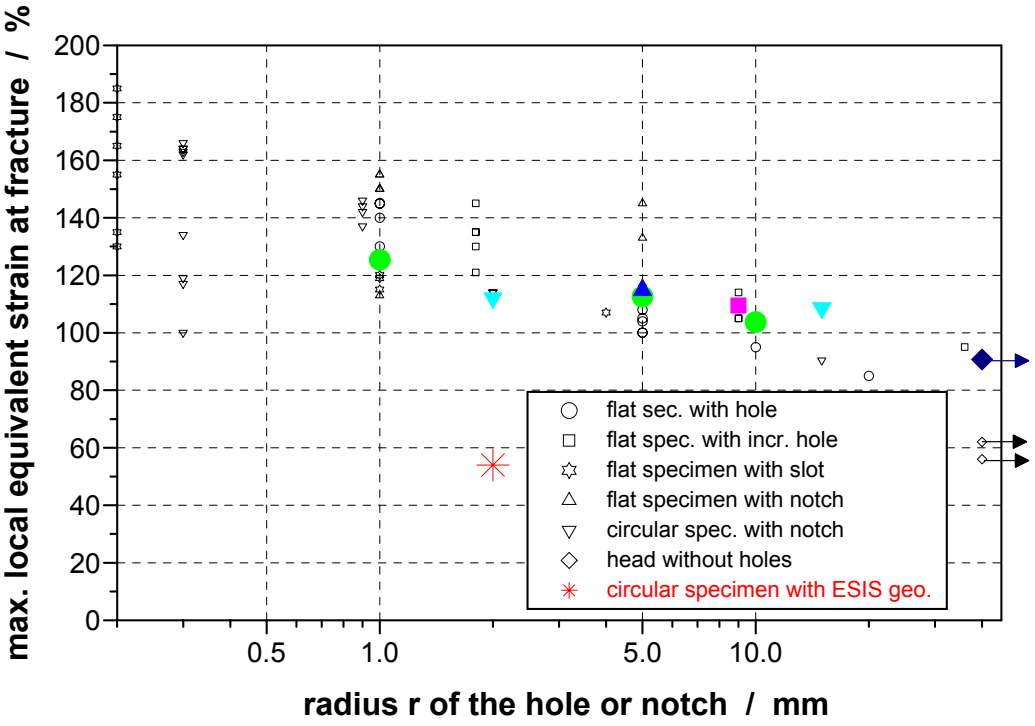

Fig. 3.2.3.1-16: Numerical (coloured full symbols) and experimental (small symbols) maximum local equivalent plastic strain at fracture initiation in dependence of the hole or notch radius

3.2.3.1.4 Conclusions

From the calculations presented the following conclusions can be drawn:

- With the Rousselier model it is possible to simulate the experimental observed load deformation and failure behaviour of the specimen tested in LISSAC. The model is able to calculate the initiation and growth of cracks. For all the calculations the same set of material parameters (stress strain curve and Rousselier parameters) is used.
- The model is able to calculate also the location of crack initiation (in the notch ground or close behind for the LISSAC specimens or in the specimen center as observed with the ESIS specimen.
- In the deformation behaviour until maximum load the Rousselier model predicts no size effect. A size effect is only predicted near the point of failure. This is in accordance to the experimental observations.
- The Rousselier model can predict the influence of the different geometries on the deformation and failure behaviour. The behaviour of the two dimensional loaded head without any holes or notches can also be predicted as for the different specimens with holes and notches.
- The fracture strains calculated with the Rousselier model are in good agreement with the experimental ones. The model also shows, that if the geometry is slightly changed (ESIS geometry) the so called fracture strain differs extremely from the results obtained from the LISSAC specimens. This behaviour is probably a result from the fact that the point of fracture initiation is at the one hand side at or near the surface (LISSAC geometries) or on the other hand in the centre of the specimen (ESIS geometry).

3.2.3.2 Gradient plasticity theory in combination with a non local damage model

Because the Gurson-Tvergaard damage model [1] initially applied by NRG did not give satisfactory results [2] the non local damage model based on gradient plasticity developed by PSI [3] has been applied. A detailed description of the work is documented in [4].

3.2.3.2.1 Theory

The theory of the used gradient plasticity model with damage is presented in chapter 3.2.1.2. The model has been implemented in the finite element program MARC [5].

3.2.3.2.2 Determination of material depending parameters

With the non-local damage model based on gradient plasticity developed by PSI a finite element calculation of a smooth standard tensile specimen beyond the point of ultimate strength in the stress-strain curve is made.

Special attention has been paid to the determination of the model parameters. EMPA performed a number of experiments with smooth tensile specimens at ambient temperature for the LISSAC material. The result of experiment GR1H has been used to determine the parameters for the PSI model. The parameters have been chosen in such a way that there is a good agreement between the experimental and numerical result for experiment GR1H (Fig. 3.2.3.2-1).

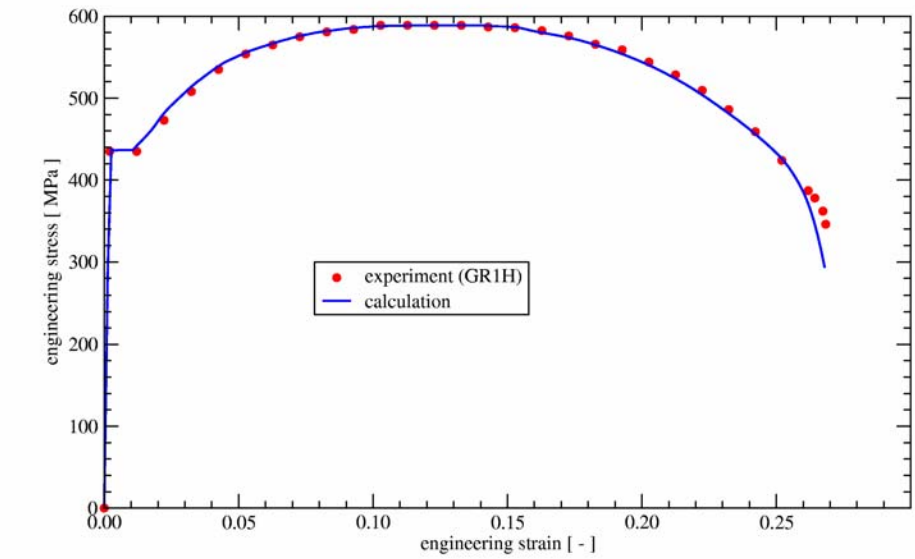

Fig. 3.2.3.2-1: Experimental and calculated result for experiment GR1H

The material parameters for the Gurson-Tvergaard damage model and the gradient plasticity model are summarized below:

$q_1 = 1.50$ $q_2 = 2.00$ $q_3 = 2.25$ $f_0 = 0.001$ $f_n = 0$

$f_c = 0.01$ $f_f = 0.15$ $f_u = 0.65$

$\varepsilon_n = 0.3$ (not relevant because no nucleation included)

$\sigma_n = 0.1$ (not relevant because no nucleation included)

$l = 0.24$ (internal length parameter)

3.2.3.2.3 Results

Circular (round) specimen with notch

The PSI model has been used to perform a finite element calculation for the tensile experiments at ambient temperature with the various sizes of a round specimen with a notch (3, 9, 20, and 150 mm diameter). All test specimen have identical geometrical proportions and differ only in size. JRC/ELSA performed also a tensile experiment with 3 mm round specimen with a notch. The specimen JRC/ELSA used has a different geometry compared to the standard geometry used by FZK and MPA. The main difference is the shorter gauge length ($1⅔ \cdot d_0$ in stead of $6 \cdot d_0$).

Fig. 3.2.3.2-2 and 3.2.3.2-3 show the axisymmetric finite element models of the JRC/ELSA and standard specimen used for the calculations. The symmetry in both specimens enables only half of the measurement section to be incorporated in the models.

The highest plastic strains (> 100%) occur at the root of the notch. Small differences can be observed in the deformation around the notch. The small specimens (3 mm) deform more than the larger specimens.

In the Fig. 3.2.3.2-4 to 3.2.3.2-11 the measured and calculated deformation behaviour of the test specimens are compared. For the 20 and 150 mm specimens the nominal stress is shown as a function of the normalized notch opening and elongation. The nominal stress, the normalized hole opening, and the elongation are defined as:

$$\sigma_{nom} = \frac{F}{\frac{\pi}{4} \cdot (d_0 - 2r_0)^2} \qquad \varepsilon_{notch} = \frac{r - r_0}{r_0} \qquad \varepsilon_{elon} = \frac{l - l_0}{l_0}$$

where:

- F : the axial force acting on the specimen
- d_0 : the initial diameter of the specimen
- l : the actual length of the measurement section
- l_0 : the initial length of the measurement section
- r : the actual notch radius (measured in axial direction)
- r_0 : the initial notch radius

For the 3 and 9 mm specimens FZK measured not the notch opening, but the specimen diameter at the bottom of the notch. From this measurement the strain is calculated as shown in Fig. 3.2.3.2-7 and 3.2.3.2-10.

$$\varepsilon = \frac{A - A_0}{A_0}$$

The experiments showed a size effect with respect to the failure strain (Fig. 3.2.3.2-4, 3.2.3.2-7, and 3.2.3.2-8). The calculations predicted a size effect with respect to the failure strain only for 3 mm specimens (Fig. 3.2.3.2-5 and 3.2.3.2-9). However, the PSI model predicted the deformation behaviour of the round specimens with a notch reasonably (Fig. 3.2.3.2-6, 3.2.3.2-10, and 3.2.3.2-11). The nominal stress and failure have been slightly overpredicted. For the small specimens (Fig. 3.2.3.2-10) this overprediction is higher than for the larger specimens (Fig. 3.2.3.2-6 and 3.2.3.2-11). Despite the fact that the JRC/ELSA and the standard 3 mm specimens have a different deformation behaviour, this deformation behaviour

has been well predicted by the PSI model with the material parameters derived from the uniaxial experiment performed by EMPA.

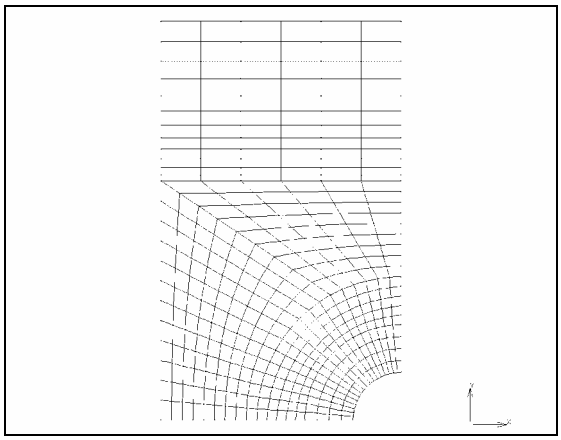

Fig. 3.2.3.2-2: Mesh 3 mm specimen (JRC/ELSA)

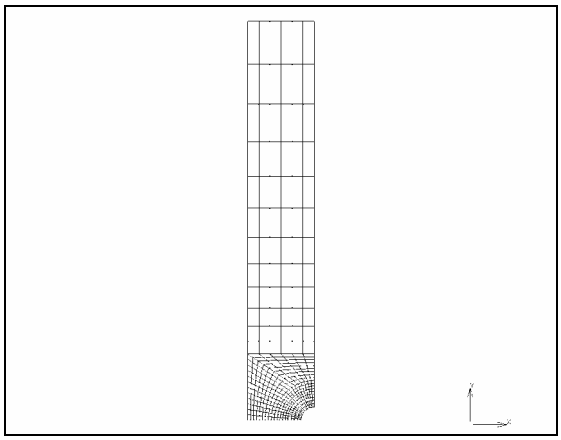

Fig. 3.2.3.2-3: Mesh standard specimen

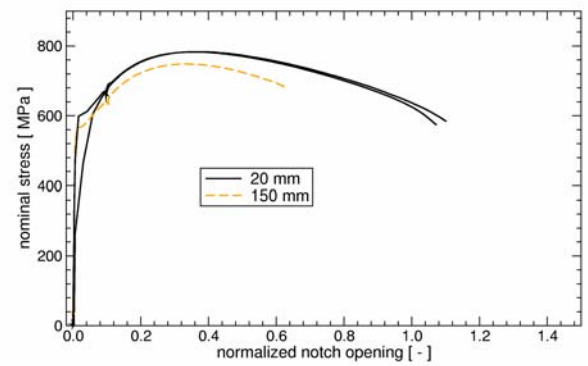

Fig. 3.2.3.2-4: Measured normalized notch opening

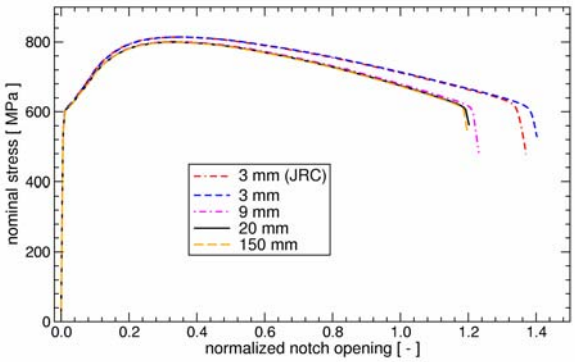

Fig. 3.2.3.2-5: Calculated normalized notch opening

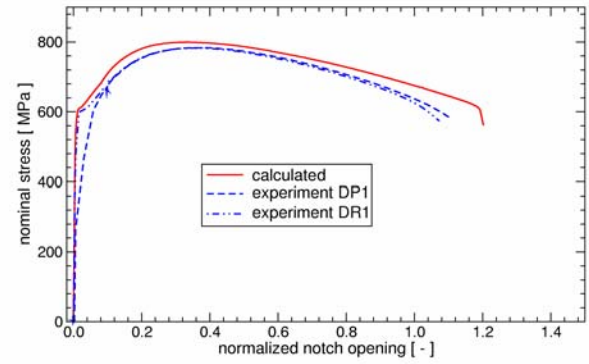

Fig. 3.2.3.2-6: Comparison normalized notch opening for 20 mm specimen

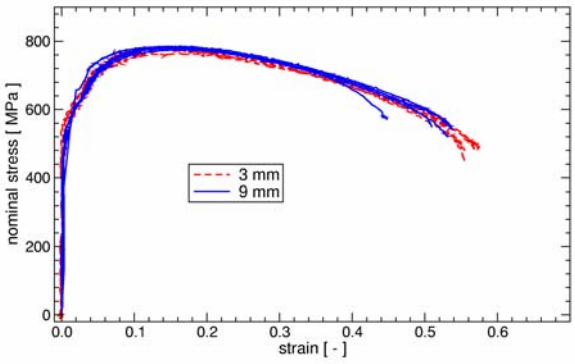

Fig. 3.2.3.2-7: Measured strain 3 and 9 mm FZK specimen

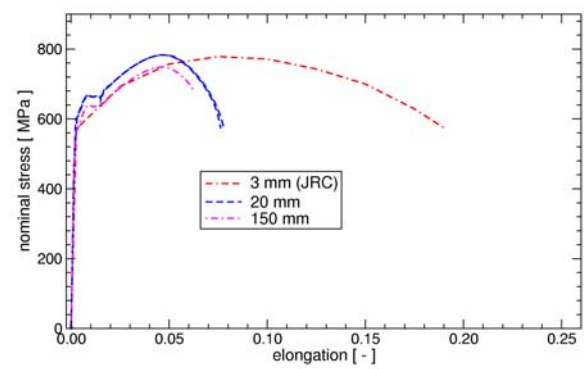

Fig. 3.2.3.2-8: Measured elongation

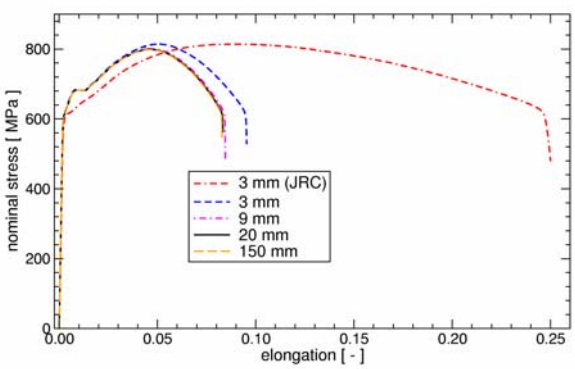

Fig. 3.2.3.2-9: Calculated elongation

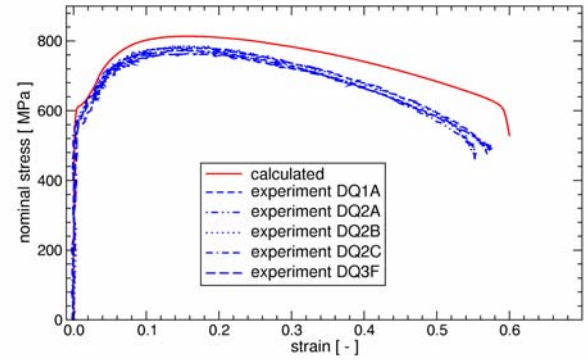

Fig. 3.2.3.2-10: Comparison strain for 3 mm standard specimen

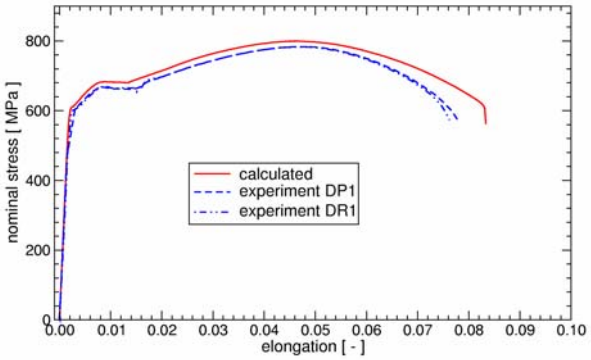

Fig. 3.2.3.2-11: Comparison elongation for 20 mm standard specimen

Flat specimen with central hole

The PSI model has been used to perform a finite element calculation for the tensile experiments at ambient temperature with the various sizes of a flat specimen with a central hole (4, 20, 40, 80, and 200 mm thickness). All test specimen have identical geometrical proportions and differ only in size. The hole diameter is half the thickness, the width is 2.5 times the thickness, and the gauge length is 6 times the thickness.

Fig. 3.2.3.2-12 shows the plane strain finite element model of the flat specimen with a central hole used for the calculations. The symmetry in the specimen enables only half of the measurement section to be incorporated in the model.

The specimens are “waisting” in the cross section through the hole centre and the hole becomes oval in axial direction. The highest plastic strains (> 100%) occur at the inside of the hole. Small differences can be observed in the deformation around the hole. Because the calculation for the small specimen (4 mm) became numerically instable earlier than the calculations for the larger specimen the larger specimen deforms stronger around the hole. The initiation of failure can be seen in the deformations.

In the Fig. 3.2.3.2-13 to 3.2.3.2-20 the measured and calculated deformation behaviour of the test specimens are compared. For the specimens the nominal stress is shown as a function of the normalized hole opening and elongation. The nominal stress, the normalized hole opening, and the elongation are defined as:

$$\sigma_{nom} = \frac{F}{(b_0 - d_0)\cdot t_0} \qquad \varepsilon_{hole} = \frac{d - d_0}{d_0} \qquad \varepsilon_{elon} = \frac{l - l_0}{l_0}$$

where:

F : the axial force acting on the specimen
b_0 : the initial width of the specimen
d : the actual hole diameter (measured in axial direction)
d_0 : the initial hole diameter
l : the actual length of the measurement section
l_0 : the initial length of the measurement section
t_0 : the initial thickness of the specimen

The experiments show a size effect with respect to the failure strains, but no size effect with repect to the ultimate strength. The calculations predict also a size effect only with respect to the failure strain (Fig. 3.2.3.2-14 and 3.2.3.2-17). However, this size effect is only apparant for the 4 mm specimen (Fig. 3.2.3.2-14 and 3.2.3.2-18). For the 4 and 40 mm specimens a comparison between the measured and calculated deformation behaviour is shown in the Fig. 3.2.3.2-15, 3.2.3.2-16, 3.2.3.2-19, and 3.2.3.2-20. For these specimens there is a reasonable agreement between the measured and calculated deformation behaviour. The experiments predict a lower yield point and a lower failure strain. The lower yield point can be explained by the scatter in the yield stress within the Biblis C vessel. The specimen used for EMPA experiment GR1H, on which the PSI model is based, is taken from a different location than the flat specimens with a central hole. The difference between the measured and predicted failure strain is less than 15%. The shape of the stress-strain curvers is reasonably predicted, especially for the 40 mm specimen.

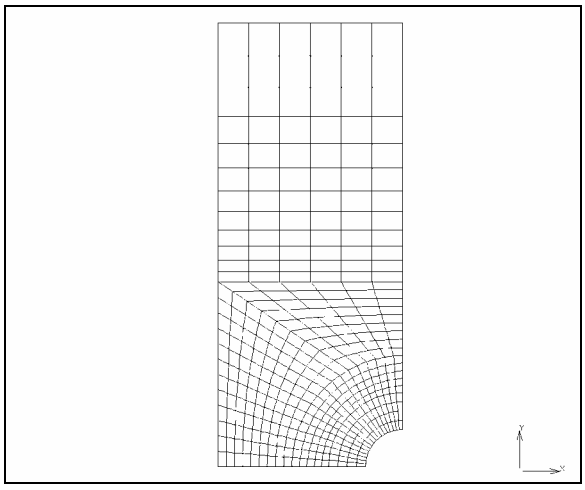

Fig. 3.2.3.2.-12: Mesh standard flat specimen with central hole

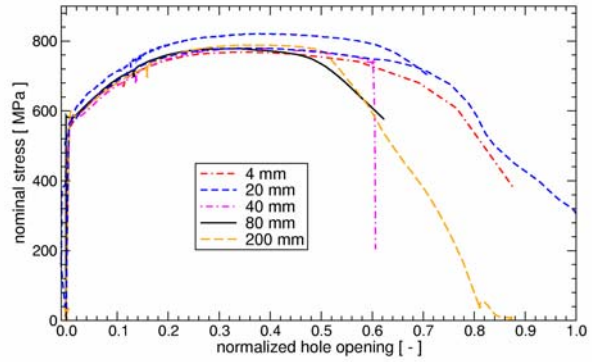

Fig. 3.2.3.2-13: Measured normalized hole opening

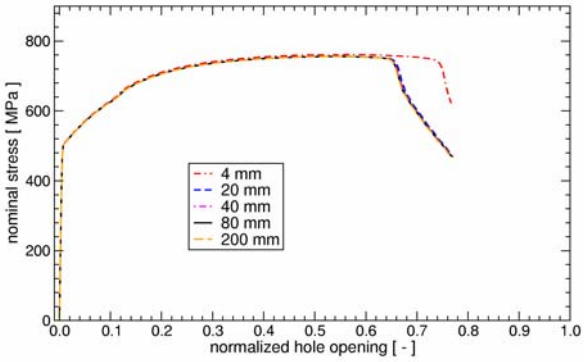

Fig. 3.2.3.2-14: Calculated normalized hole opening

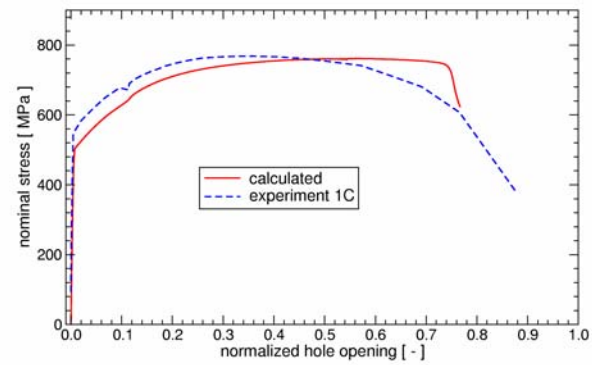

Fig. 3.2.3.2-15: Comparison normalized hole opening for 4 mm specimen

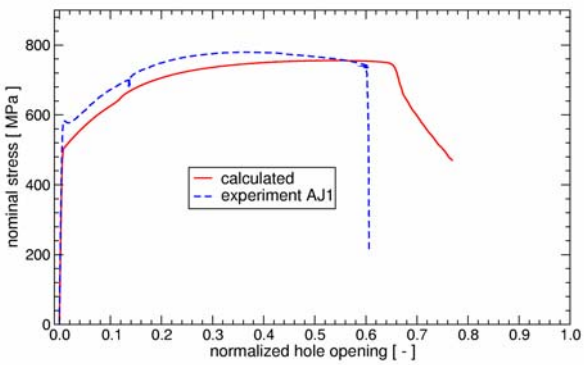

Fig. 3.2.3.2-16: Comparison normalized hole opening for 40 mm specimen

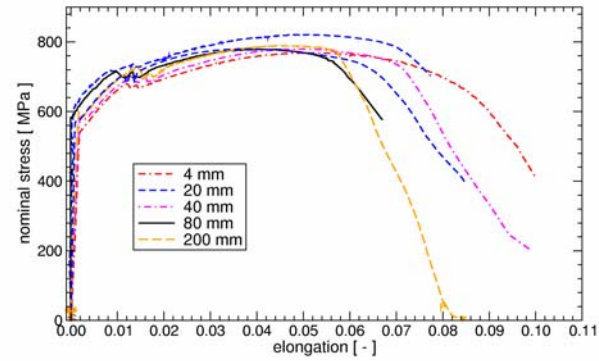

Fig. 3.2.3.2-17: Measured elongation

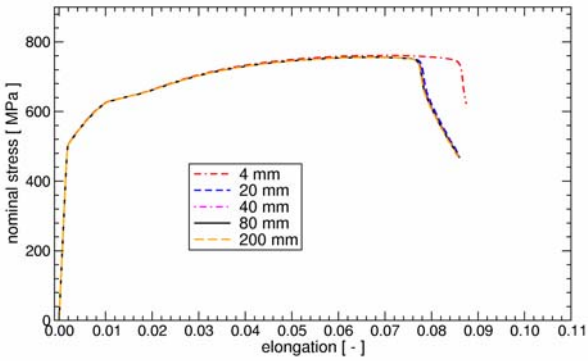

Fig. 3.2.3.2-18: Calculated elongation

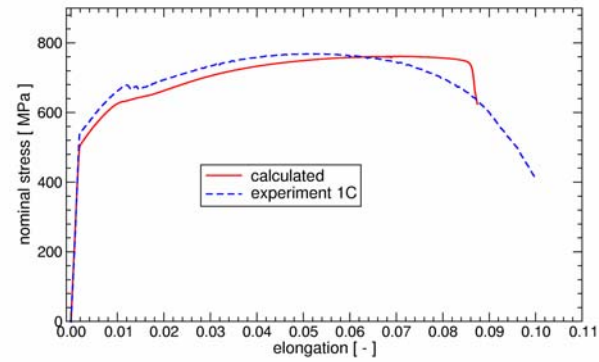

Fig. 3.2.3.2-19: Comparison elongation for 4 mm specimen

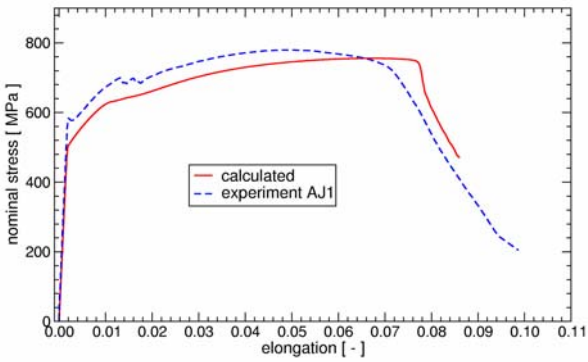

Fig. 3.2.3.2-20: Comparison elongation for 40 mm specimen

Flat specimen with double edge notch

The PSI model has been used to perform a finite element calculation for the tensile experiments at ambient temperature with the various sizes of a flat specimen with a double edge notch (4, 20, and 80 mm thickness). All test specimen have identical geometrical proportions and differ only in size. The notch diameter is half the thickness, the width is 2.5 times the thickness, and the gauge length is 6 times the thickness.

Fig. 3.2.3.2-21 shows the plane strain finite element model of the flat specimen with a double edge notch used for the calculations. The symmetry in the specimen enables it that only half the measurement section is incorporated in the model.

The specimens are “waisting” in the cross section between the notches. The highest plastic strains (> 100%) occur at the root of the notch. Small differences can be observed in the deformation around the notch. Because the calculation for the small specimen (4 mm) became numerically instable earlier than the calculations for the larger specimen the larger specimen deforms stronger around the notch. The initiation of failure can be seen in the load - deformation graph.

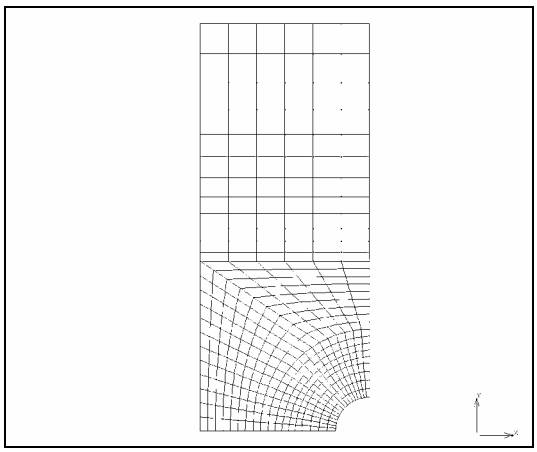

Fig. 3.2.3.2-21: Mesh standard flat specimen with double edge notch

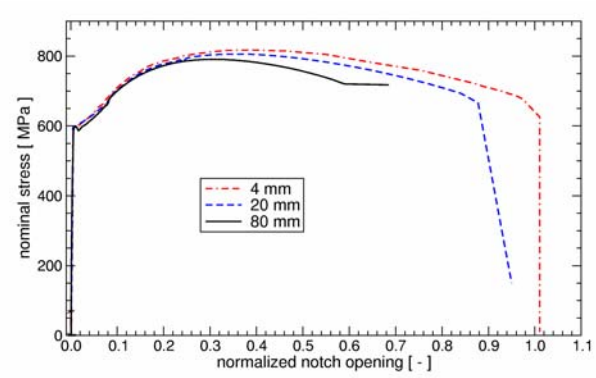

Fig. 3.2.3.2-22: Measured normalized notch opening

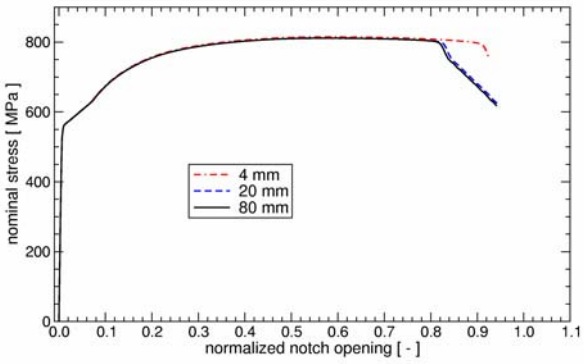

Fig. 3.2.3.2-23: Calculated normalized notch opening

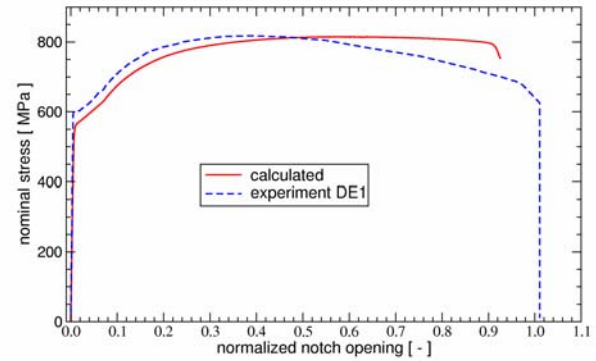

Fig. 3.2.3.2-24: Comparison normalized notch opening for 4 mm specimen

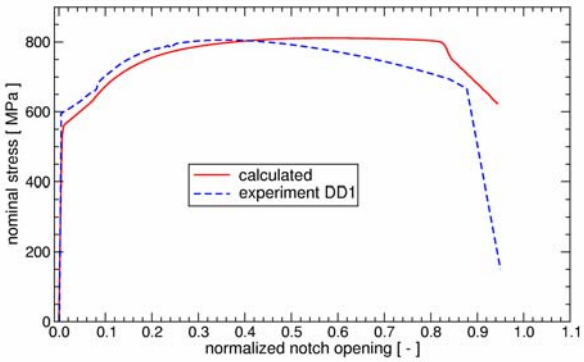

Fig. 3.2.3.2-25: Comparison normalized notch opening for 20 mm specimen

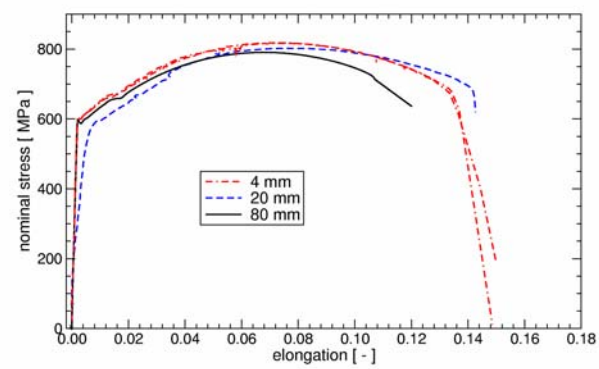

Fig. 3.2.3.2-26: Measured elongation

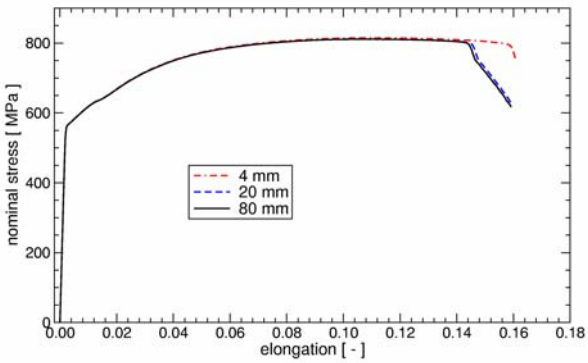

Fig. 3.2.3.2-27: Calculated elongation

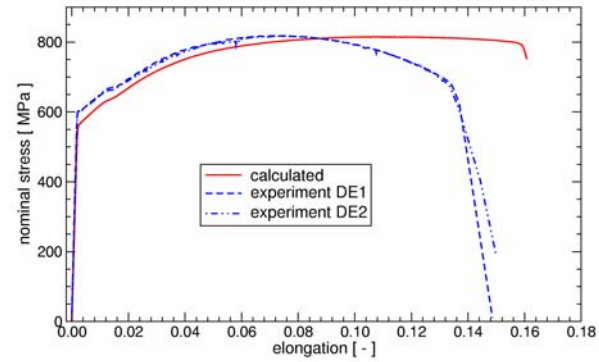

Fig. 3.2.3.2-28: Comparison elongation for 4 mm specimen

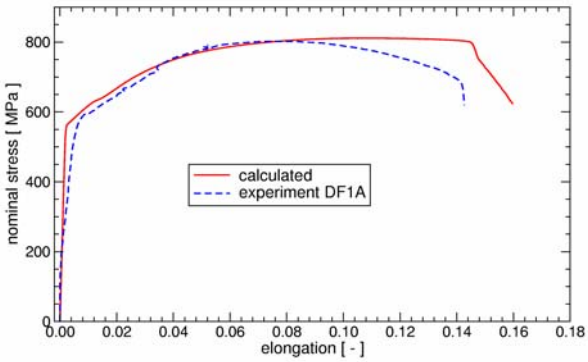

Fig. 3.2.3.2-29: Comparison elongation for 20 mm specimen

In the Fig. 3.2.3.2-22 to 3.2.3.2-29 the measured and calculated deformation behaviour of the flat test specimens with a double edge notch are compared. For the specimens the nominal stress is shown as a function of the normalized notch opening and elongation. The nominal stress, the normalized notch opening, and the elongation are defined as:

$$\sigma_{nom} = \frac{F}{(b_0 - d_0)\cdot t_0} \qquad \varepsilon_{notch} = \frac{d - d_0}{d_0} \qquad \varepsilon_{elon} = \frac{l - l_0}{l_0}$$

where:

- F : the axial force acting on the specimen
- b_0 : the initial width of the specimen
- d : the actual notch diameter (measured in axial direction)
- d_0 : the initial notch diameter
- l : the actual length of the measurement section
- l_0 : the initial length of the measurement section
- t_0 : the initial thickness of the specimen

The experiments show a size effect with respect to the failure strains, but no size effect with respect to the ultimate strength (Fig. 3.2.3.2-22 and 3.2.3.2-26). The calculations predict also a size effect, only with respect to the failure strain (Fig. 3.2.3.2-23 and 3.2.3.2-27). However, this size effect is only apparent for the 4 mm specimen (Fig. 3.2.3.2-23 and 3.2.3.2-27). For the 4 and 20 mm specimens a

comparison between the measured and calculated deformation behaviour is shown in the Fig. 3.2.3.2-24, 3.2.3.2-25, 3.2.3.2-28, and 3.2.3.2-29. The notch opening displacement predicted by the calculations is smaller than the measured notch opening displacement (Fig. 3.2.3.2-24 and 3.2.3.2-25). This is slightly more true for the 4 mm specimen than for the larger specimen. The elongation of the test specimen predicted by the calculations is larger than the measured elongation (Fig. 3.2.3.2-28 and 3.2.3.2-29). Based on the elongation the moment of failure is overestimated for the small specimen and reasonably predicted for the larger specimen. The shape of the stress-strain curves is reasonably predicted until the point of ultimate strength. Beyond that point the experimentally observed decrease of the nominal stress is not well predicted.

Compared to the round specimen with notch and the flat specimen with central hole the deformations in the flat specimen with double edge notch are much larger. Also a larger area of the specimen shows substantial deformations. The deviating calculation results beyond the point of ultimate strength can probably be explained by:
the fact that the finite element model of only the gauge length is too much simplified;
the “waisting” in the smallest cross section requires a 3-dimensional modelling.

3.2.3.2.4 Conclusions

A reasonable agreement is observed between measured and calculated deformation behaviour (notch opening displacement and elongation) for the circular specimen with a notch. The geometry of the test specimen has no influence on the results.

The deformation behaviour of the flat specimen with a central hole is also reasonably predicted. However, the agreement between the measured and calculated results is negatively affected by the fact that the material parameters for the PSI model have not been based on the average result of a number of tensile tests.

For the flat specimen with a double edge notch the calculations agree reasonably with the measurements up to the point of ultimate strength. Beyond that point the calculated results do not agree well with the measured result. This is probably due by the chosen finite element model or plain strain modelling.

The calculations only predict a remarkable size effect for the smallest specimens. This is in contradiction to the experimental observations.

3.2.4 Comparison of the theoretical models

Three different gradient plasticity approaches coupled with damage models (chapter 3.2.1)were examined and implemented in finite element codes or in an element free Galerkin method. The research works have shown that in principle the gradient plasticity models are able to predict size effects in elasticity, plasticity and damage. However the experimental results show, that a remarkable size effect is only observed in the damage phase that means in the load – deformation behaviour beyond crack initiation.

- The gradient plasticity model based on the theories of Aifantis and co-workers is able to describe the load – deformation behaviour of the experiments independent of the used mesh size. However the used damage models are not able to predict the failure strains quantitatively.
- The Gurson model extended with a gradient plasticity theory is also able to predict the experimentally observed load deformation behaviour. The model is also independent of the used mesh size. The predicted size effect in failure strains is underestimated especially for the larger specimens.
- The model using a micromorphic elasticity or plasticity theory is able to predict size effects in elasticity, plasticity and damage. However a quantitative statement could not be made due to the unknown material parameters could not be determined for the LISSAC material.

In conclusion it can be said that these types of models may yield a promising way for the element size independent description of size effects. However further investigations would be necessary to show, whether the models are really able to predict the experimental findings correctly.

The stochastic models (chapter 3.2.2) take into account the statistic nature of deformation and failure processes. Two different approaches were used within the LISSAC project.

- The stochastically extended Lemaitre model is not suitable for predicting size effects because the dominating influence of the scatter is hiding any systematic size effect. This is partly due to some restrictions of the straightforward way of the numerical implementation. However, the essential deficiency of the stochastic approach is that the physical mechanism behind the size effect in failure seems to be of a different nature.
- The second approach in this work package models the mesoscopic processes in material deformation. The randomly orientated grains with different shapes were modelled. Now numerical simulations can predict the influence of the inhomogeneous and anisotropic microstructure on the macroscopic load – deformation and failure behaviour of the material. It turns out that to some extend the microstructure is responsible for the experimentally observed size effect. Currently the predictions of the model are only of a qualitatively nature. To make quantitative predictions further considerable effort is required. The model has to be extended and verified and the model parameters have to be refined.

Finally local approach models in the classical sense (chapter 3.2.3) were used. The aspects of the discrete nature of the material (intrinsic length scales such as distance and/or size of inclusions, grain size, etc.) is taken into account by coupling the element size to the microstructure.

- The studied Rousselier damage model, included in a commercial finite element code, was able to predict the experimentally observed load – deformation and failure behaviour. The model predicts size and geometry influence on the failure strains quantitatively correct. The numerical results are in good agreement with the experimental findings. A minor disadvantage of this approach is that the mesh size is coupled to the microstructure. Due to this numerical limitations make it difficult to predict the behaviour of very small or very large specimens.
- The predictions of the Gurson Tvergaard model did not give satisfactory results. Therefore the Gurson Tvergaard model including gradient terms was used. Some of the results were promising, but more detailed verification work would be required for more definitive statements.

In conclusion it can be stated that only the Rousselier model was able to predict the size and geometry effect on the failure strains in a correct way. However the application of this model is numerically restricted due to problems resulting from the direct coupling of the element size to the microstructure of the material. A promising way to overcome this limitations could be the coupling of the Rousselier model with gradient models.

3.3 Evaluation of the results

3.3.1 Size effects

The experimental results presented in chapter 3.1.2 and 3.1.3 show that for each test family the load deformation curves are approximately size independent up to the point of failure (which, however, may be size dependent). Here the load is defined either as the force acting at the specimen divided by the relevant cross section of the specimen, or as the pressure applied at the specimen. If the maxima of the load deformation curves are reached before failure which is true in most of the cases, also the maximum loads will be approximately size independent.

These findings agree with theoretical studies in chapter 3.2.2.2, considering microstructural phenomena of the material with stochastic arrangements of grains. Considering the long term experience in material testing, the above results are not a big surprise.

The results for the failure strains presented in chapter 3.1.4.3 are more important. Some of them were not expected at the beginning of the LISSAC project. The findings can be described as follows:

- The local failure strains (logarithmic strains) are always higher than 50 %, which is much more than assumed in many analyses, so far.

- The local failure strains decrease moderately with increasing specimens, i.e. there is a moderate size effect. For the smallest specimens with thicknesses or diameters of only a few millimetres and hole or notch radii of less than 1mm the local failure strains reach about 150 %, for very large tension specimens typical for a reactor pressure vessel the local failure strains decrease to about 70 %, for large biaxial specimens they decrease to 50 to 60 %.

  This tendency is in line with the state-of-the art knowledge described in chapter 1.2.

- The parameter which describes the size effect is the radius of holes or notches located in the smallest cross section of the specimens where the stresses reach the highest values. The other dimensions of the specimens play a minor role.

  The strong influence of the radius of holes or notches on the local stress and strain is well known since many year. However the influence on the *local failure strain* was not very clear, so far.

- The type of specimens and load has only small influence on the failure strain. Tests carried out with tension and bending specimens under uniaxal load, as well as tests with plate or shell type of specimens under biaxial load yield about the same failure strains – provided the hole or notch radius is the same. This finding was not really expected when the project has been started.

- These experimental results can be confirmed by the Rousselier damage model. It was able to predict the experimentally observed size and geometry influence on the failure strains quantitatively correct. The numerical results are in good agreement with the experimental findings.

- The obtained scatter is considerable. Nevertheless the essential trends can be clearly seen and – as discussed later – reliable limits can be defined.

Some of these experimental findings about the size effects of failure strains can also be explained qualitatively by the microstructural character of the material with stochastic arrangements of grains, as discussed in chapter 3.2.2.2.

A very interesting experimental result is also obtained concerning the mode of failure. For a test with a curved biaxial specimen under static load provided by an almost incompressible liquid a rather big fragment of the specimen was completely teared off and hurled away.

The above statements concerning the failure strains can be verified, if the failure strains listed in chapter 3.1.4.3 are presented in diagrams as shown in Figs. 3.3.1-1 to 3.3.1-6.

The first diagram includes all failure strains obtained at room temperature under static load. The different types of specimens and loading are indicated by different symbols. Fat black symbols describe regular results. Red symbols mean, that the tests are impaired by poor manufacturing of the specimens; green symbols indicate that failure did not occur. Dotted, dashed or grey symbols indicate that other evaluations of the tests were performed leading to results which are less reliable, or that the results are questionable for other reseasons. For more details refer to chapter 3.1.4.3. In some cases the symbols have been shifted in horizontal direction a little bit, to allow the identification of single tests.

From Fig. 3.3.1-1 it turns out that the failure strains are indeed governed by the radius of the holes or notches, while the type of specimen and load has minor influence only. This is illustrated in Fig. 3.3.1-7 for specimens under uniaxial loading. The failure strains for all these specimens are about the same, since the hole or notch radii are the same. The large variations of the other dimensions of the specimens and whether tension or bending forces are applied is of minor influence. A corresponding illustration including also specimens under biaxial loading would be even more impressive!

The somewhat smaller failure strains obtained for bending specimens might be caused by the visual inspection of these specimens during testing. So the crack could possibly be detected at an earlier state than with the vanishing gap methods. This seems to be especially true for the biggest bending specimen where the size of the detectable crack was very small in comparison to the notch radius.

Specimens containing no holes or notches were interpreted as specimens with infinite holes or notches, i.e. $r \rightarrow \infty$. In the diagram the radius $r \rightarrow \infty$ is placed at that position of the abscissa where r would be 100 mm. With this assumption the failure strains for biaxial specimens without holes fit very well with the general trend of the other failure strains.

Note that for the biaxial specimens without holes the failure strain does not depend on the specimen size. This is in line with the finding that the size effect on the failure strain is governed by the radius of holes or notches.

The results obtained from the standard tension tests with smooth specimens (which do not belong to any test family) yield higher failure strains which do not fit with the general trend of the results. Perhaps here the radius should not be assumed to be infinite, rather the radius of the necking before failure or even the radius of the cross section should be taken as the governing parameter.

The diagram 3.3.1-2 shows the failure strains obtained for 400 °C under static load. The diagrams 3.3.1-4 and 3.3.1-5 show the failure strains obtained at room temperature and for 400 °C under dynamic load. The symbols are defined according to the same rules as used for diagram 3.3.1-1. Of special interest are the results obtained for biaxial specimens without holes under dynamic load shown in Fig. 3.3.1-4. Again it turns out that the failure strain does not depend on the specimen size, which supports the finding that the size effect is only govern by the hole or notch radius. This finding is also supported by a late experiment which could not be included in diagram 3.3.1-4, but which is mentioned in the introduction of chapter 3.1.4.3.

Comparison of the diagrams discussed above shows that a temperature increase to 400 °C and a change to dynamic load has no significant effect on the failure strain. Thus in the diagrams 3.3.1-1 and 3.3.1-2 as well as in 3.3.1-4 and 3.3.1-5 the failure strain versus the hole or notch radius can be approximated by the same straight line (straight curve). It has been determined in such a way that the sum of the squares of the deviations from the values obtained for the particular tests is minimized. Here only the reliable values for finite hole or notch radii (not the values marked by red, green, dashed or dotted symbols and not the values for $r \rightarrow \infty$) were considered.

Of course, the results obtained at 850 °C under static load shown in Fig. 3.3.1-3 and under dynamic load shown in Fig. 3.3.1-6 can hardly be described by the straight line applicable for the specimens at room temperature and at 400 °C. Rather particular straight lines representing the findings in each of the diagrams separately have been introduced. The rules are the same as explained above. However, to improve the poor data basis, for determination of the straight line representing the results at 850 °C under dynamic load, the (somewhat questionable) failure strains for r = 0.3 mm described by red circles have been included.

For 850 °C and static load the failure strain seems to be about the same as for room temperature and 400 °C, if only large notch or hole radii are considered. However the increase of the local failure strain with decreasing radius is much lower than in the cases of room temperature and 400 °C. In other words, for 850 °C and static load there is almost no size effect on the failure strain.

For 850 °C and dynamic load the failure strains are generally higher than discussed before; but again, there is almost no size effect. In fact at 850 °C it has been found that the material under dynamic loading exhibits improved behaviour both in terms of strength and deformation with respect to the static case. As mentioned already, here the data basis is rather poor and therefore conclusions should be made with caution.

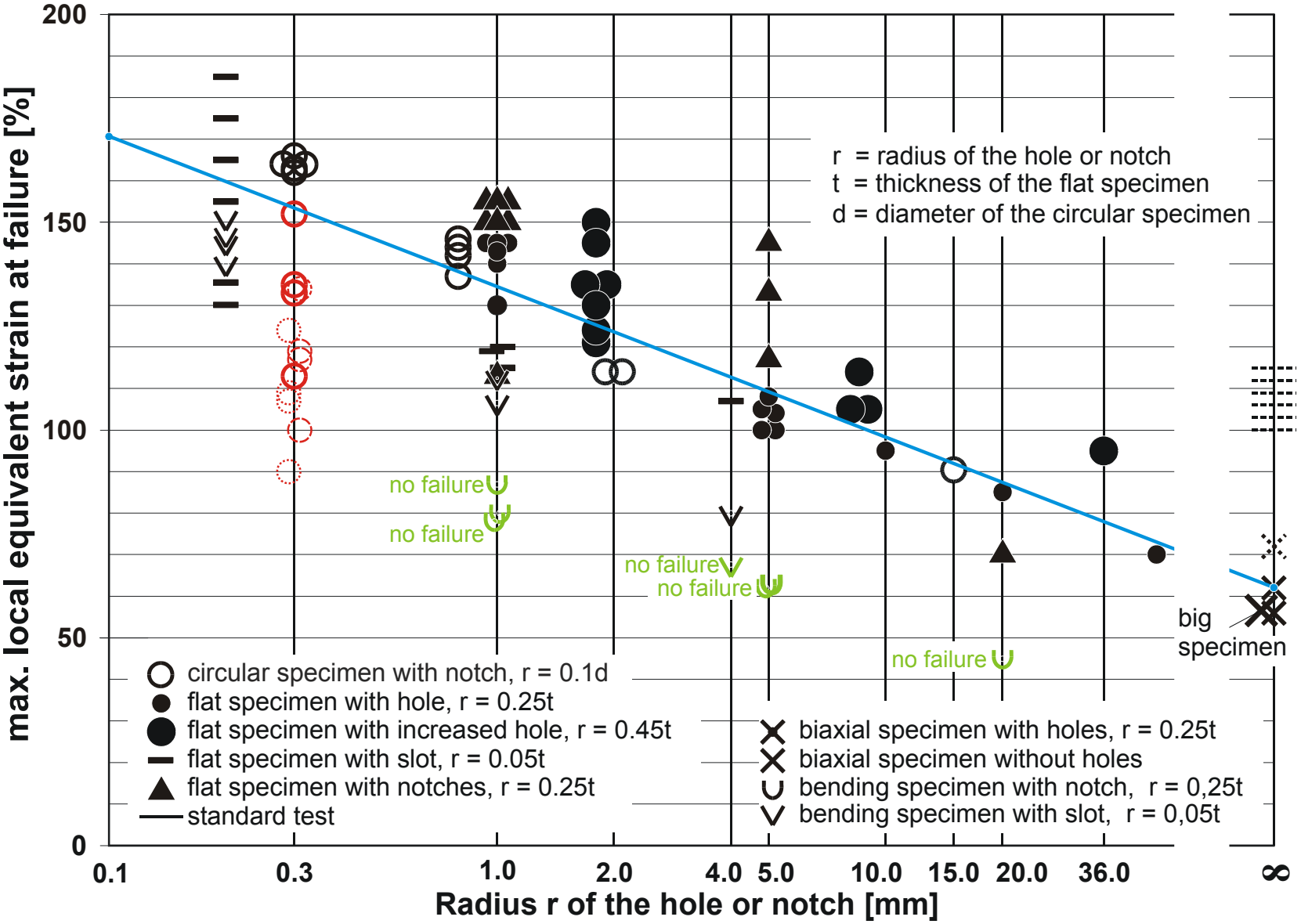

Fig. 3.3.1-1: Main results of LISSAC for RPV material at room temperature, static tests

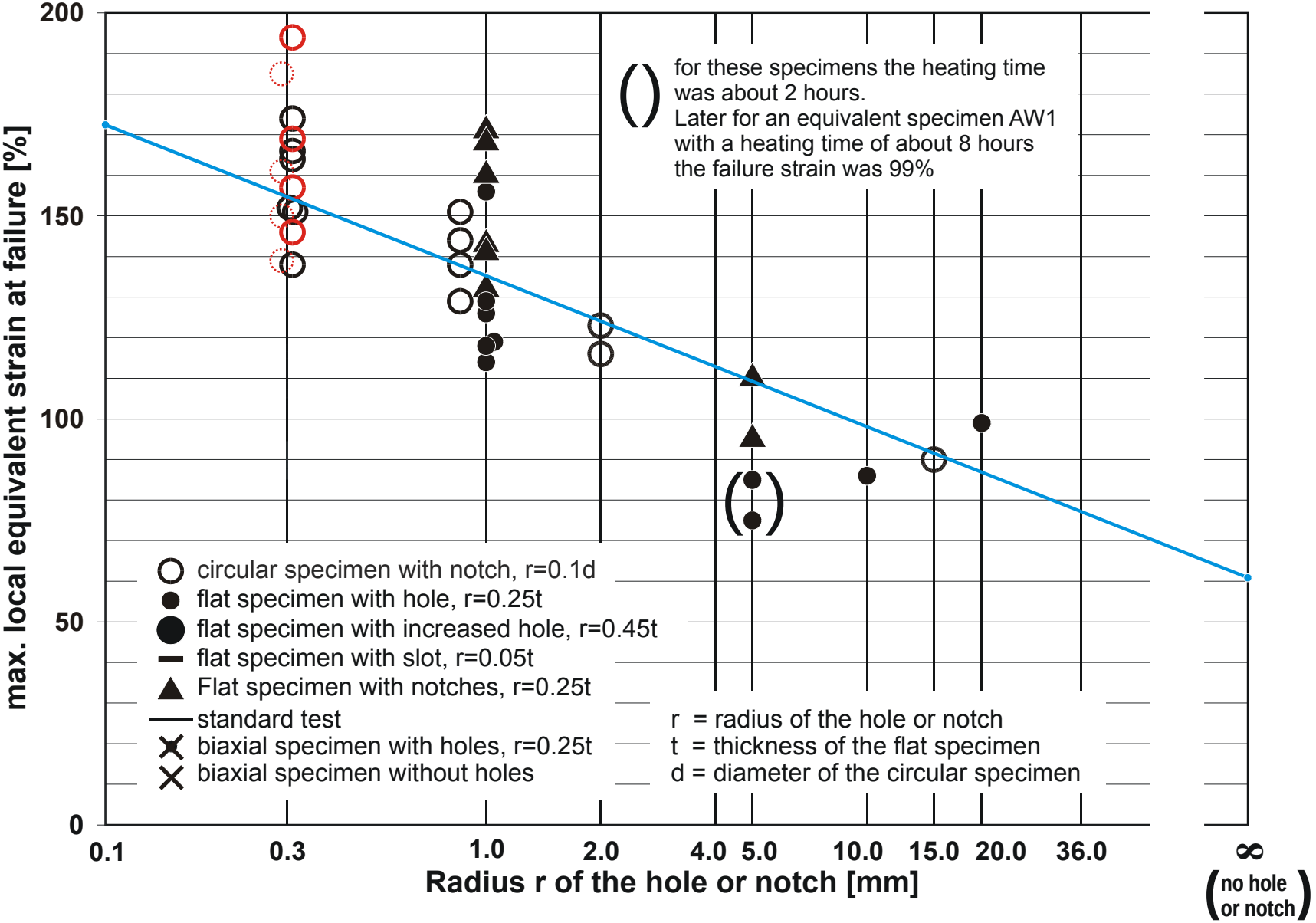

Fig. 3.3.1-2: Main results of LISSAC for RPV material at 400°C, static load

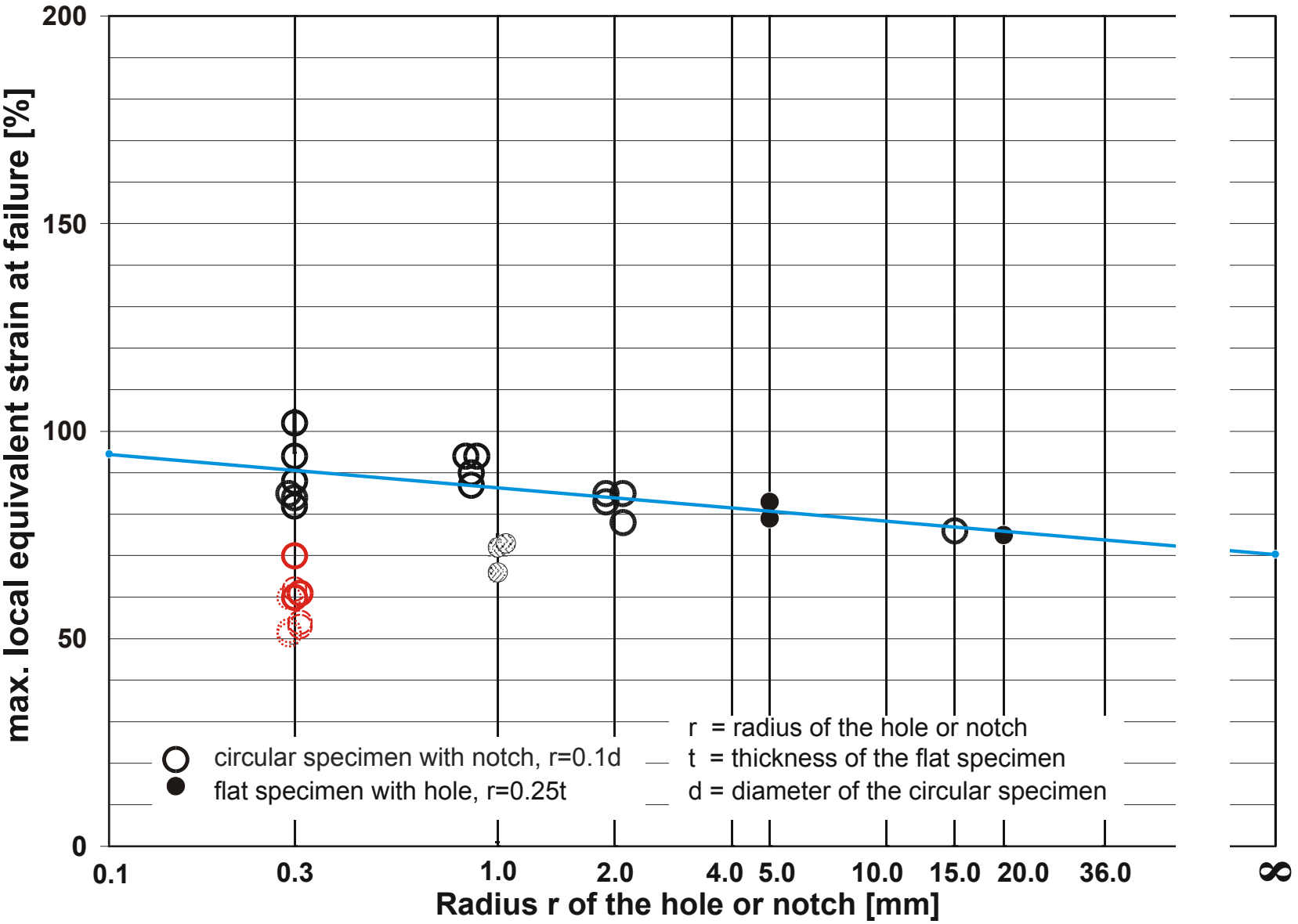

Fig. 3.3.1-3: Main results of LISSAC for RPV material at 850° C, static tests

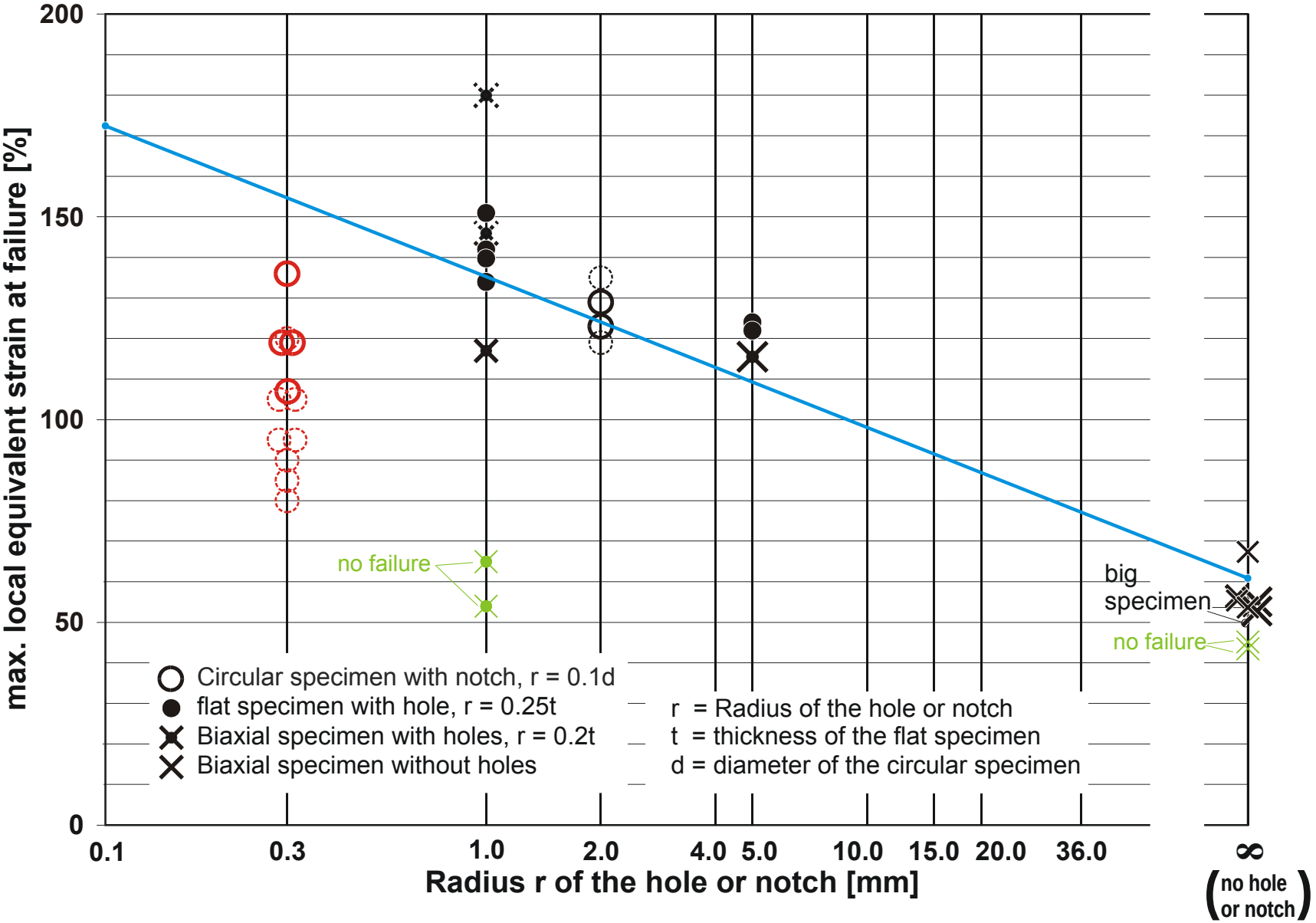

Fig. 3.3.1-4: Main results of LISSAC for RPV material at room temperature, dynamic tests

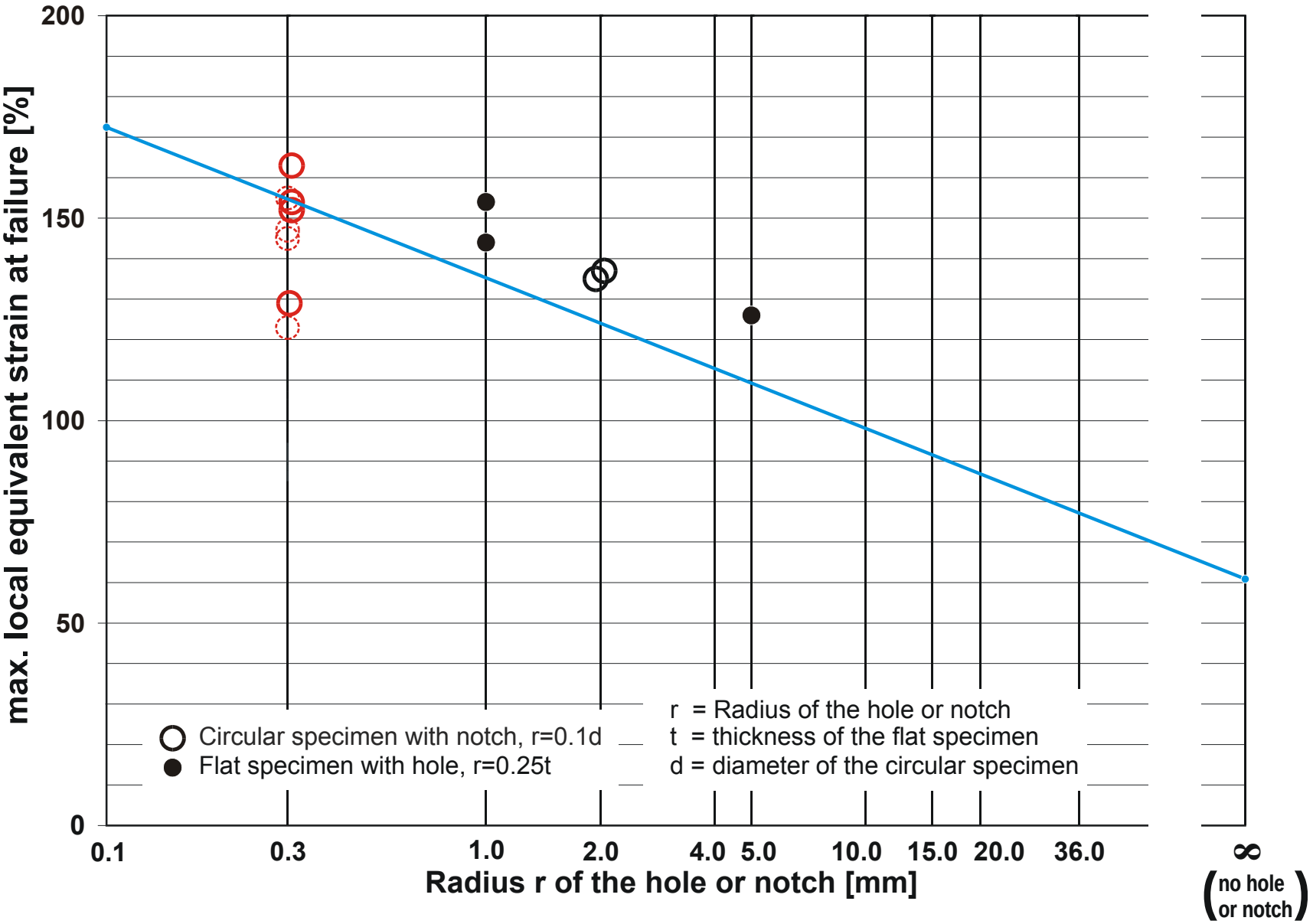

Fig. 3.3.1-5: Main results of LISSAC for RPV material at 400° C, dynamic tests

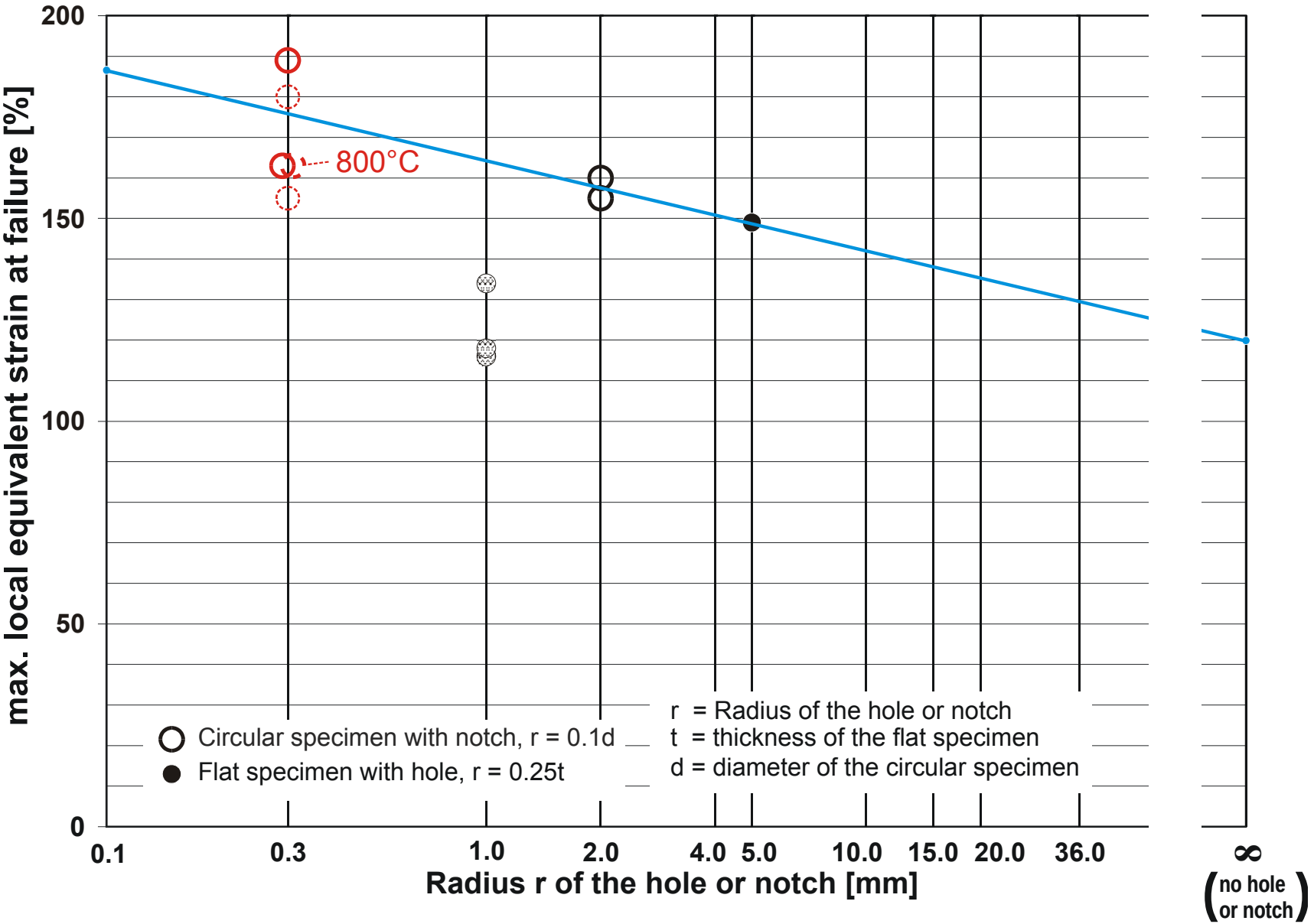

Fig. 3.3.1-6: Main results of LISSAC for RPV material at 850 ° C, dynamic tests

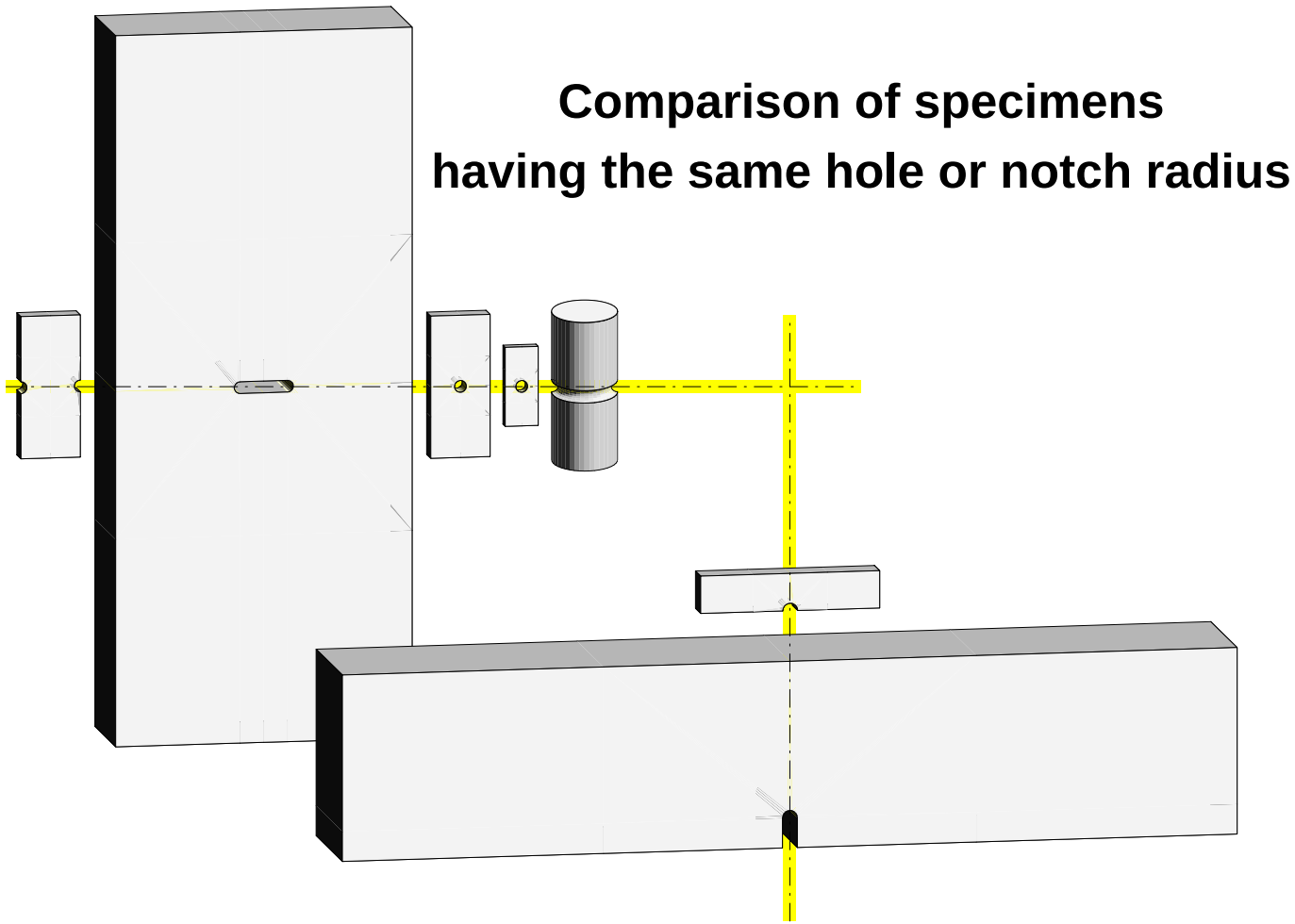

Fig. 3.3.1-7: Comparison of specimens under uniaxial loading having the same hole or notch radius, but very different size. The failure strains of all these different specimens turn out to be about the same.

3.3.2 Statistical evaluation

3.3.2.1 Prediction confidence curves for the results at room temperature and 400 °C

The results in Figs. 3.3.1-1 to 3.3.1-6 reveal significant scatter. It reflects mainly the intrinsic character of the material. As discussed in chapter 3.1.4.4, measuring errors may contribute only partly to these deviations.

By using of statistical methods, prediction confidence curves have been determined. Since a temperature increase to 400 °C and a change to dynamic load has no significant effect, all the results shown in the diagrams 3.3.1-1 and 3.3.1-2 as well as in 3.3.1-4 and 3.3.1-5 were considered, except the values for $r \rightarrow \infty$ and the values which are questionable or not applicable for other reasons (values marked by red, green, dashed or dotted symbols). The probability concept used assumes a so-called Student distribution [1, 2] for the failure strain and delivers confidence limits for arbitrary radii as shown in the Fig. 3.3.2-1. The dots describe all the failure strains considered. The straight line represents the mean values of the failure strains as introduced above. The prediction confidence curves below this straight line describe the strains where 2.5 % of the specimens are expected to fail, or 0.5 % are expected to fail, respectively.

From a safety point of view prediction confidence curves would be of interest showing the strains where much less specimens, for instance only 10^{-4} or even 10^{-6} of the specimens are expected to fail. However to obtain such curves just on the basis of statistical evaluations, a huge number of tests would be required – much more than performed within the current LISSAC project.

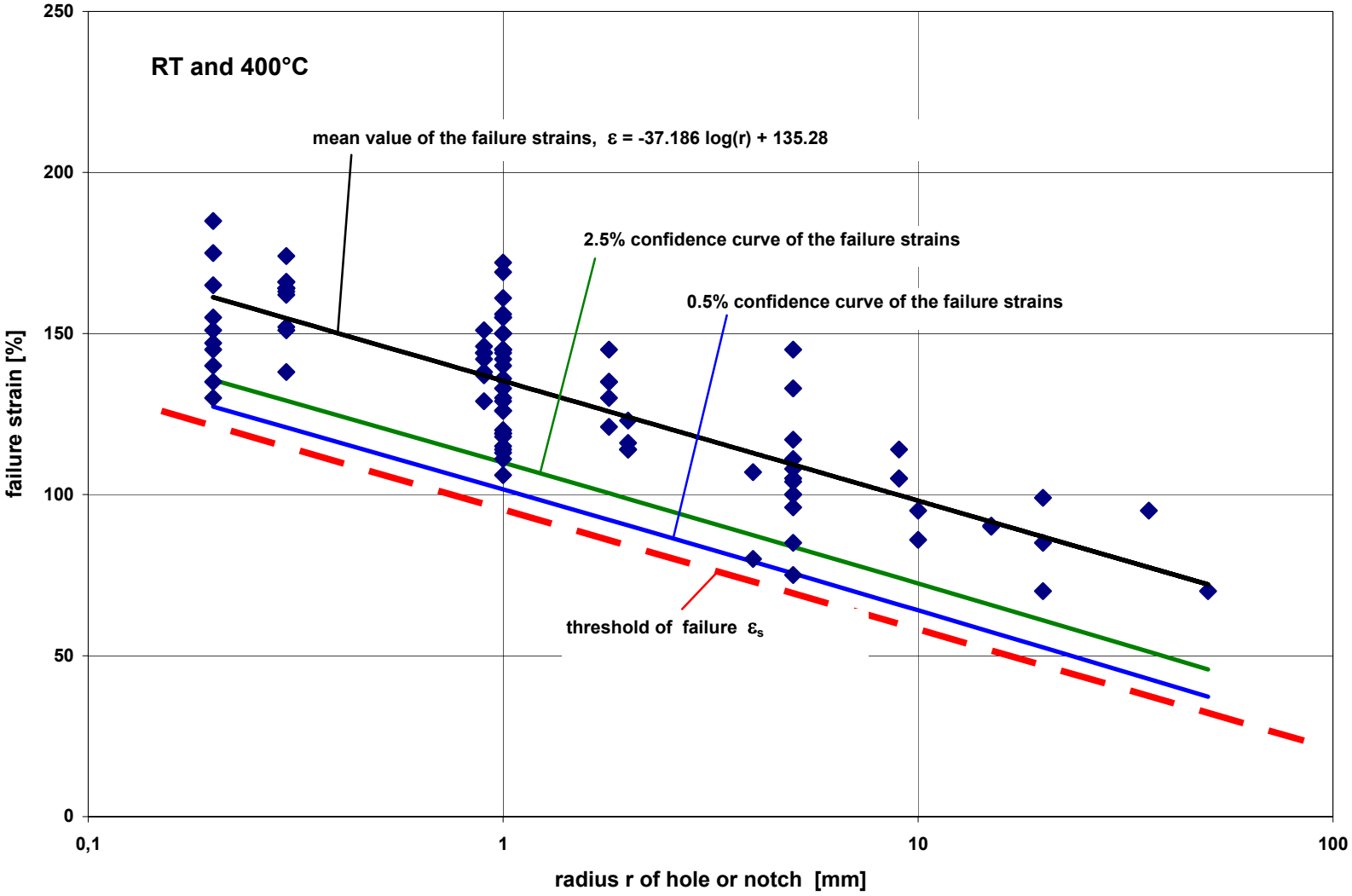

Fig. 3.3.2-1: Prediction confidence curves for the obtained failure strains

3.3.2.2 Derivation of a threshold strain

The distributions of the probability of failure based on the concept of Student, but also the distributions based on other widely used concepts, consider small probabilities of failure even for strains far away from the mean strains of failure described by the straight lines (curves) in the previous diagrams. However in many cases this assumption might not really reflect the actual physical facts.

Therefore it is interesting to determine the distribution of the frequency of failure directly from the experimental results of LISSAC. This distribution is shown in Fig. 3.3.2-2. It can be interpreted as an approximation of the distribution of the probability of failure for the relevant LISSAC specimens.

Note that these distributions are quite resistant against possible outliers. The character of these distributions may hardly be changed by one or two additional experimental results deviating significantly from the general trend.

Figure 3.3.2-2 shows clearly that the distribution approaches vanishing probability of failure more rapidly than the distributions based on the concept of Student, for instance. This has physical reasons. Failure strains much lower than the mean values may only be caused by large material defects like large inclusions, voids, cracks, etc, or by inadequate heat treatment. However most material defects are excluded by non-destructive material tests performed for the reactor pressure vessel. Consequently the probability of failure for strains much lower than the threshold ε_s marked in Fig. 3.3.2-2 is identical with the probability that large material defects have been overlooked during the non-destructive material testing or that the heat treatment was inadequate. However this probability is rather low, perhaps on the order of 10^{-4} or less.

For the further investigations it is conservatively assumed that the threshold ε_s is 40 % below the mean values of the failure strain. The resulting curve (straight line) is also introduced in Fig. 3.3.2-1. For strains below the threshold the probability of failure is govern by the reliability of the non-destructive material tests the heat treatment, etc., as explained above.

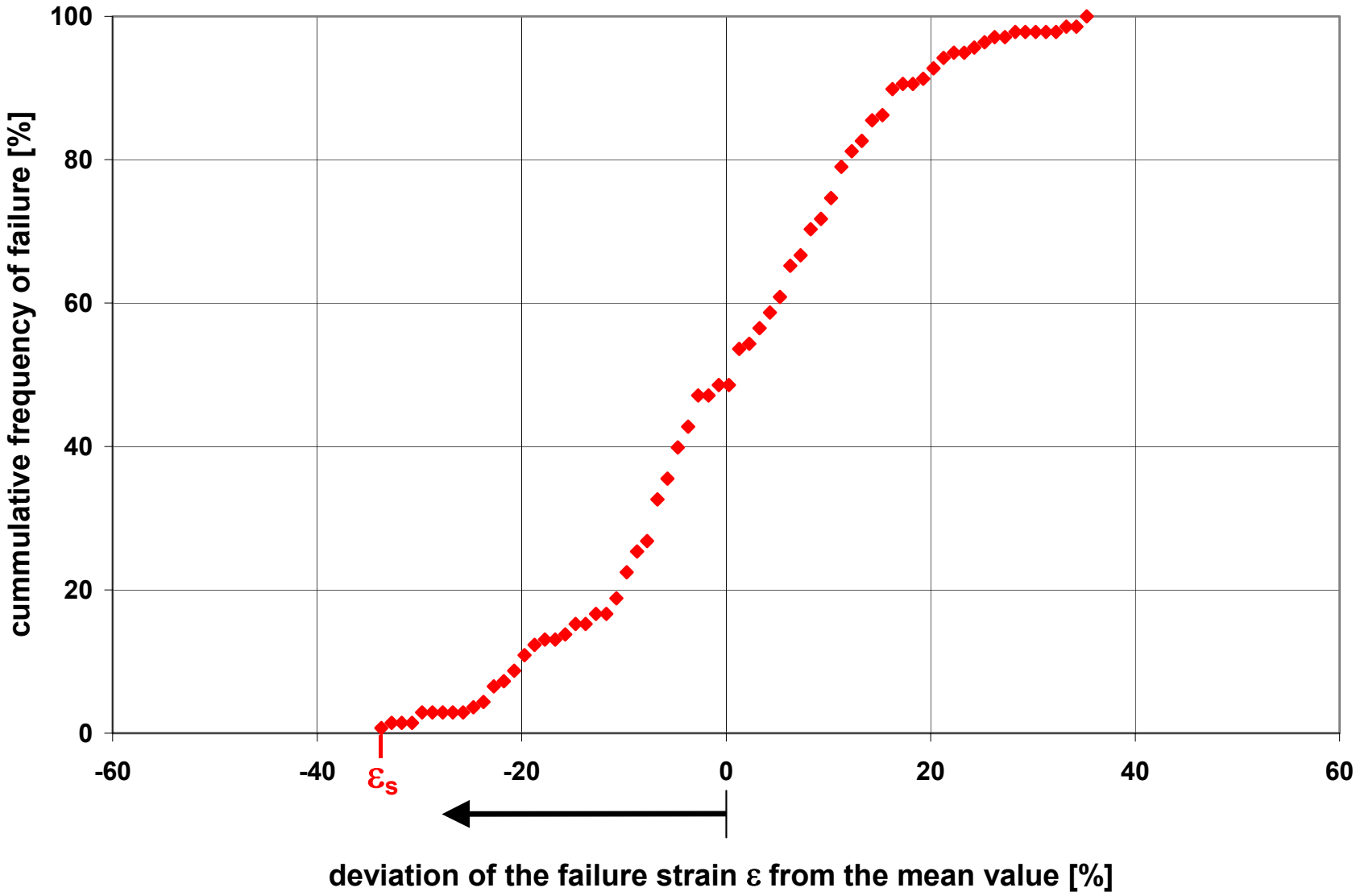

Fig. 3.3.2-2: Distribution of the probability of failure

3.3.3 Proposal of Limit Strains for Severe Accident Conditions

3.3.3.1 Proposal for the specimen shapes and load conditions investigated in the LISSAC project at room temperature and 400 °C.

Based on the experimental results evaluated above the limit strain versus the hole or notch radius is proposed as shown in Fig. 3.3.3-1. The curve consisting of two straight lines is below the 0.5%-confidence curve and somewhat below the threshold of failure ε_s. For a hole or notch radius $r \geq 100$ mm the proposed limit strain is 20 %. For a hole or notch radius $r < 100$ mm the proposed limit strain increases linearly until for $r = 1$ mm it reaches 80 %. For a hole or notch radius $r < 1$ mm a further increase of the limit strain should be considered with caution, since in this region manufacturing problems gain significant influence.

Special attention should be given to the limit strain of 20 % for specimens without holes or notches. In the prediction confidence curves the measured failure strains for these conditions were not included. However a closer view reveals that the failure strains for the smooth specimens varied between 53 % and 62 % (see Figs. 3.3.1-1 and 3.3.1-4) which is much higher than the proposed limit strain. Furthermore it should be considered that all the specimens under discussion here where tested under biaxial load which is rather realistic for the reactor pressure vessel.

If the limit strain is not exceeded, it is suggested that failure should not be considered under severe accident conditions.

3.3.3.2 Proposal for the specimen shapes and load conditions at 850 ° C

It may be expected that the scatter is about the same as for room temperature and 400 °C. Thus the limit strains for 850 °C should have the same distance from the mean values of the failure strains (described by the straight lines in Figs. 3.3.1-3 and 3.3.1-6) as in the case of room temperature and 400 °C just discussed. Note, however, that for 850 °C the data basis is much smaller and consequently also the reliability of the limit strains is smaller than for room temperature and 400 °C.

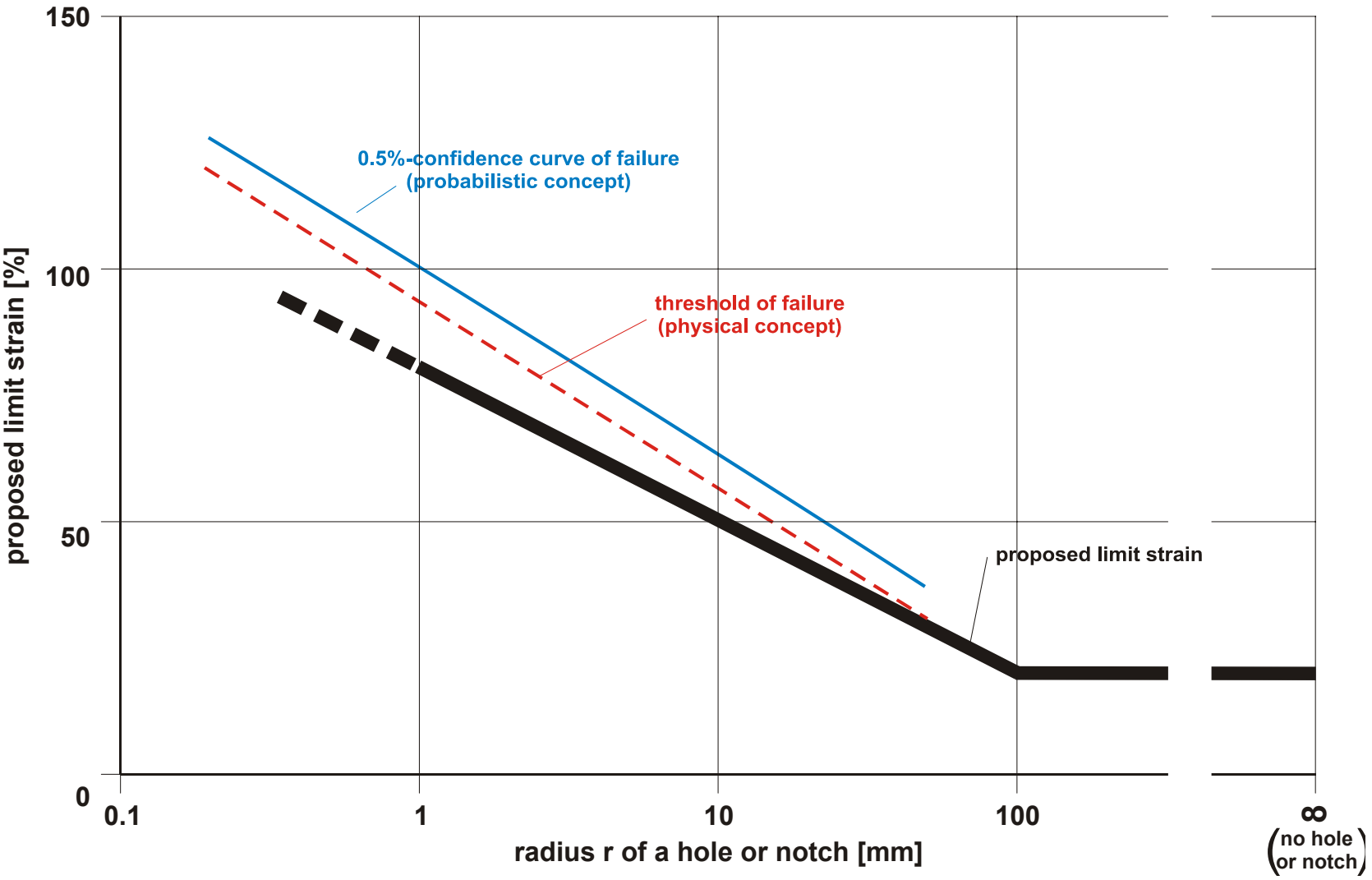

Fig. 3.3.3-1: Proposed limit strains for static and dynamic loading at room temperature and 400 °C

3.3.3.3 Extrapolation of the results to other specimen shapes and load condition

As already mentioned in chapter 3.1.4.1, the failure strains obtained and consequently the limit strains proposed are applicable for geometries and load conditions similar to those investigated in the current project. An extrapolation to other conditions should be made with caution.

Theoretical considerations show clearly that for stress distributions approaching uniform triaxiality (the same principle stress in three directions) the failure strains must reduce to very low values given by the volume expansion of the material. By the way, in many theoretical models, including models developed within this project, the volume expansion is restricted to the elastic regime or even neglected.

As a matter of fact, many severe accident conditions of the reactor pressure vessel are addressed by the current research work. But there are exceptions. At the intersection zone between reactor pressure vessel wall and nozzle, for instance, higher triaxiality of the stress conditions may occur than in the tested specimens.

Here two tension tests should be mentioned, recently carried out by MPA within another project (in chapter 3.2.3.1 referred as ESIS), but using specimens made from LISSAC material. The specimens had circular shape, diameter 18 mm, with a circumferential notch like the corresponding LISSAC specimens, notch width 4 mm, notch radius 2 mm, smallest specimen diameter 10 mm. Thus the ratio between the smallest cross section and the cylindrical cross section was 0.31, while for the corresponding LISSAC specimens this ratio was only 0.64. The broken specimens were evaluated in the same way as the LISSAC specimens (vanishing gap method using a three-dimensional measuring machine). The relative notch opening was determined to 24 % and 32 %, respectively; the failure strain was determined to 43 % and 58 %, respectively.

For comparison, the failure strain for the corresponding LISSAC specimens was 114 %. The strong deviation is assumed to be caused by the different triaxiality of the stress conditions.

Extrapolation to conditions not too far from the LISSAC test conditions are possible by using theoretical models also developed within the current project. Using the Rousselier model the failure strains for the specimens discussed above were predicted with a high accuracy for room temperature. For higher temperatures no reliable predictions can be made.

However, to get a satisfying basis for such extrapolations and to assess the limits which should not be exceeded, some additional tests with larger variations of the specimen geometry and accompanying analyses with the above models would be helpful.

3.4 Applications

3.4.1 Model experiments considering large strains

Example: Integrity of the reactor vessel head during a postulated in-vessel steam explosion

It is assumed that a steam explosion occurs in the lower plenum of the reactor pressure vessel accelerating a molten core material slug against the upper vessel head. The kinetic energy of the slug which the vessel head can safely carry has to be determined. This complex liquid structure impact problem has been solved by model experiments in scale 1:10 [1].

Figure 3.4.1-1 shows the maximum local strains in mock-ups of the vessel head, obtained for slug impact tests with different impact velocities. In scale 1:10 the impact mass was assumed to be 80 kg. Using this mass the related impact energy can be calculated. It is introduced at the abscissa, too. The different symbols address different test conditions including case A without upper internal structures, case B with only the upper grid available and case C with all the upper internal structures available. The results are linearly interpolated and extrapolated (in case B the very extended extrapolation is questionable).

According to the state-of-the-art knowledge the acceptable strain is not more than 5 %. Then the admissible liquid slug energy for case A is 0.15 MJ, for case B it is 0.43 MJ and for case C it is 1.04 MJ, as shown in the figure. (In [1] further facts had to be considered and consequently the values mentioned there are a little bit different).

As a result of the current project the acceptable strain is much higher. Using the diagram 3.3.3-1 and considering that the radius of the holes in the (real) head is 50 mm, the acceptable strain is about 28 %. Thus the admissible liquid slug energy increases to 0.3 MJ, 1.07 MJ and 1.33 MJ, respectively.

In other words, using the results of the current project, the admissible energy for case A increases by a factor 2.0, for case B it increases by a factor 2.5 and in case C it increases by a factor of about 1.3. (As a consequence of the extended extrapolation, the result for case B is questionable).

Note that simply using the impact energies where in the model experiments the heads fail, would be wrong (too optimistic) for two reasons. In the model experiments the holes in the head are smaller and consequently the failure strain is larger than for the real size head (in diagram 3.3.3-1 compare the failure strains for r=5 mm and r=50mm). Furthermore the scatter of failure would not be considered.

The conversion of the admissible impact energies determined in the model experiments into admissible energies for the real size pressure vessel is througly discussed in [1].

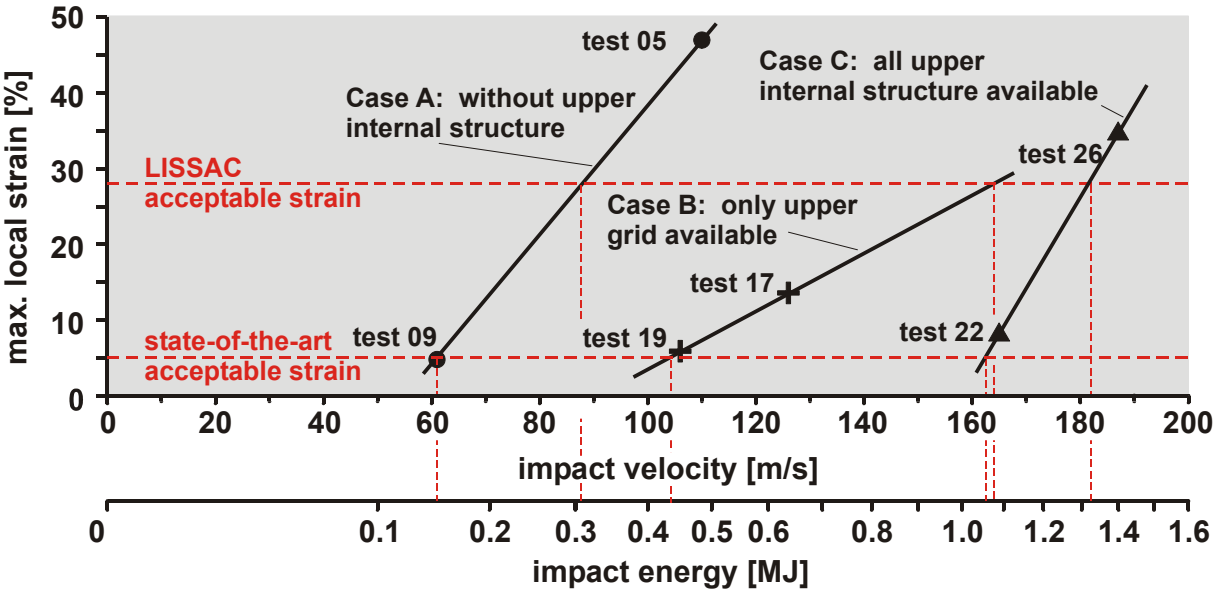

Fig. 3.4.1-1: Maximum local strain versus impact velocity or impact energy, respectively.
For different acceptable strains (state-of-the-art: 5 %; LISSAC: 28 %), different admissible energies are obtained.

3.4.2 Structural mechanics calculations allowing large strains.

Example: Analysis of the reactor vessel head

The pressure bearing capacity of the upper vessel head has been also investigated using finite element analyses applying both the code ASME III, Division 1, Appendix F 'Rules for evaluation of service loading with level D service limits' [1], as well as the admissible strains determined in the current project. The holes in the upper head have been neglected.

The ASME evaluation has been based on the results of an elastic and an elasto-plastic finite element calculation. For the later case the options for large strains and large displacements have been invoked. The results of the elasto-plastic analysis compared very well with the experimental results obtained by VTT (SAM-LISSAC-D030).

The maximum pressure load according to the ASME evaluation of the elastic calculations is 61.56 MPa. Figure 3.4.2-1 shows the distribution of the equivalent stress in the deformed upper head at this pressure. The code evaluation is performed for the two locations shown in the figure. The maximum pressure load is determined by the limit on the membrane stress in the centre of the shell (location B).

The maximum pressure load according to the ASME evaluation based on the elasto-plastic finite element calculation is 90.85 MPa. The distribution of the equivalent stress at this pressure is shown in figure 3.4.2-2. The maximum plastic strain at this pressure is approximately 3.5%. Again the maximum pressure load is determined by the stress level at the centre of the shell.

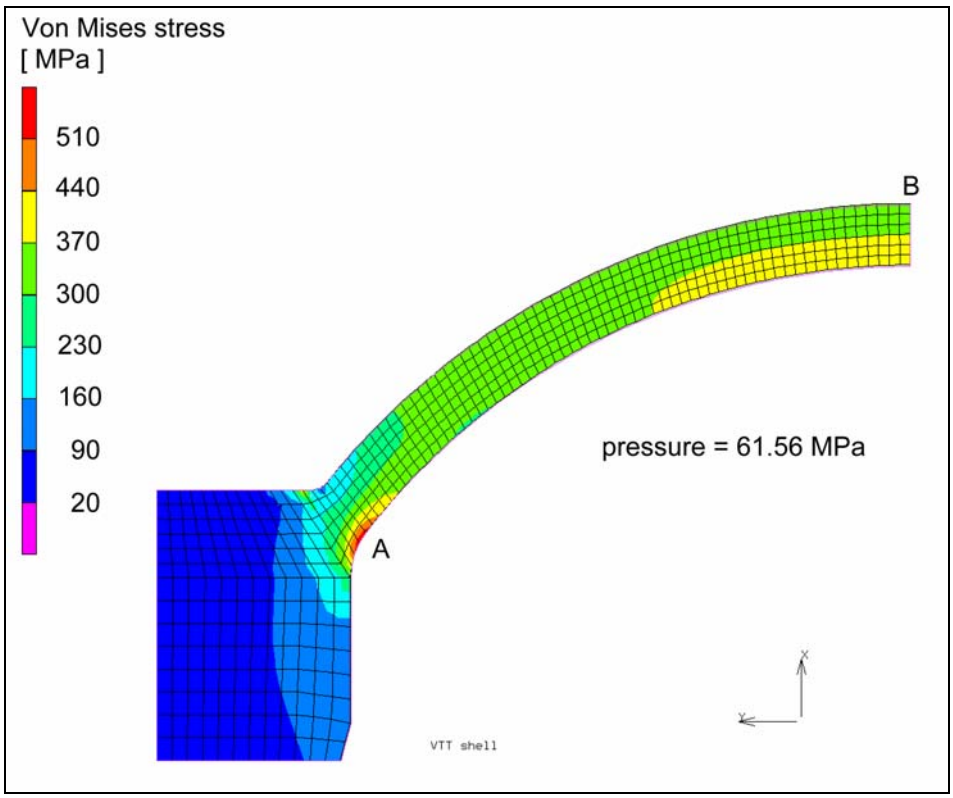

Fig. 3.4.2-1: The Von Mises stress at the pressure load according to the ASME evaluation based on an elastic FE calculation

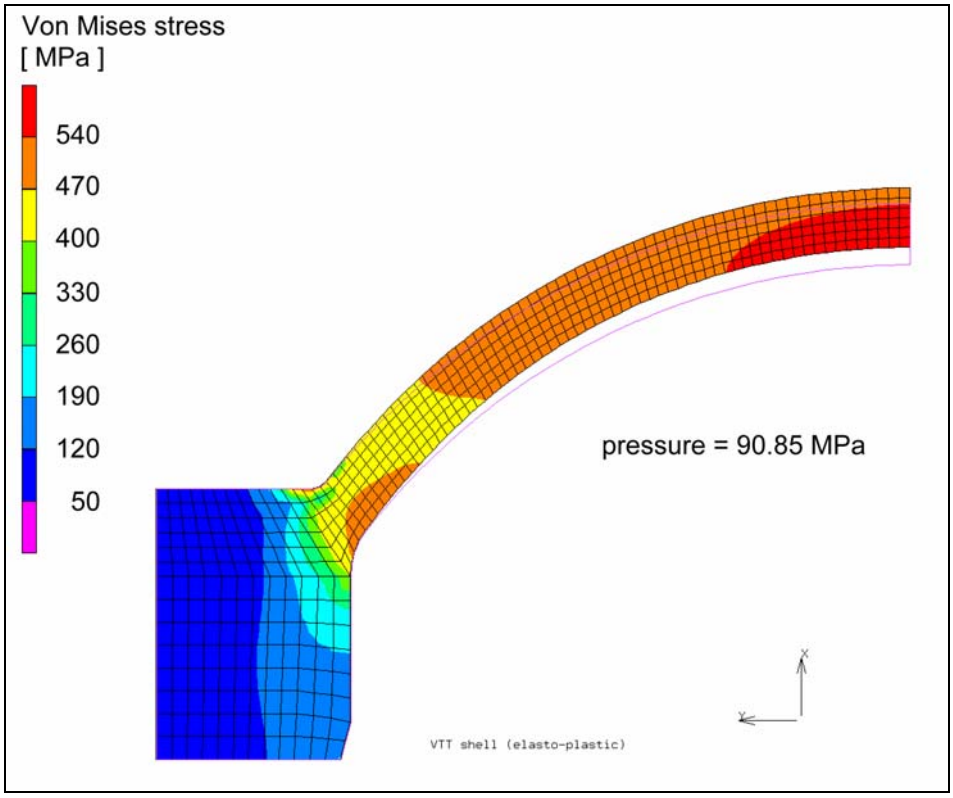

Fig. 3.4.2-2: The Von Mises stress at the pressure load according to the ASME evaluation based on an elasto-plastic FE calculation

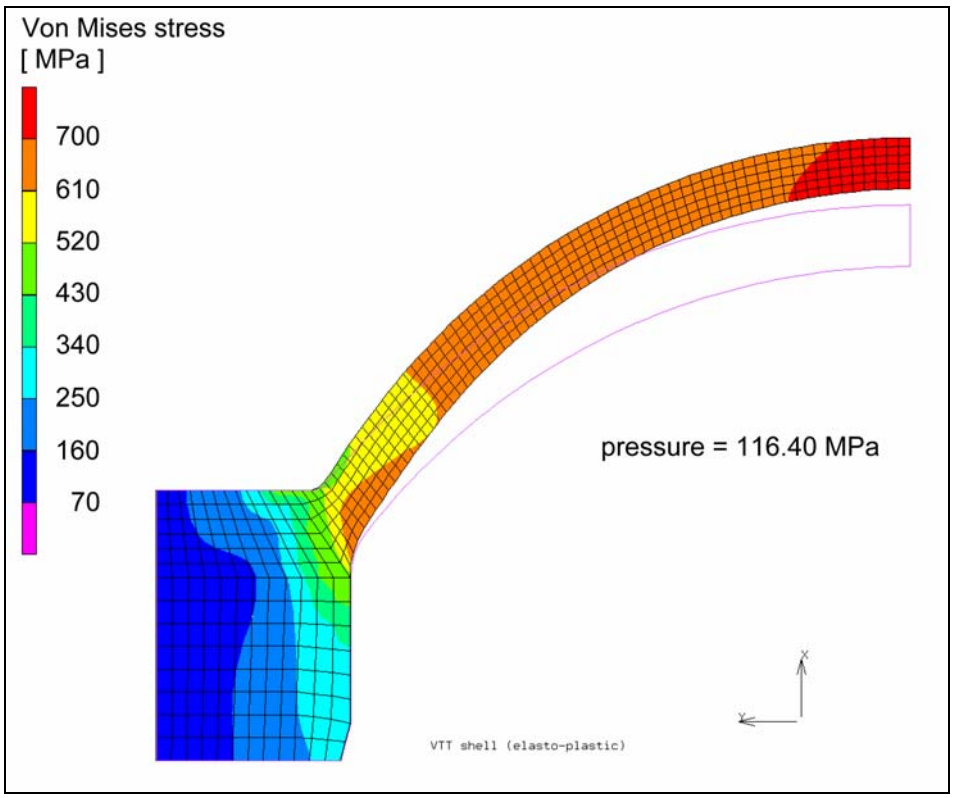

Fig. 3.4.2-3: The Von Mises stress at the pressure load according to the LISSAC admissible strains

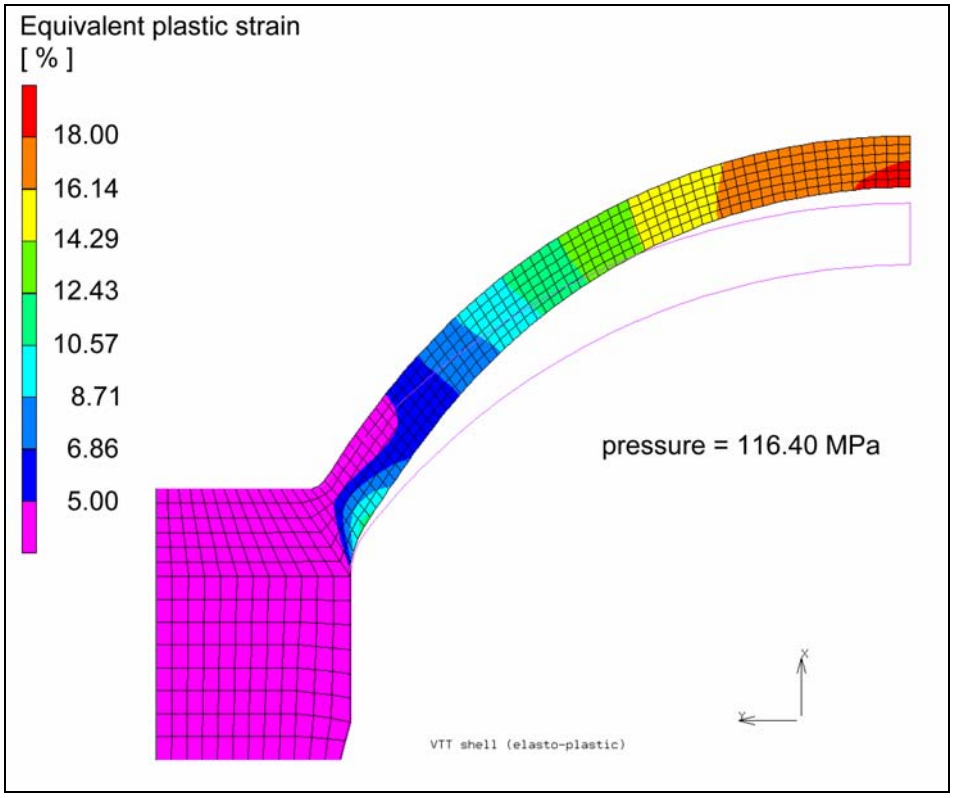

Fig. 3.4.2-4: The equivalent plastic strain at the pressure load according to the LISSAC admissible strains

In the current project a limit strain of 20% is proposed at surfaces with a curvature radius r > 100 mm. Application of this limit strain results in a maximum pressure load of 116.40 MPa. Figure 3.4.2-3 shows the distribution of the equivalent stress on the deformed geometry. Figure 3.4.2-4 shows the distribution of the equivalent plastic strain on the same geometry. It should be noted that the ASME evaluations are based on engineering stresses, while the finite element results are given as true stresses and strains. So the limit strain of 20 % from the current project is also interpreted to be an engineering strain which corresponds with a true strain of approximately 18% as shown in figure 3.4.2-4.

Thus using the admissible strains determined in the current project to calculate the maximum pressure load for the upper head results in an increase by factor 1.28 to 1.89 in comparison to the pressure load according to the ASME evaluations.

Example: Analysis of the reactor vessel support structure

Investigations were performed for a so-called support pad of a reactor pressure vessel of a four loop pressurized water reactor. The finite element discretization of the support pad with a certain section of the pressure vessel wall is shown in Fig. 3.4.2-5. Two cases were considered: Static pressure load at the **top** of the support pad and at the **bottom** of the support pad. Elastic, plastic and limit analyses were performed using a finite element code and assuming elastic plastic material behaviour at room temperature as shown in Fig. 3.1.4-4. For more details see SAM-LISSAC-DXX.

First the results were evaluated according to the ASME code [1], Subsection NB.

The maximum admissible pressure load at the top is

260 ÷ 266 MPa based on elastic-plastic analysis,
280 MPa based on limit analysis.

The maximum admissible pressure load at the bottom is

240 ÷ 256 MPa based on elastic-plastic analysis,
234 MPa based on limit analysis.

To get an impression of the results, the stress distributions from the elastic-plastic analyses are shown in Fig. 3.4.2-6.

Then the results were evaluated using a limit strain of 20 % proposed in the current project at surfaces with a curvature radius r ≥ 100 mm. Using the diagrams Fig. 3.4.2-7 showing the calculated maximum equivalent strain versus the applied pressure, one obtains

a maximum admissible pressure load at the top of

350 MPa

and a maximum admissible pressure load at the bottom of

333 MPa.

Thus using the results of the current project the admissible pressure loads increase by factor of 1.25 ÷ 1.42 in comparison to the admissible loads by applying the ASME code. This benefit is moderate. If dynamic pressure loads were considered, larger increases could be expected.

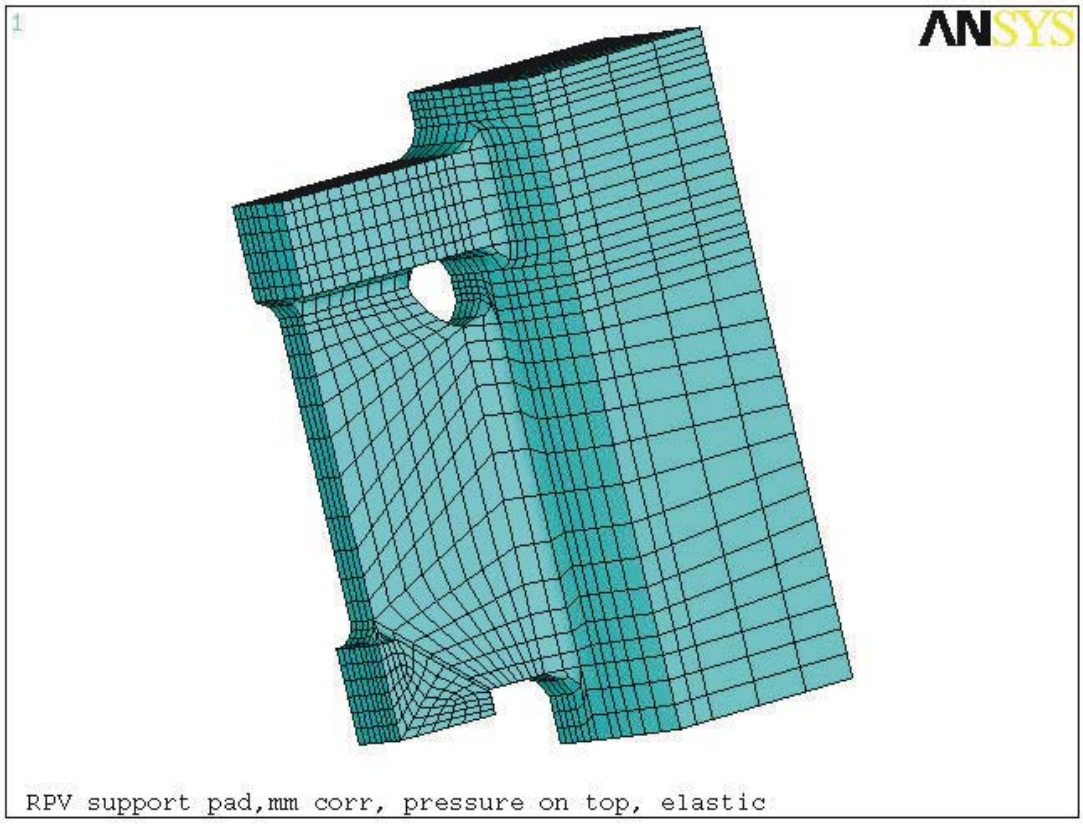

Fig. 3.4.2-5: Finite element model of the support pad with an adjacent section of the pressure vessel

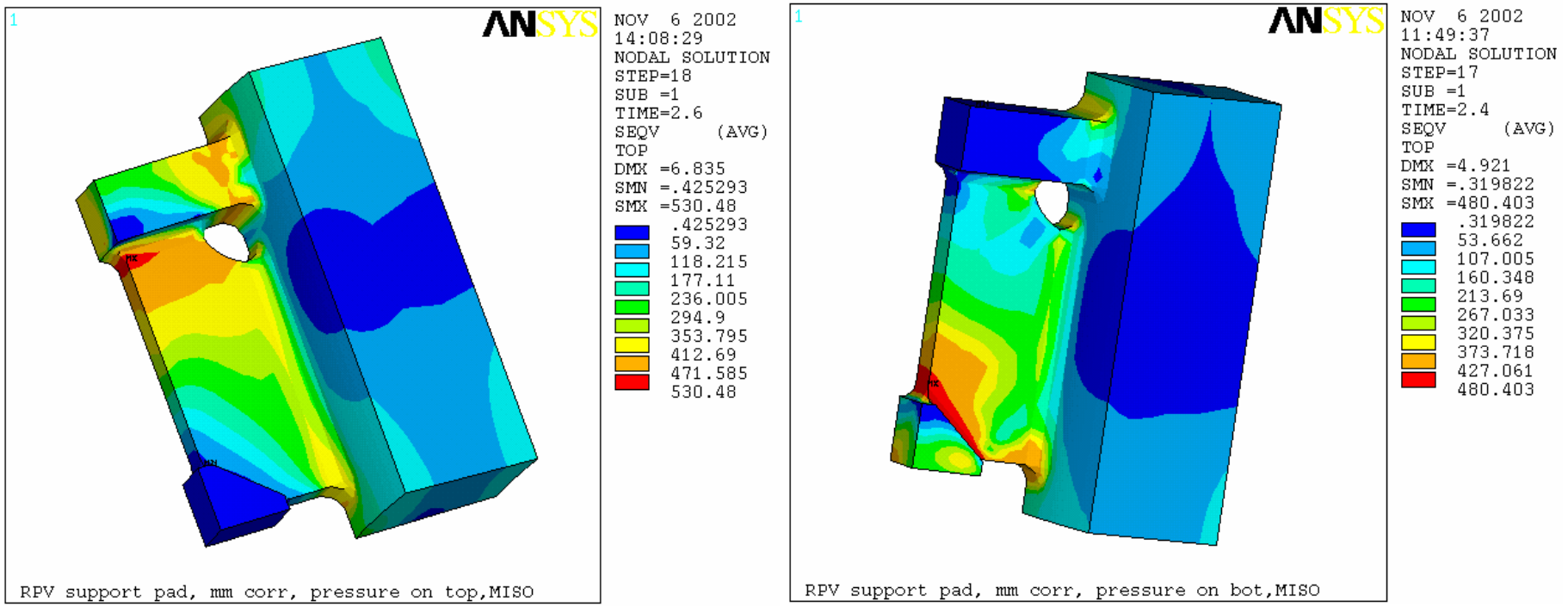

Fig. 3.4.4-6: Stress distributions in the support from elastic-plastic calculations
Left: Pressure load at the top; Right: Pressure load at the bottom

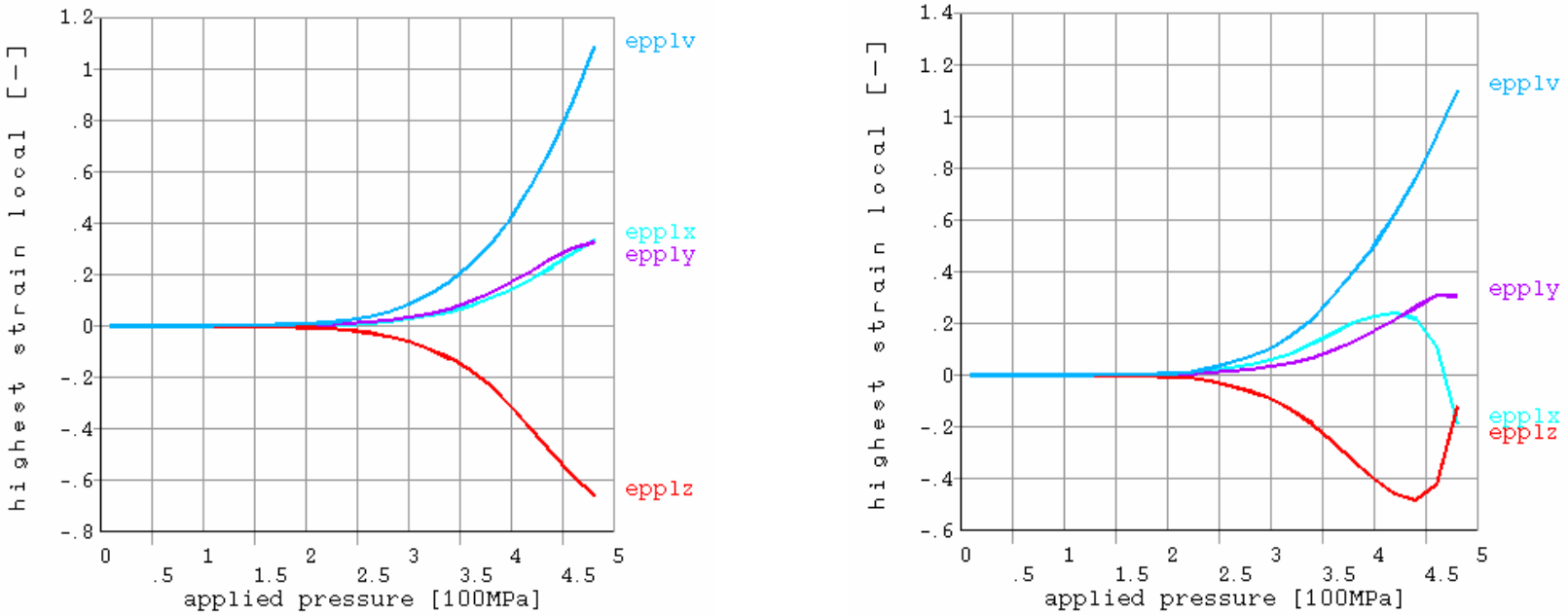

Fig. 3.4.4-7: Maximum local equivalent strain versus applied pressure load from elastic-plastic calculations
Left: Pressure load at the top; Right: Pressure load at the bottom
(epp1v: equivalent strain; epp1x, epp1y, epp1z: strain components)

4 CONCLUSIONS

Stresses versus dimensionless deformations are approximately size independent up to failure for specimens of similar geometry under similar load conditions. Also the maximum stress is approximately size independent, if failure occurs after the maximum stress is reached.

Feasible methods could be developed to determine the local failure strains – here expressed as true or logarithmic strains, respectively – for very different specimens under varying load conditions. The methods are based on post test geometrical measurements of the fracture surfaces allowing a reconstruction of the strain fields using theoretical models. The accuracy of the failure strains obtained in this way could be assessed.

The local failure strains turned out to be more than 50 % for large specimens approaching the dimensions of the reactor pressure vessel.

The local failure strains are size dependent. They reach values around 150 % for small specimens with thicknesses or diameters of a few millimetres. Refer to the diagrams Fig. 3.3.1-1 to 3.3.1-6.

The parameter describing the size effect is the radius of holes or notches located in mostly stressed specimen regions. The shape of the specimen and the type of load plays a minor role for the tests performed within the current project.

Some essential findings about size effects can be understood by theoretical studies considering the stochastic microstructural character of the material.

The scatter of the experimental results on structural failure is considerable. However there are indications that the failure strains will hardly fall below a lower threshold.

Thus limit strains depending on the hole or notch radius in the mostly stressed specimen region could be proposed. They are valid for temperatures up to 400 °C. Dynamic loads are included. Refer to the diagram Fig. 3.3.3-1. Limit strains for higher temperatures up to 850 °C may also be proposed, but the reliability is restricted.

The results are also applicable for geometries and load conditions somewhat different from those investigated in the current project. The applicability can be extended by using the recommended theoretical models developed within the current project. However care must be taken when the stress triaxiality increases. In this case the failure strain may decrease significantly.

If in severe accidents the proposed limit strains will not be exceeded, it can be assumed that the structure will not fail.

A remarkable worthmentioning result is, that under excessive load large fragments of structures can be completely torn off to become missiles. This happened during a biaxial test under quasi static load which was provided by (almost incompressible) pressurized oil.

Application of the proposed limit strains to selected severe accident problems showed that the admissible load increases by a factor between 1.25 and about 2.0 in comparison to using state-of-the-art rules.

Severe accident problems causing higher triaxialities of the stress distributions in the reactor pressure vessel seem not to play an essential role. Nevertheless the applicability of the proposed limit strains to such problems is a very interesting question. To answer it, some supplementary tests with specially chosen (and perhaps more sophisticated) specimens leading to higher triaxial stress distributions as well as accompanying calculations are recommended for a future research project.

5 REFERENCES

To 1.2

[1] Malmberg, T., Tsagrakis, I., Eleftheriadis, I., Aifantis, E.C., On the Gradient Plasticity Approach to Size Effects, Part I: Reviews, INV-REVISA (99)-P011

[2] Malmberg, T., Krompholz, K., Solomos, G., Aifantis, E.C., Investigations on Size Effects in Ferritic and Austenitic Materials, INV-REVISA (99)-P007, Proc. of the 15th Int. Conf. on Structural Mechanics in Reactor Technology (SMiRT-15), paper L06/5, Seoul, Korea, Aug. 15-20, 1999

[3] Schmitt, W., Stöckl, H., Improvement of micro-mechanical methods considering the size influence especially for the applicability with very small material volumes – clarification of problems of transferability (German), Fraunhofer-Institut für Werkstoffmechanik, Final Report T4/99, Feb. 1999

[4] Atkinson, M., Origin of size effect in indentation of metals, Int. J. Mech. Sci., 33, no. 10, 843-850, (1991)

[5] Li, H., Bradt, R.C.: The micro-hardness indentation load/size effect in rutile and cassiterite single crystals, J. of Material Sci., 28, 917-926 (1993)

[6] Stelamshenko, N.A., Walls, M.G., Brown, L.M., Milman, Y.V., Microindentation on W and M_o oriented single crystals, An STM study, Acta Metall. Mater., 41, no. 10, 2855-2865 (1993)

[7] Poole, K.J., Ashby, M.F., Fleck, N.A., Micro-hardness of annealed and work-hardened copper poly-crystals, Scripta Materialia, 34, no. 4, 559-564 (1996)

[8] Jost, A., Bigot, R., Indentation size effect: reality or artefact, J. of Material Sci., 31, 3573-3577 (1996)

[9] McElhaney, K.W., Vlasak, J.J., Nix, W.D., Determination of indenter tip geometry and indentation contact area for depth-sensing indentation experiments, J. Mater. Res., 13, no. 5, 1300-1306 (1998)

[10] Stölken, J.S., Evans, A.G,: A microbend test method for measuring the plasticity length scale, Acta Mater., 46, no. 14, 5109-5115 (1998)

[11] Bazant, Z.P., Planas, I., Fracture and size effect in concrete and other quasi-brittle materials, CRC Press LLC (1998)

[12] Docherty, J.G., Bending tests on geometrically similar notched bar specimen, Engineering , 645-647 (1932)

[13] Docherty, J.G., Slow bending tests on large notched bars, Engineering, 211-213 (1935)

[14] Brown, W.F., Lubahn, J.D., Ebert, K.J., Effects of section size on the static notch bar tensile properties of mild steel plate, Welding J., 26, 554s-559s (1947)

[15] Shearin, P.E., Ruark, A.E., Trinble, R.M., Size effects in steel and other metals from slow notch bend tests, Fracturing of Metals A.S.M., Cleveland, 167-188 (1948)

[16] Lubahn, J.D., Room temperature crack propagation and size effect on mild steel, Welding J., 34, 518s-528s (1955)

[17] Wells, A.A., The geometrical size effect in notch brittle fracture, Trans. N. Coast Inst. Eng., Shipbuilding, 71, 278-290 (1955)

[18] Lubahn, J.D., Yukawa, S., Size effects in slow notch-bend tests of a nickel-molybdenum-vanadium steel, Proc. Am. Soc. Test. Mater. 58, 661-677 (1958)

[19] Wundt, B.M., A unified interpretation of room-temperature strength of notched specimens as influenced by their size, ASME Publication, paper no. 59-MET-9 (1959)

[20] Yukawa, S., McMullin, J.G., Effects of specimen size and notch acuity on the brittle fracture strength of a heat-treated steel, Trans. ASME, J. Basic Eng. 83, 541-544 (1961)

[21] Kußmaul, K., Roos, E., Doll, W., Zirn, R., Sturm, D., Die Bedeutung von Versuchen mit Proben großer Abmessungen, Stahl u. Eisen, 104, no. 18, 913-917 (1984)

[22] Bazant, Z.P., Size effect in blunt fracture: concrete, rock, metal, J. Eng. Mech., 110, no. 4, 518-535 (1984)

[23] Bazant, Z.P., Lee, S.-G., Pfeiffers, P.A., Size effect tests and fracture characteristics of aluminium, Eng. Fract. Mech., 26, no. 1, 45-57 (1987)

[24] Pineau, A., Modelling of scatter and size effects in ductile and brittle fracture, Proc. Of the 14th Int. Conf. on Structural Mechanics in Reactor Technology (SMiRT-14), Plenary lecture 4, Lyon, France, Aug. 17-22, 1997

[25] Marini, B., Carasson, S., Widент, P., Soulat, P., Evaluation of the fracture toughness of a C-MN steel using small notched tensile specimens, in: Small Specimen Test Techniques, (Corvin, W.R., Rosinski, S.T., van Walle, E. (ed.)), ASTM STP 1329, 513-522 (1998)

[26] Giovanola, J.H., Kirkpatrick, S.W., Using the local approach to evaluate scaling effects in ductile fracture, Int. J. of Fracture, 92, 101-116 (1998)

[27] Devos, J., Ritter, B., Auerkari, P., Dupas, P., Malmberg, T., Reactor Vessel Integrity in Severe Accidents, Proc. FISA-97 EU research on severe accidents (Van Goethem, G., Keinhorst, G., Bermego, J.M., Zurita, A. (ed)), Luxembourg, Nov. 17-19, 1997, 113-122, EUR 18258 EN (1998)

[28] Nix, W.D., Gao, H., Indentation size effects in crystalline materials: a law for strain gradient plasticity, J. Mech. Phys. Sol. 46, no. 3, 411-425 (1998)

[29] Gao, H., Huang, Y., Nix, W.D., Hutchinson, J.W., Mechanism-based strain gradient plasticity, I. Theory, J. Mech. Phys. Sol., 47, 1239-1263 (1999)

[30] Aifantis, E.C., Higher order gradients and size effects, in: Size-Scale Effects in the Failure Mechanisms of Materials and Structures (Carpinteri, A. (ed.)), E & FN Spon, London, 231-242 (1996)

[31] Zhu, H.T., Zbib, H.M., Aifantis, E.C., Strain gradients and continuum modelling of size effect in metal matrix composites, Acta Mech. 121, 165-176 (1997)

[32] Tsagrakis, I., Malmberg, T., Aifantis, E.C., Gradient Plasticity and Size Effects, INV-REVISA (98)-P009, Proc. 5th National Congress on Mechanics, Ioamina, Greece, Aug. 1998, 953-960 (1998)

[33] Aifantis, E.C., Strain Gradient Interpretation of Size Effects, INV-REVISA (99)-P004, Int. J. of Fracture, 95, 299-314 (1999)

[34] Tsagrakis, I., Konstantinidis, A., Aifantis, E.C., Strain Gradient and Wavelet Interpretation of Size Effects in Yield and Strength, INV-REVISA (99)-P005

[35] Aifantis, E.C., On the role of gradients in the localisation of deformation and fracture, Int. J. Eng. Sci, 30, 1279-1299 (1992)

To 3.2.1.1

[1] Tsagrakis, I., Aifantis, E.C., Element-Free Galerkin (EFG) Implementation of a Damage Enhanced Flow Theory of Gradient Plasticity in Finite Deformations, LISSAC Contract No FIKS-CT1999-00012, Aristotle University of Thesaloniki, Laboratory of Mechanics and Materials, 12.2002.

[2] Aifantis, E.C., On the microstructural origin of certain inelastic models, J. Engng. Mat. Tech., 106, 326-330 (1984)

[3] Aifantis, E.C., The physics of plastic deformation, Int. J. Plasticity, 3, 211-247 (1987)

[4] Aifantis, E.C., On the role of gradients in the localization of deformation and fracture, Int. J. Engng. Sci. 30, 1279-1299 (1992)

[5] Aifantis, E.C., Pattern formation in plasticity, Int. J. Engng. Sci. 33, 2161-2178 (1995).

[6] Aifantis, E.C., Gradient plasticity, in: Handbook of Materials Behavior Models, (J. Lemaitre, ed.), Academic Press, New York, 281-297 (2001)

[7] Lämmer , H., Tsakmakis, Ch., Discussion of coupled elastoplasticity and damage constitutive equations for small and finite deformations, International Journal of Plasticity, 16, 495-523 (2000).

[8] Dhar, S., Sethuraman, R., Dixit, P.M., A continuum damage mechanics model for void growth and micro crack intiation, Engineering Fracture Mechanics, 53, 917-928 (1996).

[9] Bellenger, E., Bussy, P., Phenomenological modeling and numerical simulation of different modes of creep damage evolution, Int. J. Solids Structures, 38, 577-604 (2001)

[10] Belytschko, T., Lu, Y.Y., Gu, L., Element-free Galerkin methods, Int. J. Num. Methods Engng., 37, 229-256 (1994)

[11] Belytschko, T., Krongauz, Y., Organ, D., Fleming, M., Krysl, P., Meshless methods: an overview and recent developments, Comput. Methods Appl. Mech. Engng., 139, 3-47 (1996).

[12] Seidenfuss, M., Untersuchungen zur Beschreibung des Versagenverhaltens mit Hilfe von Schädigungsmodellen am Beispiel des Werkstoffes 20 MnMoNi55, Dissertation, Universität Stuttgart (1992)

To 3.2.1.2

[1] Chen J., Yuan, H., Kalkhof, D., A nonlocal damage model for elastoplastic materials based on gradient plasticity theory, PSI Bericht Nr. 01-13, Paul Scherrer Institut PSI, Villingen, Schweiz, 10.2001.

[2] Aifantis, E.C., The physics of plastic deformation, Int. J. Plasticity, 3, 211-247 (1987)

[3] Leblond, J.B., Perrin, G., Devaux, J., Bifurcation effects in ductile materials with damage localization, J. Appl. Mech., 61, 236-242 (1994)

[4] Tvergaard, V., Needleman, A., Effects of nonlocal damage in porous plastic solids, Int. J. Solids and Structure, 32, 1063-1077, (1995)

[5] Ramaswamy, S., Aravas, N., Finite element implementation of gradient plasticity models, Part I, Part II, Computer methods in Applied Mechanics and Engineering, 1163, 33-53 (1998)

To 3.2.1.3

[1] Diegele, E., Hofer, D., Tsakmakis, Ch., Simulating size effects of steel with micromorphic theories, LISSAC Contract No FIKS-CT1999-00012, Technische Universität Darmstadt, 01.2003.

[2] Diegele, E., Hofer, D., Tsakmakis, Ch., Formulation of non-local plasticity on the basis of micromorphic continua, SAM-LISSAC-D010, 2002.

[3] Diegele, E., Hofer, D., Theoretical Model of FZK for Work-package WP6 Progress February 2001 to January 2002, SAM-LISSAC-D022, 2002.

[4] Lämmer, H., Tsakmakis, Ch., Discussion of coupled elastoplasticity and damage constitutive equations for small and finite deformations, Int. J. Plasticity 16, 495-523 (2002)

[5] Lemaitre, J., Formulation and identification of damage constitutive equations. Comp. Meth. Appl. Mech. Eng., 51, 31-49 (1985)

To 3.2.2.1

[1] Jordan, T., Implementation of a stochastic material damage model – Summary, LISSAC Contract No FIKS-CT1999-00012, optimiSE GmbH Bruchsal, 02.2003.

[2] Mishnaevsky, L.L., Schmauder, S., Damage evolution and localization in heterogeneous materials under dynamical loading: stochastic modelling, Computational Mechanics, 20, no. 7, 89-94 (1997)

[3] Ostoja-Starzewski, M., Damage in Random Microstructure: Size Effects, Fractals and Entropy Maximization, in: Mechanics Pan-America-1989, ed. C.R. Steele, A.W. Leissa, M.R.M. Crespo da Silva, ASME Press, NY, 1989

[4] Oeksendal, B., Stochastic differential equations, 5th ed., Springer, Berlin (1998)

To 3.2.2.2

[1] Cizelj, L., Kovač, M., Simonovski, I., Petrič, Z., Fabjan, L., Mavko, B.: Elastic-plastic behavior of polycristaline aggregate with stochastic arrangement of grains, Final Report, LISSAC Contract No FIKS-CT1999-00012, Institut "Jožef Stefan", Ljubljana, Slovenija, 12.2002.

[2] Cizelj, L., Kovač, M., Simonovski, I., Petrič, Z., Fabjan, L., Mavko, B.: Elastic-Plastic Behavior of Polycrystalline Aggregate with Stochastic Arrangement of Grains. Project LISSAC: Final Report. Rev 0. Ljubljana, Slovenia: Jožef Stefan Institute; 2002; IJS-DP-8667.

[3] Kovač, M., Influence of Microstructure on Development of Large Deformations in Reactor Pressure Vessel Steel. Ljubljana: University of Ljubljana; to be published

[4] Nemat-Nasser, S., Hori, M., Micromechanics: Overall Properties of Heterogeneous Materials. Amsterdam: North-Holland; 1993.

[5] Huang, Y., A User-material Subroutine Incorporating Single Crystal Plasticity in the ABAQUS Finite Element Program. Cambridge, Massachussets: Harvard University; 1991; MECH-178.

[6] Asaro, R.J., Micromechanics of Crystals and Polycrystals. Micromechanics in Applied Mechanics. 1983; 23-115.

[7] Nemat-Nasser, S., Okinaka, T., Ni, L., A Physically-based Constitutive Model for BCC Crystals with Application to Polycrystalline Tantalum. J. Mechanics and Physics of Solids, 46, no. 6, 1009-1038 (1998)

[8] Cizelj, L., Kovač, M., Petrič, Z., Fabjan, L., Mavko, B., Efects of Grain Structure on Elastic-plastic Behavior of Polycrystalline Aggregate. Rev 0. Ljubljana, Slovenia: Jožef Stefan Institute ; 2002; IJS-DP-8547.

[9] Krieg, R., Aktaa, J., Diegele, E., Dolensky, B., Malmberg, T., Messemer, G., Plitz, H., Rieger, H., Schmitt, R., Julich, P., Kalkhof, D., Taja, H., Solomos, G., Aifantis, E., Cizelj, L., Caroli, C., Fokkens, J., Bhandari, S. B., Veron, P., Trauth, M., Kieselbach, R., Description of an European Research Program and First Results, Proc. Of the 16th International Conference on Structural Mechanics in Reactor Technology (SMIRT-16), Washington DC, USA, 2001

[10] Simonovski, I., Kovač, M., Cizelj, L., Correlation Length as Estimate of the Domain of Influence of Crystal Grain. Proc. of Int. Conf. Nuclear Energy for New Europe 2002; Kranjska Gora. Ljubljana: Društvo jedrskih strokovnjakov Slovenije; in print.

[11] Grimvall, G.: Thermophysical Properties of Materials. Amsterdam, North-Holland; 1999.

[12] Frost, H.J., Ashby, M.F., Deformation-Mechanism Maps. Pergamon Press; 1982; ISBN: 0-08-029338-7.

[13] Kröner, E., The Statistical Basis of Polycrystal Plasticity. in: Gittus, John; Zarka, Joseph, and Nemat-Nasser, Siavouche, Editors. Large Deformations of Solids: PhysicalBasis and Mathematical Modelling. Elsevier Applied Science, 27-40 (1986)

[14] Materna-Morris, E., Graf, P., Zimmermann, H.: Structure and Fracture of 22NiMoCr3 7, Forschungszentrum Karlsruhe, Germany, 2002

[15] Tensile Tests, Specimens 5 mm for LISSAC. EMPA; 2001; Test Report, Nr. 201951/01.

[16] Kovač, M., Cizelj, L., Mesoscopic Approach to Modeling Elastic-Plastic Polycrystalline Material Behavior. Proc. of Int. Conf. Nuclear Energy in Cental Europe 2001; Portorož, Slovenia. Ljubljana: Društvo jedrskih strokovnjakov Slovenije, 2001.

[17] Weyer, S., Experimentelle Untersuchung und mikromechanische Modellierung des Schädigungsverhaltens von Aluminiumoxid unter Druckbeanspruchung. Karlsruhe, Germany: Universität Karlsruhe; 2001.

[18] Seidenfuss, M., Review of Rousselier's damage model for describing ductile fracture, (2001)

[19] Lemaitre, J., A Course on Damage Mechanics. Springer-Verlag, 1996.

[20] Modi, A., Unstructured Mesh Generation on Planes and Surfaces using Graded Triangulation, 1997. http://bart.aero.psu.edu/btp/main/main.html.

[21] Aurenhammer, F., Voronoi Diagrams-A Survey of a Fundamental Geometric Data Structure, ACM Computing Surveys, 23, no. 3, 345-405 (1991)

To 3.2.3.1

[1] Seidenfuss M., Predictions of limit strains with the Rousselier damage model, Final Report, LISSAC Contract No FIKS-CT1999-00012, MPA Stuttgart, Germany 01.2003.

[2] ADINA 7.4, ADINA R&D, Inc., 71 Elton Avenue, Watertown, MA 02472, USA

[3] Gurland J., Plateau, J., The mechanism of ductile rupture of metals containing inclusions, Transaction of the ASM, 56, 442-454 (1963)

[4] Stroppe, H., Ermittlung der Bruchzähigkeit duktiler Werkstoffe aus Parametern der Mikrostruktur und der Fließkurve, Neue Hütte, 26. Jahrgang, Heft 12, 446-448 (1981)

[5] Rousselier, G., Ductile Fracture Models and their Potential in Local Approach of Fracture, Nuclear Engineering and Design, 105, 97-111 (1987)

[6] Demler, T., Untersuchungen zum Einfluss der Beanspruchungsgeschwindigkeit auf das Festigkeits- und Zähigkeitsverhalten von Feinkornbaustählen, Dissertation Universität Stuttgart, 1990

[7] Kußmaul, K., Klenk, A., Schüle, M., Forschungsvorhaben 1500 825 Rißverhalten bei dynamischer Beanspruchung, Abschlussbericht, MPA Stuttgart, Germany, Mai 1994

[8] Cowper, G.R., Symonds, P.S., Strain Hardening and Strain Rate Effects in the Impact Loading of Centilever Beams, Techn. Report No. 28, Contract No. 562(10), Brown University, Providence, RI, 1957

[9] Kieselbach, R., Michel, H., Tensile Tests; Specimens 5 mm for LISSAC, Test Report Nr. 201951/01, EMPA Schweiz; March 2001

[10] Seidenfuss, M., Seebich, H.-P., Predictions by the theoretical methods; Rousselier model, EU project Limit Strains for Severe Accident Conditions (LISSAC), CONTRACT N° FIKS-CT1999-00012, Deliverable D11, Work-package WP8 MPA-Stuttgart Germany, May 2002

[11] Solomos, G., Pizzinato, V., Kiefer, R., Brogneri, E., Dynamic Testing of the Pressure Vessel Steel 22NiMoCr3-7 at Room and higher Temperatures, Deliverable D8, Workpackage WP4, EU project Limit Strains for Severe Accident Conditions (LISSAC), CONTRACT N° FIKS-CT1999-00012, JRC Ispra Italy,2002

[12] Procedure to measure and calculate material parameters for the local approach to fracture using notched tensile specimens, ESIS P6-98, March 1998

[13] Krieg, R., Jordan, T., Minutes of the seventh LISSAC Project Meeting, SAM – LISSAC(02)-M11, FZK-IRS Karlsruhe Germany, 7. and 8. November 2002

To 3.2.3.2

[1] Church, J.M., LISSAC - Review of the Gurson-Tvergaard Model of Ductile Damage Accumulation, NRG report 20292/01.38931/P, 25 January 2001

[2] de Groot, S., Church, J.M., LISSAC - Study on the implementation of the Gurson-Tvergaard damage model in Finite Element code MARC, NRG report 20292/02.46866/C, 29 March 2002

[3] Chen, J., Yuan, H., Kalkhof, D., A Nonlocal Damage Model for Elastoplastic Materials based on Gradient Plasticity Theory, PSI Bericht Nr. 01-13, Oktober 2001, ISSN 1019-0643

[4] Fokkens J., Final Report, LISSAC Contract No FIKS-CT1999-00012, NRG Netherlands, 03.2003.

[5] MARC User's Manuals, MSC Software Corporation, MSC.Marc - Version 2001

To 3.3.2.1

[1] Student, The Probable Error of a Mean, Biometrika, 6, 1-25 (1908).

[2] Fisher, R. A., Statistical Methods for Research Workers, 10th ed. Edinburgh: Oliver and Boyd (1948).

To 3.4.1

[1] Krieg, R., Dolensky, B. Göller, B., Hailfinger, G., Jordan, T., Messemer, G., Prothmann, N., Stratmanns, E., Load carrying capacity of a reactor vessel head under molten core slug impact., Nucl. Eng. and Design, 2813 1-17 (2003)

To 3.4.2

[38] ASME Boiler and Pressure Vessel Code, Edition 1998 plus Addenda up to 2000, Section III, Div. 1

Detailled information about the current project is documented in the internal LISSAC reports listed below:

Dolenksy, B., Cutting Plan for the Unshaped Specimens for LISSAC, SAM-LISSAC-D001

Julisch, P., Test Results for Flat Specimens Containing one Central Hole, WP2 Specimens AK1 and AK2, thickness 20 mm, Specimen AJ1, thickness 40 mm, Room temperature, static tension, hole: half the thickness, SAM-LISSAC-D002

Dolensky, B., Revised Test Matrix and Cutting Plan for the Test Specimens, SAM-LISSAC-D003

Jordan, T., Karner, G., On a Stochastic Model for Material Damage, SAM-LISSAC-D004

Seidenfuss, M., Review of Rousselier's damage model for describing ductile fracture, SAM-LISSAC-D005

Chen, J., Yuan, H., Kalkhof, D., Wittmann, F.H., Computational investigations of ductile failure processes using a non-local micro-mechanical damage model, SAM-LISSAC-D006

Cizelj, L., Kovač, M., Constitutive Models for the Elastic-Plastic Polycrystalline Aggregate with Stochastic Arrangement of Grains, SAM-LISSAC-D007

Miliozzi, A., Caroli, C., The Lemaitre-Chaboche coupled damage elastic plastic model in the Castem 2000 code, SAM-LISSAC-D008

Church, J.M., Review of the Gurson-Tvergaard Model of Ductile Damage Accumulation, SAM-LISSAC-D009

Diegele, E., Hofer, D., Tsakmakis, Ch., Formulation of nonlocal plasticity on the basis of micromorphic continua, SAM-LISSAC-D010

Krieg, R., Aktaa, Diegele, E., Dolensky, B., Jordan, T., Malmberg, T., Messemer, G., Plitz, H., Rieger, H., Schmitt, R., Investigations to Size Effects on Plastic Deformation and Failure Behavior of Inhomogeneously Loaded Structures, SAM-LISSAC-D011

Aktaa, J., J., Hädrich, H., Julisch, P., Klotz, M., Schmitt, R., Investigations to Size Effects on Plastic Deformation and Failure Behavior of Inhomogeneously Loaded Structures, SAM-LISSAC-D012

Aifantis, E.C., On the Finite Element Solution of the Gradient Elasticity Boundary Value Problem, SAM-LISSAC-D013

Chen, J., Yuan, H., Kalkhof, D., A Nonlocal Damage Model for Elastoplastic Materials based on Gradient Plasticity Theory, SAM-LISSAC-D014

Aktaa, J., Dolensky, B., Krieg, R., Messemer, G., Schmitt, R., Julisch, P., Talja, H., Solomos, G., Kieselbach, R., Limit strains for impact load. First experimental results of an European Research Program, SAM-LISSAC-D015

Cizelj, L., Kovše , M., Petrič, Z., Fabjan, L, Mavko, B., Effects of Grain Structure on Elastic-plastic behavior of Polycrystalline Aggregate, SAM-LISSAC-D016

Seidenfuss, M., Seebich, H., Predictions by the theoretical methods, SAM-LISSAC-D017

De Groot, S., Church, J.M., Study on the Implementation of the Gurson-Tvergaard Damage Model in the Finite Element Code MARC, SAM-LISSAC-D018

Chruch, J.M., Review of the Gurson-Tvergaard Model of Ductile Damage Accumulation, SAM-LISSAC-D019

Solomos, G., Pizzinato, V., Kiefer, R., Brogneri, E., Dynamic Testing of the Pressure Vessel Steel 22 NiMoCr 37 at Room and Higher Temperatures, SAM-LISSAC-D020

Keinänen, H., Talja, H., Estimation of the limit load and strength of the LISSAC pressure test specimen, SAM-LISSAC-D021

Diegele, E., Hofer, D., Theoretical Model of FZK for Work-package WP6 Progress February 2001 to January 2002, SAM-LISSAC-D022

Jordan, T., Implementierung eines stochastischen Materialmodells, SAM-LISSAC-D023

Julisch, P., Results of Static Tensile Tests with Large Specimens, SAM-LISSAC-D024

Krieg, R., Dolensky, B., Methods to determine the local failure strains for the broken LISSAC specimens, SAM-LISSAC-D025

Benhamou, C., Standard Tensile Tests for Material Qualification, SAM-LISSAC-D026

Krieg, R., Dolensky, B., Finite element calculations with ABAQUS for the LISSAC tension specimens with holes or notches, SAM-LISSAC-D027

Dolensky, B., Messemer, G., Lux, M., Prothmann, N., Rieger, H., Experiments and calculations for curved biaxial specimens without and with holes under dynamic load, SAM-LISSAC-D028

Hailfinger, G., Krieg, R., Failure strains determined for the LISSAC tests, SAM-LISSAC-D029

Talja, H., Experiments and calculations for curved biaxial specimens without and with holes under static loading, SAM-LISSAC-D030

Aktaa, J., Klotz, M., Schmitt, R., Results of Static Tensile Tests with Medium and Small Specimens at Room Temperature, SAM-LISSAC-D031

Hartmann, G., Kieselbach, R., Michel, H., Results of Static Tensile Tests with Medium and Small Specimens at Elevated Temperatures Results of Bending Tests, SAM-LISSAC-D032

Solomos, G., Results of dynamic Tests, SAM-LISSAC-D033

Schramm, K., Analysis of the reactor vessel support structure, SAM-LISSAC-D034

Tsagrakis, I., Aifantis, E.C., Element-Free Galerkin (EFG) Implementation of a Damage Enhanced Flow Theory of Gradient Plasticity in Finite Deformations, SAM-LISSAC-D035

Cizelj, L., Kovač, M., Simonovski, I., Petrič, Z., Fabjan, L., Mavko. B., Elastic-Plastic behaviour of polycrystalline aggregate with stochastic arrangement of grains, SAM-LISSAC-D036

Malmberg, T., Similarity and size effects in the quasi-static testing of notched specimens – a review, SAM-LISSAC-D037